
The Dark Side of the Higgs

Searches for dark matter with a focus on invisibly decaying Higgs bosons using the full Run-2 dataset of the CMS experiment at the LHC

By

ESHWEN BHAL



School of Physics
UNIVERSITY OF BRISTOL

A dissertation submitted to the University of Bristol in accordance with the requirements for award of the degree of DOCTOR OF PHILOSOPHY in the Faculty of Science.

DECEMBER 2020

Word count: number in words

ABSTRACT

Dark matter is a poorly-understood phenomenon in nature. Though substantial evidence corroborates its existence, only few characteristics have been determined. One goal of the Large Hadron Collider (LHC) at CERN is to produce dark matter in high energy proton-proton collisions, potentially allowing insight into its currently-mysterious origins. Many hypotheses have been postulated regarding its nature, two of which are investigated in this thesis: invisible decays of the Higgs boson, and the production of semi-visible jets. The data used is from the LHC Run-2 era and recorded by the CMS experiment, corresponding to an integrated luminosity of 137 fb^{-1} at a centre of mass energy of 13 TeV.

The branching ratio of the Higgs boson to invisible states is predicted as 0.1 % in the standard model. Enhancements from a coupling to dark matter may be detectable at the LHC. A search is performed in final states comprising jets and missing transverse momentum targeting three of the Higgs boson's production modes: $t\bar{t}H$, VH , and ggH . With the full Run-2 dataset from CMS, no significant deviation from the standard model was observed. Results are presented as an upper limit on the measured cross section times branching ratio over the standard model Higgs boson cross section at a 95% confidence level. For the $t\bar{t}H$ -tagged, VH -tagged, and ggH -tagged events, observed (expected) limits of XX (YY), XX (YY), and XX (YY), respectively were achieved. A combined Run-2 limit of XX was observed and YY expected. Interpretations are provided in simplified dark matter scenarios.

Dark matter may exist in a Hidden Valley dark sector connected to the visible universe via a leptophobic mediator. Analogous to QCD, dark quarks may be produced in the LHC, hadronising and decaying into a mixture of visible and invisible particles (a semi-visible jet). The behaviour of simulated signal from s - and t -channel production modes in the CMS detector—and variables discriminating it from background—is explored. The transverse mass of the dijet system was found to be the most effective.

DEDICATION AND ACKNOWLEDGEMENTS

This work is dedicated to my grandfather, Dato' Mahindar Singh Bhal, who was able to begin this journey with me but sadly unable to finish it. There are far too many people and too little space to individually thank everyone who has accompanied me during this PhD, but I'll try my best.

Firstly, to my supervisor, Dr. Henning Flächer. Your advice and guidance over the course of this degree has been instrumental to achieving it, as well as encouraging my growth as a researcher.

Secondly, to all my colleagues at the University of Bristol. Very little would have been achieved without your help. From scientific discussions in the pub to pub discussions in the physics building, they have all been fruitful either directly or by helping me detach from work. Special thanks are in order to Simone and Sam Maddrell-Mander in my cohort, who have put up with my complaining during the stressful times, as well as Ben Krikler and Olivier Davignon, the postdocs who likely helped me solve the issues I was complaining about.

To my friends from Monmouth that include my best friends in the world, Mike, James, Sneddon, (Mini) Sam, and Matt Bristow. You've been on this adventure with me since our school days and had my back the entire time. We've been through the highest, lowest, and most hilarious times together. I can definitively say I would not be the person I am today without you.

To my friends from LTA and those based at CERN, especially Dwayne, Vukasin, and Matt Heath. You became my second family while I was in Geneva. I'll miss the skiing, trips into the city, games, and general banter.

To my undergraduate cohort from Exeter. Though our meet ups are rare, I always look forward to our group holidays and hope they continue far into the future.

Lorenza Iacobuzio, you get a special mention. While we weren't especially close until recently, you've been my sage, partner in food, and exceptional friend when I've needed it the most.

Finally, and most importantly, my family deserve my thanks. You have been there for me since the very beginning supporting me through school, undergrad, PhD, and every other endeavour. To my grandparents, uncles, aunties, and cousins, my siblings Joe, Lydia, Sitara, and Arjen, my stepmum Nadia, and my cat Pixie, I am sincerely grateful to have you in my lives. But above all else, to my mum Meeta and dad Kiron, I could not have done any of this without you and as such, you have my deepest and most heartfelt love and gratitude.

AUTHOR'S DECLARATION

I declare that the work in this dissertation was carried out in accordance with the requirements of the University's *Regulations and Code of Practice for Research Degree Programmes* and that it has not been submitted for any other academic award. Except where indicated by specific reference in the text, the work is the candidate's own work. Work done in collaboration with, or with the assistance of, others, is indicated as such. Any views expressed in the dissertation are those of the author.

SIGNED: DATE:

TABLE OF CONTENTS

	Page
List of Figures	xi
List of Tables	xvii
1 Introduction	1
1.1 Evidence for dark matter	1
1.1.1 Alternative theories to dark matter	3
1.2 Overview of dark matter searches	4
1.2.1 Dark matter searches at the LHC	4
2 The standard model and beyond	9
2.1 The standard model of particle physics	9
2.1.1 Particles of the standard model	10
2.1.2 Symmetries and gauge invariance	11
2.1.3 Electroweak symmetry breaking and the Higgs mechanism	12
2.1.4 Masses of the fermions	15
2.1.5 Limitations of the standard model	15
2.2 Theoretical motivations for, and descriptions of, dark matter	16
2.3 Measuring the branching ratio of invisibly decaying Higgs bosons	18
2.3.1 Production modes of the Higgs boson	19
2.3.2 Results of previous searches	22
2.4 Searches for semi-visible jets	22
2.4.1 Kinematics and free parameters of the model	24
3 The LHC and the CMS experiment	27
3.1 The Large Hadron Collider	27
3.1.1 A proton's journey	28

TABLE OF CONTENTS

3.1.2	Luminosity	30
3.1.3	Pileup	31
3.1.4	Evolution of the LHC	31
3.2	The CMS experiment	33
3.2.1	The CMS detector	34
3.2.2	Data acquisition and triggering	40
3.2.3	Simulating CMS data	44
3.2.4	Jet energy corrections in the Level-1 Trigger	44
4	Definitions of physics objects and observables	49
4.1	Ubiquitous observables and quantities in collider physics	49
4.1.1	Transverse momentum (\vec{p}_T)	49
4.1.2	H_T	50
4.1.3	Missing transverse momentum (\vec{p}_T^{miss})	50
4.1.4	Transverse mass (m_T)	50
4.2	Classification of analysis-level physics objects	51
4.2.1	Jets	51
4.2.2	Boosted topologies originating from top quarks and electroweak bosons	54
4.2.3	Muons	55
4.2.4	Electrons	55
4.2.5	Photons	56
4.2.6	Tau leptons	57
4.2.7	Overlap removal	58
4.2.8	Revised energy sums \vec{p}_T^{miss} , H_T , and \vec{H}_T^{miss}	58
5	Search for semi-visible jets	59
5.1	Analysis summary	59
5.2	Signal simulation overview	60
5.3	Generation in PYTHIA	61
5.4	Showering in PYTHIA	61
5.4.1	Hadronisation of dark quarks	61
5.4.2	Jet clustering	63
5.4.3	Filtering events	64
5.5	Generation in MADGRAPH	64
5.5.1	MADGRAPH run settings	65
5.5.2	s -channel	66

5.5.3	<i>t</i> -channel	68
5.6	PYTHIA-MADGRAPH comparisons for <i>s</i> -channel signal	70
6	Search for invisibly decaying Higgs bosons	75
6.1	Overview of the analysis	75
6.1.1	Analysis strategy	76
6.2	Only tools and forces: software and toolkits	77
6.3	Data and simulation	78
6.3.1	Data	78
6.3.2	Simulated signal processes	79
6.3.3	Simulated background processes	79
6.3.4	Cross section reweighting	81
6.4	Categorisation of the production modes	81
6.4.1	<i>t</i> <i>tH</i> subcategories	83
6.4.2	<i>VH</i> subcategories	83
6.4.3	<i>ggH</i> subcategories	83
6.4.4	Optimisation of the categories	84
6.5	Signal region, control region, and sideband definitions	87
6.5.1	The signal region	88
6.5.2	Control regions	89
6.5.3	Sidebands to the signal region	94
6.6	Event selection	95
6.6.1	Preselection	97
6.6.2	Additional filters	98
6.6.3	Mitigating the HEM issue	99
6.7	Weights, corrections, and systematic uncertainties for simulation	100
6.7.1	Pileup reweighting	101
6.7.2	Higher order corrections to <i>V</i> + jets samples	102
6.7.3	Efficiency of the triggers	103
6.7.4	Top quark processes	105
6.7.5	Object-level scale factors and uncertainties	108
6.7.6	Minor contributions	110
6.8	Statistical model and fit	111
6.8.1	Binning	113
6.8.2	Background estimation	114

TABLE OF CONTENTS

6.9	Analysis of the $t\bar{t}H$ mode	117
6.10	Analysis of the VH mode	123
6.11	Analysis of the ggH mode	127
6.12	Combined results	132
6.13	Interpretations in simplified dark matter scenarios	135
6.13.1	Higgs portal model with the standard model Higgs boson	135
6.13.2	Constraints on a standard model-like Higgs boson	136
7	Conclusions	139
7.1	$H \rightarrow$ invisible	139
7.2	Semi-visible jets	140
A	Post-fit distributions from the Higgs to invisible analysis	143
A.1	Post-fit distributions of the control regions in the $t\bar{t}H$ category	143
A.2	Post-fit distributions of the control regions in the VH category	147
A.3	Post-fit distributions of the control regions in the ggH category	150
Bibliography		153
Glossary		167
Acronyms		169

LIST OF FIGURES

FIGURE	Page
1.1 A visual representation of the three main types of dark matter detection: direct, indirect, and production	5
1.2 The expected masses and interaction cross sections of some dark matter candidates. The LHC, with its centre of mass energy of 13 TeV, is best suited to targeting WIMPs	6
2.1 A depiction of the Higgs potential V as a function of the component fields	13
2.2 A measure of the comoving number density of WIMP dark matter as a function of time with projections for different particle masses	17
2.3 A subset of the Feynman diagrams for the four predominant production mechanisms of the Higgs boson at the LHC	20
2.4 Example Feynman diagrams for the two main production modes of semi-visible jets. A Z' boson mediates the s -channel process while a bi-fundamental Φ mediates the t -channel process	24
2.5 The constituents of a semi-visible jet as a function of its invisible fraction	25
2.6 The typical direction of the missing transverse energy relative to the semi-visible jets as a function of the invisible fraction r_{inv}	25
3.1 A schematic of the CERN accelerator complex	29
3.2 The average number of pileup interactions per bunch crossing at CMS during Run-2 of the LHC	32
3.3 The integrated luminosity of pp collision data delivered to CMS during Run-2 of the LHC	33
3.4 A cutaway diagram of the CMS detector with all of the principal components labelled. This detector configuration was used for the 2017–18 data taking years	35
3.5 A quadrant of the CMS detector illustrating the main subsystems with their radius R , longitudinal distance z , and pseudorapidity η from the interaction point	36

LIST OF FIGURES

3.6	A transverse slice through the barrel section of the CMS detector with the main subsystems and components visible	40
3.7	A summary of the CMS Level-1 Trigger data flow from the hits recorded by the subsystems to the Global Trigger	42
3.8	Examples of correction curves used to calibrate the jet energies in two $ \eta $ bins	46
3.9	The energies of matched pairs of jets from simulation in the entire barrel and end cap, in the pileup 40–50 range, before and after jet energy corrections have been applied	47
3.10	The response curves in each $ \eta $ bin as a function of p_T^{L1} , in the pileup 40–50 range, before and after jet energy corrections are applied	47
5.1	A diagram of the mass insertion decay of π_{dark} mesons in the s -channel semi-visible jet model	62
5.2	The dependence of the dark force scale Λ_{dark} on the dark hadron mass m_{dark} for each value of α_{dark} used in the thesis	63
5.3	Distributions of the transverse mass of the dijet system m_T for s -channel semi-visible jet samples emulating the 2016 data taking period. In each panel, one of the free parameters of the model is varied with respect to the benchmark point SVJ_3000_20_0.3_peak	67
5.4	Distributions of the transverse mass of the dijet system m_T for s -channel semi-visible jet samples emulating the 2016 data taking period. In each panel, one of the free parameters of the model is varied with respect to the benchmark point SVJ_2000_20_0.5_peak	69
5.5	Distributions of several observables for the models SVJ_1000_20_0.3_peak, SVJ_-3000_20_0.1_peak, and SVJ_3000_20_0.9_peak	71
5.6	Distributions of several observables for the models SVJ_3000_20_0.5_peak, SVJ_-3000_50_0.3_peak, and SVJ_4000_20_0.3_peak	72
6.1	Distributions of $\tilde{\omega}_{\min}$ in the signal region in the $t\bar{t}H$, VH , and ggH categories, along with the significance—using several figures of merit—if a cut is placed to the right of a given value	87
6.2	Composition of each subcategory in the signal region for simulated signal and background processes after the analysis-level selection	89
6.3	Composition of each subcategory in each of the control regions for simulated background processes after the analysis-level selection	92

6.4	The fraction of impure photons in data as a function of p_T for each data taking year in Run-2	94
6.5	Data-simulation comparisons of the p_T^{miss} distribution in the tight double sideband for the combined boosted and resolved categories for the $t\bar{t}H$ and VH processes, using the full Run-2 dataset	96
6.6	Data-simulation comparisons of the p_T^{miss} distribution in the loose double sideband for the combined boosted and resolved categories for the $t\bar{t}H$ and VH processes, using the full Run-2 dataset	96
6.7	Data-simulation comparisons of the p_T^{miss} distribution in the $H_T^{\text{miss}}/p_T^{\text{miss}}$ sideband for the combined boosted and resolved categories for the $t\bar{t}H$ and VH processes, using the full Run-2 dataset	96
6.8	Data-simulation comparisons of the p_T^{miss} distribution in the tight $\tilde{\omega}_{\min}$ sideband for the combined boosted and resolved categories for the $t\bar{t}H$ and VH processes, using the full Run-2 dataset	97
6.9	Data-simulation comparisons of the p_T^{miss} distribution in the loose $\tilde{\omega}_{\min}$ sideband for the combined boosted and resolved categories for the $t\bar{t}H$ and VH processes, using the full Run-2 dataset	97
6.10	The azimuthal angle of the \vec{p}_T^{miss} in the $t\bar{t}H$ and VH categories before and after applying the selections designed to mitigate the HEM issue in 2018	100
6.11	The pseudorapidity of the electron in the VH category of the $e + \text{jets}$ control region before applying the selection designed to mitigate the HEM issue in 2018	101
6.12	NLO k -factors—as a function of the generator-level boson p_T and leading jet p_T —used to reweight events in LO QCD W and $Z + \text{jets}$ simulation to NLO accuracy in QCD	103
6.13	NLO k -factors as a function of generator-level boson p_T used to reweight QCD $V + \text{jets}$ events generated at LO electroweak accuracy	104
6.14	Scale factors accounting for the efficiencies of the HLT $p_T^{\text{miss}} - H_T^{\text{miss}}$ cross triggers in each data taking year of Run-2	106
6.15	The deviations relative to the nominal weight of the combinations of QCD renormalisation and factorisation scale variations. They are presented as a function of p_T^{miss} in the $t\bar{t}H$ categories for the $t\bar{t}$ samples	107
6.16	The ratio of the NNLO to NLO $t\bar{t}$ cross section as a function of top quark p_T . The fit to the distribution—along with the uncertainties in the parameters—are shown	108
6.17	An infographic showcasing the role of each analysis region in the final fit	115

LIST OF FIGURES

6.18 Observed and expected 95 % CL upper limits on the Higgs boson to invisible state branching fraction in the $t\bar{t}H$ category, for both the individual subcategories, and the combination of them, for each data-taking year in Run-2	119
6.19 Pre-fit and post-fit yields in the signal region for each $t\bar{t}H$ subcategory and p_T^{miss} bin for the 2016 dataset	120
6.20 Pre-fit and post-fit yields in the signal region for each $t\bar{t}H$ subcategory and p_T^{miss} bin for the 2017 dataset	121
6.21 Pre-fit and post-fit yields in the signal region for each $t\bar{t}H$ subcategory and p_T^{miss} bin for the 2018 dataset	122
6.22 Observed and expected 95 % CL upper limits on the Higgs boson to invisible state branching fraction in the VH category, for both the individual subcategories, and the combination of them, for each data-taking year in Run-2	123
6.23 Pre-fit and post-fit yields in the signal region for each VH subcategory and p_T^{miss} bin for the 2016 dataset	124
6.24 Pre-fit and post-fit yields in the signal region for each VH subcategory and p_T^{miss} bin for the 2017 dataset	125
6.25 Pre-fit and post-fit yields in the signal region for each VH subcategory and p_T^{miss} bin for the 2018 dataset	126
6.26 Observed and expected 95 % CL upper limits on the Higgs boson to invisible state branching fraction in the ggH category, for both the individual subcategories, and the combination of them, for each data-taking year in Run-2	128
6.27 Pre-fit and post-fit yields in the signal region for each ggH subcategory and p_T^{miss} bin for the 2016 dataset	129
6.28 Pre-fit and post-fit yields in the signal region for each ggH subcategory and p_T^{miss} bin for the 2017 dataset	130
6.29 Pre-fit and post-fit yields in the signal region for each ggH subcategory and p_T^{miss} bin for the 2018 dataset	131
6.30 Observed and expected 95 % CL upper limit on the Higgs boson to invisible state branching fraction $\mathcal{B}(H \rightarrow \text{invisible})$ and the corresponding profile likelihood ratio as a function of it, for both the individual categories that target a specific production mode, as well as the combination of them, for the 2016 dataset . . .	132
6.31 Observed and expected 95 % CL upper limit on the Higgs boson to invisible state branching fraction $\mathcal{B}(H \rightarrow \text{invisible})$ and the corresponding profile likelihood ratio as a function of it, for both the individual categories that target a specific production mode, as well as the combination of them, for the 2017 dataset . . .	133

6.32	Observed and expected 95 % CL upper limit on the Higgs boson to invisible state branching fraction $\mathcal{B}(H \rightarrow \text{invisible})$ and the corresponding profile likelihood ratio as a function of it, for both the individual categories that target a specific production mode, as well as the combination of them, for the 2018 dataset	133
6.33	Observed and expected 95 % CL upper limit on the Higgs boson to invisible state branching fraction $\mathcal{B}(H \rightarrow \text{invisible})$ and the corresponding profile likelihood ratio as a function of it, for both the individual data taking years, as well as the combination of them, for the full Run-2 dataset	134
6.34	Observed and expected 95 % CL upper limit on the Higgs boson to invisible state branching fraction $\mathcal{B}(H \rightarrow \text{invisible})$ and the corresponding profile likelihood ratio as a function of it, for both the individual categories, as well as the combination of them, for the full Run-2 dataset	134
6.35	90 % confidence level upper limits on the spin-independent dark matter-nucleon scattering cross section in Higgs portal models, where the standard model Higgs boson decays into a pair of scalar (solid orange) or fermion (dashed red) dark matter particles	136
A.1	Post-fit yields for each $t\bar{t}H$ subcategory and p_T^{miss} bin in the lepton control regions for the 2016 dataset	144
A.2	Post-fit yields for each $t\bar{t}H$ subcategory and p_T^{miss} bin in the lepton control regions for the 2017 dataset	145
A.3	Post-fit yields for each $t\bar{t}H$ subcategory and p_T^{miss} bin in the lepton control regions for the 2018 dataset	146
A.4	Post-fit yields for each VH subcategory and p_T^{miss} bin in the lepton and photon control regions for the 2016 dataset	147
A.5	Post-fit yields for each VH subcategory and p_T^{miss} bin in the lepton and photon control regions for the 2017 dataset	148
A.6	Post-fit yields for each VH subcategory and p_T^{miss} bin in the lepton and photon control regions for the 2018 dataset	149
A.7	Post-fit yields for each ggH subcategory and p_T^{miss} bin in the lepton and photon control regions for the 2016 dataset	150
A.8	Post-fit yields for each ggH subcategory and p_T^{miss} bin in the lepton and photon control regions for the 2017 dataset	151
A.9	Post-fit yields for each ggH subcategory and p_T^{miss} bin in the lepton and photon control regions for the 2018 dataset	152

LIST OF TABLES

TABLE	Page
2.1 A summary of the fermionic particles of the standard model	11
2.2 A summary of the bosonic particles of the standard model	11
2.3 Cross sections of the $H \rightarrow$ invisible signal processes in the analysis	20
2.4 The most recent searches for invisibly decaying Higgs bosons with 2016 data from CMS, and the upper limits on the $H \rightarrow$ invisible branching ratio at 95 % confidence level achieved	23
3.1 The integrated luminosity delivered by the LHC during Run-2 which were recorded and certified by CMS	32
3.2 Some of the important parameters defining the performance of the LHC at the end of Run-2, for the High-Luminosity LHC, and the design specification	34
4.1 The requirements for a jet to pass tight identification for data taken in 2016, and to Monte Carlo events emulating that year	52
4.2 The requirements for a jet to pass tight identification for data taken in 2017, and to Monte Carlo events emulating that year	53
4.3 The requirements for a jet to pass tight identification for data taken in 2018, and to Monte Carlo events emulating that year	53
4.4 Requirements used to define the veto and tight electron IDs in the barrel region (supercluster $ \eta \leq 1.479$)	55
4.5 Requirements used to define the veto and tight electron IDs in the end cap region (supercluster $ \eta > 1.479$)	56
4.6 Requirements used to define the loose and medium photon IDs in the barrel region of the detector ($ \eta \leq 1.479$)	57
4.7 Requirements used to define the loose and medium photon IDs in the end cap region of the detector ($ \eta > 1.479$)	57

LIST OF TABLES

6.1	Categorisation of the $t\bar{t}H$, VH , and ggH production modes in the analysis	82
6.2	The trigger thresholds required for events to enter the signal region in each data taking year	88
6.3	The trigger requirements for events to enter the $e + \text{jets}$ or $ee + \text{jets}$ control regions, if they originate from the dataset of e -based triggers	91
6.4	The trigger requirements for events to enter the $e + \text{jets}$ $ee + \text{jets}$, or $\gamma + \text{jets}$ control regions, if they originate from the dataset of γ -based triggers	91
6.5	Definitions of the data sidebands used to determine the QCD multijet background in the signal region for all categories in the analysis	95
6.6	Sources of uncertainty in the luminosity measurements for each year of Run-2 .	111
6.7	The experimental uncertainties present in the analysis, the type of uncertainty, and impact on (the p_T^{miss} distribution/signal strength parameter), along with the years and simulated samples affected	112
6.8	The binning scheme used to categorise events in terms of p_T^{miss}	114
6.9	Observed and expected upper limits on $\mathcal{B}(H \rightarrow \text{invisible})$ for each category and dataset in the analysis.	132

INTRODUCTION

Wonder is the beginning of wisdom.

— Socrates

The universe, in all its vastness, structure, natural laws and chaos, is comprised of only three principal components: visible matter, the ingredients of stars, planets and life, is the only one we interact with on a regular basis; dark energy, a force or manifestation of something even more mysterious, responsible for the accelerating expansion of the universe, is almost entirely unknown; and dark matter, a substance invisible in all sense of the word, that binds galaxies together and influences large scale structure in the cosmos, is the focus of this thesis.

1.1 Evidence for dark matter

The earliest evidence for a large, non-luminous component of the galaxy stretches back to the 1920s when Jacobus Kapteyn attempted to explain the motion of stars in the Milky Way [100]. Since then, a wealth of independent astrophysical observations have reinforced the existence of this aggregation not just in our own, but in countless other galaxies and cosmological bodies. The Coma Cluster is a famous example: 90 % of its mass is thought to arise from dark matter, confirmed by its large mass-to-light ratio of $400 M_{\odot}/L_{\odot}$ [144]. Further evidence is that the rotation curves of most galaxies are roughly flat [118], contrary to the expected Keplerian relationship ($v_r \propto r^{-1/2}$) expected from solely visible matter. On

a galactic scale, dark matter is sprinkled in a mostly spherical halo that spans beyond the observable disc. The inclusive dark matter mass increases linearly [78] to compensate for the decline expressed by visible matter [37, 84]. Gravitational lensing is another observational tool subject to influence from dark matter. Images of galaxies and other objects captured by this method appear distorted from a large gravitational field between the source and observer warping its local spacetime [96]. Arcs, ellipses and Einstein rings of smeared galaxies are often seen when dark matter is present.

While there are no widely-accepted estimations, it is believed that 85–95 % of the Milky Way is comprised of dark matter [28, 29, 98]. Though these approximations include non-visible identifiable matter such as dim stars, black holes and neutron stars, the term *dark matter* typically reserved for the non-luminous, *non-baryonic* segment that pervades the cosmos. From the latest results of the Planck mission, the energy density of the observable universe is composed of 26.5 % dark matter [8]. This result follows the Lambda cold dark matter (Λ CDM) model to describe the constituents and evolution of the universe, which is often referred to as the cosmological analog of the standard model of particle physics (SM). From the calculations, postulations, and observations presented above, the following properties of dark matter can be deduced:

- It is electrically neutral as it does not interact with electromagnetic radiation. Hence, the adjective “dark” in dark matter.
- It is non-relativistic, or *cold*. Its velocity within galaxies is similar to the inhabiting stars [34, 93], since the combination of visible and dark matter drives the measured rotation curves. One small caveat is that galactic dark matter *must* be cold since a velocity above the gravitational escape velocity of the galaxy would eject high speed particles.
- It is stable, at least on the timescale of the current age of the universe. Dark matter production is postulated to have occurred only in the early universe via a thermal freeze-out mechanism (see Chpt. 2.2). Hence, the remaining fraction has been present for a considerable time. Since most galaxies are dominated by dark matter and the gravitational influence from only the visible matter is too small to maintain itself, they could not have developed without it. This supports the idea of bottom-up structure formation in the universe; smaller galaxies form around gravitational potential wells provided by coalescing dark matter, then merge to form larger structures [143].
- Its interaction with matter and itself is very weak, or even non-existent. The Bullet Cluster—an astronomical object consisting of two colliding galaxy clusters—is the best

example of this inference. From measurements of, predominantly, x-ray emission and gravitational lensing, it was found that while there is substantial dark matter present, interaction with itself and the visible matter surrounding it was minimal at most [49]. A kinematic explanation for the spherical distribution and low velocity of dark matter in galaxies can be explained by its collisionless nature. During the formation of a galaxy or stellar system, visible matter frequently collides, dissipating angular momentum and collapsing into a disc.

1.1.1 Alternative theories to dark matter

Though little is intrinsically known about dark matter since all evidence stems from its gravitational influence, there are alternative theories that may explain the observations presented above. However, the scientific community can exclude many of these. Mismeasurements of the amount of baryonic matter such as neutrinos, neutrons, and interstellar gas are among the simpler propositions.

The neutrino flux from stars [REF] and the cosmic neutrino background [142] are precise and well-tested. Even considering the upper limits on neutrino masses [114], they cannot make a significant contribution to the dark matter content in the universe. This is even discounting their highly relativistic nature, where myriad experimental evidence suggests dark matter is cold.

One can also use the Cosmic Microwave Background to calculate the average photon and neutrino densities, and Big Bang Nucleosynthesis calculations to determine the baryonic matter density (see Ref. 82 for results with the latest Planck mission data). These can be compared to other measurements, e.g., mass-to-light ratios averaged across the universe, to reveal a discrepancy [71].

Neutrons cannot contribute to dark matter because isolated neutrons are unstable, decaying in a matter of minutes [140]. Transforming into charged protons and electrons, they interact strongly with light and therefore contribute to the luminous matter content.

Modified Newtonian dynamics (MOND) is a hypothesis that aims to explain phenomena typically associated with dark matter instead by modifications to Newton's laws of motion. There exist many theories and interpretations derived from this principle, though any one strand that tries to explain an observation usually fails to satisfy other phenomena or apply to length scales that general relativity may predict well. For example, observations of the Bullet Cluster [49] have discredited many popular MOND models.

1.2 Overview of dark matter searches

While observational evidence has so far lain with astrophysics, a theoretical description and discovery of dark matter may fall into the realm of particle physics with the numerous, novel experimental searches underway. The detection of dark matter can be classified into three distinct methods with unique signatures (paired with a visual summary in Fig. 1.1):

- **Direct:** dark matter may interact with visible matter on small scales, scattering SM particles [123]. The recoil these SM particles experience could be detected by highly-sensitive, low background experiments such as LUX-ZEPLIN (LZ) [11] that specialises in the search for WIMP dark matter at a large range of masses.
- **Indirect:** if dark matter interacts with itself, it may annihilate to produce showers of high energy photons or pions. Background estimation is difficult since the signatures can be highly model-dependent. The particles may be of a continuum—from hadronisation and radiation of the decay products—or contain features, such as internal radiation from the propagator in the interaction or from loop-level processes [69]. Large ranges of the annihilation cross section and dark matter mass can be probed with telescopes already searching for these characteristic events.
- **Production:** dark matter may have been abundantly produced in the hot, early universe. High energy particle accelerators such as the LHC can reproduce these conditions, with the WIMP miracle (see Chpt. 2.2) reinforcing the idea that dark matter may exist in these accessible mass ranges. Many beyond the standard model (BSM) theories accommodate dark matter candidates with a diverse spectrum of final states that can be investigated by analysing LHC data.

1.2.1 Dark matter searches at the LHC

Since detection at the CMS experiment from the production mechanism is the focus of this thesis, it is important to establish the current state of dark matter searches at the Large Hadron Collider (LHC); the world’s most powerful particle accelerator that provides the infrastructure for CMS to collect data. Both machines are described in detail in Chpt. 3, and as such only a summary will be provided here. The LHC principally collides protons at centre of mass energies up to $\sqrt{s} = 13$ TeV. These exceptionally high energies allow the conditions in the very early universe to be simulated in which heavy, unstable particles were produced plentifully. As a result, many theories can be investigated that predict heavy particles that do not exist in the universe today. Some of these, such as supersymmetry (SUSY) [113],

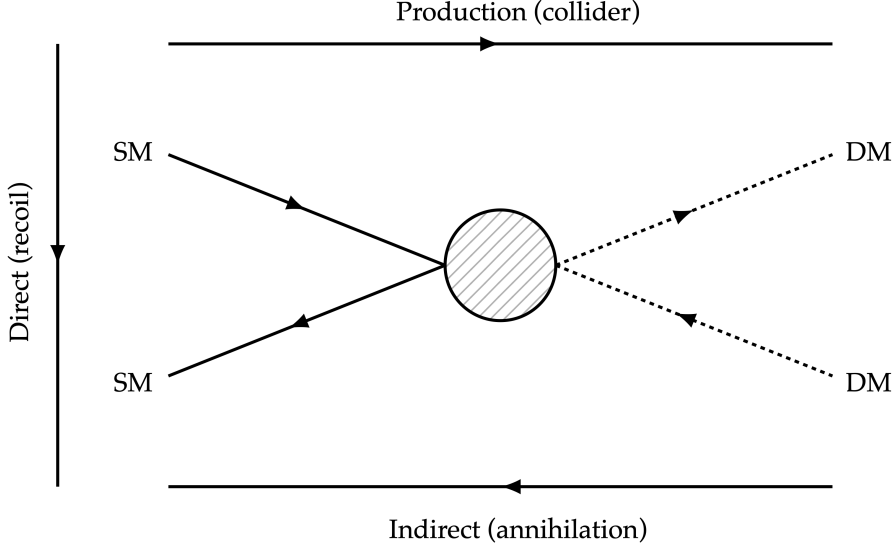


Figure 1.1: A visual representation of the three main types of dark matter detection: direct (dark matter recoiling from standard model particles); indirect (annihilation of dark matter); and production (dark matter created in high energy physics collisions).

sterile neutrinos [77], and Kaluza-Klein states [90] contain dark matter candidates that can be specifically searched for, or indirectly inferred if a theory is experimentally proven. Despite the success of the standard model in explaining much of the natural world, it does not substantiate the existence of dark matter. BSM theories can therefore gain traction. Fig. 1.2 illustrates the masses and interaction cross sections of many dark matter candidates. Weakly Interacting Massive Particles (WIMPs) (highlighted by the purple rectangle) are the subject of many searches at the LHC since the expected mass ranges and cross sections are accessible there.

Two avenues are usually considered when attempting to discover dark matter: explicit searches for the signatures of dark matter production, and anomalies in precision measurements. The former is quite common, with many theories and models tested at the LHC's general purpose detectors, ATLAS and CMS. Searches at CMS have been performed for promptly-decaying and *long-lived* supersymmetry in hadronic final states (in which contributions were made by myself) [102, 127]. Searches for specific supersymmetric particles in a variety of decay modes have been conducted by both experiments [41]. In many of these cases, the lightest supersymmetric particle (LSP) is considered to be a dark matter candidate. R -parity conservation is predicted (or even enforced) in many SUSY models [113], which prevents the decay of LSP and any lighter, standard model particles that have been observed to be stable. While supersymmetry is the most popular BSM theory, due in part

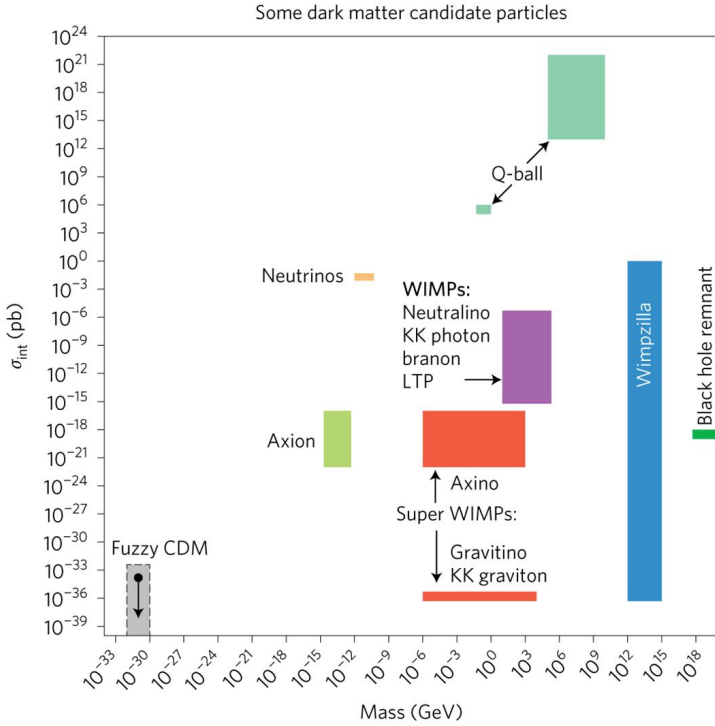


Figure 1.2: The expected masses and interaction cross sections of some dark matter candidates. The LHC, with its centre of mass energy of 13 TeV, is best suited to targeting WIMPs. Figure acquired from Ref. 69.

to its numerous interpretations and approaches for discovery, many others have also been explored at the LHC. From microscopic black holes [105], to [OTHERS], there are extensive propositions that have the potential to uproot the standard model. The analyses above are usually characterised by large “missing” transverse momentum (explained further in Chpt. 4.1.3), a quantity that represents the momenta of particles invisible to the detector, such as dark matter. Chpt. 5 discussion is presented for a search for dark matter that utilises this variable.

Precision measurements of standard model parameters is the other method often consulted in the hopes of attributing anomalies to new physics. For example, attempts to explain anomalies in the $b \rightarrow s$ transition include dark matter candidates [43, 141]. An investigation how the measurement of the Higgs boson to invisible state branching ratio is extensively detailed in Chpt. 6 along with interpretations that can accommodate dark matter.¹

There is significant motivation to study dark matter from a wider, as well as a more personal, viewpoint. It is important to understand how the universe operates, and dark matter opens up the potential for new physics that improves our understanding of nature.

¹Maybe add another example of anomalies in precision measurements

My personal interests include the blend of particle physics and astrophysics, the opportunity to discover, and add to humanity’s collective wisdom. With 137 fb^{-1} at $\sqrt{s} = 13 \text{ TeV}$ from CMS during Run-2 of the LHC, there is great potential to constrain some of the properties of dark matter. This thesis showcases the motivation for, and results of, searches for invisibly decaying Higgs bosons and semi-visible jets with the full Run-2 dataset collected by the CMS experiment. A theoretical foundation is laid out in Chpt. 2 for the characteristics of the expected signal, building on top of the standard model which is briefly recapitulated. Chpt. 3 consists of the predominant aspects of the design and capabilities of the Large Hadron Collider, and the detector composition and data acquisition at the CMS experiment. Physics objects and quantities are defined in Chpt. 4 that are subsequently utilised in the analysis chapters: signal simulation studies of semi-visible jets are presented in Chpt. 5, and the search for invisibly decaying Higgs bosons is described in Chpt. 6. Finally, a summary of this thesis and conclusions drawn from the obtained results form Chpt. 7.²

²Add another figure or two somewhere to help separate the text? Maybe an astronomical image of the Bullet Cluster/dark matter distribution in a cosmological object, or a gravitational lensing ring from dark matter

THE STANDARD MODEL AND BEYOND

It doesn't stop being magic just because you know how it works.

— Terry Pratchett

This thesis is comprised of experimental searches for dark matter and new physics. Chpt. 6 delves deeply into the predominantly-featured search for an invisibly decaying Higgs boson. A small chapter is dedicated to the pursuit of semi-visible jets with Chpt. 5. Before visiting either of which, the theoretical and phenomenological motivations must be understood to corroborate the motivation for searches at the Large Hadron Collider. In this chapter, a brief recap of the standard model—with emphasis on the Higgs mechanism—will be presented along with its shortcomings, foremost the lack of a dark matter candidate. Theoretical descriptions of dark matter that best fit the relic density and astrophysical observations will then be discussed. Specific interpretations in the forms of semi-visible jets and invisibly decaying Higgs bosons are lastly examined that provide the background for the respective analysis chapters.

2.1 The standard model of particle physics

The standard model of particle physics (SM) is the best description of nature the human race has to offer. Three of the four fundamental forces are encapsulated by it: the strong (nuclear)

force, the weak (nuclear) force, and electromagnetism.¹ The latter two may instead be considered components of a single *electroweak* force, unified above an energy of $\mathcal{O}(100 \text{ GeV})$; the LHC, with collision energies far above this threshold, observes much electroweak physics. All of the elementary particles—the quarks, leptons, gauge bosons, and the Higgs boson—and their interactions with each other are contained within the standard model. These are described initially in Chpt. 2.1.1, following a recap of the role symmetries and gauge invariance play in their interactions with Chpt. 2.1.2. Then, in Chpt. 2.1.3, the Higgs mechanism and its eponymous boson, and how they factor in to the decomposition of the electroweak force into the electromagnetic and weak forces are explained. In that passage and in Chpt. 2.1.4, the acquisition of mass by the electroweak gauge bosons and fermions are respectively described.

2.1.1 Particles of the standard model

The standard model contains a relatively small, but diverse “zoo” of particles. They can be divided into two distinct categories based on their internal property *spin*: fermions with half-integer spin, comprising the quarks and leptons that constitute matter; and bosons with integer spin, mediating the interactions (i.e., the forces) between themselves and the fermions.

Six types, or *flavours*, of quark and six flavours of lepton exist, arranged in three generations. Particles between generations share many similarities, the largest differentiator being mass. In the quark sector, the first generation contains the up u and down d , the second the charm c and strange s , and the third the top t and bottom b . The former particle in each generation carries an electric charge of $+2/3$ of the elementary charge e while the latter a value of $-1/3$. All quarks also carry colour charge, allowing them to combine into colour-neutral composite *hadron* particles such as protons and neutrons. Quarks can interact via all of the forces in the standard model.

In the lepton sector, each generation consists of a massive particle with electric charge $-1e$, and an associated electrically neutral, and extremely light, neutrino. The three generations consist of the electron e and electron neutrino ν_e , the muon μ and muon neutrino ν_μ , and the tau τ with the tau neutrino ν_τ . Charged leptons can interact via electromagnetism and the weak force. Though the neutrinos, lacking any electric charge, only interact via the weak force. The main properties of the fermions are summarised in Tab. 2.1.

Each force is carried by one or more spin-1 gauge boson, acting to mediate the fermions’ interactions. Eight flavours of the massless, electrically neutral gluon g carries the strong force, while the equally massless and chargeless photon γ mediates the electromagnetic interaction.

¹Add a table of the relative strengths and ranges of the forces?

Type	Generation	Particle	Spin	Electric charge	Mass
Quark	1	Up (u)	1/2	$+2/3 e$	$2.2^{+0.5}_{-0.4} \text{ MeV}/c^2$
		Down (d)	1/2	$-1/3 e$	$4.7^{+0.5}_{-0.3} \text{ MeV}/c^2$
	2	Charm (c)	1/2	$+2/3 e$	$1.28^{+0.03}_{-0.04} \text{ GeV}/c^2$
		Strange (s)	1/2	$-1/3 e$	$95^{+9}_{-3} \text{ MeV}/c^2$
	3	Top (t)	1/2	$+2/3 e$	$173 \pm 0.4 \text{ GeV}/c^2$
		Bottom (b)	1/2	$-1/3 e$	$4.18^{+0.04}_{-0.03} \text{ GeV}/c^2$
Lepton	1	Electron (e)	1/2	$-1 e$	$0.511 \text{ MeV}/c^2$
		Electron neutrino (ν_e)	1/2	0	$< 0.2 \text{ eV}/c^2$
	2	Muon (μ)	1/2	$-1 e$	$106 \text{ MeV}/c^2$
		Muon neutrino (ν_μ)	1/2	0	$< 0.2 \text{ eV}/c^2$
	3	Tau (τ)	1/2	$-1 e$	$1.777 \text{ GeV}/c^2$
		Tau neutrino (ν_τ)	1/2	0	$< 0.2 \text{ eV}/c^2$

Table 2.1: A summary of the fermionic particles of the standard model. Masses obtained from Ref. 140.

Three massive bosons mediate the weak interaction, the charged W^\pm and neutral Z . A scalar (spin-0) Higgs boson H is the excitation of the Higgs field that acts to bestow mass to the elementary particles. All of the bosons are summarised in Tab. 2.2.

Force	Particle	Spin	Electric charge	Mass
Strong	Gluon (g)	1	0	0
	Photon (γ)	1	0	0
Weak	W bosons (W^\pm)	1	$\pm 1 e$	$80.38 \pm 0.01 \text{ GeV}/c^2$
Weak	Z boson (Z)	1	0	$91.19 \text{ GeV}/c^2$
—	Higgs boson (H)	0	0	$125.18 \pm 0.16 \text{ GeV}/c^2$

Table 2.2: A summary of the bosonic particles of the standard model. Masses obtained from Ref. 140.

2.1.2 Symmetries and gauge invariance

The standard model is a gauge quantum field theory: particles are characterised by excitations of quantum fields and their interactions described by continuous gauge symmetry groups. A symmetry is a feature in a theory where a quantity is preserved under specific transformations. This is significant for understanding what interactions are allowed by each force. An $SU(3)$ gauge group represents the interactions in the strong force, and an $SU(2) \times U(1)$ gauge group for the electroweak force. Decomposition into the weak force and electromagnetism results

in separate $SU(2)$ and $U(1)$ groups, respectively. The interactions of the standard model as a whole can then be expressed as the product $SU(3) \times SU(2) \times U(1)$.

Noether's theorem associates a continuous symmetry of a physical system, that does not affect its Lagrangian, to a conserved charge or current [117]. A consequence of which is that an interaction represented by a particular group must conserve the charges associated to the symmetries of said group. The generators of the group² correspond to the gauge invariant fields that mediate the associated force, i.e., the gauge bosons in the SM, enforcing the conservation of the charges.³ With the $SU(3)$ strong force, the mediating gluons carry colour charge. The photon γ of $U(1)$ electromagnetism conserves electrical charge. While the bosons of the $SU(2)$ weak force conserve weak isospin. As the SM is described by the product of these gauge groups, it includes only gauge invariant fields that preserve the Lagrangian and equations of motions under the allowed transformations or interactions.

Symmetries in the standard model require the gauge bosons to be massless. For electromagnetism and the strong force, this is no issue. However, the bosons mediating the weak force have been determined experimentally to be massive [21, 25], posing a problem. One solution is to introduce a new field that can break the symmetry of the $SU(2)$ group without affecting the gauge invariance elsewhere in the SM. This led to the introduction of the Higgs field.⁴

2.1.3 Electroweak symmetry breaking and the Higgs mechanism

As mentioned earlier, the electromagnetic and weak forces are unified into the electroweak force above a certain energy threshold. In this regime, the electroweak bosons and fermions must be massless to maintain gauge invariance. The former obtain their mass by interacting with the Higgs field, the mechanism through which is labelled the *Higgs mechanism* [80, 87, 94].⁵

The simplest model by which the Higgs mechanism can be accommodated in the SM is

²There are $N^2 - 1$ generators for $SU(N)$ and N^2 for $U(N)$. This is what gives rise to the eight gluons of the strong force, three (W^+ , W^- , and Z) bosons of the weak force, and the single photon of electromagnetism.

³Not entirely sure if this bit is correct, since e.g., electromagnetism must conserve charge but the photon doesn't carry charge.

⁴There are many who deserve credit for formulating the theory. However, for concision, it will be referred to as the *Higgs field* or *Higgs mechanism* henceforth.

⁵The fermions (except perhaps neutrinos), also obtain their masses by interacting with the Higgs field. However, the term “Higgs mechanism” in the standard model is reserved for the procedure by which the electroweak bosons acquire mass.

by introducing an $SU(2)$ doublet of complex scalar Higgs fields:

$$(2.1) \quad \Phi = \begin{pmatrix} \phi^+ \\ \phi^0 \end{pmatrix} = \frac{1}{\sqrt{2}} \begin{pmatrix} \phi_1 + i\phi_2 \\ \phi_3 + i\phi_4 \end{pmatrix}$$

It possesses four degrees of freedom, i.e., one per gauge boson in the electroweak sector. The fields introduce additional terms in the standard model Lagrangian, most importantly a potential of the form

$$(2.2) \quad V(\Phi) = \mu^2 \Phi^\dagger \Phi + \lambda (\Phi^\dagger \Phi)^2$$

which is the most general scalar potential that is also $SU(2) \times U(1)$ invariant. With both quadratic and quartic components, positive value of both free parameters μ^2 and λ would yield a single stable minimum for the potential. In a physical context, this would correspond to the universe pre-electroweak symmetry breaking. But by setting $\lambda > 0$ and $\mu^2 < 0$, what was once the minimum becomes an unstable local maximum and a new, degenerate circle of minima in the $\phi_1 - \phi_2$ plane can be found with values

$$(2.3) \quad \Phi^\dagger \Phi|_{\min} = -\frac{\mu^2}{2\lambda}$$

forming the familiar “wine bottle” potential. An illustration with a toy Higgs boson is given in Fig. 2.1.

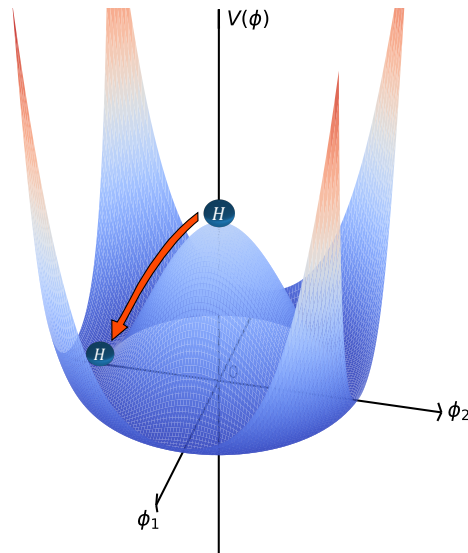


Figure 2.1: A depiction of the Higgs potential V as a function of the component fields. The Higgs boson is initially at $(\phi_1, \phi_2) = (0, 0)$, an unstable local maximum. It then tumbles into the minimum value of V and triggers electroweak symmetry breaking.

To spontaneously break the $SU(2) \times U(1)$ symmetry of the electroweak force, a non-zero vacuum expectation value v must be assigned from the set of minima belonging to the potential V . Since the freedom to select a potential is a symmetry, assigning a value breaks said symmetry. For the fields ϕ_1 , ϕ_2 , and ϕ_4 , v can simply be set to zero. However, as a neutral field, ϕ_3 must be assigned a non-zero value in order for the photon to remain massless after electroweak symmetry breaking. It is allocated a value

$$(2.4) \quad \langle 0 | \phi_3 | 0 \rangle = v^2 = -\frac{\mu^2}{\lambda}$$

By expanding Φ around the chosen vacuum and using the unitary gauge, it can be seen that all of the fields other than ϕ_3 —known as *Goldstone fields* in this paradigm—are eliminated. The originally massless electroweak bosons then gain mass by “eating” the Goldstone bosons.

The masses of the electroweak bosons can then be calculated using the vacuum expectation value, and the coupling strengths of the weak force g and electromagnetism g' :

$$(2.5) \quad \begin{aligned} m_W &= \frac{1}{2}gv, \\ m_Z &= \frac{1}{2}(g \cos \theta_w + g' \sin \theta_w)^2 v = \frac{1}{2} \frac{gv}{\cos \theta_w} \end{aligned}$$

where θ_w is the *weak mixing angle* or *Weinberg angle*. It is a quantity that represents the degree to which the weak and electromagnetic forces mix, defined as

$$(2.6) \quad \cos \theta_w = \frac{m_W}{m_Z} \text{ or } \tan \theta_w = \frac{g'}{g}$$

It is somewhat of a free parameter in the standard model with its value constrained by measuring the W and Z boson masses. With the latest values from Ref. 140, $\theta_w = 28.74^\circ$ and $v = 246 \text{ GeV}/c^2$. The mass of the Higgs boson is given by⁶

$$(2.7) \quad m_H = \sqrt{2\lambda v^2} = \sqrt{-2\mu^2}$$

Stuff I may not need to include: The EW bosons and photons are represented as W_1 , W_2 , and W_3 boson fields carrying weak isospin, and the B boson field of weak hypercharge. At energies below electroweak unification, the Higgs mechanism spontaneously breaks the $SU(2) \times U(1)$ symmetry, decoupling electromagnetism from the weak force. The W_1 and W_2 fields transform into W^+ and W^- bosons, gaining their 80 GeV mass:

$$(2.8) \quad W^\pm = \frac{1}{\sqrt{2}}(W_1 \mp iW_2)$$

⁶Is this to first order, since there are VVH, VVHH, HH, etc. self-interactions?

While the W_3 and B fields mix to produce the massless photon and massive Z boson:

$$(2.9) \quad \begin{pmatrix} \gamma \\ Z \end{pmatrix} = \begin{pmatrix} \cos \theta_w & \sin \theta_w \\ -\sin \theta_w & \cos \theta_w \end{pmatrix} \begin{pmatrix} B \\ W_3 \end{pmatrix}$$

In the new U(1) symmetry group of electromagnetism, the electric charge quantum number manifests as a combination of weak hypercharge and a component of weak isospin.

2.1.4 Masses of the fermions

The quarks and leptons in the SM acquire their masses from the Higgs field from a Yukawa coupling y_f , which describes the interaction between a scalar (Higgs) field and Dirac (fermion) field. As a function of y_f and the vacuum expectation value of the Higgs field, the fermion masses are calculated as

$$(2.10) \quad m_f = \frac{1}{\sqrt{2}} y_f v$$

They are directly proportional to their coupling strength to the Higgs and are all free parameters in the SM so must be constrained by experiment. The decay width Γ of the Higgs boson into fermions is computed as

$$(2.11) \quad \Gamma(H \rightarrow f\bar{f}) = \frac{m_H}{8\pi} \left(\frac{m_f}{v} \right)^2 N_c \left(1 - \frac{4m_f^2}{m_H^2} \right)^{\frac{3}{2}}$$

which is proportional to the squared mass of the decay products. The *branching ratio* \mathcal{B} —the probability of a particle decaying into a given final state—is simply the ratio of the partial width to the total width, the latter being the sum of partial widths for all of particle's decay modes.⁷

2.1.5 Limitations of the standard model

Despite the standard model providing precise predictions of three of the four fundamental forces and the particles that they interact with, there are many experimental observations that it cannot currently explain. Neutrino masses, dark matter, dark energy, and gravity all escape its description. Many of the important parameters do not have predicted values and so must be experimentally measured.

The Hierarchy Problem is one of the more serious issues facing the standard model. It may be explained in different manners that emphasize certain aspects. But inherently, it is

⁷Not sure how much of the Higgs mechanism and fermion mass stuff I need to reference.

a question of the disparity between energy scales of the fundamental forces—particularly relating to the weak force and gravity. The masses of the intermediate vector, and Higgs, bosons of $\mathcal{O}(100 \text{ GeV}/c^2)$ are much smaller than than the Planck mass of $\mathcal{O}(10^{19} \text{ GeV}/c^2)$. The mass term for the Higgs boson is $\mu^2 \Phi^\dagger \Phi$ in the SM. Invariance under a gauge or global symmetry in the Higgs field H leads to the mass being open to radiative corrections up to the Plank scale.⁸ It appears that, in nature, these very large corrective terms to the Higgs boson mass cancel to give the familiar $m_H = 125 \text{ GeV}/c^2$ [4, 45]. It is deemed unnatural to expect cancellations to such a degree, i.e., one part in 10^{17} . This *fine-tuning* of parameters in the standard model is something that unified or natural theories desperately try to avoid.

Some BSM theories like supersymmetry provide well-motivated cancellations by introducing supersymmetric particles. In certain scenarios, some of these particles should exist at the TeV scale. In the SM, the largest correction to the Higgs mass derives from the top quark, since its Yukawa coupling to the Higgs is the strongest. At one-loop order, new physics at $\mathcal{O}(\text{TeV})$ scale is required, with new particles coupling to the Higgs field to prevent these corrections from being unreasonably large [81]. Arguments such as this give credence to new physics being discoverable at particle accelerators such as the Large Hadron Collider.

2.2 Theoretical motivations for, and descriptions of, dark matter

Dark matter may have been forged in the universe via one of many possible mechanisms. The most popular is described as a *thermal freeze-out* process. In the hot, early universe when the thermal background allowed spontaneous pair production of particle dark matter, it was generated in abundance. During this period, the particles may also have frequently annihilated seeing that the cosmos was still small. Inevitably, the universe expanded and cooled; the temperature became too low to allow significant production [26]. Matter was further separated and the dark matter annihilation rate decreased, leaving a behind the *thermal relic* that is observed today. These remaining particles were attracted via gravity, forming filaments throughout the universe. The potential wells they induced allowed the progenitors of galaxies to form within.

Full derivations of the thermal freeze-out of dark matter can be found in literature [31, 86], with the WIMP Miracle as a consequence: with relatively few assumptions, the correct dark matter relic abundance can be recovered by requiring a WIMP mass of $\mathcal{O}(\text{GeV-TeV})$,

⁸Justify this more?

dependent on the annihilation cross section. This is a range accessible at contemporary colliders such as the LHC, and perhaps coincidentally, around the electroweak energy scale. It is common for figures that depict the WIMP dark matter density over time to plot the yield n_χ/s as a function of the dimensionless parameter $x = m_\chi/T$. In the former variable, n_χ is the number density and s is the entropy density. In the latter, m_χ is the dark matter mass and T is the average temperature of the universe, which serves as a measure of its age due to the temperature decreasing over time. An example is given in Fig. 2.2.

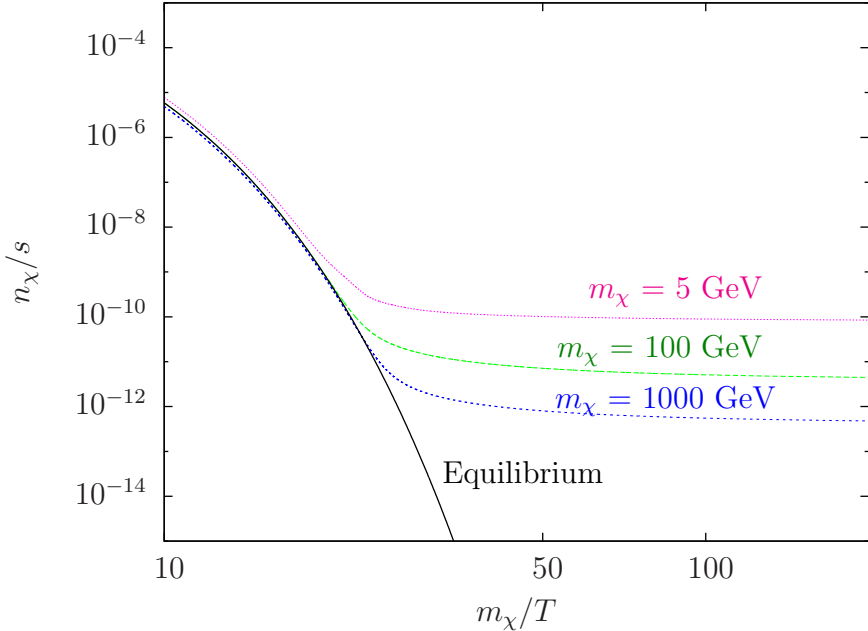


Figure 2.2: A measure of the comoving number density of WIMP dark matter as a function of time with projections for different particle masses. A higher mass must be balanced by a larger annihilation cross section to achieve the correct relic density, to which it tends asymptotically from the point of decoupling. The black curve represents the scenario in which dark matter remains in equilibrium with the standard model. Figure taken from Ref. 89.

The time of the dark matter freeze out epoch is somewhat insensitive to the mass and annihilation cross section. Approximate solutions to the Boltzmann equation for time-dependent n_χ —where dark matter is modelled as a weakly-interacting, diffuse gas of particles—suggest $x_f \sim 20$ [31, 112]. Stronger dark matter interaction leads to decoupling at a later time and a lower number density. The approximate value of x_f is significant in that it supports the electroweak-scale mass of WIMPs.

Another popular mechanism, targeting low-mass dark matter, is the *freeze-in* process [88, 108]. In this postulate, dark matter is not produced thermally in the early universe. Instead, it emerges through interactions between SM particles such as collisions, or decays of those

heavier than dark matter. The comoving density increases with time until it plateaus from of the cooling of the universe, where SM particles are generally stable enough and too low energy to produce dark matter in any meaningful quantity. The relic abundance can therefore be reclaimed from a combination of the initial thermal distributions, the dark matter mass, and the interaction strength, similar to the freeze-out process. In order to obey cosmological observations, particularly the fact that it is cold, the masses expected for freeze-in dark matter particles are of $\mathcal{O}(\text{keV})$ or heavier.

2.3 Measuring the branching ratio of invisibly decaying Higgs bosons

The Higgs boson has caught the attention of the high energy physics community, and even the public eye, like no other particle in recent memory. Its discovery in the $H \rightarrow \gamma\gamma$ and $H \rightarrow ZZ \rightarrow 4\ell$ channels in 2012—*independently by both CMS [45] and ATLAS [4]*—realised one of the paramount goals of the LHC’s construction. The particle itself is not necessarily exciting. Rather, it confirms the existence of the Higgs *field* that pervades the universe and gives mass to the elementary particles via the exchange of its eponymous boson [80, 87, 94]. Its discovery, one might think, was the end of the discussion of the Higgs boson. However, it was only the beginning.

Many observations of the Higgs, such as its predominant decay mode $H \rightarrow b\bar{b}$, were not seen until recently by CMS [125] or ATLAS [3]. Constraints on its other properties have also been placed, such as its resonance width and branching ratios \mathcal{B} to several final states. Fully understanding the Higgs boson is important to understanding the Higgs field and the wider standard model. Precision measurements in tension with SM predictions can also be a window to new physics. Measuring the $H \rightarrow$ invisible branching ratio aims to do just that.

The only SM process in which Higgs boson can decay invisibly is $H \rightarrow ZZ \rightarrow 4\nu$ ⁹ with a branching ratio of $\mathcal{O}(0.1\%)$ [91]. The leading observed experimental upper limits on this measurement are 19 % from CMS [135] and 26 % from ATLAS [2], far higher than the predicted value. If undiscovered invisible particles, perhaps dark matter, couple to the Higgs field the branching ratio will be enhanced.¹⁰ Experimental evidence shows the coupling strength to proportionally follow the mass of the particle, as verified in ATLAS and CMS’

⁹A direct decay to neutrinos is possible if they acquire their mass from the Higgs field. But as the coupling would be of a Yukawa form and the upper limit on the SM neutrino masses is very small, the branching ratio is expected to be heavily suppressed.

¹⁰Do I need to give a more mathematical motivation for the BR being enhanced/what kind of values the BR is expected to be from various DM models?

2.3. MEASURING THE BRANCHING RATIO OF INVISIBLY DECAYING HIGGS BOSONS

latest measurements [138]. A considerably large enhancement may allow for this process to be observed at the LHC. At the very least, a more accurate constraint on the branching ratio is able to exclude some models of dark matter, such as those described in Refs. 75, 99.

There is no reason to assume dark matter does *not* interact with the Higgs field, since it bestows mass to all known elementary particles (a small caveat, perhaps, being neutrinos).¹¹ Higgs *portal* models have been theorised that connect the visible sector of the standard model to a dark sector where particle dark matter resides [20, 23]. Certain models also predict a detectable presence at the LHC from a sufficient production rate [36], perhaps even with data obtained during Run-2 [7].

An analysis in search of this decay is provided thoroughly in Chpt. 6. Constraints on the experimental side stem largely from the different channels in which a Higgs boson can be produced. These are outlined in Chpt. 2.3.1, and must all be considered when examining such a rare process that is also difficult to distinguish amongst a large background. Previous results from searches for individual modes, including subsequent combinations, are documented in Chpt. 2.3.2.

2.3.1 Production modes of the Higgs boson

At the LHC, the most common mechanisms for producing a Higgs boson are vector boson fusion (VBF), gluon-gluon fusion (ggF or ggH), associated production from top quarks ($t\bar{t}H$), and associated production from a vector boson (VH). Feynman diagrams of these processes are shown in Fig. 2.3. Additional diagrams for ggH involve a square top quark loop. The ZH process can be initiated by $gg \rightarrow ZH$ as well as $pp \rightarrow ZH$. They have very different characteristics, production rates, and event signatures, complementing each other and allowing a single analysis to cover all bases with orthogonal parameter spaces to target them individually. One common feature of these final states is the presence of at least one quark. The hadronic constituents in the decay products of a collision often shower due to colour confinement, producing collimated sprays of hadrons called *jets*. In a detector, these are represented by clusters of hadronic energy deposits. Algorithms at each stage of data acquisition (see Chpt. 3.2.2) can reliably connect these back to the individual quark decays so one has some certainty of the process they are observing.

The cross section of each mechanism at $\sqrt{s} = 13$ TeV is detailed in Tab. 2.3.

¹¹Do I need to give some mathematical motivation as to *why* dark matter would couple to the Higgs? Or is the fact that it has mass enough justification?

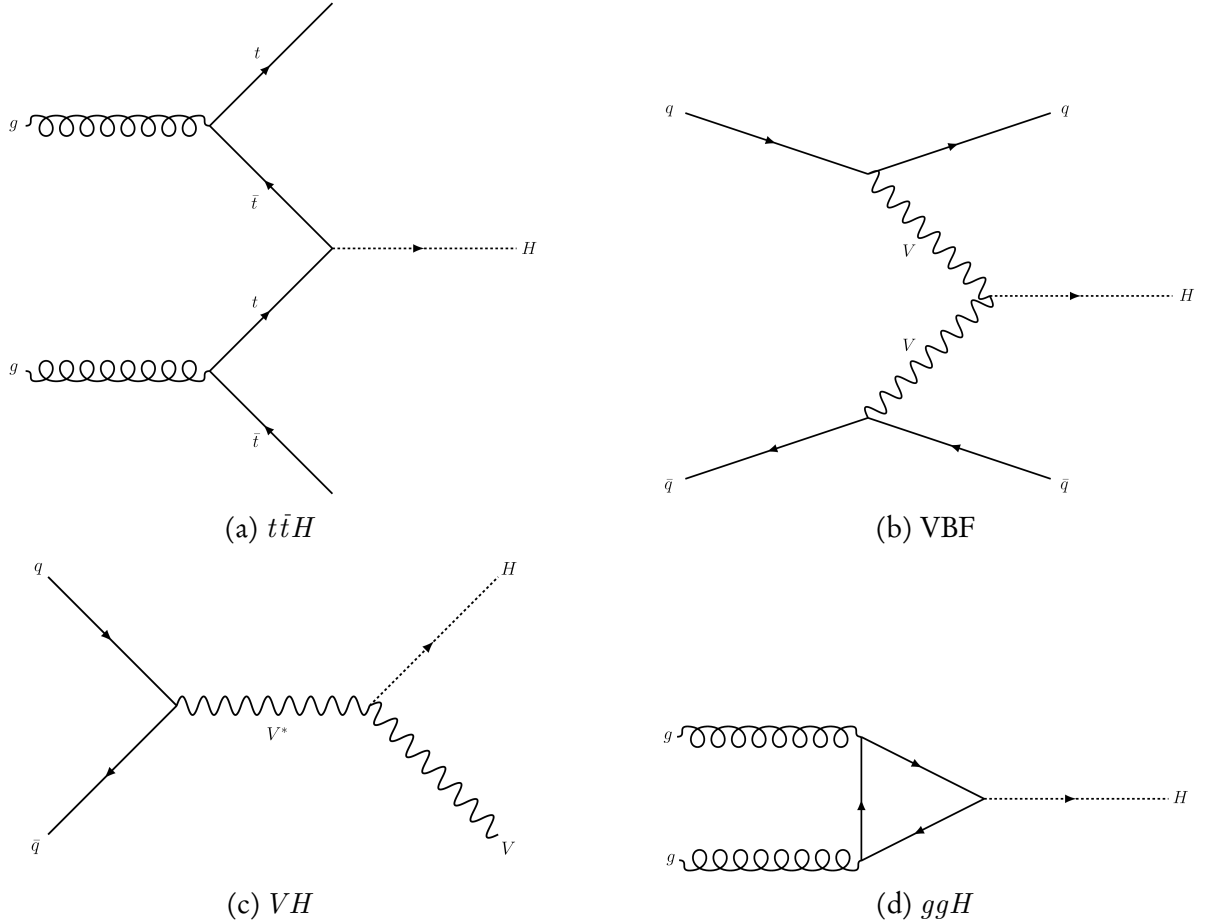


Figure 2.3: A subset of the Feynman diagrams for the four predominant production mechanisms of the Higgs boson at the LHC.

Mode ($H \rightarrow$ invisible)	Cross section (pb)	Accuracy
VBF	3.77	NNLO QCD and NLO electroweak
$t\bar{t}H$	5.07×10^{-1}	NLO QCD and NLO electroweak
W^+H	8.31×10^{-1}	NNLO QCD and NLO electroweak
W^-H	5.27×10^{-1}	NNLO QCD and NLO electroweak
$pp \rightarrow ZH$	8.84×10^{-1}	NNLO QCD and NLO electroweak
$gg \rightarrow ZH$	1.23×10^{-1}	LO QCD (NLO + NLL corrections)
ggH	4.86×10^1	N3LO QCD and NLO electroweak

Table 2.3: Cross sections of the $H \rightarrow$ invisible signal processes in the analysis. They are calculated at $\sqrt{s} = 13$ TeV at the highest orders available and obtained from Ref. 42. The simulation datasets are generated with a 100 % branching ratio of the Higgs boson to invisible states, and in the VH processes the V decays in all cases to $q\bar{q}$.

2.3.1.1 Vector boson fusion (VBF)

A VBF topology is exhibited by a t -channel exchange of two vector bosons radiated by the incident quarks, which then combine to form a new particle such as a Higgs boson. Since the masses of the W and Z bosons are more than half the Higgs mass, it can easily be produced on shell. The recoil of the quarks from the Higgs boson characterises the visible system: two jets with a large combined invariant mass, usually with a large separation in pseudorapidity η but small in azimuthal angle.¹² The jets move in opposite directions, one in $+\eta$ and the other in $-\eta$, but are usually contained in the same horizontal half of the detector.

2.3.1.2 Associated production from top quarks ($t\bar{t}H$)

In $t\bar{t}H$, a $t\bar{t}$ pair is produced. A virtual top quark t and antiquark \bar{t} produced in association with their real counterparts annihilate to produce the Higgs boson. As it decays invisibly, it is the remaining t and \bar{t} in the event that lead to three classes of final state. The t quark decays almost exclusively to $b W^+$ (and $\bar{t} \rightarrow \bar{b} W^-$) [140]. In a resolved system where top quarks possess low to moderate momentum, the multitude of available b -tagging algorithms can distinguish the decays of the b quark. The products of the W boson is the determining factor of the final state. Hadronically-decaying W s ($W \rightarrow q\bar{q}$), of course, produce pairs of jets. But they can also decay into a lepton and neutrino. The final states then all have p_T^{miss} and up to two b -jets in common. Several jets may accompany them (the hadronic channel), or fewer jets with a single lepton (the *semi-leptonic* channel), or two leptons (the *dileptonic* channel). The magnitude and direction of the p_T^{miss} in the latter two channels may be affected by the neutrinos, depending on their direction and energy.

In a boosted system where the top quarks have significant p_T , it is often difficult to tag b -jets, especially if one is searching in the hadronic channel. The decay products are not well separated and can merge into large, “fat” jets. Recently-developed algorithms can assist in this case by inspecting these fat jets to classify, for example, boosted topologies originating from t quarks as well as V bosons to identify $t\bar{t}H$ events.

2.3.1.3 Associated production from a vector boson (VH)

A Higgs boson is radiated by the vector boson V in the VH mechanism. Parallels can be drawn with $t\bar{t}H$ as the decay of the V determines the search channel. Resolved and boosted systems are also possible. In the resolved case, a dijet pair with an invariant mass close to that of the parent boson would distinguish the hadronic channel. b -taggers can be exploited if

¹²These coordinates are described in Chpt. 3.2.1.1.

the decay is to a b quark, i.e., $Z \rightarrow b\bar{b}$.¹³ Single lepton channels are possible for WH and dilepton for ZH . For a boosted V , one expects the products to be collimated into a single AK8 jet, at least in the hadronic channel. As with $t\bar{t}H$, we take advantage of DEEPAK8 to capture these scenarios.

2.3.1.4 Gluon-gluon fusion (ggH)

Despite ggH having the largest cross section of the four modes, its upper limit on $\mathcal{B}(H \rightarrow \text{invisible})$ is the weakest. The Higgs boson is created through the loop-level fusion of the initial state gluons, normally mediated by a top quark since it has the largest coupling to the Higgs. With no additional final state particles at first order, searches for this production mode usually involve initial state radiation from the gluons or the loop. As such, the signature is at least one jet and p_T^{miss} .

2.3.2 Results of previous searches

Many previous analyses have investigated the $H \rightarrow \text{invisible}$ decay, in some cases from dedicated searches, but often as an afterthought or interpretation of the main analysis. VBF is the most sensitive production mode. This is demonstrated in Tab. 2.4¹⁴ by the upper limits attained compared to the other mechanisms. In Ref. 135, a combination was performed by CMS over all the production modes detailed in the table (with the exception of $t\bar{t}H$). Using the recent 2016 measurements as well as data taken from Run-1 and 2015, this combined observed upper limit sits at 19 %, while the expected is 15 %. With only data from Run-1 and 2015 (the previous combination) the observed and expected upper limits of 24 % and 23 %, respectively, were found [106].

2.4 Searches for semi-visible jets

Many searches for dark matter presume it is a WIMP-like particle because of the considerations discussed in Chpt. 2.2. In the LHC, the signatures of WIMPs would be driven by large missing transverse momentum recoiling from visible matter in the event. Monojet [104] and dijet [134] searches are able to exploit this, for example. However, no sign of WIMPs have been observed yet. Thankfully, a boundless supply of alternative theories exist, with possible

¹³Other potential decay modes, such as $W \rightarrow bu$ and $W \rightarrow bc$ are suppressed in the CKM matrix, yielding small production rates at the LHC.

¹⁴Might be good to add a row with the combined (bar $t\bar{t}H$) result with only 2016 data.

Targeted mode	Analysis	Final state	Observed UL	Expected UL
VBF	Ref. 135	VBF-jets + p_T^{miss}	33 %	25 %
$ZH(Z \rightarrow \ell\ell)$	Ref. 131	$Z(\rightarrow \ell\ell) + p_T^{\text{miss}}$	40 %	42 %
$t\bar{t}H$	Ref. 83	$t\bar{t}(\rightarrow \text{jets}/\ell/\ell\ell) + p_T^{\text{miss}}$	46 %	48 %
$VH(V \rightarrow q\bar{q})$	Ref. 128	$V(\rightarrow qq) + p_T^{\text{miss}}$	50 %	48 %
ggH	Ref. 128	jets + p_T^{miss}	66 %	59 %

Table 2.4: The most recent searches for invisibly decaying Higgs bosons with 2016 data from CMS, and the upper limits (UL) on the $H \rightarrow$ invisible branching ratio at 95 % confidence level achieved. Only the VBF analysis is a dedicated search, while the others are interpretations of the results obtained in their respective primary analyses. For the $t\bar{t}H$ analysis, the hadronic (jets), semi-leptonic (ℓ), and dileptonic ($\ell\ell$) channels were combined.

signatures equally as varied. Though the p_T^{miss} could still be one of the characteristics by which the dark matter can be inferred, a plethora of topologies and discriminating observables are possible. The dynamics that govern dark matter may be confined to a *dark sector* or *hidden sector*, inhabited by new forces and particles.

A dark sector may be largely inaccessible, as in some Hidden Valley¹⁵ scenarios [139], but communicate with the visible sector through a portal interaction. An example from SM particles could be the Higgs boson bridging the visible and hidden sectors, as mentioned in Chpt. 2.3. Many interesting and novel signatures can be probed by LHC experiments from models like these. Dark forces with energy scales in the tens of GeV and mediator masses up to several TeV may be accessible. If they share parallels with the standard model, the mechanisms can be explained for the dark matter presence and relic density arising from a baryon-like asymmetry.

Proposed in Refs. 67, 68, a strongly-coupled dark sector in a Hidden Valley is imagined with interactions analogous to QCD.¹⁶ The portals allowing the dark and visible sectors to communicate can be decomposed into a leptophobic Z' (*s*-channel) and bi-fundamental Φ (*t*-channel) mediator. In the *t*-channel case, Φ is a representation of both the visible and dark QCD gauge groups. Depictions of the processes above are given in Fig. 2.4. In the LHC, protons could collide at energies high enough to access the dark sector. From either the resonant production of a Z' or exchange of a Φ , dark quarks χ ¹⁷ are produced. Below a

¹⁵A Hidden Valley is a schema where the standard model is extended by a non-abelian group. SM particles are uncharged under this group. The new, light particles from this extension are the opposite: charged under the new group and neutral under the SM gauge group. A heavy mediator carries both charges, acting as a portal between the standard model and Hidden Valley particles.

¹⁶Do I need to mention that this dark sector is $SU(2)_{\text{dark}}$, and write the lagrangian for how it couples to SM via dark weak force?

¹⁷Not to be confused with stable dark matter that is often denoted by the symbol χ .

dark confinement scale Λ_{dark} , hadronisation takes place to coalesce them into dark hadrons. Depending on the species, some of these dark hadrons are stable (i.e., a source of dark matter), while others are unstable and decay back into visible sector particles, namely standard model quarks. The final state is then a shower of two jets each interspersed with dark matter: *semi-visible jets*.

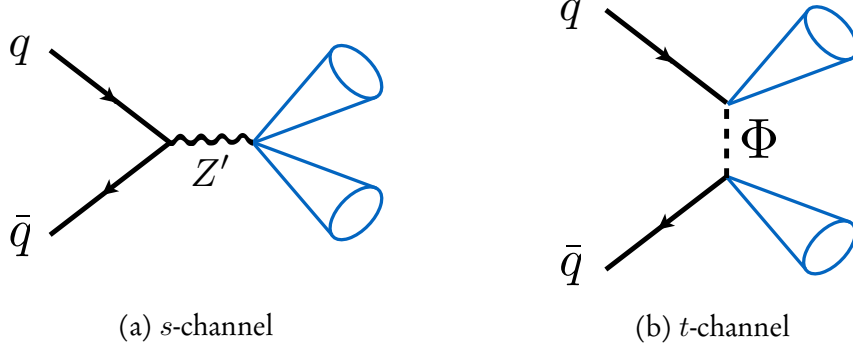


Figure 2.4: Example Feynman diagrams for the two main production modes of semi-visible jets. A Z' boson mediates the *s*-channel process while a bi-fundamental Φ mediates the *t*-channel process. Figure from Ref. 68.

2.4.1 Kinematics and free parameters of the model

The kinematics of semi-visible jets are heavily influenced by the following free parameters of the model: the mass of the mediator ($m_{Z'}$ or m_Φ), the dark coupling strength (α_{dark}), the dark quark mass (m_χ), and the invisible fraction (r_{inv}).

– $m_{Z'}/m_\Phi$: Since the energies of the colliding protons have an upper limit, the conservation of energy (or momentum) imposes one for the on-shell production/exchange of the mediator particle. In the *s*-channel process, production of the Z' is resonant. Consequently, its mass is possible to recover by calculating the dijet mass m_{jj} or transverse mass m_T .

– α_{dark} : In Ref. 68, this is defined as $g_\chi^2/4\pi$ (where g_χ is the coupling constant between the dark quarks and mediator). Analogous to QCD, the dark coupling runs as a function of the energy scale, influencing Λ_{dark} . At 1 TeV,

$$(2.12) \quad \Lambda_{\text{dark}} = 1000 \text{ [GeV]} \exp\left(\frac{-2\pi}{\alpha_{\text{dark}} b}\right)$$

where $b = \frac{11}{3}N_c - \frac{2}{3}N_f$ is related to the number of dark colours and flavours, respectively.

- m_χ : This parameter does not directly affect much, but is related to the dark hadron mass ($m_{\text{dark}} = 2m_\chi$) and Λ_{dark} . The combination of the two properties affects the shower dynamics. Note that while Ref. 68 describes some of these to be insensitive, a parameter scan over these two variables are necessary in the search described in Chpt. 5.
- r_{inv} : This is defined as the fraction of produced invisible particles that remain stable, at least over timescales where they interact with a detector. When generating simulated samples, r_{inv} can be interpreted as the *probability* of a dark hadron remaining stable. While this variable is not inherent within the model, it is one that can parametrise many underlying components. As a result, visualisation of the shower and direction of \vec{p}_T^{miss} is much more intuitive, as demonstrated in Figs. 2.5 and 2.6, respectively. A large value of r_{inv} would yield a similar final state to a WIMP search.

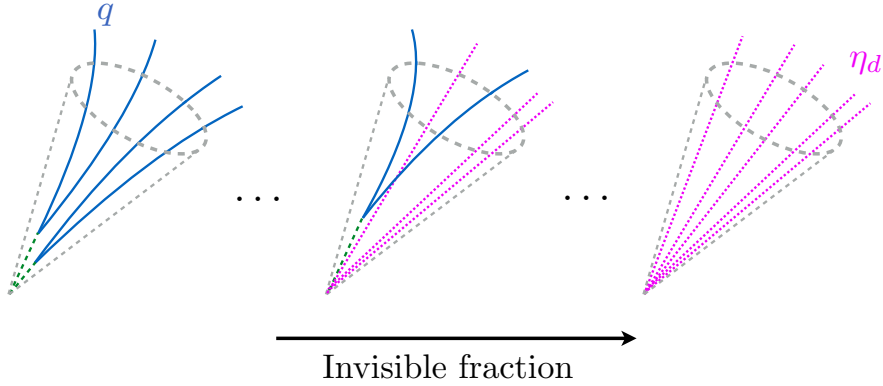


Figure 2.5: The constituents of a semi-visible jet as a function of its invisible fraction r_{inv} . Figure taken from Ref. 68.

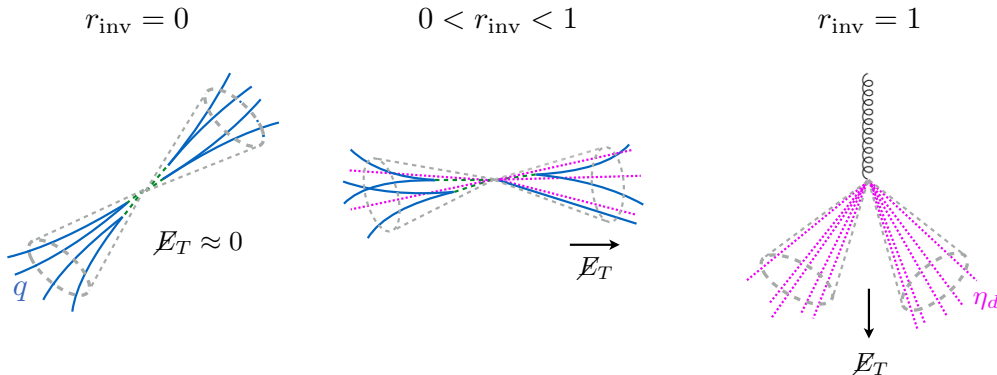


Figure 2.6: The typical direction of the missing transverse energy \cancel{E}_T (or p_T^{miss}) relative to the semi-visible jets as a function of their invisible fraction r_{inv} . Figure from Ref. 68.

In the search for semi-visible jets in Chpt. 5, only the s -channel process has been analysed with LHC data with publication on the horizon. Generator studies have been additionally performed for the t -channel interaction and the analysis is underway. In the s -channel search, mediator masses of up to several TeV are accessible, and intermediate values of r_{inv} are most sensitive. Hence, the typical signature is a dijet pair with each jet likely to contain a different invisible fraction, leading to the \vec{p}_T^{miss} aligned with one of the jets. WIMPs, on the other hand, completely recoil from the visible matter, and so jets may be more collimated with small separation. The p_T^{miss} is also larger and possibly more isolated. The phase space exploited by this model is often rejected by dark matter searches since the final state can be easily mimicked by mismeasured QCD. A sizeable background from this process would therefore be present. However, jet substructure techniques and machine learning algorithms have developed rapidly in the recent years, and it is possible to disentangle signal and background with some certainty.

One interesting aspect of the model is the potential for signatures with displaced vertices, so called long-lived particles or *emerging jets* on account of the decay to visible states occurs a sufficient distance from the primary vertex. Some searches have already been performed for this final state from a different interpretation of a strongly-coupled dark force [136] to supersymmetry contexts [127]. These are not considered in Chpt. 5, so the dark hadrons are assumed to decay promptly. Long-lived interpretations have been noted as possible extensions to the search, however.

THE LHC AND THE CMS EXPERIMENT

No one can whistle a symphony. It takes a whole orchestra to play it.

— H.E. Luccock

This chapter concerns the experimental setup. CERN, the European Organisation for Nuclear Research (*Organisation Européenne pour la Recherche Nucléaire*), is the organisation that manages the machines discussed and is a pioneer in the high energy physics community. Its most notable—the Large Hadron Collider—provides the CMS experiment with proton-proton collision data that is then stored, corrected, and then used by physicists for analysis. Ranging from standard model precision measurements, searches for new physics, the development of tools and algorithms to aid the previous two, these and much more are studied by the collaboration. CMS is described in detail, from its hardware and subdetectors to its data acquisition and trigger system. Special attention is given to the derivation of jet energy corrections (JEC) in the Level-1 Trigger (L1T) as a portion of this PhD has been devoted to them.

3.1 The Large Hadron Collider

Deep underground beneath the Franco-Swiss border lies the Large Hadron Collider (LHC), a synchrotron particle accelerator 27 km in circumference. As the largest machine in the world, the LHC stands as a testament to the importance of fundamental science and the dedication to which it is pursued. Predominantly a proton collider, lead and xenon ions

have also been injected for novel and unique studies. Four primary experiments are situated at their own interaction points where the two beams of particles are brought into contact: CMS (Compact Muon Solenoid), a general purpose detector with interests in precision measurements, searches for new physics, and many other avenues; ATLAS (A Toroidal LHC ApparatuS), a counterpart to CMS at its antipode on the LHC ring; LHCb, designed to study the decay of B hadrons; and ALICE (A Large Ion Collider Experiment), primarily studying heavy ion collisions and the quark-gluon plasma.

Four additional, smaller experiments are stationed in the LHC tunnel that are much more specialised than those aforementioned: TOTEM (TOTal Elastic and diffractive cross section Measurement) shares the CMS cavern with three subdetectors positioned near the beam line, performing proton structure and interaction cross section studies; LHCf shares the ATLAS cavity and is concerned with detecting neutral pions in the forward direction to explain the origins of high energy cosmic rays; FASER (ForwArd Search ExpeRiment) is another forward-based detector near ATLAS and searches for light, weakly interacting particles; finally, MoEDAL (Monopole and Exotics Detector at the LHC) is installed in proximity to LHCb and aims to detect magnetic monopoles and other exotic particles.

The technical design report for the LHC can be found at Ref. 38, detailing the ring itself, infrastructure, general services, and the injector chain.

3.1.1 A proton’s journey

A proton destined for the LHC begins its journey as a hydrogen atom in a little, red bottle. Around 3×10^{14} protons are supplied to each beam in the LHC, with billions of refills available in this single container. Once the hydrogen atoms leave the source, they are stripped of their electrons, and [sent] to the linear accelerator LINAC2.¹ This is the start of a long voyage through the accelerator complex (visualised in Fig. 3.1).

Given a modest boost to 50 MeV, the protons are sequentially fed from LINAC2 into the Proton Synchrotron Booster (PSB) that accelerates them further to 1.4 GeV. Another upsurge is provided once the protons travel to the Proton Synchrotron (PS), this time to 26 GeV. Then, the final energy increase received before entering the LHC comes from the Super Proton Synchrotron (SPS), leaving the protons at 450 GeV. Once injected into the LHC, they are finally accelerated to their peak; up to 6.5 TeV from a sequence of radio frequency cavities over the course of twenty minutes. The oscillation frequency of these cavities is precisely tuned and timed to give protons the appropriate kicks and accelerate them

¹As of the end of Run-2, LINAC2 has been decommissioned. It has been replaced by LINAC4 in preparation for Run-3.

3.1. THE LARGE HADRON COLLIDER

to the desired energy. Since there is a distribution of proton energies in the beam, those that enter a cavity slightly out of time with a different energy than expected consequently become sorted into *bunches*. The remainder of the LHC ring is used to steer the beam with the aid of over 1,200 liquid helium-cooled superconducting dipole magnets. It is also focused by almost 400 equivalently-cooled quadrupole magnets to increase the rate of proton collisions.

One beam consists of a *train* of up to 2,808 bunches spaced 25 ns apart, each with 115 billion protons. Using bunches provides an advantage to the experiments at each of the interaction points. Discrete collisions take place between bunches in the opposing beams at 40 MHz as opposed to continuous streams of protons. This allows for estimates of pileup interactions that can be filtered out, and would otherwise introduce miscalculations of sums like p_T^{miss} and H_T . The data recorded by each experiment is naturally separated by the bunch crossing or *event*—an event being the products of the collisions in a bunch crossing, including any pileup interactions along with the nominal collision.

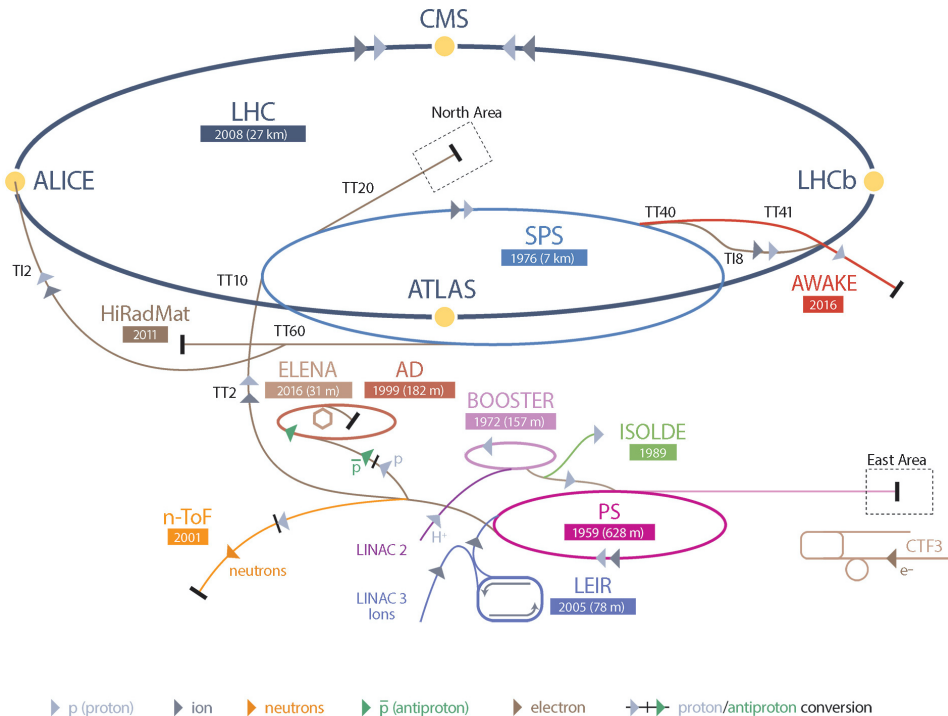


Figure 3.1: A schematic of the CERN accelerator complex. Various particles are shown from their sources to the detectors they are observed at. Figure obtained from Ref. 124.

3.1.2 Luminosity

The *luminosity* of a particle accelerator is, along with centre of mass energy, a quantitative measure of its performance. It also often used to denote the amount of data delivered to, or collected by, the receiving detector. A full derivation of this quantity can be found in Ref. 92, and as such, only a summary is given here. The *instantaneous luminosity* L , typically quoted in $\text{cm}^{-2} \text{s}^{-1}$, is defined as

$$(3.1) \quad L = \frac{1}{\sigma_p} \frac{dN}{dt}$$

where N is the number of collisions and σ_p is the production cross section. In the LHC, because many final states are possible, σ_p is not generally known. It can be measured, however. A recent paper from LHCb measured the extrapolated inelastic cross section (which is the important component for LHC collisions) to be $75.4 \pm 5.4 \text{ mb}$ at $\sqrt{s} = 13 \text{ TeV}$ [5], allowing an estimate of the collision rate. For two colliding beams split into bunches with the constituents in each bunch distributed according to a gaussian profile,

$$(3.2) \quad L = \frac{N_1 N_2 f N_b}{4\pi \sigma_x \sigma_y} \cdot F$$

where N_1 and N_2 are the number of particles in a bunch in beams 1 and 2, respectively, N_b is the number of bunches per beam, f is the revolution frequency (11,245 Hz for protons in the LHC), and σ_x and σ_y are the horizontal and vertical sizes of the beam, respectively.

The geometric reduction factor F is unity for beams colliding head on. However, in the LHC, the beams collide at an angle known as the *crossing angle* to reduce the effects of pileup. At the start of a fill when the number of protons in the LHC is at its maximum, the crossing angle at each interaction point is approximately $300 \mu\text{rad}$. As the runs progress, more protons collide and the luminosity decreases. One of measures taken to recover luminosity and keep the LHC as efficient as possible is to reduce the crossing angle. By the end of the fill, it can be as small as $240 \mu\text{rad}$.

The instantaneous luminosity can be increased further by the inclusion of more bunches per beam, decreasing the size of a beam through improved quadrupole magnets, and by reducing the crossing angle. Tuning these parameters led the LHC to reach its design luminosity of $10^{34} \text{ cm}^{-2} \text{s}^{-1}$ in 2016. It had more than doubled by the end of Run-2.

Integrating the the instantaneous luminosity over a period of time yields the *integrated luminosity* $L_{\text{int.}}$:

$$(3.3) \quad L_{\text{int.}} = \int L dt$$

These values are often quoted by experiments in units of *inverse femtobarn* (fb^{-1}) as an indicator of the amount of collision data collected. A barn is a unit equal to 10^{-28} m^2 and used to express cross sectional area in nuclear and particle physics. Thus its reciprocal, the same units as integrated luminosity, gives a good sense of scale that relates cross sections of individual processes to the total amount of data. Tab. 3.1 gives the integrated luminosities over Run-2 delivered by the LHC and collected by CMS. Taking 139 fb^{-1} from this table, and assuming the inelastic pp cross section above gives an estimate of 10^{16} collisions recorded by CMS over Run-2 (excluding pileup interactions).

3.1.3 Pileup

At the high instantaneous luminosity of the LHC, multiple interactions per bunch crossing—known as *pileup*—are frequent. The expected, or nominal, number of collisions per bunch crossing is one, but because of all the factors that increase the luminosity, many *softer* collisions also take place. Pileup interactions can produce many low- p_T objects, and near-collinear to the beam (detecting particles in this region is essential for some analyses). These additional objects can contaminate the reconstruction of the final state from the nominal collision, and as such affect the direction and magnitude of the \vec{p}_T^{miss} . When one aims to increase the luminosity to collect more data, the more severe pollution from pileup is an inevitable consequence. The distribution of pileup events in CMS during Run-2 can be seen in Fig. 3.2.

There are strategies in place in the LHC and the anchored experiments to mitigate pileup. Introducing, or increasing, a crossing angle between the beams reduces the effect. Decreasing the crossing angle increases the overlap between bunches at each intersection—since they have a non-negligible length—leading to more collisions. Track reconstruction algorithms are very efficient at connecting particles to their primary vertices, and therefore particles originating from pileup vertices can be identified and removed [1, 44]. At CMS, various methods are available in the calorimeter triggers to subtract the effects of pileup.

3.1.4 Evolution of the LHC

The LHC began operating in 2010 at a centre of mass energy of $\sqrt{s} = 7 \text{ TeV}$; 3.5 TeV per beam. A modest increase to 8 TeV was achieved for 2012 until the end of Run-1 in 2013. Long Shutdown 1 then commenced where maintenance work was carried out, and upgrades to the accelerator and experiments were performed. Notably, the superconducting magnets were improved to safely handle much more energetic beams.

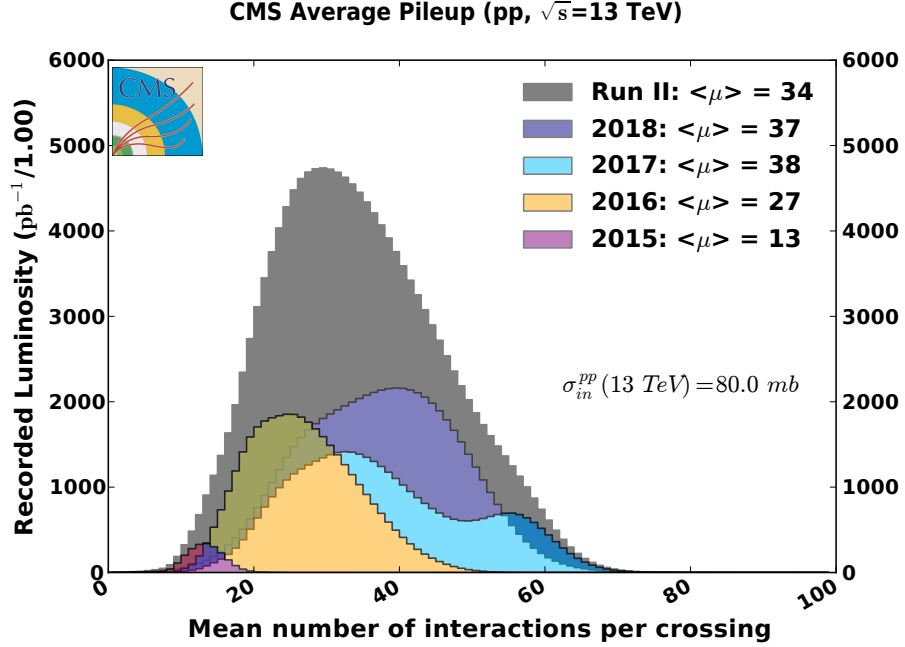


Figure 3.2: The average number of pileup interactions per bunch crossing at CMS during Run-2 of the LHC. Figure obtained from Ref. 53.

The LHC resumed operation in 2015, marking the start of Run-2 and further pushing the frontiers of high energy physics with a centre of mass energy of $\sqrt{s} = 13\text{ TeV}$. While valuable data was taken that year, it was not until 2016 when substantial datasets were amassed. Therefore, when analysts refer to the “full Run-2 dataset,” they typically do not include data from 2015. It requires as much care as the other years with respect to implementing corrections and addressing systematic uncertainties, and so on, for only a very small gain in integrated luminosity. Run-2 ended in 2018 with—omitting the 2015 dataset— 158.6 fb^{-1} of pp collisions delivered, 146.5 fb^{-1} of which were recorded by CMS who certified 137.2 fb^{-1} suitable for analysis [53, 59]. A breakdown by year is presented in Tab. 3.1 with a visual chart in Fig. 3.3. By comparison, the LHC delivered only 6.2 fb^{-1} at 7 TeV and 23.3 fb^{-1} at 8 TeV over the course of Run-1.

Integrated luminosity	2015	2016	2017	2018	Full Run-2
Delivered by LHC (fb^{-1})	4.2	41.0	49.8	67.9	162.9
Recorded by CMS (fb^{-1})	3.8	37.8	45.0	63.7	150.3
Certified by CMS (fb^{-1})	2.3	35.9	41.5	59.7	139.5

Table 3.1: The integrated luminosity delivered by the LHC during Run-2 which were recorded and certified by CMS. Typically, only the 2016–18 datasets are analysed since 2015 accrued little data compared to the other years. Numbers obtained from Refs. 53, 59.

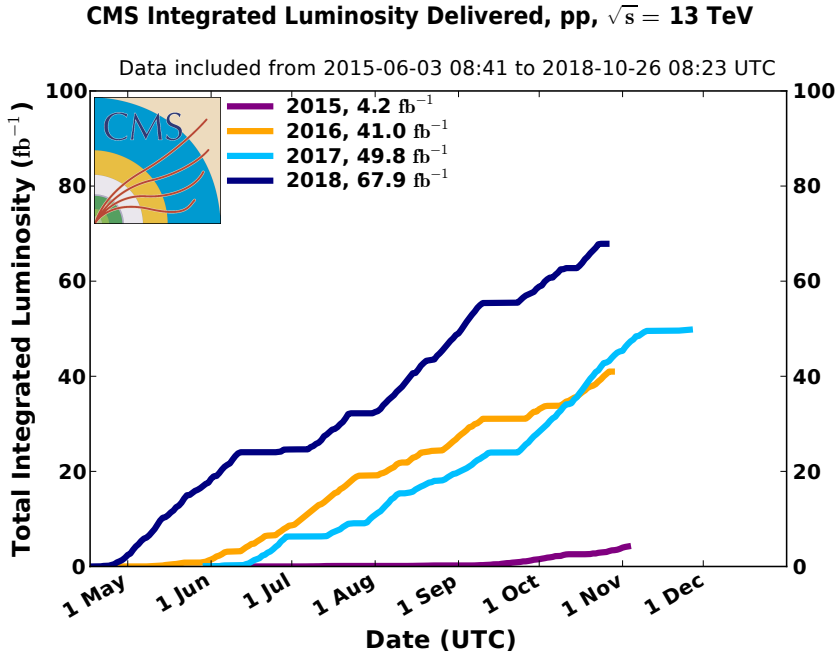


Figure 3.3: The integrated luminosity of pp collision data delivered to CMS during Run-2 of the LHC. Figure obtained from Ref. 53.

In addition to the upgrades that have so far been performed, a much grander change is on the horizon. In 2027, the High Luminosity Large Hadron Collider (HL-LHC) improvements are set to be introduced with the primary purpose of increasing the luminosity by up to a factor of ten: more powerful magnets for focusing the beam, crab cavities for increasing the bunch overlap area, shielding and more radiation-resistant components, an upgrade to many of the boosters in the accelerator complex, and much more. A summary of the important parameters at three stages of the LHC’s life is given in Tab. 3.2.²

3.2 The CMS experiment

The Compact Muon Solenoid (CMS) collaboration was formed in 1992 with a letter of intent circulated to the high energy physics community for a general purpose detector to be built at the LHC [73]. Though its emphasis was the detection of the Higgs boson, the myriad avenues for which physics could be studied was also acknowledged. Just under five hundred people from sixty two institutes were part of the original letter. At the time of writing over five thousand physicists, engineers, technical and administrative staff, and students, spanning

²Should I add a column for the Tevatron, as a comparison to/sense of scale for the LHC’s numbers? Or maybe discuss the Tevatron qualitatively somewhere.

Parameter	End of Run-2	HL-LHC	Design
Beam energy (TeV)	6.5	7	7
Bunches per beam	2,556	2,748	2,808
Protons per bunch	1.5×10^{11}	2.2×10^{11}	1.5×10^{11}
Crossing angle (μrad)	300	590	285
Instantaneous luminosity ($\text{cm}^{-2}\text{s}^{-1}$)	2.1×10^{34}	7.2×10^{34} *	1.0×10^{34}
Integrated luminosity per year (fb^{-1})	68	250	40
Average pileup per bunch crossing	34	140	27

Table 3.2: Some of the important parameters defining the performance of the LHC at the end of Run-2, for the High Luminosity Large Hadron Collider, and the design specification. Several values in this table were obtained from Refs. 17, 32.

* Does not account for the large increase to virtual luminosity from the introduction of crab cavities.

over two hundred institutes in fifty countries, comprise the collaboration. Working tirelessly in harmony, with ingenuity, cooperation, and a drive for exploring the frontiers of particle physics, almost one thousand publications have been produced with data collected by the experiment. These range from exotic/BSM searches, standard model precision measurements, B -physics, top quark physics, heavy ions, and more. This wide scope of topics cements CMS as a versatile and world-leading detector, and collaboration as a whole.

3.2.1 The CMS detector

The machine itself—aptly named the CMS Detector—lives a hundred metres underground at Interaction Point 5, just outside the town of Cessy in France. Constructed over several years, the detector was separated into fifteen sections. Each was built on the surface and lowered into the experimental cavern with an incredibly small tolerance of a few centimetres. Here, they were joined together to assemble the 14,000 tonne goliath. The finished detector is a hermetic cylinder enclosing the LHC beam pipe, measuring 21 m in length (plus a little extra from the bolt-on forward calorimeters) and 15 m in diameter. Its etymology stems from how *compact* (relatively speaking) the detector is since its weight is twice that of ATLAS in only one sixth of the volume, it has a subsystem dedicated to detecting *muons*, and a *solenoid* is used to generate the magnetic field.

A kaleidoscope through which we see the subatomic, CMS is designed to detect all manner of particles as accurately as possible. To accomplish this, the detector is divided into four major subsystems (or subdetectors): the silicon tracker, the electromagnetic calorimeter (ECAL), the hadron calorimeter (HCAL), and the muon chambers. These are each explained in more

detail below, with a graphic of the entire detector presented in Fig. 3.4 and a transverse slice through it in Fig. 3.6.

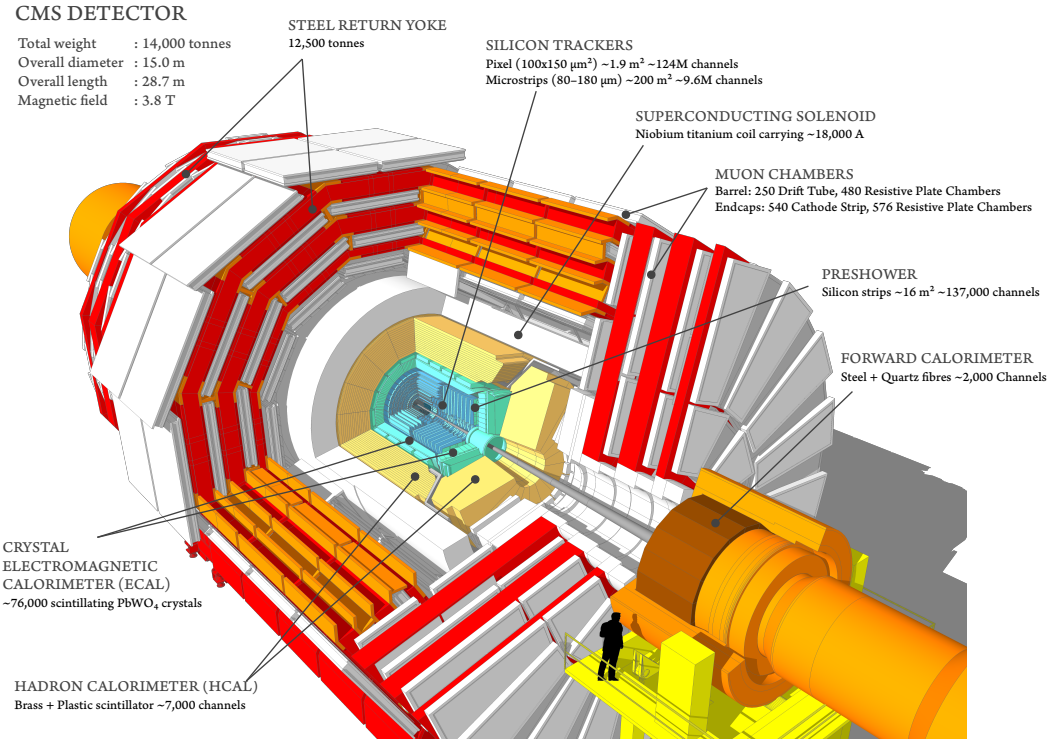


Figure 3.4: A cutaway diagram of the CMS detector with all of the principal components labelled. This detector configuration was used for the 2017–18 data taking years, where the coverage of the pixel detectors in the silicon tracker were upgraded. Image taken from Ref. 120.

3.2.1.1 Geometry

Collider physics tends to use certain conventions when describing the positions of particles in a detector. The azimuthal angle ϕ is the same variable as in cylindrical coordinates with a range $[-\pi, \pi]$. Pseudorapidity, denoted by η , is a coordinate that describes the angle between a particle and the longitudinal axis of the detector (the beam line):

$$(3.4) \quad \eta = -\ln \left[\tan \left(\frac{\theta}{2} \right) \right]$$

where θ is the angle between the particle's three-momentum \vec{p} and the positive direction of the beam axis. So as $\theta \rightarrow 0^\circ$ (the beam line), $\eta \rightarrow \infty$. Generally, particles with large η escape the detector which is why forward calorimeters are in place. The transverse momentum of

a particle can be found with $p_T = |\vec{p}|/\cosh \eta$. The convention in hadron colliders is to use η over the rapidity y , where the latter is Lorentz invariant and tends to the former in the limit $|\vec{p}| \gg m$. However, in cases such as jet clustering, soft particles are included and so y is defined:

$$(3.5) \quad y = \frac{1}{2} \ln \left(\frac{E + p_L}{E - p_L} \right)$$

where p_L is the longitudinal component of the momentum. The subdetectors of CMS are nominally separated into several sections dependent on their geometry or layout, and it is useful to divide them into η ranges to demonstrate their coverage. *Barrel* sections are cylindrical around the beam line while *end caps* are usually discs or plates perpendicular to it. The following subsections describe them in detail. One quadrant of CMS showing the η divisions can be seen in Fig. 3.5.

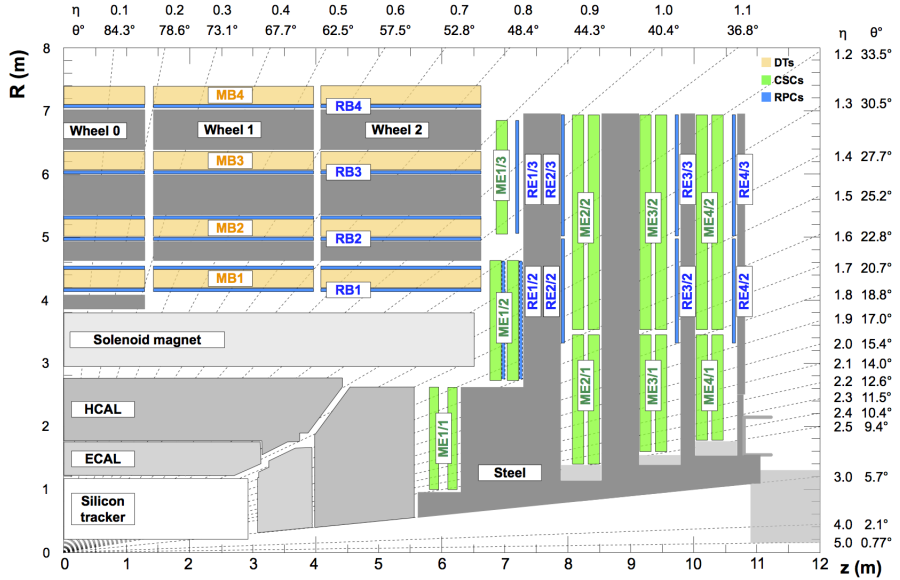


Figure 3.5: A quadrant of the CMS detector illustrating the main subsystems with their radius R , longitudinal distance z , and pseudorapidity η from the interaction point. The grey box at $3 < |\eta| < 5$ and $11 < z < 12$ m is the hadron forward calorimeter. Figure taken from Ref. 115.

The distance between two objects can be found with the variable ΔR :

$$(3.6) \quad \Delta R = \sqrt{(\Delta\eta)^2 + (\Delta\phi)^2}$$

It is often used as a parameter in jet clustering to define the enclosing cone, or between reconstructed objects for assessing overlap.

3.2.1.2 The tracker

When a collision occurs, the ejected particles first encounter the silicon tracker that extends from 4 cm to just under 1 m in radius [66, 101]. Longitudinally, it is confined to $|\eta| < 2.5$, known as the *central region*. The barrel and end cap sections are bound by $|\eta| \lesssim 1.6$ and $1.6 \lesssim |\eta| < 2.5$, respectively.

Consisting of tens of millions of pixels and microstrips, the positions of particles can be recorded to within 10 μm . Initially, the pixel detector was arranged in three layers, covering 1 m^2 and consisting of 66 million channels. It was upgraded for the 2017–18 run period to introduce a fourth layer, increasing its coverage to 1.9 m^2 with 124 million channels. The many layers of strip modules enclose the pixel detector. Since the tracker is the closest subsystem to the interaction point, the components must be extremely radiation-tolerant to withstand the bombardment of particles during every collision.

Track-finding algorithms use pattern recognition to determine whether the hits from multiple layers in the tracker can be correlated and reconstructed to originate from individual particles. Each is suited to different types of track, p_{T} threshold, and location. Vertex reconstruction algorithms are employed to determine the primary vertex. Any secondary vertices transverse (for example, in b -jets) or longitudinal (pileup) to the beam line may also be distinguished. The momentum of particles can be measured from the curvature of the track from the magnetic field induced by the solenoid (see Chpt. 3.2.1.5).³ One of the algorithms, the gaussian sum filter (GSF) method, is used extensively in the HLT for triggering on electrons and photons [16].

3.2.1.3 The ECAL

After the tracker, the particles can interact with the ECAL [35, 63]. The 76,000 lead-tungstate crystals scintillate the incoming light, where the attached avalanche photodiodes record energy deposits in the barrel region ($|\eta| < 1.48$) belonging to charged particles and photons. Vacuum phototriodes are instead glued to the crystals in the end caps ($1.48 < |\eta| < 2.96$) as they are subject to higher radiation doses. A lead-silicon preshower detector precedes the end cap crystals to improve spatial resolution and discrimination of multiple particles. Electronics for groups of 5×5 crystals (the ECAL component of a *trigger tower*) read out the data and deliver it to the trigger system (see Chpt. 3.2.2).

The ECAL is designed to identify charged particles, primarily electrons and photons. The $H \rightarrow \gamma\gamma$ and $H \rightarrow ZZ \rightarrow 4\ell$ processes were kept in mind, as an ardent focus was on

³Should I mention something about resolution as well?

discovering the Higgs boson. These particles are usually stopped entirely in the subdetector. Charged hadrons, muons, and tau leptons (τ), however, only deposit a sliver of energy in the ECAL, and so information from the other subdetectors is required in their cases. Measuring the energy of electrons and photons is complex and corrects for many factors to maintain a high precision. Among them are a cluster correction (as several hits in a cluster can belong to one object, especially when they electromagnetically shower), a time-dependent response correction from the laser monitoring system that measures the crystal transparency, and an intercalibration correction that accounts for the non-uniform response of the crystals and photodetectors. The energy resolution in the ECAL σ_E^{ECAL}/E can be quantified as

$$(3.7) \quad \left(\frac{\sigma_E^{\text{ECAL}}}{E}\right)^2 = \left(\frac{S}{\sqrt{E}}\right)^2 + \left(\frac{N}{E}\right)^2 + C^2$$

where E is the energy in GeV, S is a stochastic term, N represents noise in the detector electronics, and C a constant. For electrons in the barrel during Run-1, the terms were measured to be $S = 0.028$, $N = 0.12$, and $C = 0.003$ [97], yielding a resolution of 0.5 % for a 100 GeV electron.

3.2.1.4 The HCAL

Hadronic particles propagate past the ECAL into the HCAL [64]. The barrel ($|\eta| < 1.30$) and end cap ($1.30 < |\eta| < 2.96$) regions both consist of brass absorber⁴ and plastic scintillator with wavelength-shifting fibre. Arranged in wedges in the barrel and discs in the end cap, hybrid photodiodes record the signal in either case. This yields 7,000 detection channels. Due to colour confinement, hadrons are much more prone to showering than charged leptons. Additional scintillator tiles are placed outside the yoke of solenoid in the barrel region to capture the tails of these showers.

Unlike the ECAL which only covers the barrel and end cap, the HCAL also has a component in the forward region of the detector: the hadron forward calorimeter (HF). Composed of steel absorber and quartz fibres with 1,000 channels on each side, and occupying $2.96 < |\eta| < 5.19$,⁵ it is designed to detect particles with trajectories close to the beam line. The additional function of measuring the luminosity delivered to, and collected by, the experiment is also served. Cherenkov light kindled in the fibres is funnelled into photomultiplier tubes that collect the signal. Particles that enter the HF are usually not supplemented by tracker or

⁴Famously, a large component of the brass used to build the end caps came from over 1 million decommissioned Russian naval artillery shells left over from World War II.

⁵I'm not entirely sure what the bounds of the HF are. Literature seems to define it as $3.0 < |\eta| < 5.0$, but in the JEC the edge of the final $|\eta|$ bin is 5.191.

ECAL information. As such, the energy and momentum of particles can be determined only by the subdetector.

Each cell of the HCAL maps onto a given number of ECAL crystals, forming trigger towers or calorimeter towers that are important when collecting data (see Chpt. 3.2.2). The towers project mostly-radially from the interaction point. Their granularity is greatest at low η , and decreases with increasing η . Information from both subdetectors is used to identify jets, muons, and taus, as well as any electrons or photons that penetrate through the ECAL. Readout electronics are mounted to the various components of the HCAL to deliver to the trigger system. The response and transparency of modules is corrected for in a similar way to the ECAL, as is intercalibration.

3.2.1.5 The magnet and muon chambers

The three subsystems described above are encased in a massive superconducting solenoid [65], making up 12,500 of the 14,000 tonne detector. It generates a magnetic field of 3.8 T and 2.4×10^9 J of energy, making it the largest store of energy in the world for a single magnet. The field allows for the transverse momentum of a charged particle to be precisely measured, since the field propels it into a circular orbit. The magnetic force qvB exerted is equal to the centripetal force mv^2/r , and therefore the radius of the orbit is proportional to the momentum.

An iron return yoke interspersed with the muon chambers [110] constitute the rest of the detector, extending from a radius of around 3 m to 7.5 m. The iron yoke confines the magnetic field to the volume of the detector and provides a 2 T field in the opposite direction to that found farther inward. Since muons are much heavier than electrons and have high p_T , they penetrate farther than the bounds of the ECAL and deposit little energy in the process. The final states of several interesting decays include muons, such as with the Higgs boson. Consequently, constructing a dedicated subdetector is therefore essential.

There are four muon stations, as can be seen by the orange strips in Fig. 3.6, separated by layers of the return yoke. 480 resistive plate chambers and 250 drift tubes reside in the central barrel region of $|\eta| < 1.2$. The end caps are populated with 576 resistive plate chambers, complemented by 540 cathode strip chambers. Its limits are $0.9 < |\eta| < 2.4$, though the resistive plate chambers terminate at $|\eta| = 1.9$. Like many of CMS' subdetector components, they are designed parallel and perpendicular to the beam line, not according to η . With such large segments at high radius in the muon chambers, a small overlap is therefore present. This $0.9 < |\eta| < 1.2$ sector is sometimes referred to as the *overlap region*. The pseudorapidity range of the muon chambers' end cap is restricted compared to the ECAL and HCAL to (mostly)

align with the tracker, and the steel that surrounds the structure takes up the remainder of the η that the former two occupy.

All of the detectors in the muon chambers take advantage of gaseous ionisation, as it is much less expensive than the silicon used in the tracker while still providing excellent resolution. If a muon enters a cell in a drift tube or cathode strip chamber, its position can be measured by the length of time taken for the gas it ionises to drift to the anode wire of said cell in the presence of a strong electric field. The latter can additionally utilise the induced charge on the cathode strips for improved spatial resolution. The resistive plate chambers work on a similar principle, but use parallel plate capacitors and are predominantly used for timing purposes when the data is sent to the trigger system. To measure the momentum of the muons, information from both the tracker and muon detector are used where possible.⁶

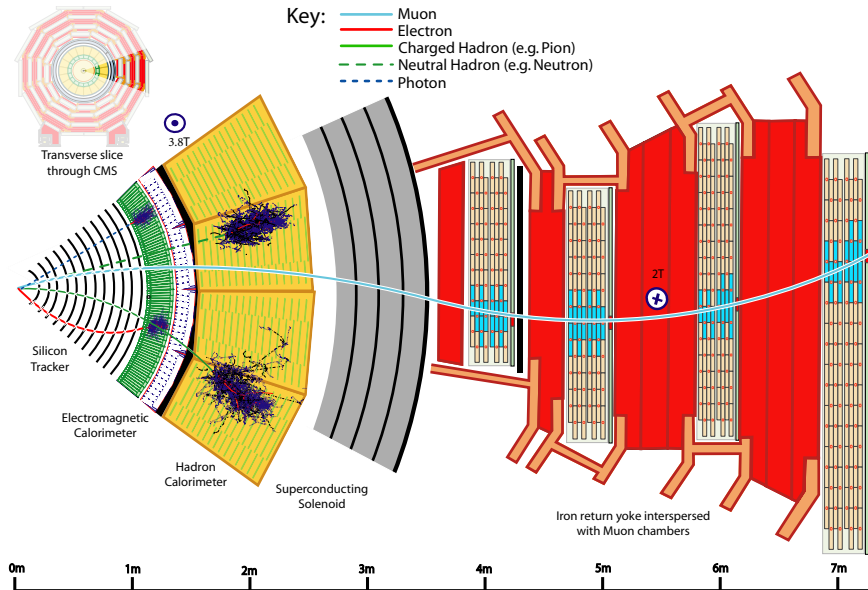


Figure 3.6: A transverse slice through the barrel section of the CMS detector with the main subsystems and components visible. Several particles produced at the primary vertex and their interactions with the detector are also depicted. Figure obtained from Ref. 126.

3.2.2 Data acquisition and triggering

With the enormous collision rate at the CMS interaction point, acquiring data requires some thought and ingenuity. Today's electronics cannot handle the bandwidth from recording

⁶Maybe mention the upgrades done between Run-1 and Run-2 (each subsystem), and possibly even the planned upgrades for Run-3 and Phase-2.

every single collision, $\mathcal{O}(1 \text{ petabyte/s})$. As such, a *trigger* is used to select the events that may be of use to analysers. In CMS, a two stage trigger [30] is used: the Level-1 Trigger (L1T), implemented in the detector hardware; and the High-Level Trigger (HLT) [47], a software farm to further reduce the events selected at Level-1. The trigger is part of the larger data acquisition (DAQ) system. An intricate network of custom electronics and commercial processors—a union of hardware, firmware, and software—are interconnected by multi-gigabit links to record the products of the highest-energy manmade collisions on Earth.

3.2.2.1 The Level-1 Trigger

The Level-1 Trigger is a set of algorithms (a trigger menu) implemented in custom hardware designed to reduce the event rate from 40 MHz to a maximum of 100 kHz. FPGA and ASIC chips contain the algorithms in firmware, with timing systems synchronised with the LHC clock. When a collision occurs, particles interact with the detector and hits are registered by the components.

Coarsely-segmented data is read out from the ECAL and HCAL through a two-layer Calorimeter Trigger. These are arrays of custom processors located at Point 5. Layer-1 receives the calorimeter data from upwards of one thousand fibre optic links, each with multi-gigabit bandwidths. The information from the two subsystems are combined into calorimeter towers, and some simple position- and energy-dependent calibrations are applied.⁷ The data from Layer-1 is then transmitted to Layer-2, again over many high-bandwidth optical links. Here, physics object candidates are identified (jets, e , γ , τ).⁸ Additional calibrations are applied to them (for example, in Chpt. 3.2.4), and simple pileup subtraction is performed. Energy sums are also calculated at this stage, such as E_T^{miss} , H_T , and H_T^{miss} .

In parallel, the various subdetectors in the muon chambers pass information through successive stages, and is then combined with some of the calorimeter information in a sorting/merging/isolation layer. The output from this layer is combined with the remaining information within Layer-2 in the Global Trigger, a series of μ TCA boards with FPGAs. The trigger menu lives here, and all of the information gathered—object candidates, energy sums, beam conditions—is provided to it. These triggers may be dependent on the presence of a single object or the number of objects of a single class (e.g., one muon, two jets), multiple classes of object (cross triggers), the energy sums, the topologies of objects, and more. The latency given to make a decision on whether to keep or reject an event is 4 μs . A diagram of this data flow is given in Fig. 3.7.

⁷Mention something about trigger primitives here?

⁸An overview of the latest Run-2 algorithms for object identification can be found in Ref. 145.

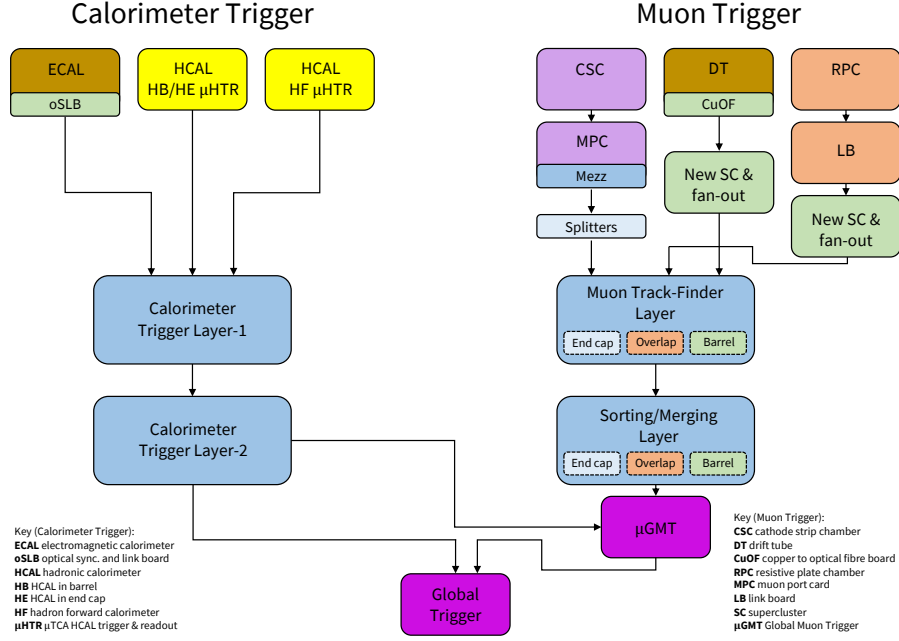


Figure 3.7: A summary of the CMS Level-1 Trigger data flow from the hits recorded by the subsystems to the Global Trigger. Figure reproduced from Ref. 74.

A small subset of data from the L1T is diverted for monitoring purposes. During data taking periods, CMS has a plethora of members that participate in the supervision and maintenance of the experiment. At Point 5, shifters monitor the systems in real time, collecting information from various sources. Data acquisition, data quality, access to the experimental cavern, the L1T, and the HLT are among them. Experts in these, and more specific subsystems, are on call on a rotating period. My responsibilities have included in-person shifts for the Level-1 Trigger and on call expertise for Layer-2 of the Calorimeter Trigger.

3.2.2.2 The High-Level Trigger

Events that pass a logical OR of the triggers at Level-1 are transmitted to the HLT. The higher resolution data collected at the point of collision is available, along with information from the tracker. Populated with Intel Xeon processors (high core count CPUs), approximately 22,000 cores are available (by the end of Run-2) to process the data sent from the L1T. In order to avoid a back-log, a 100 kHz input rate allows a HLT node \sim 220 ms to make a decision. High-level software in the cmssw environment (written in C++ and Python) is executed. A larger and more complex trigger menu is available, including the possibility analysis-specific triggers (such as those that target VBF topologies in Chpt. 6). Complex variables such as α_T can even be calculated and triggered on.

Physics objects are reconstructed further, with algorithms such as anti- k_T used to cluster jets [40]. Using a distance parameter—related to the radius of the cone surrounding the hadrons—of 0.4 denotes a jet as *AK4*, while a value of 0.8 is used to cluster fat jets and are known as *AK8*. Additional classification algorithms are also applied to objects, such as the DEEPCSV neural network [129] to identify *b*-jets. A global event reconstruction from the PARTICLE FLOW algorithm (PF) [61, 126] is performed as well. Some of these algorithms can be computationally expensive. Consequently, only approximations/parametrisations are used at HLT level. The full-scale versions of these kind of algorithms are re-run on the retained events in later stages of postprocessing.⁹

The HLT reduces the event rate from the maximum 100 kHz input substantially to around 1 kHz. The data stream of $\mathcal{O}(6 \text{ GB s}^{-1})$ is then subject to further processing before the analysts access it. As well as the data being stored on networked hard drives at sites across the globe, back ups are made to magnetic tape for long term storage. As with the Level-1 Trigger, some data is redirected for monitoring, object calibrations, and alignment of detector components.

3.2.2.3 Data reduction and compression

Several data tiers are used in CMS to serve different purposes. All sorted in ROOT file containers,¹⁰ RAW data is repacked straight from prompt reconstruction. The files are then converted to the RECO tier where objects are fully reconstructed. Files are large (around 1.3–1.4 MB per event) and usually only kept for a short period of time for detector-related studies. The subset designed for analysis is designed Analysis Object Data (AOD). However, the level of compression is not ideal, especially with the volume of data amassed in Run-2. This is why miniAOD was developed. By *slimming* the trees in the files (removing unnecessary branches) and using smaller numeric data types, the footprint is roughly 10–15 % that of AOD.

An even more drastic reduction was made possible by the introduction of the nanoAOD tier. The methods used to shrink AOD to miniAOD are applied more aggressively, and a flat tree structure (with only leaves, and no nested levels) is utilised for simpler access to data. This allows for much smaller file sizes $\mathcal{O}(1\text{--}2 \text{ kB/event})$. Exporting to other data structures for integration with external libraries, such as numpy and pandas, is also achievable. While nanoAOD is unable to cover all analyses because of its reduced event content, it is suitable in our search for invisibly decaying Higgs bosons.

⁹If more detail is required here, I should make a separate subsubsection and discuss.

¹⁰Event and ancillary data are stored in tree structures (otherwise known as *ntuples*), with *branch* and *leaf* levels that contain more specific quantities such as muon p_T , or jet η .

3.2.3 Simulating CMS data

Data recorded by CMS is paramount for analyses searching for new physics. However, simulated samples are also of high importance. Events for specific processes are generated using Monte Carlo (MC) random sampling, and the output datasets are often collectively referred to by the method—*Monte Carlo* or *MC*. The datasets are often generated with large numbers of events to minimise the associated statistical uncertainty. MC samples are useful in a variety of cases: understanding the kinematics of signal processes in searches for new physics, modelling background processes that can mimic signal, and comparisons to data for validation purposes.

A matrix element generator such as MADGRAPH [14] or POWHEG [85, 116] models the hard scattering process, usually at leading order (LO) but sometimes at higher orders. Events then pass through a hadroniser (usually PYTHIA [137] in CMS) to model hadronisation of quarks and gluons, sometimes known as the *parton shower*—the softer radiation that accompanies the hard scatter. Jets are clustered here by, for example, the anti- k_T algorithm. The particles are also run through a detector simulation that emulates the configuration and response of the detector in different years. Material interactions and emulation of the triggers are included. GEANT4 [10] provides this in CMS. Once the particles have been appropriately simulated, they are given the same postprocessing treatment as actual data, such as executing object-tagging algorithms so that the data and simulated samples are as comparable as possible.

3.2.4 Jet energy corrections in the Level-1 Trigger

Recording the properties of hadrons that are amalgamated into jets is not always consistent across the detector. While the components go through quality control, there is inevitably some variation in their performance. They can degrade at different rates. Some may also receive hits more often than others and be subject to greater radiation damage. As a result, non-uniformity of the detector response—as functions of p_T and η —must be compensated for. For jets, this comes in the form of jet energy corrections (JEC).

As outlined in Chpt. 3.2.2.1, the trigger primitives from the ECAL and HCAL enter Layer-1 of the Calorimeter Trigger, where coarse position- and energy-dependent calibrations are applied. Objects such as jets are initially identified in Layer-2, and preliminary calibrations correct their energy. Disregarding these, even at this early stage in the data acquisition workflow, can affect the efficiency and rate of the Level-1 Trigger. It is therefore important to re-derive the calibrations regularly, since the configuration of the detector and beam conditions change over the lifetime of the experiment.

When a new round of calibrations are derived, there are many steps before this one. Preceding it, Layer-1 experts calculate their scale factors for the calorimeter towers. Once performed, the jet energy corrections are then derived in cmssw. From early 2017 to mid-2018, I was responsible for procuring the JEC. The repository is accessible at <https://github.com/eshwen/L1JetEnergyCorrections>.

3.2.4.1 The procedure

QCD multijet MC datasets with a large p_T range are used to derive the Layer-1 and Layer-2 calibrations. Corresponding jets in data for this process can often be mismeasured (so providing good calibrations in the most difficult scenario is a good test), and MC events contain *truth-level* information from the generator. Ntuples are made from these which have the Layer-1 corrections applied. Referring to the processing chain in Chpt. 3.2.3, the jets these calibrations are derived for are post-hadronisation, but before interaction with the detector. They are referred to as *Level-1 (L1) jets*. The reference jets directly from the generator (GenJets as colloquialised in CMS) are important for matching to our L1 jets to ensure jets from the parton shower—that have no well-defined source—are not mistakenly being used.

The reference and L1 jets are matched using the variable ΔR (see Eq. 3.6). The algorithm used to match the jets does so by inspecting each L1 jet in descending p_T and searching for a reference jet with $\Delta R < 0.25$. If there is more than one match, the reference jet with the smallest ΔR is taken. Then the next L1 jet (and so on) follows the same procedure, with the previous reference jet removed from the matching collection.

The pairs of jets are categorised into sixteen bins of $|\eta|$, the highest granularity available since the calibrations must run quickly on hardware. Each bin is then analysed in turn. Within each $|\eta|$ bin, the jet pairs are subdivided into bins of the transverse momentum of the reference jet ($p_T^{\text{ref.}}$).¹¹ The bin widths, like $|\eta|$, are variable. The ratio of the transverse momentum of the L1 jet (p_T^{L1}) to $p_T^{\text{ref.}}$ is taken for each pair of jets. Our metric for measuring the detector response is the mean of these ratios:

$$(3.8) \quad r_j = \left\langle p_T^{\text{L1}} / p_T^{\text{ref.}} \right\rangle$$

The reciprocal of r_j vs. p_T^{L1} is inspected and a correction curve is fitted. A gaussian captures

¹¹Should I add tables somewhere of the $p_T^{\text{ref.}}$ and $|\eta|$ bins for the calibrations?

the peak at low p_T and the following equation¹² is used for the tail:

$$(3.9) \quad p_T^{L1, \text{corr.}} = p_T^{L1} \cdot \left(p_0 + p_1 \cdot \text{erf} \left(p_2 \cdot \left(\log_{10} p_T^{L1} - p_3 \right) \right) \right. \\ \left. + p_4 \cdot \exp \left(p_5 \cdot \left(\log_{10} p_T^{L1} - p_6 \right)^2 \right) \right)$$

The starting parameters for the function may not be adequate for all cases, so they are often tuned to capture the low- p_T spike and high- p_T plateau (see Fig. 3.8 for an example). The value of this fit function in each $p_T^{\text{ref.}}$ bin is exported.

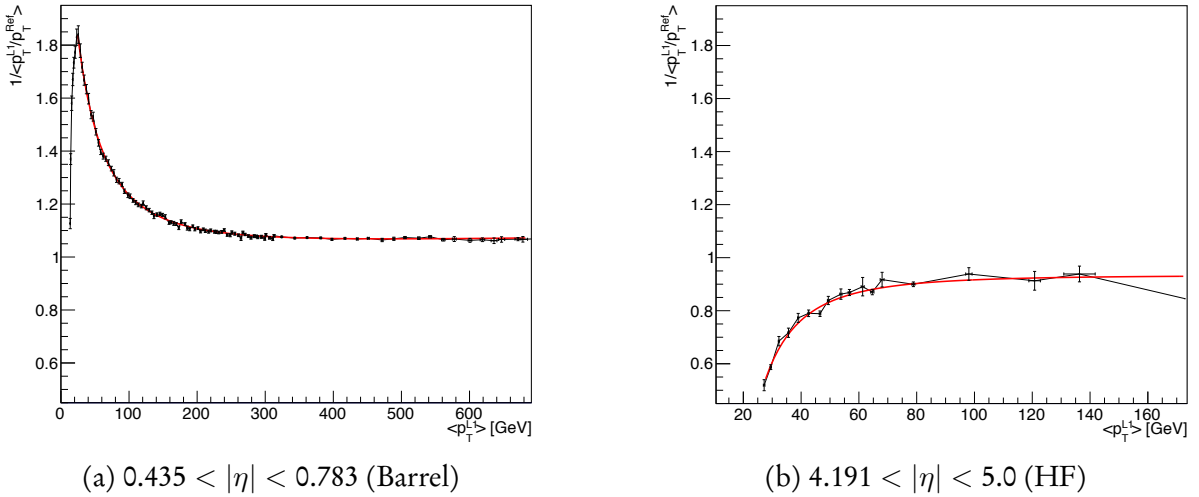


Figure 3.8: Examples of correction curves used to calibrate the jet energies in two $|\eta|$ bins. The reciprocal of the response is plotted against the p_T of the Level-1 jet, and a complex function (Eq. 3.8) fits the points. These plots are from the jet energy corrections performed on 2018 QCD Monte Carlo.

Once all $|\eta|$ bins have been inspected, the calibrations are consolidated in several forms. A machine-readable lookup table is included in the firmware of the Layer-2 hardware, so that the corrections are applied in the trigger. A version is added to the Level-1 Trigger packages in CMSSW so that the next steps in the calibration chain can utilise them.

A closure test is conducted to validate the corrections that were produced. The MC ntuples are regenerated with the JEC applied. Jet matching is performed and the calibrations are checked. Many diagnostic and performance plots are produced to ensure the calibrations are functioning as expected. These can be inclusive of the number of pileup interactions, or split into ranges to see if the calibrations differ between them. Examples of these are Fig. 3.9 showing scatter plots of $p_T^{\text{ref.}}$ vs. p_T^{L1} before and after JEC are applied, and Fig. 3.10 illustrating the response.

¹²Go into more detail regarding the equation? Reasoning, etc.

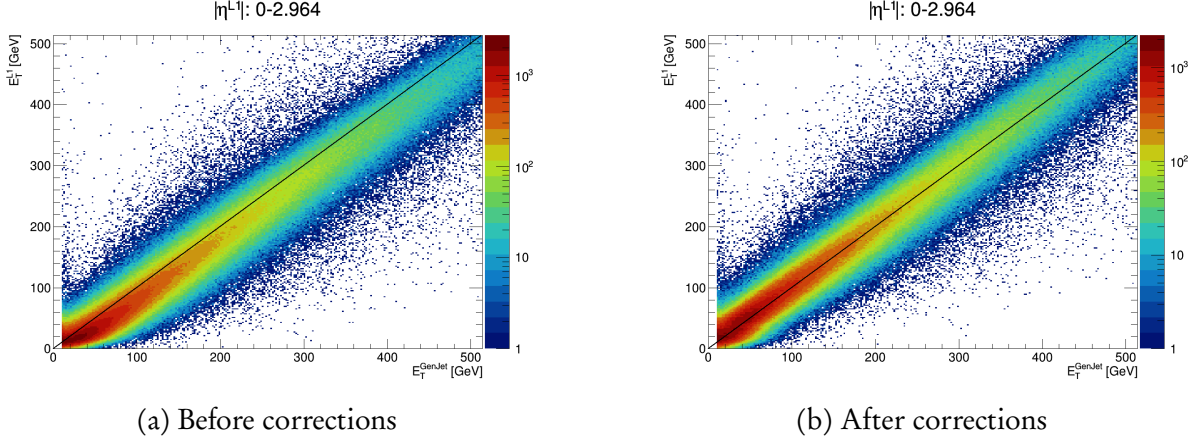


Figure 3.9: The energies of matched pairs of jets from simulation in the entire barrel and end cap, in the pileup 40–50 range, before and after jet energy corrections have been applied. An equivalent plot using jets from LHC data is expected to look similar after applying these calibrations.

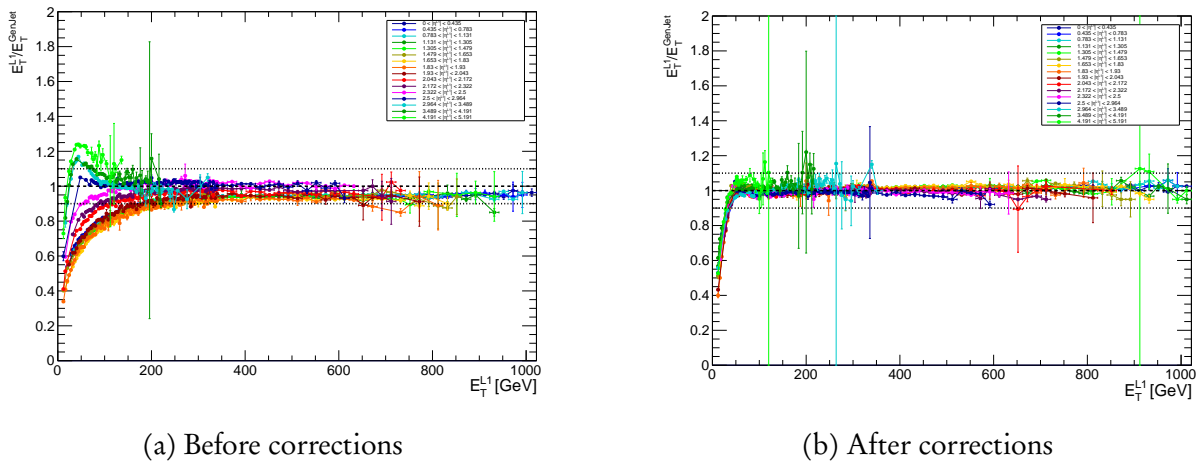


Figure 3.10: The response curves in each $|\eta|$ bin as a function of p_T^{L1} , in the pileup 40–50 range, before and after JEC are applied. Note that in panel b, the x -axis is the corrected p_T^{L1} .

After calibrations, the energies of the generator and L1 jets are much more comparable and have a smaller spread. The jet energy corrections perform well as intended across wide ranges of pileup and jet p_T , providing confidence for accurate calibrations in the calorimeter when data are collected.

DEFINITIONS OF PHYSICS OBJECTS AND OBSERVABLES

You know when grown-ups tell you everything's going to be fine, but you really think they're lying to make you feel better? Everything's going to be fine.

— The Eleventh Doctor, *Doctor Who*

This chapter first discusses some prevalent variables used in the analyses presented in this thesis. Accordingly, it is practical to consolidate their definitions here. The rest of the chapter is devoted to classification of the physics objects that inform the analysis in Chpt. 6.

4.1 Ubiquitous observables and quantities in collider physics

4.1.1 Transverse momentum (\vec{p}_T)

In the LHC (or any other hadron collider), the longitudinal momenta of the proton constituents that collide are typically unknown. However, the momentum transverse to the beam is zero before the collision, and must be zero afterward after due to momentum conservation. This is why the transverse momentum of a particle or physics object (\vec{p}_T for the vector quantity, p_T for its magnitude) is a useful variable in an analysis.

4.1.2 H_T

For analyses focused on hadronic objects—such as branches of supersymmetry where a large jet multiplicity is expected—it is practical to define the total amount of hadronic activity in an event. The scalar sum of the transverse momentum of the jets is symbolised as H_T :

$$(4.1) \quad H_T \equiv \sum_{\text{jets}} p_T$$

Typically, a lower limit on the p_T is used when calculating the H_T , so jets below this threshold do not factor into the sum. This is to avoid low momentum jets attributed to pileup events (see Chpt. 3.1.3) and soft radiation.

4.1.3 Missing transverse momentum (\vec{p}_T^{miss})

The missing transverse momentum \vec{p}_T^{miss} is defined as the negative vector sum of the \vec{p}_T of all identified particles in an event. It is a term often used interchangeably with missing transverse energy (MET, \vec{E}_T^{miss}). Undetected particles from neutrinos or dark matter, or mismeasured kinematic properties of identified particles, will introduce an imbalance in the vector sum of the \vec{p}_T . Hence, the \vec{p}_T^{miss} will be non-zero. Formally,

$$(4.2) \quad \begin{aligned} \vec{p}_T^{\text{miss}} &\equiv - \sum_i^{N_{\text{particles}}} \vec{p}_{T,i} \\ p_T^{\text{miss}} &\equiv \left| \vec{p}_T^{\text{miss}} \right| \end{aligned}$$

The hadronic-only counterpart to this variable, \vec{H}_T^{miss} , is the negative vector sum of the jet transverse momenta in an event:

$$(4.3) \quad \begin{aligned} \vec{H}_T^{\text{miss}} &\equiv - \sum_j^{N_{\text{jets}}} \vec{p}_{T,j} \\ H_T^{\text{miss}} &\equiv \left| \vec{H}_T^{\text{miss}} \right| \end{aligned}$$

As with H_T , the H_T^{miss} is often calculated with a lower limit on the jet p_T .

4.1.4 Transverse mass (m_T)

The transverse mass m_T of a particle—or the collective products of a decay—is the component of its invariant mass in the transverse plane. In a hadron collider context, this observable is often used when one of the decay products is invisible or unidentified, i.e., as \vec{p}_T^{miss} . When

searching for semi-visible jets, the m_T of the dijet system is very reliable in recovering the Z' mass. Einstein's equation $E^2 = (pc)^2 + (m_0c^2)^2$ can be reformulated for each daughter particle in a decay as

$$(4.4) \quad E_T^2 = m_0^2 + p_T^2$$

where E_T is the transverse energy. The transverse mass of the system is then

$$(4.5) \quad \begin{aligned} m_T^2 &= (E_{T,1} + E_{T,2})^2 - (\vec{p}_{T,1} + \vec{p}_{T,2})^2 \\ &= m_1^2 + m_2^2 + 2(E_{T,1}E_{T,2} - \vec{p}_{T,1} \cdot \vec{p}_{T,2}) \end{aligned}$$

In the case of one unidentified daughter, the \vec{p}_T^{miss} may substitute a particle in the first line of Eq. 4.5. If one also treats the daughters as massless, i.e., if $p_T \gg m_0$ like with boosted leptons, the formula approximates to

$$(4.6) \quad m_T^2 = 2p_T p_T^{\text{miss}} (1 - \cos(\Delta\phi))$$

where $\Delta\phi = \phi - \phi(p_T^{\text{miss}})$, and p_T and ϕ are from the identified daughter.

4.2 Classification of analysis-level physics objects

The physics that occurs at the high energies the LHC is capable of is not simple. That makes the recording of particles and events overall a non-trivial undertaking. Based on complex hardware and software, research, and the experience of previous experiments, establishing physics objects and variables from an analyst's standpoint is thankfully straightforward. The basic definitions are already included into the ROOT files we use, with ancillary selections on top for the analysis-level objects. All of the descriptions that follow apply both to data and simulated samples, unless otherwise stated.

Different working points for the identification of many objects are available from the respective Physics Object Groups (POGs), trading efficiency for purity the tighter the restrictions are. *Veto*, *loose*, *medium*, and *tight* criteria exist for most objects. We denote particles with a subscript that signifies the working point. The requirements of which are elaborated upon in the ensuing subsections.

4.2.1 Jets

In the nanoAOD data tier, a jet is defined as an AK4-clustered, charged hadron-subtracted object reconstructed with the PARTICLE FLOW algorithm, with jet energy corrections applied

and a $p_T > 15 \text{ GeV}$ prerequisite. For the analysis, we then apply the *latest* JEC and jet energy resolution (JER) treatments to both data and simulation to determine the p_T . Those with $p_T > 30 \text{ GeV}$ are kept. The JER is worse in data than in simulation, so jets in the latter are smeared to describe the former more accurately.

The tight, with or without an additional lepton veto, PF identification requirements are also mandatory to establish a sufficient degree of purity with a very high efficiency ($> 98\%$ in all $|\eta|$ regions). These are documented in Tabs. 4.1, 4.2, and 4.3. For all years, both the identification and background rejection efficiencies are above 98 % in the barrel and end caps.

A jet suspected to originate from a b -quark, or “ b -jet,” is described by a nanoAOD AK4 jet with corrected $p_T > 20 \text{ GeV}$ and within the acceptance of the tracker— $|\eta| < 2.4$ in 2016, and < 2.5 onward. It is also required to satisfy the medium working point (a mis-tag rate of 1 %) from the DEEPCSV algorithm [129].

4.2.1.1 Jet identification criteria in 2016

The tight and tight + lepton veto ID specifications are detailed in Tab. 4.1. Specifically to this year, all jets are required to fulfill the criteria for the tight pileup ID to ensure they do not originate from pileup vertices. The algorithm that gives the pileup ID is based on a boosted decision tree trained on 2016 samples. It incorporates tracker information, jet topology, and constituent multiplicity as discriminating variables.

Criterion	$ \eta \leq 2.4$	$2.4 < \eta \leq 2.7$	$2.7 < \eta \leq 3.0$	$ \eta \geq 3.0$
Neutral hadron fraction	< 0.90	< 0.90	< 0.98	—
Neutral EM fraction	< 0.90	< 0.90	> 0.01	< 0.90
# constituents	> 1	> 1	—	—
Muon energy fraction	$< 0.80^*$	$< 0.80^*$	—	—
Charged hadron fraction	> 0	—	—	—
Charged multiplicity	> 0	—	—	—
Charged EM fraction	$< 0.99 \text{ (} 0.90^* \text{)}$	—	—	—
# neutral particles	—	—	> 2	> 10

Table 4.1: The requirements for a jet to pass tight identification for data taken in 2016, and to Monte Carlo events emulating that year. Information taken from Ref. 56.

* Only applies to the tight + lepton veto ID.

4.2.1.2 Jet identification criteria in 2017

The tight and tight + lepton veto ID conditions are detailed in Tab. 4.2. Jets with $p_T < 50 \text{ GeV}$ are required to meet the tight pileup ID criteria. Any jets with a raw (uncorrected) transverse

4.2. CLASSIFICATION OF ANALYSIS-LEVEL PHYSICS OBJECTS

momentum $p_T^{\text{raw}} < 50 \text{ GeV}$ within the region $2.65 < |\eta| < 3.139$ are vetoed due to noise in the ECAL end cap.

Criterion	$ \eta \leq 2.4$	$2.4 < \eta \leq 2.7$	$2.7 < \eta \leq 3.0$	$ \eta \geq 3.0$
Neutral hadron fraction	< 0.90	< 0.90	—	> 0.02
Neutral EM fraction	< 0.90	< 0.90	> 0.02, < 0.99	< 0.90
# constituents	> 1	> 1	—	—
Muon energy fraction	< 0.80*	< 0.80*	—	—
Charged hadron fraction	> 0	—	—	—
Charged multiplicity	> 0	—	—	—
Charged EM fraction	< 0.80*	—	—	—
# neutral particles	—	—	> 2	> 10

Table 4.2: The requirements for a jet to pass tight identification for data taken in 2017, and to Monte Carlo events emulating that year. Information taken from Ref. 57.

* Only applies to the tight + lepton veto ID.

4.2.1.3 Jet identification criteria in 2018

The tight and tight + lepton veto ID specifications are detailed in Tab. 4.3.¹ As in 2017, jets with $p_T < 50 \text{ GeV}$ must fulfill the tight pileup ID conditions.²

Criterion	$ \eta \leq 2.6$	$2.6 < \eta \leq 2.7$	$2.7 < \eta \leq 3.0$	$3.0 < \eta \leq 5.0$
Neutral hadron fraction	< 0.90	< 0.90	—	> 0.20
Neutral EM fraction	< 0.90	< 0.99	> 0.02, < 0.99	< 0.90
# constituents	> 1	—	—	—
Muon energy fraction	< 0.80*	< 0.80*	—	—
Charged hadron fraction	> 0	—	—	—
Charged multiplicity	> 0	> 0	—	—
Charged EM fraction	< 0.80*	< 0.80*	—	—
# neutral particles	—	—	> 2	> 10

Table 4.3: The requirements for a jet to pass tight identification for data taken in 2018, and to Monte Carlo events emulating that year. Information taken from Ref. 58.

* Only applies to the tight + lepton veto ID.

¹There's probably a more elegant way to write the ID criteria, since the same variables are used for all years and the same thresholds in many cases. But until I figure it out, separate tables for each year will have to do

²Is it worth going into the pileup ID spec.?

4.2.2 Boosted topologies originating from top quarks and electroweak bosons

Many traditional methods have been developed to tag jets originating from heavy particles, such as top quarks, vector bosons and Higgs bosons. Though, there are limitations with all of these, and in the era of machine learning a plethora of new tools have arisen. One such algorithm—DEEPAK8—has been developed by physicists in CMS to classify jets that originate from numerous heavy particle decays. In the analysis in search of invisibly decaying Higgs bosons, specific interest is paid to those coming from top quarks and vector bosons in order to assist the categorisation of the $t\bar{t}H$ and VH signals. The design and optimisation of the algorithm is described in Ref. 60.³

The algorithm operates on AK8 jets. Following the same reconstruction and identification prescription as AK4 jets, they differ only in the cone size and p_T requirement. Hadrons are clustered with the anti- k_T algorithm using a radius parameter of 0.8 instead of the usual 0.4, and must possess a $p_T > 170 \text{ GeV}$. The corrections and uncertainties from JER and JES are also propagated identically.

The ensuing selections are applied to AK8 jets to classify them, as recommended by the DEEPAK8 developers:

- Boosted top:
 - $p_T > 400 \text{ GeV}$
 - $105 < m_{\text{SD}} < 210 \text{ GeV}$
 - t vs. QCD discriminator score with the tight working point (1 % mis-tag rate)
- Boosted V :
 - $p_T > 200 \text{ GeV}$
 - $65 < m_{\text{SD}} < 105 \text{ GeV}$
 - W vs. QCD discriminator score with the tight working point (1 % mis-tag rate)

Orthogonality is ensured between the two classifications from the soft drop mass m_{SD} [109] window. The quantity is corrected for pileup contributions using the PUPPI algorithm [33]. Tight working points that effectively separate the jets from QCD background ensure a high purity collection. Boosted V jets are not further separated into W - and Z -tagged since the mass degeneracy makes this inherently difficult. The W vs. QCD discriminator is therefore used to tag both.

³Not sure if I should give a summary of the development and features of the algorithm here.

4.2.3 Muons

The reconstruction and identification criteria for muons is described in significant detail in Ref. 130. From there, a loose muon μ_{loose} satisfies the loose muon identification requirements. Additionally, $|\eta| < 2.4$, $p_T > 10 \text{ GeV}$, and the loose working point of the PARTICLE FLOW relative isolation parameter (Eq. 5.4 in Ref. 126) $I_{\text{PF}} < 0.25$ must be satisfied. A tight muon μ_{tight} meets the tight muon ID requirements from Ref. 130, $|\eta| < 2.4$, $p_T > 20 \text{ GeV}$, and the tight working point for the relative isolation ($I_{\text{PF}} < 0.15$).

The relative isolation parameter is the ratio of the sum of track, HCAL and ECAL energies within $\Delta R < 0.4$ of the muon to the particle's momentum. The loose and tight working points are designed to give efficiencies of 98 % and 95 %, respectively.

4.2.4 Electrons

Electrons in the analysis are labelled as veto (e_{veto}) or tight electrons (e_{tight}), depending on which POG ID requirements are fulfilled. For 2016–18, version 2 of the cut-based identification scheme (tuned using 2017 samples), is applied. These are distinguished for the barrel region in Tab. 4.4, and end cap region in Tab. 4.5. The veto and tight ID specifications are designed for average efficiencies of 95 % and 70 %, respectively.⁴

Criterion	Veto	Tight
Full $5 \times 5 \sigma_{i\eta i\eta}$	< 0.0126	< 0.0104
$ \Delta\eta_{\text{in}}^{\text{seed}} $	< 0.00463	< 0.00255
$ \Delta\phi_{\text{in}} $	< 0.148	< 0.022
H/E	$< 0.05 + \frac{1.16}{E_{\text{SC}}} + \frac{0.0324\rho}{E_{\text{SC}}}$	$< 0.026 + \frac{1.15}{E_{\text{SC}}} + \frac{0.0324\rho}{E_{\text{SC}}}$
Relative isolation with $A_{\text{eff.}}$	$< 0.198 + \frac{0.506}{p_T}$	$< 0.0287 + \frac{0.506}{p_T}$
$ E_{\text{ECAL}}^{-1} - p_{\text{Tracker}}^{-1} $	< 0.209	< 0.159
Expected missing inner hits	≤ 2	≤ 1
Pass conversion veto	yes	yes

Table 4.4: Requirements used to define the veto and tight electron IDs in the barrel region (supercluster $|\eta| \leq 1.479$). Information taken from Ref. 54.

The variable $\sigma_{i\eta i\eta}$ is the energy-weighted standard deviation of the ECAL crystal η , centred on the local energy maximum, in this case using the full 5×5 crystal information from the calorimeter tower. $\Delta\eta_{\text{in}}^{\text{seed}}$ and $\Delta\phi_{\text{in}}$ are the differences in pseudorapidity and azimuthal angle, respectively, between the supercluster (seed in the case of $\Delta\eta$) and the track. H/E is

⁴Can't find background rejection efficiencies on twiki pages.

Criterion	Veto	Tight
Full $5 \times 5 \sigma_{i\eta i\eta}$	< 0.0457	< 0.0353
$ \Delta\eta_{\text{in}}^{\text{seed}} $	< 0.00814	< 0.00501
$ \Delta\phi_{\text{in}} $	< 0.19	< 0.0236
H/E	$< 0.05 + \frac{2.54}{E_{\text{SC}}} + \frac{0.183\rho}{E_{\text{SC}}}$	$< 0.0188 + \frac{2.06}{E_{\text{SC}}} + \frac{0.183\rho}{E_{\text{SC}}}$
Relative isolation with $A_{\text{eff.}}$	$< 0.203 + \frac{0.963}{p_{\text{T}}}$	$< 0.0445 + \frac{0.963}{p_{\text{T}}}$
$ E_{\text{ECAL}}^{-1} - p_{\text{Tracker}}^{-1} $	< 0.132	< 0.0197
Expected missing inner hits	≤ 3	≤ 1
Pass conversion veto	yes	yes

Table 4.5: Requirements used to define the veto and tight electron IDs in the end cap region (supercluster $|\eta| > 1.479$). Information taken from Ref. 54.

the ratio of the candidate’s central energy deposit in the HCAL to the ECAL. The relative isolation parameter is computed in the same way as muons (Eq. 5.4 in Ref. 126), but uses a cone of $\Delta R < 0.3$ instead of 0.4. The isolation threshold takes the effective area $A_{\text{eff.}}$ into account. Along with ρ —a parameter in the FASTJET package [39] used for jet finding—these are used for estimating the contamination from pileup in an event. E_{SC} is the energy of the supercluster, and is used to scale the isolation requirement. From material interactions within the tracker, photons may convert into e^+e^- pairs. A dedicated veto aims to mitigate this effect.

Common to all electrons in the analysis, we place a cut of $|\eta| < 2.5$ so they are reconstructed with tracker information. To further utilise the subdetector, impact parameter conditions on the transverse and longitudinal directions ensure they originate sufficiently close to the primary vertex: $d_0 < 0.05$ cm and $dz < 0.1$ cm in the barrel, with $d_0 < 0.1$ cm and $dz < 0.2$ cm in the end cap. The e_{veto} and e_{tight} sets are only separated by the identification prerequisites above, and transverse momentum. A veto electron requires $p_{\text{T}} > 10$ GeV, and a tight electron $p_{\text{T}} > 40$ GeV.

4.2.5 Photons

Photons are identified in a similar manner to electrons—using version 2 of the cut-based scheme for 2016–18, optimised with 2017 Monte Carlo. We define loose γ_{loose} and medium photons γ_{medium} that fulfill the corresponding working point criteria for identification. For inclusivity, the latter is used instead of the tight working point. These are detailed in Tab. 4.6 and Tab. 4.7 for the barrel and end cap regions, respectively. The loose photon ID specification is designed to be 90 % efficient, and the medium ID 80 %. In the barrel and end caps, the

loose ID rejects 86 % and 77 % of background, respectively, while the medium ID removes 89 % and 82 %, respectively. Both collections must also pass the electron conversion veto to ensure they originate promptly from the primary vertex.

Criterion	Loose	Medium
H/E	< 0.04596	< 0.02197
$\sigma_{i\eta i\eta}$	< 0.0106	< 0.01015
ρ -corrected PF charged hadron isolation	< 1.694	< 1.141
ρ -corrected PF neutral hadron isolation	$< 24.032 + X + Y$	$< 1.189 + X + Y$
ρ -corrected PF photon isolation	$< 2.876 + Z$	$< 2.08 + Z$

Table 4.6: Requirements used to define the loose and medium photon IDs in the barrel region of the detector ($|\eta| \leq 1.479$). The factors $X = 0.01512 p_T$, $Y = 2.259 \times 10^{-5} p_T^2$, and $Z = 0.004017 p_T$ in the isolation criteria are used to scale the threshold. Information taken from Ref. 55.

Criterion	Loose	Medium
H/E	< 0.0590	< 0.0326
$\sigma_{i\eta i\eta}$	< 0.0272	< 0.0272
ρ -corrected PF charged hadron isolation	< 2.089	< 1.051
ρ -corrected PF neutral hadron isolation	$< 1.922 + X + Y$	$< 2.718 + X + Y$
ρ -corrected PF photon isolation	$< 4.162 + Z$	$< 3.867 + Z$

Table 4.7: Requirements used to define the loose and medium photon IDs in the end cap region of the detector ($|\eta| > 1.479$). The factors $X = 0.0117 p_T$, $Y = 2.3 \times 10^{-5} p_T^2$, and $Z = 0.0037 p_T$ in the isolation criteria are used to scale the threshold. Information taken from Ref. 55.

The variables $\sigma_{i\eta i\eta}$ and ρ follow the same definitions as in Chpt. 4.2.4. The ρ -corrected isolation is calculated by taking the maximum of zero, and the difference between the PARTICLE FLOW isolation and possible contamination from pileup:

$$(4.7) \quad I_{\text{PF}}^{\text{corr.}} = \max(I_{\text{PF}} - \rho A_{\text{eff.}}, 0)$$

As well as the ID, the two collections diverge further due to η and p_T requirements. A loose photon is characterised by $|\eta| < 2.5$ and $p_T > 15 \text{ GeV}$, while a medium photon must be central ($|\eta| < 1.442$) and possess $p_T > 230 \text{ GeV}$.

4.2.6 Tau leptons

The only purpose tau leptons τ serve in the analysis is to veto events that contain them. These are denoted as *very loose* taus $\tau_{\text{v. loose}}$. Version 2 of the multivariate identification algorithm

is used for all years, and tau leptons must pass the very loose criteria. Dedicated multivariate discriminators against electrons and muons are provided and employed, passing the loose and very loose working points, respectively. Kinematically, a $\tau_{v.\text{ loose}}$ also requires $p_T > 20 \text{ GeV}$, $|\eta| < 2.3$, and $dz < 0.2 \text{ cm}$.

4.2.7 Overlap removal

Particle detection is not a straightforward process. As such, there may be particles identified close together in an event either due to real physics or misreconstruction. To ensure only well-measured and correctly-identified objects are used in analysis, particles considered to be overlapping are removed—or *cross cleaned*—between the different classes. This is performed in the following order.

Muons are first identified, followed by electrons. Cross cleaning is performed against the μ_{loose} collection of objects, so electrons are not counted in the event if they are within $\Delta R < 0.3$ of one. Photons are next in the list. Both the γ_{loose} and γ_{medium} collections are cross-cleaned against μ_{loose} and e_{veto} objects in the event with $\Delta R < 0.3$. The same collections and separation are used to remove overlap with the set $\tau_{v.\text{ loose}}$ leptons. Finally, jets are identified, with those in the AK4 collection requiring a separation of $\Delta R > 0.4$ from any electron, muon, and photon defined previously.

4.2.8 Revised energy sums \vec{p}_T^{miss} , H_T , and \vec{H}_T^{miss}

Most CMS analyses, including those presented in this thesis, define the missing transverse momentum with the *type-I correction*: corrections to the JER and JES are applied as in Chpt. 4.2.1, and so the corrected jet \vec{p}_T are propagated to the calculation of \vec{p}_T^{miss} . Uncertainties are calculated in the same manner as jets.

In 2017, significant noise in the ECAL end cap affected jets and p_T^{miss} , leading to potentially large energy mismeasurements. These quantities were recomputed after reconstruction, and carried through the analysis.

The scalar sum H_T and negative vector sum of hadronic transverse momentum \vec{H}_T^{miss} are broadly defined in Chpts. 4.1.2 and 4.1.3, respectively. They are calculated from the analysis-level AK4 jets with $p_T > 30 \text{ GeV}$, as detailed in Chpt. 4.2.1.

Regarding the \vec{p}_T^{miss} and \vec{H}_T^{miss} , in most cases the magnitudes (p_T^{miss} and H_T^{miss} , respectively) are the important quantities used in the event selection and other aspects of the analysis.

SEARCH FOR SEMI-VISIBLE JETS

Of darkness visible so much be lent, as half to show,
half veil, the deep intent.

— Alexander Pope

Access to the dark side of the universe is under a complex lock, seemingly unbreakable judging by the efforts of the past. A portal bridging the visible world to a realm of dark QCD, however, may be discoverable at the LHC. This chapter is dedicated to a novel search for semi-visible jets, characterised by hadronic final states and moderate missing transverse momentum.

5.1 Analysis summary

The analysis in search for semi-visible jets is formed of a collaboration amongst the University of Bristol, University of Maryland, University of Rochester, Universität Zürich, and the Fermi National Accelerator Laboratory (FNAL). The s -channel production mode with the full Run-2 dataset of CMS is the subject of the current analysis. A dijet final state with moderate p_T^{miss} is expected. The transverse mass of the dijet system m_T —calculated with Eq. 4.5—is used as the search variable. Confirmed by the distributions in this chapter for simulated signal, a peak close to $m_{Z'}$ can be captured. With the inclusion of the p_T^{miss} , the resolution of m_T is better than simply the dijet mass (m_{jj}) which would otherwise be used to recover the peak. The authors of Ref. 68 also demonstrate that sensitivity is stronger with

m_T over m_{jj} . Novel techniques are utilised, such as the development of a boosted decision tree to tag semi-visible jets and distinguish them from mismeasured QCD jets. A complete description of the s -channel analysis as of September 2019 can be found in Ref. 119.

My contribution is predominantly the development and understanding of signal simulation in `MADGRAPH5_AMC@NLO` [15] for both the s -channel and t -channel aspects of the model. As such, the remainder of the chapter is focused on their discussion. The code I developed to perform the simulation is being used for the future analysis of the t -channel mode as well as a low-mass boosted Z' search.

5.2 Signal simulation overview

In the main analysis, `PYTHIA8` [137] is employed to generate the s -channel signal as it can parametrise all the relevant aspects of the model in a simple manner with high signal efficiency. `MADGRAPH` is the often-preferred generator as it can handle more complex models and decays. A higher degree of customisation and tuning of parameters is also possible. For the s -channel mode, modelling of the hard process should be equivalent between `PYTHIA` and `MADGRAPH` at leading order (LO). In the former the properties, interactions, and decays of the dark sector particles are implemented via the Hidden Valley module, available from `PYTHIA` 8.226. Samples generated with `MADGRAPH` are hadronised by `PYTHIA` as part of the full simulation chain within `CMSSW`. Jet matching and filter efficiencies may noticeably reduce the final number of events. The t -channel model is possible to parametrise in `PYTHIA`, but due to its complexity we favour `MADGRAPH`. Hadronisation, however, is still performed by `PYTHIA`. In all cases, signal samples are generated at LO.

All the details for s -channel signal generation with `PYTHIA8` is given in Chpts. 5.3 and 5.4. This avenue was developed primarily by collaborators at FNAL. An equivalent implementation from myself where the hard scatter is modelled in `MADGRAPH5_AMC@NLO`, as both an alternative and cross-check to the `PYTHIA` version, is chronicled in Chpt. 5.5. A description of the t -channel process is also present in the section. The parameters defining the shower were synchronised between myself and the FNAL colleagues. Comparisons between the `PYTHIA` and `MADGRAPH` implementations are discussed in Chpt. 5.6.

For all spectra, no additional object corrections or selections were performed and were direct from the simulation pipeline. Reconstructed jets satisfy the tight identification criteria given in Tabs. 4.1, 4.2, or 4.2 depending on the data taking year. The missing transverse momentum p_T^{miss} contains the type-I correction as outlined in Chpt. 4.2.8. Similarly, the rest of the objects in the ntuples contain at least minimal quality assurances prior to any

analysis-level selection.

The distributions that pepper the remainder of the chapter are generated with 2016 detector conditions and reconstruction. As the analysis began in 2017, the 2016 dataset was the only complete one intending to be used. Since it was the most mature and had been studied in depth by the Collaboration, the simulation should be highly representative of what could be observed in the data from that period. Selecting one year also ensures consistency across all of the plots even though they should not significantly change year-to-year.

5.3 Generation in PYTHIA

The Hidden Valley module allows for simulating $q\bar{q} \rightarrow Z' \rightarrow \chi\bar{\chi}$, where the Z' is acts as intended—a vector portal between the visible and dark sectors. Since we expect a small percentage of them to decay visibly, a branching ratio to each of the six SM quarks is set to 0.003. The remaining fraction of 0.982 decay to $\chi\bar{\chi}$, where χ is a Hidden Valley particle charged only under that gauge group. The masses of the Z' and χ , and the narrow width of the Z' for resonant production can be given. Showering in the dark and visible sectors is then performed as in Chpt. 5.4. For both the complete event generation, and for hadronisation in the case of MADGRAPH generation, PYTHIA 8.230 was used.

5.4 Showering in PYTHIA

Once the hard process has been simulated, showering of the dark and visible particles is performed. This can be separated into three separate steps. The *parton shower* itself is where undecayed free quarks and gluons fragment and radiate due to their high energies. At *hadronisation*, the showered partons coalesce into composite hadrons due to colour confinement. Finally, the *underlying event* is the simulation of the previous two steps for any additional, softer collisions that occur between constituents of the incident particles, separate from the hard interaction. Often, the sum of all of these steps is just referred to as the *parton shower* or *hadronisation*.

5.4.1 Hadronisation of dark quarks

Dark quarks hadronise into one of two species of dark meson (as the number of dark flavours $N_f = 2$) that correspond to particles from the Hidden Valley module: π_{dark} and ρ_{dark} , that are pseudoscalar and vector, respectively. Each possess flavour-diagonal and off-diagonal

variants. They are generated probabilistically with a ratio of 1:3. Dark hadrons are set to decay invisibly with a branching fraction r_{inv} . Remaining decay modes are to SM quarks via a virtual Z' since it is the leptophobic portal between the dark and visible sectors. Decays of ρ_{dark} are democratic, i.e., with equal probability to accessible SM quark-antiquark pairs.¹ Specifically, ρ_{dark} particles with $m_{\text{dark}} > 2m_b$ have a 1/5 probability to decay to a u, d, c, s , or b . For $2m_c < m_{\text{dark}} < 2m_b$, b quarks are excluded and the branching ratio increases to 1/4 for the remaining species. The c quark is removed—and branching ratio modified—in the same manner for $m_{\text{dark}} < 2m_c$.

The decays of the π_{dark} mesons, however, are through a mass insertion. They couple to the longitudinal component of the Z' , assumed to arise from a leptophobic Higgs sector in an analogous manner to the electroweak bosons. Running quark masses are accounted for, as calculated in Ref. 79, since the decays are produced at the Higgs mass scale. Branching fractions to the SM quarks are therefore based on the squares of the *running* masses over the *pole* masses. A graphical representation of the mass insertion decay is provided in Fig. 5.1.

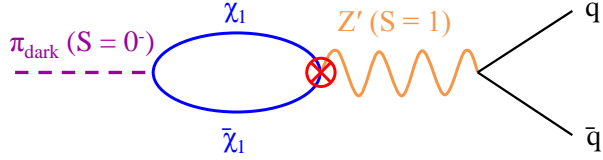


Figure 5.1: A diagram of the mass insertion decay of π_{dark} mesons in the s -channel semi-visible jet model.

We encode the dark confinement scale Λ_{dark} and running dark coupling α_{dark} , based on the dark hadron mass as given below. PYTHIA is now aware of the energy scales by which to hadronise and decay the dark sector particles. Final state dark radiation is also permitted, with a minimum p_T of $1.1\Lambda_{\text{dark}}$ as imposed by PYTHIA.

5.4.1.1 Simpler parametrisation of α_{dark}

For simplicity, the values of α_{dark} used in the scan of parameter points are based on the value of Λ_{dark} that maximises the dark hadron multiplicity in an event. The dependence was very small on $m_{Z'}$, and instead was modelled as a function of m_{dark} by performing a fit. The value of Λ_{dark} that leads to the largest number of dark hadrons ($\Lambda_{\text{dark}}^{\text{peak}}$) is

$$(5.1) \quad \Lambda_{\text{dark}}^{\text{peak}} = 3.2m_{\text{dark}}^{0.8}$$

¹Top quarks are excluded in all cases, since in the scan of model parameters where we predict the greatest sensitivity, the dark mesons are always too light to decay on shell to a $t\bar{t}$ pair.

which gives the parameter $\alpha_{\text{dark}}^{\text{peak}} = \alpha_{\text{dark}}(\Lambda_{\text{dark}}^{\text{peak}})$ calculated according to Eq. 2.12. Variations on α_{dark} are calculated by scaling it by a factor 0.5 and 1.5, yielding $\alpha_{\text{dark}}^{\text{low}} = 0.5\alpha_{\text{dark}}^{\text{peak}}$ and $\alpha_{\text{dark}}^{\text{high}} = 1.5\alpha_{\text{dark}}^{\text{peak}}$. For the purposes of emphasizing the effect of the choice of α_{dark} on the kinematics of the signal, an additional variation was introduced: $\alpha_{\text{dark}}^{\text{v. high}} = 2\alpha_{\text{dark}}^{\text{peak}}$. The advantage of denoting the dark coupling strength with “peak,” “low,” and “high,” enables a more intuitive understanding of the parameter over a numerical value. Eq. 5.1 also means that we can simply vary Λ_{dark} (and therefore α_{dark}) as a function of m_{dark} for each configuration of parameters in a scan of the model. Fig. 5.2 illustrates the evolution of Λ_{dark} as a function of m_{dark} for each value of α_{dark} we consider.

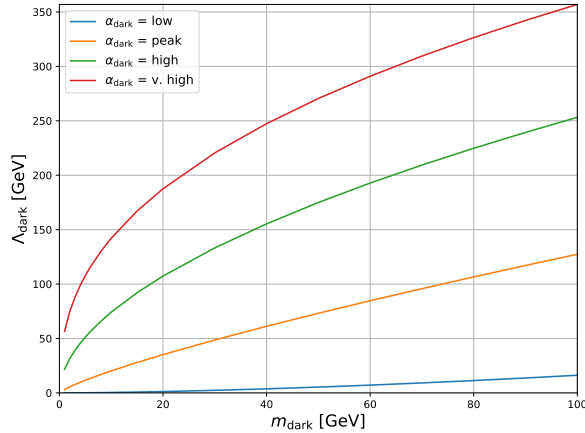


Figure 5.2: The dependence of the dark force scale Λ_{dark} on the dark hadron mass m_{dark} for each value of α_{dark} used in the thesis.

5.4.2 Jet clustering

The softer, visible radiation is simulated, and the clustering of SM hadrons into jets happens in the hadroniser. The algorithm logic is known as “sequential recombination,” where particles are successively combined until certain criteria are met. In PYTHIA, clustering stops above the merging scale known as the qCut, which we set to 125 GeV. For events generated in MADGRAPH and interfaced with PYTHIA for the parton shower, it is recommended that $\text{qCut} > 1.1 \times \text{xqcut}$. The xqcut denotes the merging scale in MADGRAPH. Referring to the transverse momentum, the symbol k_{T} is traditionally used in naming algorithms such as the anti- k_{T} algorithm. For consistency within this thesis, however, p_{T} will be used.

For given particles i and j , distance between them d_{ij} , and to the beam d_{iB} , are calculated

as in Ref. 122:

$$(5.2) \quad d_{ij} = \min(p_{Ti}^{2k}, p_{Tj}^{2k}) \frac{\Delta R_{ij}}{R^2}, \\ d_{iB} = p_{Ti}^{2k}$$

where, in the rapidity-azimuthal ($y - \phi$) plane, R is the radius of the cone—defined as 1.0 to match the merging parameters used in **MADGRAPH**. ΔR_{ij} is the separation between i and j ,² and k defines the algorithm choice: $k = -1$ in the anti- k_T algorithm, $k = 0$ in the Cambridge-Aachen algorithm, and $k = 1$ in the k_T algorithm. Our choice is the latter for the same reason as the cone radius size.

If $d_{ij} < d_{iB}$, the particles i and j are combined, replacing the individual constituents in the list of inputs. Otherwise, particle i is designated as a jet and removed from list of inputs. For all combinations of particles remaining in the input list, the distances are recalculated until all objects possess a p_T above the merging scale. Once the algorithm has finished, we are left with fully-clustered jets. Matching is performed between the clustered jets and original partons to avoid double counting. Events with insufficiently-matched jets are rejected. A minimum number of jets may also be specified and events with fewer than this are rejected. A larger r_{inv} tends to reduce the merging and matching efficiencies since more energy is locked in the dark sector and fewer jets are clustered above the merging scale.

5.4.3 Filtering events

Two filters are implemented in **PYTHIA** that reject events with unrealistic decays: a Z_2 symmetry in the model requires invisibly decaying dark hadrons to produce the dark matter particles in pairs, and an invisibly decaying Z' must do so into a $\chi\bar{\chi}$ pair. Coupled with the efficiency of the jet matching and clustering algorithms—which only significantly affects events generated externally and decayed with **PYTHIA**—there are multiple sources of inefficiency in the generation. Tuning the merging scale and matching parameters based on r_{inv} may yield in more effective generation. Aggregated over all sources, efficiency on the order of 15–20 % are expected for most **MADGRAPH** samples.

5.5 Generation in **MADGRAPH**

The **MADGRAPH5_AMC@NLO** 2.6.0 event generator is able to simulate the hard scatter for both the s - and t -channel UV completions of the model, i.e., the decay of the Z' into $\chi\bar{\chi}$ in the

²This is calculated with Eq. 3.6 where η is replaced with y from Eq. 3.5.

s -channel mode, and the exchange of the Φ to transform $q\bar{q}$ into $\chi\bar{\chi}$ in the t -channel mode. Up to two additional standard model quarks or gluons may accompany the final state for either mode. The particles, couplings, and other parameters required to describe the models are defined using the FEYNRULES package [13]. Of the four principal free parameters from Chpt. 2.4.1, the mediator mass and m_χ are defined at this stage.

The s -channel process is a modified version of the spin-1 “DMsimp” class of simplified dark matter models [24]. The t -channel description is completely custom. Both were initially acquired by the analysis team from one of the authors of Ref. 68 at <https://github.com/smsharma/SemivisibleJets>. At the time, it contained only one set of mass points. For the work presented here, this has been greatly expanded allowing any combination of Z' , Φ , and χ masses and couplings. All signal samples produced with MADGRAPH that feature in this thesis were done so with <https://github.com/eshwen/SemivisibleJets>.

In addition to the hard process, the full cmssw simulation pipeline can also be executed. This enables hadronisation and decays of both the SM and dark quarks in PYTHIA (as detailed in Chpt. 5.4). The remaining free parameters of the model— α_{dark} and r_{inv} —are specified there. Subsequently, detector conditions and material interactions can be modelled in the 2016, 2017, and 2018 data taking periods of CMS. The parton distribution functions used in centrally-produced CMS simulation for each data taking period are also applied to these semi-visible jet samples for consistency.

Common to both the s - and t -channel signal models generated for these studies, the couplings between the mediator and SM quarks g_q —also the mediator and dark quarks g_χ —are set to 1.0. Coupling strengths are furthermore independent of the dark and SM quark flavours. The number of dark flavours N_f and dark colours N_c each have values of 2. Both affect the dark force scale as per Eq. 2.12. Individually, former parameter allows for the production of two types of dark hadron, described in Chpt. 5.4, while the latter sets the dark colour composition of the dark gluon g_{dark} .

5.5.1 MADGRAPH run settings

Somewhat decoupled from the parameters of the signal models themselves, there are many important, adjustable settings controlled by the run card that affect the behaviour of MADGRAPH. The most notable of which is the parton/jet merging scale, denoted as the `xqcut`. MADGRAPH has difficulty simulating soft, collinear physics. To avoid this, a threshold may be placed on the `xqcut` to only generate sufficiently energetic events. Between two partons i

and j , the k_T is given as

$$(5.3) \quad k_T^2 = 2 \min(p_{Ti}, p_{Tj}) [\cosh(\eta_i - \eta_j) - \cos(\phi_i - \phi_j)]$$

where η and ϕ are the pseudorapidity and azimuthal angle, respectively. Complete definitions are presented in Chpt. 3.2.1.1. Events with $k_T < \text{xqcut}$ are not simulated. In essence, the xqcut is a measure of the required separation between partons in the event. We set a value of 100 GeV in the analysis for consistency with Ref. 68. This interpretation of a merging scale is similar, but not quite the same, as PYTHIA's discussed in Chpt. 5.4.

The choice of parton distribution function also lives in the run card. As stated above, this changes to reflect the data taking period that is emulated. Preferences for particle separation, momentum and direction cuts, beam energy, and the QCD renormalisation and factorisation scales are some of the additional settings that can be customised.

5.5.2 s -channel

In the description of the s -channel model, the leptophobic Z' is a spin-1 boson with vector couplings to the dark and SM quarks. A width $\Gamma_{Z'} = 10$ GeV is specified; small enough to allow its resonant production. The dark quarks themselves are Dirac spinors with dark colour quantum numbers. Real and complex scalar dark quarks also exist in the files detailing the model, but are decoupled and not generated in our implementation. Consideration of these supplementary species of particle are beyond the scope of this thesis.

Cross sections for this process are calculated at NLO as a function of $m_{Z'}$, assuming resonant production and a universal quark coupling. Events in simulation are weighted by the cross multiplied by integrated luminosity of the full Run-2 dataset for an estimation of the production rate over this era of the LHC.

It is important to understand the influence each free parameter of the model exerts on the kinematics of the final state. In which observables the variations of a given parameter manifest can aid in disentangling potential signal from background. The sensitivity, or lack thereof, of a parameter on the search variable also creates a sensible range for which to constrain the set of signal samples that must be generated. Signal models are given a label as $\text{SVJ}_{-\langle m_{\text{mediator}} \rangle - \langle m_{\text{dark}} \rangle - \langle r_{\text{inv}} \rangle - \langle \alpha_{\text{dark}} \rangle}$. A benchmark point was chosen in the analysis with $m_{Z'} = 3000$ GeV, $m_{\text{dark}} = 20$ GeV, $r_{\text{inv}} = 0.3$, and $\alpha_{\text{dark}} = \text{peak}$, labelled as $\text{SVJ_3000_20_0.3_peak}$. The choice is motivated by Ref. 67 and considerations of the other attributes of the signal provided in this chapter. Fig. 5.3 shows the m_T in the case where a single free parameter was varied with respect to the benchmark point. A glimpse into the sensitivity of the parameter on the kinematics is evident.

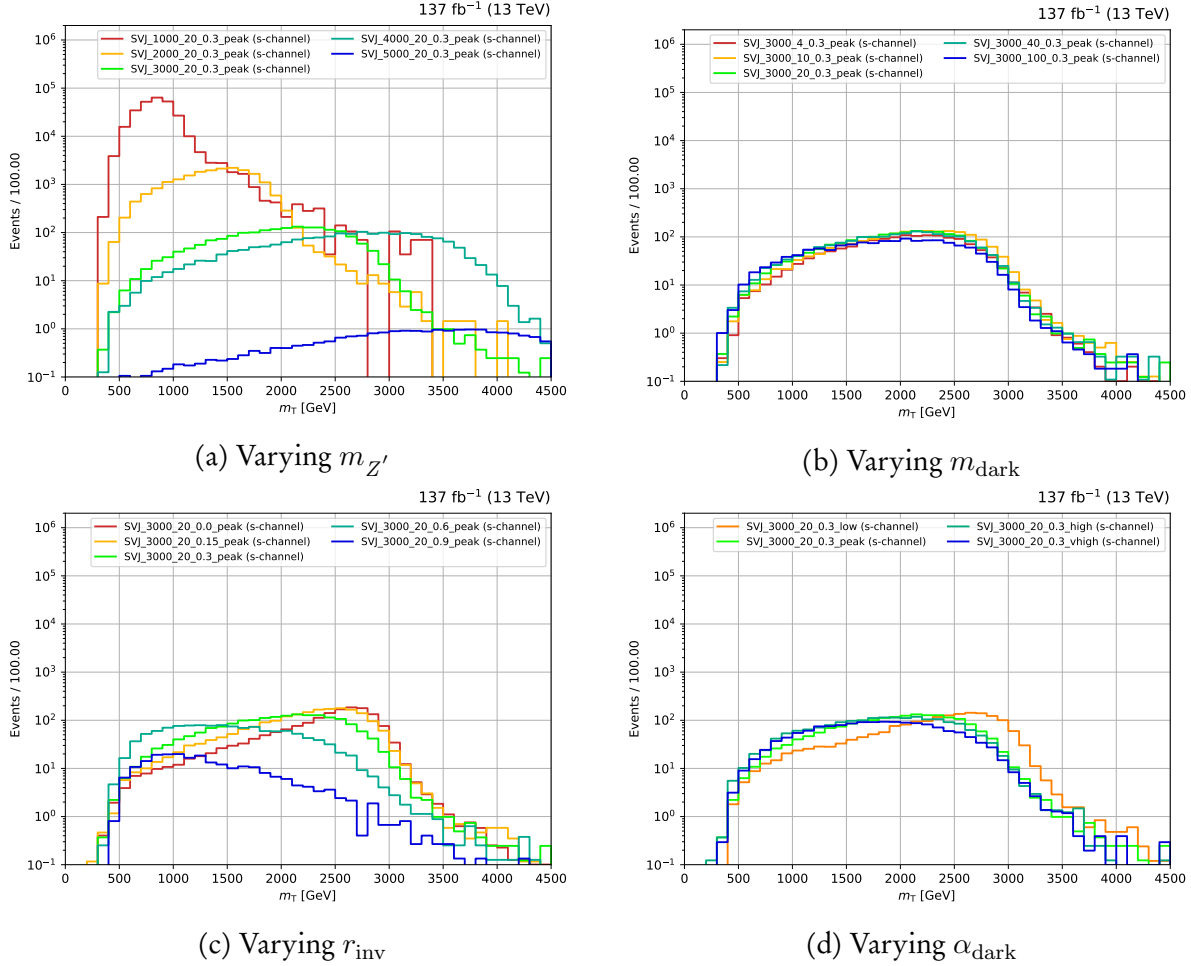


Figure 5.3: Distributions of the transverse mass of the dijet system m_T for s -channel semi-visible jet samples emulating the 2016 data taking period. In each panel, one of the free parameters of the model is varied with respect to the benchmark point SVJ_3000_20_0.3_-peak (bright green line).

Perhaps expectedly, $m_{Z'}$ appears to have the largest influence on the kinematics of the signal. Both the normalisation and shape of the distributions are significantly affected. A lower $m_{Z'}$ recovers the peak near the mediator mass more effectively. Surprisingly, varying the dark hadron mass did little to the distribution. Though, the transverse mass is more sensitive to the clustered jets and \vec{p}_T^{miss} as a whole rather than the shower constituents themselves. The momentum of the jets will also be highly correlated to $m_{Z'}$ since m_{dark} is usually small in comparison, boosting the dark hadrons significantly. Varying r_{inv} shows an interesting trend. A smaller value reshapes the m_T distribution toward the $m_{Z'}$ peak. Since the visible jets in the system are naturally resolved better than the \vec{p}_T^{miss} , recovering $m_{Z'}$ is an easier task. Similarly to m_{dark} , the choices of α_{dark} featured only have a small impact on the m_T spectrum. As

with r_{inv} , a smaller value leans more toward the $m_{Z'}$ peak. This can only happen to a point, however, because a model with an α_{dark} value too small refuses to shower in PYTHIA.

For both m_{dark} and α_{dark} , checking many other observables leads to the same conclusion given above: the kinematics of the model do not appear particularly sensitive to changes in those parameters. This can be a positive consequence as it reduces the phase space required in the search for semi-visible jets and permits optimisation of the analysis for $m_{Z'}$ and r_{inv} .³

5.5.3 t -channel

For the t -channel model, several pseudoscalar bifundamentals Φ couple to fermionic dark quarks. While only one flavour of mediator exists for s -channel process, numerous exist for t -channel. Each flavour of Φ couples to a given SM quark flavour, and is charged under electromagnetism with a value matching that of its coupled quark.⁴ The cross sections for this process were calculated by MADGRAPH at LO, varying most strongly as a function of m_{Φ} . A small dependence on m_{χ} was observed, and naturally no effect from α_{dark} or r_{inv} since they only act at the hadronisation step.

The t -channel aspect of the signal has not been studied in as great a detail as s -channel. It also exhibits less distinguishing kinematic characteristics, making it more difficult to determine the phase space and discriminating variables to separate it from the standard model background. Nevertheless, simple distributions with a range of parameter points are presented. These are intended to demonstrate how it would manifest in the LHC, and how different the signature is from the s -channel model. Motivated by the sensitivities demonstrated by the theorists in Ref. 68, the benchmark point SVJ_2000_20_0.5_peak is chosen. As with the s -channel UV completion, each free parameter is varied individually with respect to the benchmark point, the results of which for the m_T distribution are shown in Fig. 5.4.⁵

Analogously to the s -channel signal, the kinematics of the t -channel aspect of the model are dominated by the mediator mass and invisible fraction. The transverse mass exhibits a peak, but consistently at 700–900 GeV, seemingly regardless of m_{Φ} .⁶ Shallower tails beyond the peak are seemingly observed for lower m_{Φ} , although the normalisation from the cross section may be partially responsible. Though this distribution is not as distinguishing as with s -channel since there is no resonance or equivalent kinematic edge, it is more discriminatory than other variables investigated such as p_T^{miss} or H_T . Lack of statistical precision dominates

³ Could also qualitatively compare my samples to the 2017 theory paper, e.g., plotting $\Delta\phi_{\text{min}}$ and showing that the shapes are the same.

⁴ Is this for charge conservation?

⁵ Only looking at m_T as it seems the most discriminatory of all the ones I've made so far.

⁶ Not entirely sure where this comes from.

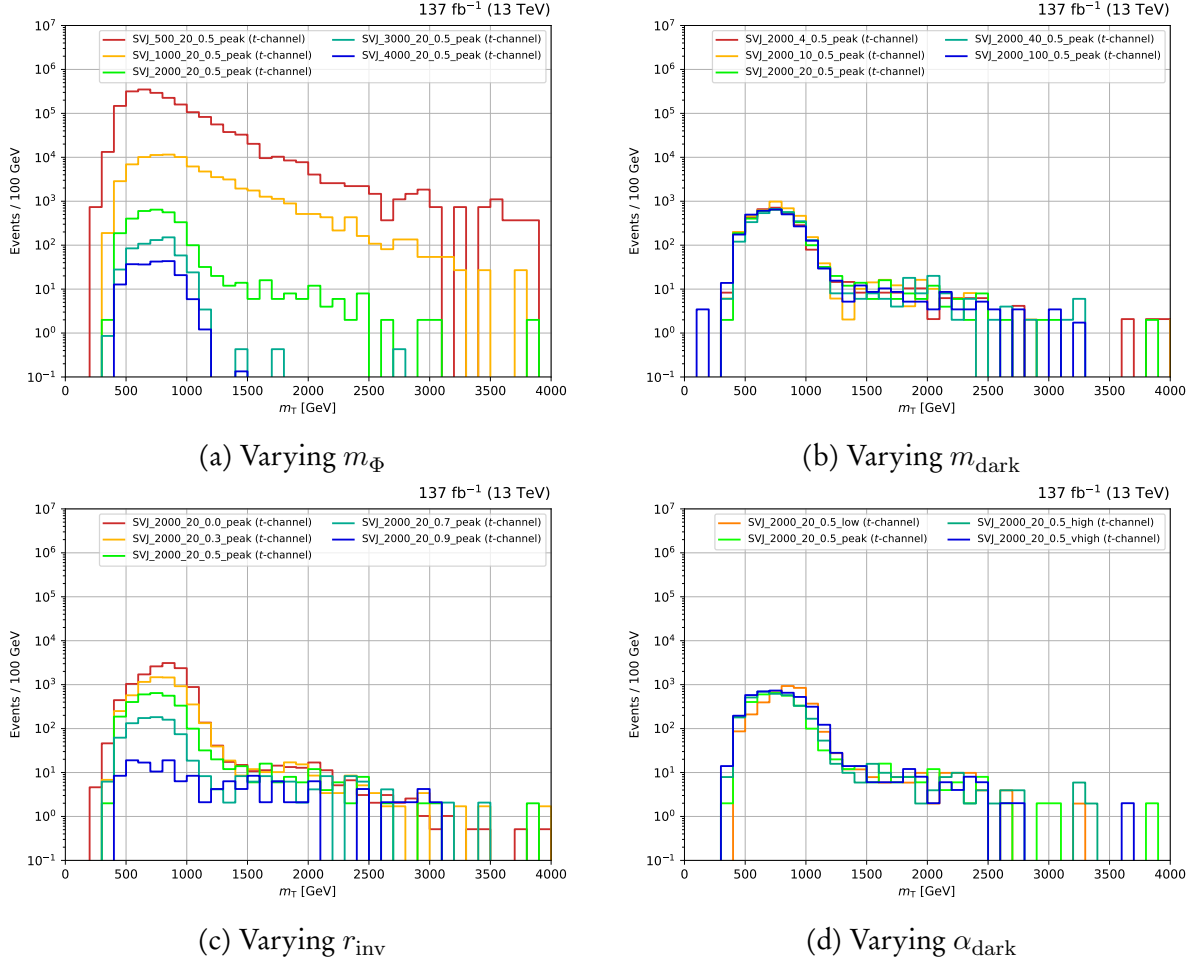


Figure 5.4: Distributions of the transverse mass of the dijet system m_T for t -channel semi-visible jet samples emulating the 2016 data taking period. In each panel, one of the free parameters of the model is varied with respect to the benchmark point SVJ_2000_20_0.5_-peak (bright green line).

the curves at higher m_T for larger m_Φ . Accounting for this, however, and observing the general trend does reveal shapes comparable to smaller m_Φ . For low m_Φ , a reasonably large fraction of signal remains at high m_T . This is true in all panels of Fig. 5.4, suggesting a cut could be placed on the observable to reject background if not used as the search variable.

m_{dark} and α_{dark} have little effect on the m_T . Within statistical fluctuations, the distributions for varying m_{dark} look identical. It is difficult to tell if α_{dark} has much effect on the kinematics overall, since the values used to vary the parameter were based on the shower of the s -channel signal. Reevaluation may be required in the t -channel case. The $\alpha_{\text{dark}}^{\text{low}}$ curve is peaked at slightly higher m_T than the others. With a lower threshold for dark hadronisation, a greater number of dark hadrons would likely be produced meaning a greater number that

decay into visible hadrons. Since measuring the visible aspect of an event is more accurate than the \vec{p}_T^{miss} , a more resolved peak would be observed.

The impact of r_{inv} on the m_T is similar to the s -channel signal insofar that the resolution of the bump is highly dependent on it. The peak near 1 TeV is recovered more effectively with a lower invisible fraction. Again, this is likely due to the enhanced resolution of jets over \vec{p}_T^{miss} . The feature of identifying the peak at higher m_T with smaller r_{inv} may also be for the same reason.

5.6 PYTHIA-MADGRAPH comparisons for s -channel signal

PYTHIA8 is described as a multipurpose generator, meaning it has the flexibility to simulate many kinds of processes from QCD and electroweak SM, SUSY, technicolour, and leptoquarks. Its status as the de facto standard for the parton shower and hadronisation means interfacing between that step and the hard process is simple. The use of Sudakov form factors and resummation also yield realistic jet structure. However, it is difficult to simulate processes more complex than LO, and support for generating new models must sometimes be specifically added to the program.

MADGRAPH5_amc@NLO, on the other hand, is an automatic matrix element generator. It calculates the scattering matrix element for each subprocess for a given final state,⁷ with Feynman rules to generate each diagram within a subprocess. Integration is performed over the phase space for each subprocess to give the cross section. Generator- and phase space-level cuts are easy to implement, so that only signal in the phase space regions of interest are simulated. Systematic uncertainties from the generation step are also simple to extract in the situations they are important to an analysis. High order processes, such as NLO and NNLO, can be simulated. While extremely taxing computationally, it is a straightforward implementation on the user side.

To verify that both PYTHIA and MADGRAPH are suitable generators, 100,000 events were generated for a selection of parameter points with each program independently. Six models encompassing a sufficient range of $m_{Z'}$, m_{dark} , and r_{inv} were chosen: SVJ_1000_20_0.3_peak, SVJ_3000_20_0.1_peak, SVJ_3000_20_0.5_peak, SVJ_3000_20_0.9_peak, SVJ_3000_50_0.3_peak, and SVJ_4000_20_0.3_peak. For all the simulation steps after the initial generation (described in more detail in Chpt. 3.2.3), identical implementations were used. This was to

⁷With our semi-visible jets model, around 50 subprocesses exist for the s -channel mode, while approximately 820 exist for t -channel.

5.6. PYTHIA-MADGRAPH COMPARISONS FOR S-CHANNEL SIGNAL

compare the differences due only to the generator. No analysis-level selections were applied either for the same purpose.

Below are some of the important and insightful distributions for the s -channel production mode: m_T , the number of jets (with the large cone size equivalent to AK8 jets in the anti- k_T algorithm), the ratio of p_T^{miss} to m_T , and the minimum azimuthal angle between the p_T^{miss} and two leading jets $\Delta\phi_{\min}(j_{1,2}, p_T^{\text{miss}})$. The ratio between the MADGRAPH-generated and PYTHIA-generated sample for a given model is also shown. For readability, plots are split into two sets comprising three models each. Fig. 5.5 showcases SVJ_1000_20_0.3_peak, SVJ_3000_20_0.1_peak, and SVJ_3000_20_0.9_peak, while Fig. 5.6 shows SVJ_3000_20_0.5_peak, SVJ_3000_50_0.3_peak, and SVJ_4000_20_0.3_peak.

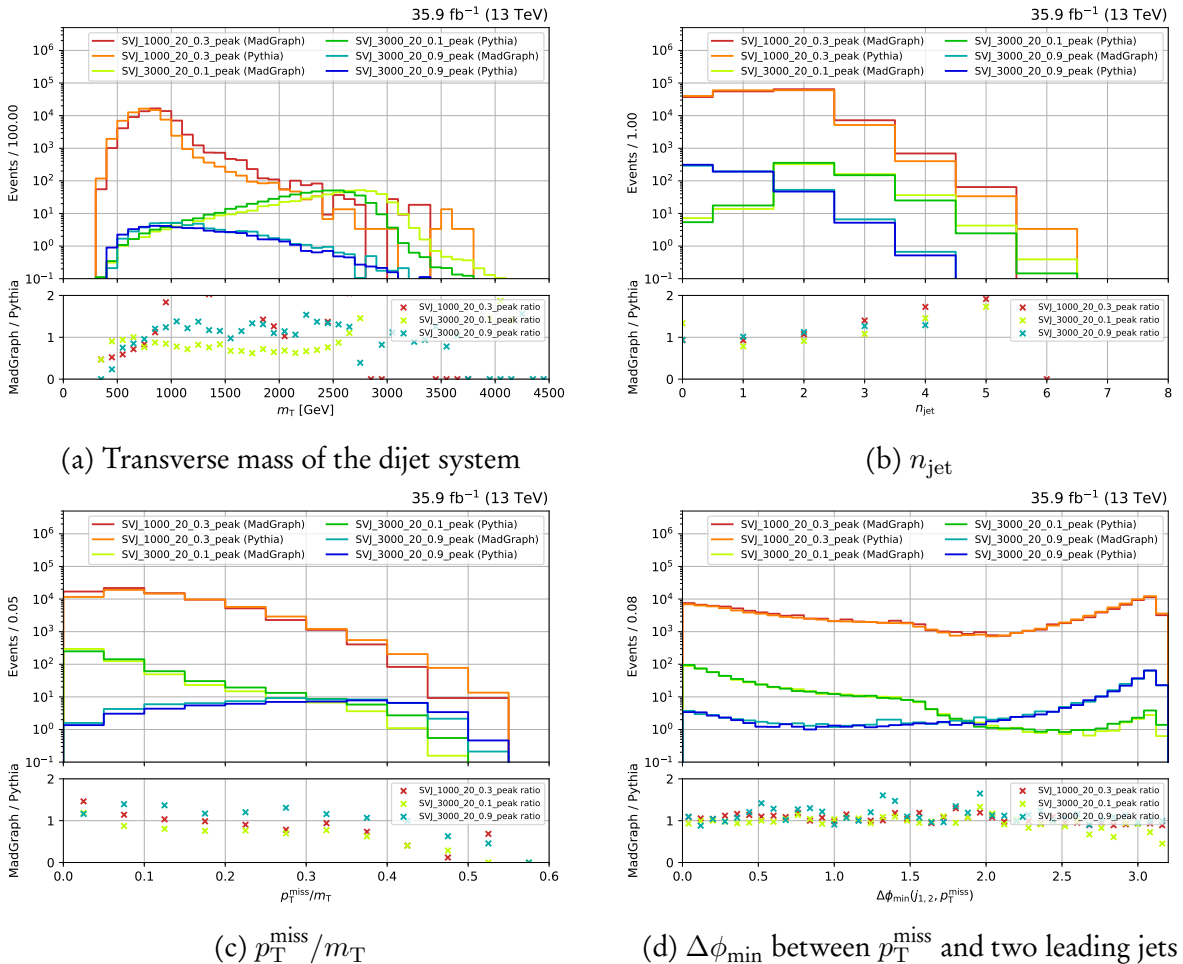


Figure 5.5: Distributions of several observables for the models SVJ_1000_20_0.3_peak, SVJ_3000_20_0.1_peak, and SVJ_3000_20_0.9_peak. Generation in MADGRAPH5_aMC@NLO is compared to PYTHIA8, with the ratios between them for each model displayed in the respective subplot.

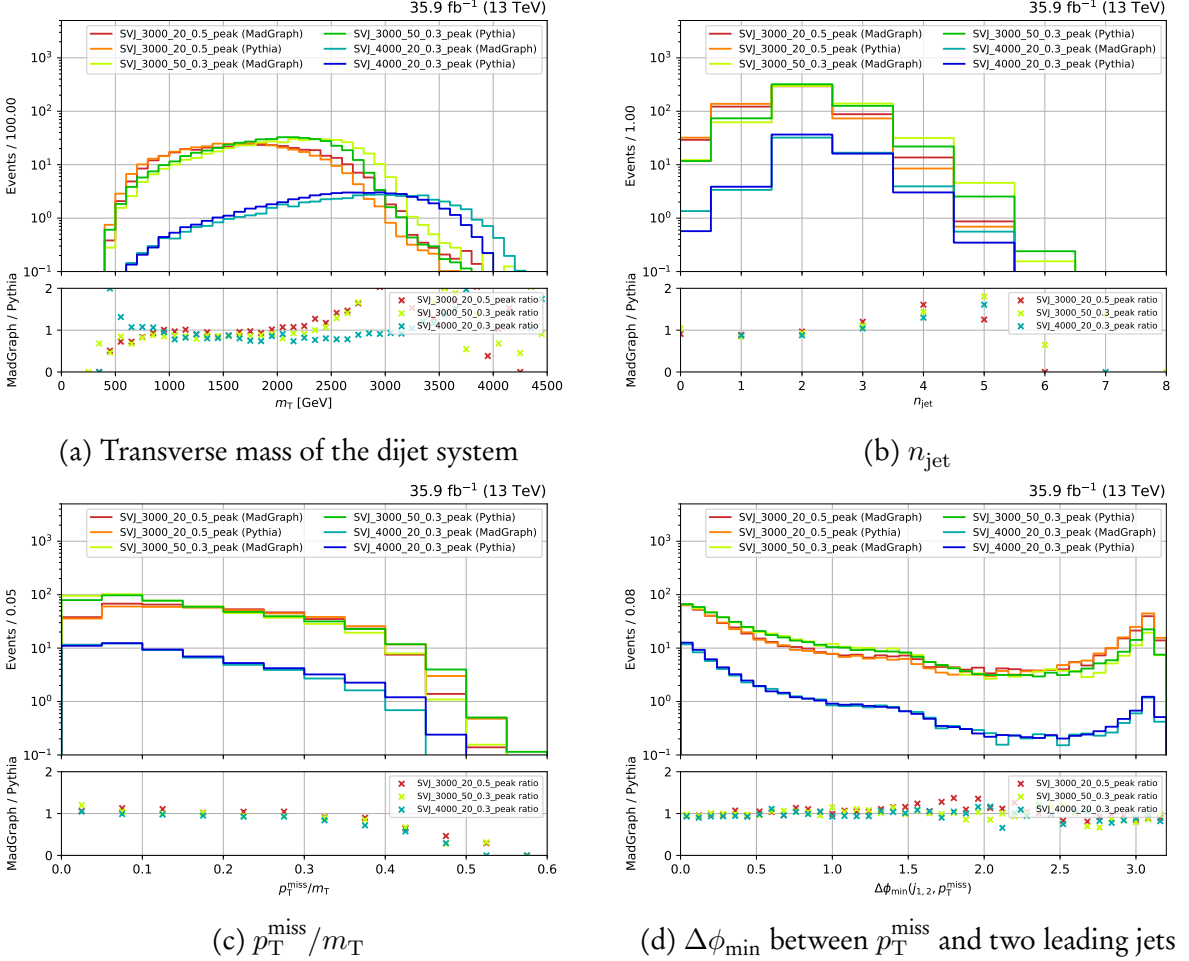


Figure 5.6: Distributions of several observables for the models `SVJ_3000_20_0.5_peak`, `SVJ_3000_50_0.3_peak`, and `SVJ_4000_20_0.3_peak`. Generation in `MADGRAPH5_amc@NLO` is compared to `PYTHIA8`, with the ratios between them for each model displayed in the respective subplot.

In general, the distributions above—as well as the others investigated such as $p_{\text{T}}^{\text{miss}}$, $H_{\text{T}}^{\text{miss}}$, and jet p_{T} —show reasonable agreement between the two generators. In particular, position variables such as η and ϕ of the jets and energy sums harmonise well. This is to be expected since those variables can be largely model-independent. A noticeable difference is in the m_{T} spectrum, where the shapes look similar but shifted to higher energies for the `MADGRAPH` samples. This may be attributed to the `xqcut`, or differences in the QCD scale. Tuning the `xqcut` in `MADGRAPH` or `qCut` in `PYTHIA` may be able to reduce the gap between them, especially if a relationship between the two merging scales can be derived for this model. For both generators, the peak close to the Z' mass can be recovered if the invisible fraction is small enough. This makes the transverse mass a more appealing search variable.

Both the n_{jet} and p_T^{miss}/m_T show trends in the MADGRAPH/PYTHIA ratio. A higher jet multiplicity is seen in the MADGRAPH samples, possibly due to the additional jets allowed in the matrix element calculation. For lower values of r_{inv} , a peak is seen at $n_{\text{jet}} = 2$, as expected given the theory. More jets may be generated from initial or final state radiation, or the dark shower prompting large-width leading or subleading semi-visible jet causing one to be clustered as two. The larger invisible content of the high r_{inv} samples naturally shows a lower number of jets; fewer are likely to pass the qCut threshold since a larger momentum fraction of each semi-visible jet is invisible.

Larger values of r_{inv} in Fig. 5.5 manifest in an interesting $\Delta\phi_{\min}$ spectrum. A double peak structure is demonstrated in samples with lower values. In the case of dijet events, an imbalance in the invisible content of each semi-visible jet may cause the p_T^{miss} to be aligned with the one containing the largest invisible fraction. In other scenarios, one of the two semi-visible jets may not be clustered if its invisible content is too large (i.e., if its visible content is too small). Then, in these single jet events, the p_T^{miss} would appear to recoil from the only clustered jet. Higher values of r_{inv} would cause this to happen more frequently, mimicking a WIMP signature. Failing to cluster a semi-visible jet may also result in the muddied m_T distribution as the \vec{p}_T^{miss} may not be resolved well enough.

For all of these comparisons, statistical limitation is an issue as it is only feasible to generate a rather limited sample size. Since those from PYTHIA have, by design, a higher jet matching and clustering efficiency, statistical power suffers partially for the MADGRAPH samples. Higher efficiencies are usually achieved by samples with a lower r_{inv} —expected since jet matching depends solely on the visible portion of the event.

In summary, an investigation has been performed into the generation and comprehension of the s and t production channels of semi-visible jets. Progress has been made into understanding how simulated events would manifest in the detector, how variations of the important free parameters in the model affect the kinematics, and which variables would be sensitive in a search for them. The mediator mass influences the model’s observable characteristics the most, affecting both the shapes of distributions and cross section significantly. Variables such as the transverse mass of the dijet system are able to emphasize the peak at the mediator mass in the s -channel mode, and to a lesser degree in the t -channel mechanism. Effective discrimination between signal and the dominant backgrounds is expected. Comparisons between the MADGRAPH5_amc@NLO and PYTHIA8 event generators were also conducted for several combinations of parameters in the s -channel aspect of the model. In most cases, reasonable agreement was found, with the major differences appearing to stem from the modelling of jets. Either would be suitable for use in the main analysis.

SEARCH FOR INVISIBLY DECAYING HIGGS BOSONS

Invisibility—there are things we can't see now, that are there, that are embedded, that it really takes time in order to be able to see. There are many ghosts that are lurking around and lingering through us that takes the technology of another generation or so in order to uncover and show what those stains and strains and perceived flaws really we're building towards.

— Lynn Hershman Leeson

Particles that escape the detector unseen in any experiment make them, by design, notoriously difficult to search for. The Higgs boson is particularly challenging with its small production rate at the LHC and a commensurate prediction of the invisible state branching ratio. As described in Chpt. 2.3, the leading estimates are still far higher than the standard model's value. For the best chance of observing this decay, the inclusion of all of the Higgs boson's production modes is a necessity.

6.1 Overview of the analysis

The analysis discussed in the remainder of the chapter is a dedicated search for invisibly decaying Higgs bosons in hadronic final states, incorporating three of the four main production modes. In contrast to many of the previous analyses that separately set limits on

$\mathcal{B}(H \rightarrow \text{invisible})$ by reinterpretation, this approach has many benefits. A simultaneous search for several production modes allows the construction of search regions to target each one, embedding orthogonality to avoid overlap between them. Data and simulation samples, recipes for corrections and systematic uncertainties, the analysis framework, and results can all be shared to provide a cohesive and consistent environment from which to perform the analysis. As well as streamlining the process of the final combination over each production mechanism, communication when establishing the analysis ensures each can cover as much phase space as possible without the trouble of overlap or contamination.

Direct collaboration between the University of Bristol and Imperial College London divides up the task of analysing the various Higgs boson production modes appropriately. This thesis focuses on $t\bar{t}H$, VH and ggH mechanisms. Those at Imperial College London, who have a long history with the VBF search [46, 135], assume responsibility of this process. Results will be shared between the institutes after the publication of this document to achieve a fully combined limit on $\mathcal{B}(H \rightarrow \text{invisible})$.

6.1.1 Analysis strategy

Emphasis is placed on $t\bar{t}H$ and VH as they are novel dedicated searches. The ggH mechanism also under our charge, and accordingly will be given attention. Given the LHC is a *hadron* collider, hadronic final states are naturally chosen for this analysis. Missing transverse energy from the purely-invisible decay of the Higgs—and hadronic activity from the particles associated with the production mechanism—constitute the final state, often known as a “jets + \vec{p}_T^{miss} ” search. In lieu of this, the dominant background processes from the standard model include QCD with high jet multiplicity, invisible decays of the Z boson, and those where the leptons from the decay are “lost” (ℓ_{lost}) from misidentification or are outside the bounds of the detector acceptance. The latter is predominantly populated by $t\bar{t}$ and leptonically decaying W bosons. To accurately estimate their presence in the signal region of the analysis, dedicated methods are employed. Control regions separated by lepton and photon multiplicity predict the lost lepton and $Z \rightarrow \nu\bar{\nu}$ processes. Sidebands to the signal region, where one or two selections otherwise designed to reject QCD multijet events are inverted, give rise to phase spaces enriched in them. A data-driven approach utilises these to predict the multijet background in the signal region.

Definitions of the physics objects used analysis-wide have already been discussed in Chpt. 4.2. The data from CMS and from simulation are reported in Chpt. 6.3. Categorisation of events to highlight the production modes is illustrated in Chpts. 6.4. These are further separated into the various phase space regions in Chpt. 6.5. Application of the event selection

in Chpt. 6.6 is intended to separate signal from background and discard poorly measured events. Many cuts are universal, though some are category- or region-specific to mitigate problems found only there, or to further separate signal and background. Corrections to simulation, designed to describe the data more accurately, and associated systematic uncertainties are discussed in Chpt. 6.7. The culmination of all of the aforementioned sections is in the fit of signal and background simultaneously in the signal and control regions to data in Chpt. 6.8. Estimation of the dominant background processes from the control regions and sidebands—and how they are incorporated into the fit—are as well documented. Results of the analysis of the $t\bar{t}H$, VH , and ggH modes are illustrated in Chpts. 6.9, 6.10 and 6.11, respectively. A combination of all of the production modes and data taking years to yield the final result close the chapter in Chpt. 6.12 along with interpretations in simplified dark matter scenarios.

6.2 Only tools and forces: software and toolkits

Analysing high energy physics data is a long and complex task with many stages that must be stitched together. In the analysis described in this chapter, the first step involves a light skim—or reduction of events—of the remotely-available datasets is effectuated with nanoAOD-tools.¹ Operating on the nanoAOD data tier, the repository contains centrally-maintained corrections and systematic uncertainties related to physics objects. Custom modules are applied on top. Processing the datasets on the Worldwide LHC Computing Grid, output is stored on networked university storage elements for improved performance of the later stages of the analysis.

Skimmed data is analysed predominantly using the FAST set of tools, developed by colleagues at the University of Bristol. A suite of packages harmoniously work together to run most components of an analysis. The event selection and categorisation, as well as many studies and measurements of the data are conducted at this stage. Use of vectorisation and industry-standard Python libraries such as numpy and pandas allow complex and efficient processing with simple syntax. Visualisation can also be achieved with interfaces to matplotlib.

Output from the previous stage is processed through the fit of signal and background to data. Specification of all aspects are handled with the HiggsAnalysis-CombinedLimit package.² A plethora of diagnostic information is available for understanding the effects of systematic uncertainties and other aspects of the analysis on the results.

¹See <https://github.com/cms-nanoAOD/nanoAOD-tools> for the original fork of the repository.

²See <https://github.com/cms-analysis/HiggsAnalysis-CombinedLimit/> for the repository.

6.3 Data and simulation

6.3.1 Data

The data collected by the CMS experiment that is used in the analysis corresponds to an integrated luminosity of 137.2 fb^{-1} , and recorded from 2016–2018. A breakdown by year is given in Tab. 3.1. At over three times the volume at $\sqrt{s} = 13 \text{ TeV}$ analysed in previous searches, there is potential to substantially lower the ceiling of $\mathcal{B}(H \rightarrow \text{invisible})$. Data is split into *primary datasets* that are grouped by the class of HLT path that an event triggered. The signal region, QCD sidebands, and muon control regions use the primary dataset composed of p_T^{miss} and H_T^{miss} combination triggers, where muons are excluded from the sums. The datasets made use of in the electron and photon control regions consist of triggers based on the properties of those objects. These were separate for 2016 and 2017, then merged for 2018.

Some serious issues arose during Run-2 that had to be mitigated after the events were reconstructed. With the high collision rate at CMS, in order to properly correlate the hits in the subdetectors with the correct particles and events they are attributed to, the timing infrastructure must be very precise. Timing scans are conducted frequently during runs to correct or compensate for any shifts that may occur. However, in 2016 and 2017, the gradual timing drift in the ECAL was not correctly propagated to the Level-1 trigger primitives. This resulted in a significant fraction of them in the forward direction (as the effect increases with η) being mistakenly associated to the previous bunch crossing: *pre-firing*. One rule at Level-1 forbids two consecutive bunch crossings from firing signals to the trigger system. But, a consequence of this—in addition to not finding the primitive in the nominal bunch crossing—is that events can be vetoed if a significant amount of ECAL energy is found in the $2 < |\eta| < 3$ part of the end cap. It is observed only in data, and so a correction is applied to MC (see Chpt. 6.7.6) to account for the effect.

In 2018, a sector of the HCAL end cap lost power, leaving the approximate area bound by $\eta \in [-3.0, -1.4]$ and $\phi \in [-1.57, -0.87]$ inoperative for the remainder of the year. Of the 59.7 fb^{-1} recorded and certified for use in 2018, 38.6 fb^{-1} were affected. With this section missing, it was more difficult to accurately record the properties of jets, and therefore reliably calculate the \vec{p}_T^{miss} . Studies performed showed an excess in data in the affected area of the $\phi(\vec{p}_T^{\text{miss}})$ distribution of most regions and categories. To mitigate this issue, the cuts in Chpt. 6.6.3 were added to the preselection.

6.3.2 Simulated signal processes

All Monte Carlo datasets used in this analysis were produced centrally as outlined in Chpt. 3.2.3. The signal samples are generated at NLO with the POWHEG generator interfaced with PYTHIA8. When reweighting events for their cross section, they are specified at the highest accuracy available as given in Tab. 2.3. The samples are produced with a Higgs boson mass of $m_H = 125$ GeV and assumes a 100 % branching ratio to invisible states. In each of the VH channels, the vector boson decays to $q\bar{q}$. Different final states were not considered. Simulation of the VBF process is included as it is expected to overlap with the ggH phase space.

When simulating 2016 data, the tuning of the shower parameters in PYTHIA was labelled CUETP8M1 [103] (the standard at the time), whilst for 2017 and 2018 datasets the newer CP5 version [132] was used.

6.3.3 Simulated background processes

Monte Carlo datasets for many processes³ are used in the analysis to accurately represent the standard model background. Every one uses PYTHIA8 to hadronise the events generated by the hard scatter. The underlying event tune applied in the hadroniser follows the same prescription as with signal—CUETP8M1 for simulating 2016 while CP5 is used thereafter. The only exception is the $t\bar{t} + \text{jets}$ background, for which *all* samples were generated with the CP5 tune. They are described as follows:⁴

- Drell-Yan ($Z \rightarrow \ell\ell$) + jets: The Drell-Yan process occurs when the quark of one incident proton annihilates with the antiquark in the oncoming proton, producing a neutral vector boson (a Z in this case) from a QCD vertex. It subsequently decays to a lepton pair, so while absent in the signal region, it is dominant in the dilepton control regions used to model the $Z(\rightarrow \nu\bar{\nu}) + \text{jets}$ process. The datasets are generated at LO accuracy with MADGRAPH5_AMC@NLO, where a dilepton mass cut of 50 GeV is applied.
- Multiboson: This background encompasses the production of two (diboson) or three (triboson) electroweak bosons. They may decay into charged leptons with or without neutrinos, but also hadronically, producing jets. A mixture of the two in an event will lead to similar signatures to that of the signal. The diboson processes are both

³In this subsection, I use the word “process” a lot. What alternatives can I use? Decay, dataset, mechanism, background?

⁴Not sure if I should use a long, sprawling list, or just have a separate paragraph for each process, maybe with the process name in bold.

generated and showered with PYTHIA8 at LO. For triboson events, on the other hand, MADGRAPH5_AMC@NLO at NLO accuracy models the hard scatter.

- Electroweak $V + 2$ jets: The production of electroweak bosons from an electroweak vertex is a minor background in the signal region. But as above, they may produce genuine p_T^{miss} from the decay of the V . The datasets are generated at LO with MADGRAPH5_AMC@NLO.⁵
- $\gamma + \text{jets}$: Events with photons are vetoed in the signal region. However, this is the largest contributor to the $\gamma + \text{jets}$ control region that predicts—along with the dilepton control regions—the $Z(\rightarrow \nu\bar{\nu}) + \text{jets}$ contribution to the signal region. These datasets are generated at NLO with MADGRAPH5_AMC@NLO in bins of γp_T .
- QCD multijet: The most common type of event produced in pp collisions at the LHC is several jets from QCD vertices. These typically do not have large p_T^{miss} , but are prone to mismeasurements that can artificially increase it. As such, they serve as a non-negligible background in the analysis. The datasets are produced at LO by MADGRAPH5_AMC@NLO.
- Single top: Events with one final-state top quark are a subdominant background in the analysis, but are important to consider, especially in the $t\bar{t}H$ categories. These electroweak-induced processes include s -channel and t -channel production where a *four-flavour scheme* [107] in the event generator is used for treatment of b quarks. This approach considers the b as massive, and as such, may only enter the final state. Associated production with a W boson (known as tW) is also considered with a five-flavour scheme, i.e., b quarks may be considered massless and can appear in both the initial and final states. For all of these channels, the events are produced at NLO. Modelling the hard scatter for the s -channel diagram is performed with MADGRAPH5_AMC@NLO. The t -channel and tW mechanisms are generated with POWHEG, with the former decaying the W exchanged by the initial state b and q with MADSPIN [22] to include spin correlations.
- $t\bar{t} + \text{jets}$: The QCD-induced process presents a major background, largely in the $t\bar{t}H$ categories. Large p_T^{miss} can arise in lost lepton scenarios. The three channels (hadronic, semi-leptonic, and dileptonic) are modelled with POWHEG at NLO accuracy.
- $t\bar{t}X + \text{jets}$: These are rare processes where a boson X (γ, W, Z, H) is produced in association with a $t\bar{t}$ pair. Several combinations of the decays of the $t\bar{t}$ and X are

⁵Mention something about the M-50 cut (dilepton mass > 50 GeV?), and maybe about the Vs only decaying into lnu, ll and nunu (perhaps that's what the 'electroweak' vertex means)

covered. All of the datasets are generated at NLO. The $t\bar{t}\gamma + \text{jets}$ and $t\bar{t}W + \text{jets}$ datasets use `MADGRAPH5_AMC@NLO`, and decay the particles with `MADSPIN`. $t\bar{t}Z + \text{jets}$ uses `MADGRAPH5_AMC@NLO` without the two aforementioned additions. Meanwhile, $t\bar{t}H + \text{jets}$ (where the H decays to visible states) is generated with `POWHEG`.

- $W(\rightarrow \ell\nu) + \text{jets}$: A QCD-induced process, this decay is dominant in the single lepton control regions. If the lepton is lost, the p_T^{miss} can be inflated and lead to a significant contribution in the signal region. The datasets are produced at LO with `MADGRAPH5_AMC@NLO`.
- $Z(\rightarrow \nu\bar{\nu}) + \text{jets}$: From the presence of neutrinos, the genuine \bar{p}_T^{miss} from this channel is a dominant background in the signal region. As with many of the above, the datasets are generated at LO accuracy with `MADGRAPH5_AMC@NLO`.

6.3.4 Cross section reweighting

Cross sections are specified at the highest order available, except for the LO $V + \text{jets}$ processes that require reweighting, expounded in Chpt. 6.7.2. Since an arbitrary number of events can be generated for simulation, and a larger number of events gives higher statistical precision, events in these datasets need to be reweighted to normalise their presence in a given region or category. To first order, the weight applied is

$$(6.1) \quad w_\sigma = \frac{\sigma L_{\text{int.}}}{N\varepsilon}$$

where σ is the cross section of the process at the order it was generated, $L_{\text{int.}}$ is the integrated luminosity of the LHC data it is being compared to, N is the number of events in the dataset before any analysis-level cuts are applied (or the sum of the generator weights), and ε is the filter efficiency.

6.4 Categorisation of the production modes

To extract maximum sensitivity to the $H \rightarrow \text{invisible}$ decay from the analysis, categories are established to target each of the production modes. From first principles, the topologies outlined in Chpt. 2.3.1 provide an initial direction of the expected structure. Steps are taken to ensure the categories that target the production mechanism—and the subcategories that capitalise on specific topologies within the mechanism—are orthogonal. Additional cuts based on optimisation studies in Chpt. 6.4.4 are also implemented, devising the categories in Tab. 6.1.

Category	Subcategory	n_{jet}	n_b	n_t	n_V	QCD reduction	Signal enhancement
$t\bar{t}H$	2Boosted	≥ 0	≥ 1	2			
	1t1b	≥ 3	1	1	0		
	1t2b	≥ 3	≥ 2	1	0		—
	1W1b	≥ 3	1	0	1		
	1W2b	≥ 3	≥ 2	0	1	$\tilde{\omega}_{\min} > 0.3,$ $\Delta\phi_{\min} > 0.5$	
	5j1b	5	1	0	0		$\Delta\phi(b_1, \vec{p}_T^{\text{miss}}) > 1.0,$
	6j1b	≥ 6	1	0	0		$\Delta\phi(j_1, \vec{p}_T^{\text{miss}}) > \pi/2$
	5j2b	5	≥ 2	0	0		$\Delta\phi(b_1, \vec{p}_T^{\text{miss}}) > 1.0,$
	6j2b	≥ 6	≥ 2	0	0		$\Delta\phi(b_2, \vec{p}_T^{\text{miss}}) > \pi/2$
VH	2j0b	2	0	0	0		$m_{jj} \in [65, 105]$
	2j1b	2	1	0	0	$\tilde{\omega}_{\min} > 0.3,$	$m_{jj} \in [65, 105]$
	2j2b	2	2	0	0	$\Delta\phi_{\min} > 0.5$	$m_{jj} \in [65, 105]$
	1V	0	0	0	1		—
ggH	2jM	2	0	0	0		$m_{jj} \notin [65, 105]$
	3j	3	0	0	0	$\tilde{\omega}_{\min} > 0.3,$	—
	4j	4	0	0	0	$\Delta\phi_{\min} > 0.5$	—
	5j	≥ 5	0	0	0		—

Table 6.1: Categorisation of the $t\bar{t}H$, VH , and ggH production modes in the analysis. Each subcategory highlights one of the possible final states of the mechanism, accounting for inefficiencies in object tagging or reconstruction. In the ggH 2jM subcategory, the dijet mass requirement ensures orthogonality with VH 2j0b.

In the table, the number of jets n_{jet} refers specifically to the number of AK4-clustered jets that do not overlap with a boosted t or V jet to avoid double counting objects, i.e., an AK4 jet within $\Delta R < 0.8$ of a boosted object does not count toward the n_{jet} requirement in the subcategory definition. This is not the case for b -jets as boosted AK8 jets can conceal b -jets from the decay of the primary particle. The overlap removal between AK4 and AK8 jets only applies to the categorisation and does not affect selections made on jets in Chpt. 6.6.

For categorisation and the analysis altogether, n_{jet} and n_b are counted independently, so no overlap removal is performed. For example, the VH 2j2b requires two jets, both of which are b -tagged.

In the $t\bar{t}H$ and VH categories, ancillary groupings of subcategories may be of interest: 2Boosted, 1t1b, 1t2b, 1W1b, and 1W2b target boosted decays of the top quark and may be collectively designated the “ $t\bar{t}H$ boosted” category; resolved decays are the focus of the remaining subcategories, appropriately named the “ $t\bar{t}H$ resolved” category; then, assembling the 2j0b, 2j1b, and 2j2b VH subcategories elicits the “ VH resolved” moniker. Low yields may be observed in individual subcategories, so using these grouped alternatives is useful to

quickly inspect the wider effect of changes to the analysis.

Chpts. 6.4.1, 6.4.2, and 6.4.3 explain the reasoning behind the jet-based requirements in Tab. 6.1. Optimisation of the category definitions for QCD multijet suppression and signal enhancement are described in Chpt. 6.4.4.

6.4.1 $t\bar{t}H$ subcategories

The subcategories comprising the $t\bar{t}H$ channel are designed to capture both boosted and resolved topologies. The boosted top quark- and vector boson-tagged jets (n_t and n_V , respectively) are defined in Chpt. 4.2.2. The remaining subcategories in the class are to account for inefficiencies in detection and tagging, i.e., events where only one of the top quarks or W bosons are identified. Requirements on the number of b -jets effectively distinguish background from signal.

For lower energy events, the decay products of the top quarks are spread further apart, allowing individual jets to be reconstructed. The $t\bar{t}H$ resolved subcategories, as in the boosted case, are intended to compensate for identification or reconstruction inefficiencies. In the 6j1b and 6j2b subcategories, while only six jets are expected from a $t\bar{t}$ decay, initial and final state radiation may be present. The products of $t\bar{t} + X$ events can also yield additional jets. While only two b quarks are expected in $t\bar{t}H(H \rightarrow \text{invisible})$, the b -jet requirement is left open ended in the 5j2b and 6j2b subcategories. This allows for mis-tagged b -jets to still enter the category, and is much more prevalent in true $t\bar{t} (+X)$ decays than other processes.

6.4.2 VH subcategories

As with $t\bar{t}H$, the categorisation of the VH channel aims to encapsulate boosted and resolved decays of the vector boson. In the resolved case, a dijet signature is expected. Both W and $Z \rightarrow q\bar{q}$ populate the 2j0b subcategory, while $Z \rightarrow b\bar{b}$ ideally falls into 2j2b. Events with one of the two b -jets unidentified is the reasoning for the 2j1b subcategory.

In high energy events, the decay products of the vector boson are merged into a single fat jet. Consequently, only a single V -tagged object is required in the 1V subcategory and the soft drop mass window substitutes m_{jj} from its resolved counterparts.

6.4.3 ggH subcategories

Gluon-gluon fusion is difficult to distinguish in terms of jet characteristics as an invisibly decaying Higgs boson only allows radiation to signal its presence. Subcategories for this channel are therefore based solely on the number of jets in the event.

An additional one-jet category was considered to tag ggH . While previous analyses have used a single category that encompasses events with at least one high p_T jet, we found adequate sensitivity by dividing it into separate bins of n_{jet} . Due to the angular variables we use only being effective for higher jet multiplicity, it was difficult to accommodate and optimise the one-jet category that ultimately did little to improve the overall result. It was therefore removed.

6.4.4 Optimisation of the categories

While first principles are a good starting point to categorise events and accentuate the Higgs production modes, they allow much room for improvement. QCD multijet is still a prominent background, especially in the $t\bar{t}H$ and ggH categories. Historically, variables such as $\Delta\phi_{\min}^*$ and α_T have been used to suppress it, as in the previous supersymmetry analysis I was a part of (Ref.[127](#)).

6.4.4.1 Angular variables for QCD suppression

Recently, more elaborate variables have been developed to better remove multijet background events in analyses with hadronic final states. Colleagues at the University of Bristol have designed a family of them [\[121\]](#), and for the analysis $\tilde{\omega}_{\min}$ was chosen to suppress said background. In the paper, noticeable improvement is demonstrated over previous variables (particularly $\Delta\phi_{\min}^*$, which is used there as a benchmark for comparisons). Optimisation was performed for $\tilde{\omega}_{\min}$ on a per-category, over a per-subcategory, basis to avoid excessive fine tuning for the many subcategories in the analysis.

The motivation behind the variable $\tilde{\omega}_{\min}$ is to minimise the H_T^{miss} by varying the p_T of one of the jets in the event. For mismeasured jets, it is typically the magnitude rather than the direction of the transverse momentum that is affected. Hence, a jet whose p_T can be varied such that the H_T^{miss} can be greatly reduced suggests it was mismeasured. For each jet i , the ratio between its p_T and the H_T^{miss} is defined as f_i . The variable $\sin \Delta\tilde{\phi}_i$ is the factor that scales the H_T^{miss} to its minimised value based on the varied p_T of jet i :

$$(6.2) \quad \sin \Delta\tilde{\phi}_i = \begin{cases} \sin \Delta\phi_i & \text{if } f_i + \cos \Delta\phi_i \geq 0, \\ \sqrt{1 + f_i^2 + 2f_i \cos(\Delta\phi_i)} & \text{otherwise} \end{cases}$$

where $\Delta\phi_i$ is the azimuthal angle between jet i and the \vec{H}_T^{miss} . The factor is derived from geometrical arguments in the normalised p_T plane (where $H_T^{\text{miss}} = 1$). Finally, the angular

variable $\tilde{\omega}_i$ is defined with respect to the aforementioned variables:

$$(6.3) \quad \begin{aligned} \tilde{\omega}_i &= \frac{\sin \Delta\tilde{\phi}_i}{f_i}, \\ \tilde{\omega}_{\min} &= \min_{i \in \text{jets}} \tilde{\omega}_i \end{aligned}$$

To reject mismeasured multijet events manifesting in jets aligned with p_T^{miss} , a simple cut of $\Delta\phi_{\min}(j_{1,2,3,4}, p_T^{\text{miss}})$ —contracted to $\Delta\phi_{\min}$ —above 0.5 was first introduced. Correlations between $\Delta\phi_{\min}$ and $\tilde{\omega}_{\min}$ were found to be minimal, and as such each variable would suppress multijet events with different characteristics.

Various metrics, or *figures of merit*, were considered for the threshold on which to cut in $\tilde{\omega}_{\min}$. In a counting experiment, a known Poisson-distributed background B yields a statistical uncertainty—assuming one standard deviation—of \sqrt{B} . A signal count S can then be statistically significant (i.e., unlikely to be a statistical fluctuation of the background) if it is greater than the uncertainty on the background. This, somewhat simplistic, method gives the standard deviation for the expected signal with respect to background—often just referred to as the *expected significance* Z —as

$$(6.4) \quad Z_{\text{Poisson}} = \frac{S}{\sqrt{B}}$$

An estimate of the overall effect of systematic uncertainties on the background $\sigma_{B, \text{syst.}}$ can also be incorporated, leading to

$$(6.5) \quad Z_{\text{Poisson}} = \frac{S}{\sqrt{B + (\sigma_{B, \text{syst.}} B)^2}}$$

Another figure of merit is to use the significance from an *Asimov dataset*—which replaces the [ensemble] of different datasets by a single representative one [70]. The median significance can then be extracted. Colloquially ascribed the *Asimov significance*. In many fields, including particle physics, a likelihood ratio is used for hypothesis testing. This is described in the context of the analysis in Chpt. 6.8. The asymptotic limit, where the sample size is large (as in the case for LHC data and simulation), can also be exploited as a property within the likelihood model. In this regime, the Asimov significance Z_{Asimov} can be expressed as

$$(6.6) \quad Z_{\text{Asimov}} = \sqrt{2 \left((S + B) \cdot \ln \left(1 + \frac{S}{B} \right) - S \right)}$$

reducing to Eq. 6.4 for $S \ll B$. Including a systematic uncertainty expands Eq. 6.6 to

$$(6.7) \quad Z_{\text{Asimov}} = \sqrt{2 \left((S + B)c_1 - \frac{B^2}{\sigma_{B, \text{syst.}}^2} c_2 \right)}, \text{ where}$$

$$c_1 = \ln \left(\frac{(S + B) \cdot (B + \sigma_{B, \text{syst.}}^2)}{B^2 + (S + B)\sigma_{B, \text{syst.}}^2} \right), \quad c_2 = \ln \left(1 + \frac{\sigma_{B, \text{syst.}}^2 S}{B(B + \sigma_{B, \text{syst.}}^2)} \right)$$

While these are quantitative measures of the sensitivity with a given analysis configuration, they are only a guide to inform an analyst of a more specific area of phase space to consider, rather than providing a precise cut for the given variable. To derive the appropriate cut for each category, all simulated signal and background events were processed through the analysis. They were categorised according to Tab. 6.1. For each subcategory, the significances for both methods were calculated, with and without an estimated 5 % systematic uncertainty on the background distribution. To estimate the significance for a category, the significances for each subcategory were summed in quadrature. Fig. 6.1 demonstrates the results as a function of $\tilde{\omega}_{\min}$ for the $t\bar{t}H$, VH , and ggH categories with the 2017 datasets. The preselection from Chpt. 6.6.1 and $\Delta\phi_{\min} > 0.5$ were applied.

It is obvious that the shapes and magnitudes of the significance distributions are sensitive to the inclusion of an estimated systematic uncertainty. Increasing its size affects the shape little, though impacts the magnitude more significantly. In bins with high background occupancy, even a small systematic uncertainty can wash out traces of signal. The thresholds chosen for $\tilde{\omega}_{\min}$ do not necessarily maximise the significance—where the Asimov method with $\sigma_{B, \text{syst.}} = 5\%$ was the leading choice—but to sufficiently separate signal and background, while not removing too many events. The control regions in the analysis perform better estimations of their responsible backgrounds when adequately populated. Reducing the event counts in the control regions too greatly with the $\tilde{\omega}_{\min}$ cut can therefore cause problems in multiple aspects of the analysis.

6.4.4.2 Other optimisations

In the “signal enhancement” column of Tab. 6.1, selections were made to distinguish signal from leading backgrounds. The $t\bar{t}H$ resolved subcategories employ requirements on the azimuthal angle between the missing transverse momentum and either the leading jet, leading b -jet, or subleading b -jet. These are specifically to differentiate $t\bar{t}H$ signal from $t\bar{t}$ background, as the former has been shown to exhibit larger separation between the jets and p_T^{miss} than the latter. A window on the dijet mass is applied to the VH resolved categories to reconstruct the

6.5. SIGNAL REGION, CONTROL REGION, AND SIDEBAND DEFINITIONS

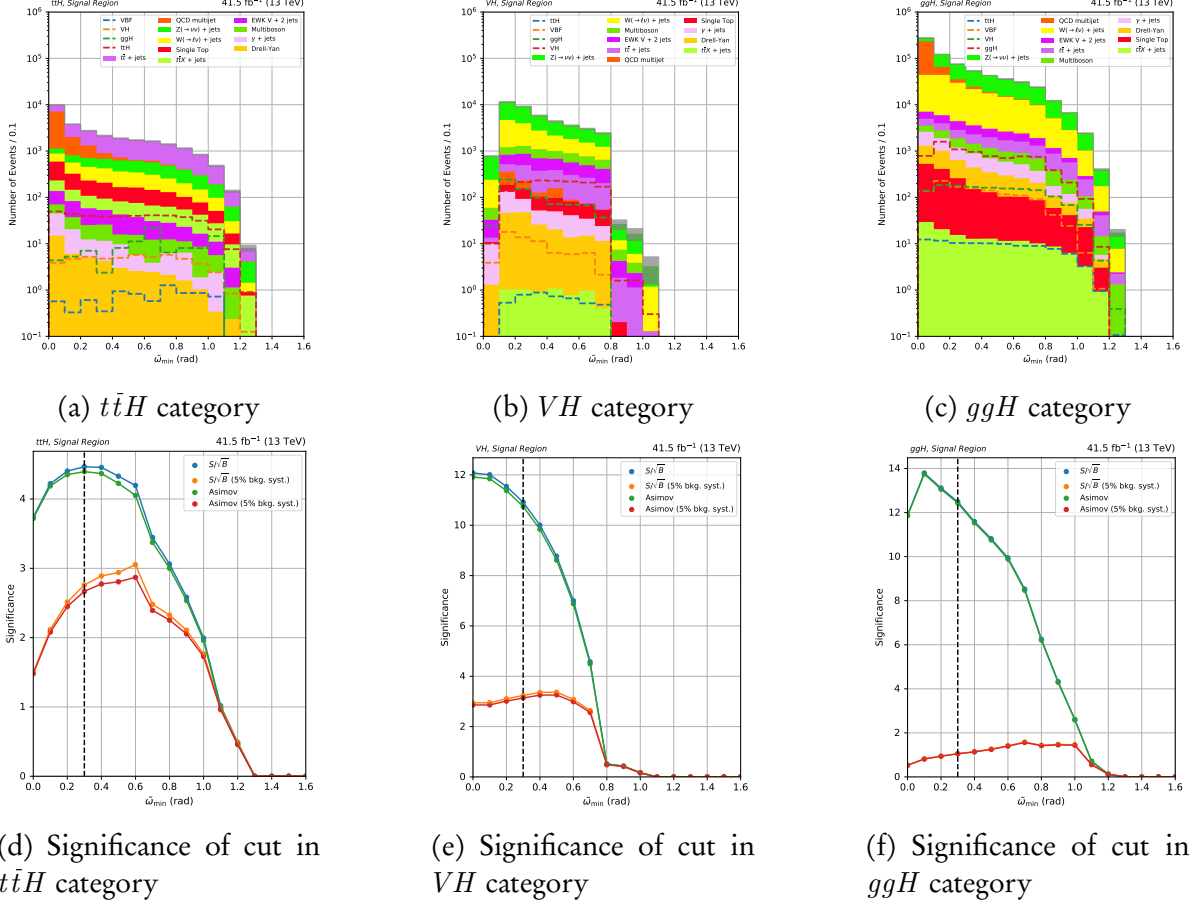


Figure 6.1: Top row: distributions of $\tilde{\omega}_{\min}$ in the signal region in the $t\bar{t}H$, VH , and ggH categories. Bottom row: the significance—using several figures of merit—if a cut is placed to the right of a given value of $\tilde{\omega}_{\min}$ in each category. The black dotted line indicates the threshold used in the analysis. These are showcased after the analysis-level selection on signal and background simulation for the 2017 data-taking era.

W and Z mass. The 15 GeV below m_W and above m_Z allow some leeway to accommodate jet resolution effects. For the ggH 2jM subcategory, the dijet mass must fall outside of the window to avoid overlap with VH 2j0b.

6.5 Signal region, control region, and sideband definitions

Several regions of phase space are explored in the analysis. The signal region is accompanied by control regions and sidebands to aid in the prediction of certain backgrounds, as explained below. The preselection is applied to every region, so they are separated by the CMS datasets used, the High-Level Trigger requirements, and object and/or kinematic selections.

6.5.1 The signal region

The signal region is the area of parameter space where we expect the signal to manifest, and the background to be reduced sufficiently that the potential presence of signal in data can be statistically verified. In this analysis, only hadronic final states are permitted. Events with leptons, photons and taus meeting the loose or veto criteria in Chpt. 4.2 are vetoed.

Events must satisfy a logical or of HLT cross-triggers for PARTICLE FLOW $p_{\text{T}}^{\text{miss}}$ and $H_{\text{T}}^{\text{miss}}$ calculated without muons,⁶ and at least one jet fulfilling the tight ID criteria (see Chpt. 4.2). The triggers are illustrated in Tab. 6.2.

Year	$p_{\text{T}, \mu}^{\text{miss}}$ (GeV)	$H_{\text{T}, \mu}^{\text{miss}}$ (GeV)	H_{T} (GeV)	n_{jet}	with tight ID
2016	90	90	—	—	≥ 1
	100	100	—	—	≥ 1
	110	110	—	—	≥ 1
	120	120	—	—	≥ 1
2017	120	120	—	—	≥ 1
	120	120	60	—	≥ 1
2018	120	120	—	—	≥ 1

Table 6.2: The trigger thresholds required for events to enter the signal region in each data taking year. Each quantity is computed with the PARTICLE FLOW algorithm at HLT level. The variables $p_{\text{T}}^{\text{miss}}$ and $H_{\text{T}}^{\text{miss}}$ do not include muons in the calculations.

The relative composition in each subcategory of the signal region for signal and background are illustrated in Fig. 6.2, highlighting the effectiveness to which the subcategories capture the targeted topologies, and the dominant background processes, respectively. The $t\bar{t}H$ subcategories, especially those designed to tag boosted top quarks and vector bosons are very pure in $t\bar{t}H$. Similarly, the VH and ggH subcategories predominantly consist of events from the production mode of focus. Contamination from the VBF process is present at a low level, most notably in the ggH subcategories given the similar topologies. ggH signal permeates several subcategories as the second largest component. This is likely due to its high cross section (more than fifty times any other individual process) and its ability to mimic the final states of the other signals. $t\bar{t} + \text{jets}$ is the dominant background for the $t\bar{t}H$ subcategories as expected, with $Z(\rightarrow \nu\bar{\nu}) + \text{jets}$ leading in the others. $W(\rightarrow \ell\nu) + \text{jets}$ also contributes a reasonable fraction.

⁶Why/how exactly is this done? Can muons fake jets, and so these calculations omit muons matched to jets at PF/HLT level?

6.5. SIGNAL REGION, CONTROL REGION, AND SIDEBAND DEFINITIONS

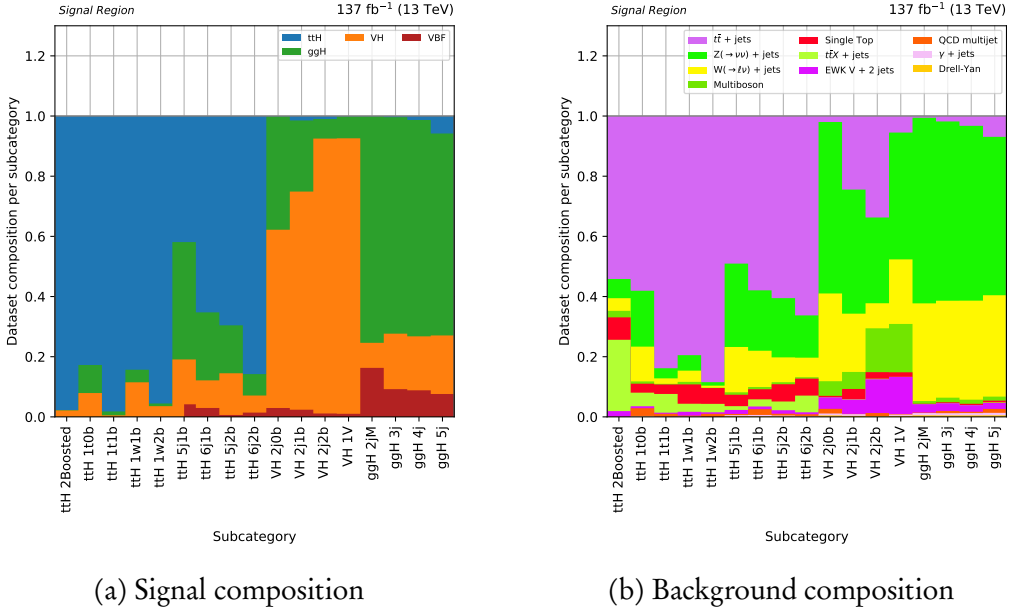


Figure 6.2: Composition of each subcategory in the signal region for simulated signal and background processes after the analysis-level selection.

6.5.2 Control regions

Control regions serve two complementary purposes in many analyses: the prediction of certain backgrounds that dominate in the signal region, as a more accurate method than using the yields directly from Monte Carlo; and to validate the data, MC, and corrections or weights applied. They are orthogonal to the signal region and to each other by way of lepton or photon requirements, and by triggers that may pertain to those objects. Control regions are also designed to, ideally, be devoid of signal. Contamination is sometimes present, but at a very small level. Five control regions are used in the analysis: $\mu + \text{jets}$, $\mu\mu + \text{jets}$, $e + \text{jets}$, $ee + \text{jets}$, and $\gamma + \text{jets}$. The criteria for the objects—which are defined explicitly in Chpt. 4.2—are summarised in the list below.

- $\mu + \text{jets}$: one tight muon μ_{tight} with $p_T > 20 \text{ GeV}$ and a transverse mass (as calculated in Eq. 4.6) in the range $50 < m_T^\mu < 110 \text{ GeV}$
 - $\mu\mu + \text{jets}$: one tight muon μ_{tight} with $p_T > 20 \text{ GeV}$, and one loose muon μ_{loose} with $p_T > 10 \text{ GeV}$ that has opposite charge, with a combined invariant mass of $60 < m_{\mu\mu} < 120 \text{ GeV}$ in the VH and ggH subcategories, while instead $75 < m_{\mu\mu} < 105 \text{ GeV}$ in the $t\bar{t}H$ subcategories. The leading muon (regardless of whether it is the tight or loose one) is required to possess $p_T > 110 \text{ GeV}$
 - $e + \text{jets}$: one tight electron e_{tight} with $p_T > 40 \text{ GeV}$ and $50 < m_T^e < 110 \text{ GeV}$

- $ee + \text{jets}$: one tight electron e_{tight} with $p_T > 40 \text{ GeV}$, and one veto electron e_{veto} with $p_T > 10 \text{ GeV}$ that has opposite charge, with a combined invariant mass of $60 < m_{ee} < 120 \text{ GeV}$ in the VH and ggH subcategories, while instead $75 < m_{ee} < 105 \text{ GeV}$ in the $t\bar{t}H$ subcategories. The leading electron (regardless of whether it is the tight or loose one) is required to possess $p_T > 110 \text{ GeV}$
- $\gamma + \text{jets}$: one medium photon γ_{medium} with $p_T > 230 \text{ GeV}$

The transverse mass cuts in the single lepton control regions reduce the effect of signal contamination, specifically from $t\bar{t}H$ since its m_T generally eclipses that of $t\bar{t}$.⁷ The trigger requirements for the $\mu + \text{jets}$ and $\mu\mu + \text{jets}$ control regions are the same as for the signal region (Tab. 6.2) since the same primary dataset is used.⁸

In the $\mu\mu + \text{jets}$ and $ee + \text{jets}$ control regions, the $m_{\ell\ell}$ window is halved for the $t\bar{t}H$ subcategories compared to the others to reduce contamination from $t\bar{t}$, granting a higher purity $Z(\rightarrow \ell^+\ell^-) + \text{jets}$ region. The leading lepton p_T requirement is increased in these regions for all categories also for purity purposes.

The $e + \text{jets}$ and $ee + \text{jets}$ control regions take advantage of the increased statistical power of two primary datasets in both 2016 and 2017, characterised by electron and photon triggers. In 2018, they were merged into a single e/γ primary dataset. Tabs. 6.3 and 6.4 elucidate how the trigger requirements are specified for each year. As before, each quantity and object is defined at HLT level. If an event aims to enter the $e + \text{jets}$ or $ee + \text{jets}$, and is from the dataset of e -based triggers, the criteria for either of the two triggers for the given year in Tab. 6.3 must be satisfied. If an event aims to enter either control region and is from the primary dataset of γ -based triggers, the failure of both of the electron triggers in Tab. 6.3 and the passing of any of the photon triggers in Tab. 6.4 are required. This condition avoids double counting events that also appear in the electron trigger-based dataset. In 2018, any of the year's triggers in Tabs. 6.3 and 6.4 may be satisfied. For Monte Carlo events, as they are not categorised by trigger, they may pass any of the triggers in either table for their respective year.⁹

For the $\gamma + \text{jets}$ control region, we take data from CMS originating only from the dataset of γ -based triggers. Data and MC must satisfy any of the triggers from Tab. 6.4 for the

⁷The m_T for a $t\bar{t}$ event with \vec{p}_T^{miss} solely from the neutrino (in $t \rightarrow b W$, $W \rightarrow \ell\nu$) should be in a window around the W mass. Introducing additional decay products such as the Higgs boson increase it.

⁸If we decide to go ahead, mention somewhere that the angular variable cuts in the categorisation table are not applied in the control regions to improve stats. The MET shapes were found to be consistent if they were applied vs. not applied. And the expected limit from a CR-only fit improved across the board when removed.

⁹See if I can describe the trigger requirements in a more elegant way. Might be easier give the descriptions and actual HLT path names a bit earlier, then just reference the HLT path names in the list.

6.5. SIGNAL REGION, CONTROL REGION, AND SIDEBAND DEFINITIONS

Year	$E_{T,SC}^e$ threshold (GeV)	e WP	Calorimeter ID	GSF track-SC matching
2016	27	Tight	—	—
	105	—	Very tight	Tight
2017	35	Tight	—	—
	115	—	Very tight	Tight
2018	32	Tight	—	—
	115	—	Very tight	Tight

Table 6.3: The trigger requirements for events to enter the $e + \text{jets}$ or $ee + \text{jets}$ control regions, if they originate from the dataset of e -based triggers. Selections are on the transverse energy of the supercluster $E_{T,SC}$, the working point of the candidate electron, ID of the candidate in the calorimeters, and the matching between the gaussian sum filter (GSF)-fitted track and supercluster, all at HLT level.

respective year.

Year	E_T^γ threshold (GeV)	H/E
2016	165	< 0.1
	175	—
2017	200	—
2018	200	—

Table 6.4: The trigger requirements for events to enter the $e + \text{jets}$ $ee + \text{jets}$, or $\gamma + \text{jets}$ control region, if they originate from the dataset of γ -based triggers. Selections are on the transverse energy E_T of the candidate, and the ratio of the candidate’s central energy deposit in the HCAL to the ECAL (H/E), all computed at HLT level.

In each of the control regions, the \vec{p}_T^{miss} is recalculated without the objects used to define said region to model the process it is predicting. In essence, these objects are treated as a source of missing momentum. Conditions in the event selection and binning that refer to p_T^{miss} use the recalculated quantity when applied to the control regions. Using the $\mu + \text{jets}$ control region as an example, the new \vec{p}_T^{miss} is the vector sum of the old \vec{p}_T^{miss} and the tight muon \vec{p}_T . The single lepton control regions estimate the semi-leptonic $t\bar{t} + \text{jets}$ and $W(\rightarrow \ell\nu) + \text{jets}$ backgrounds. In both cases, they may enter the signal region if the lepton is lost, becoming a source of p_T^{miss} . The dilepton and $\gamma + \text{jets}$ regions consider $Z(\rightarrow \nu\bar{\nu}) + \text{jets}$. The former parallels the decay as it is enriched in $Z(\rightarrow \ell^+\ell^-) + \text{jets}$ —possessing very similar kinematic properties while being much easier to detect, improving statistical accuracy. The latter region substitutes the $Z \rightarrow \nu\bar{\nu}$ decay with a photon.

The relative composition of the background processes in each control region after the analysis-level selection is summarised in Fig. 6.3. As desired, the single lepton control regions

are very similar and dominated by the $t\bar{t}$ and $W \rightarrow \ell\nu$ process, corresponding to the lost lepton backgrounds in the signal region. The dilepton regions also possess a very similar composition to each other, enriched in Drell-Yan $Z \rightarrow \ell\ell$ (a proxy for the $Z \rightarrow \nu\bar{\nu}$ background in the signal region), and to a lesser extent $t\bar{t}$ and $t\bar{t}X$ which contain several dileptonic decay channels. In the $\gamma + \text{jets}$ control region, expectedly the $\gamma + \text{jets}$ process dominates virtually every subcategory apart from a sizeable $t\bar{t}\gamma$ presence in some of the boosted $t\bar{t}H$ cases. QCD multijet events make up a consistent, small fraction of the events. Rather than the yields from MC as they would likely consist of jets misidentified as photons, its presence in this region is estimated from a data driven purity measurement explained in Chpt. 6.5.2.1. Data and background yields from simulation from every control regions in each period of Run-2 can be found in App. A.

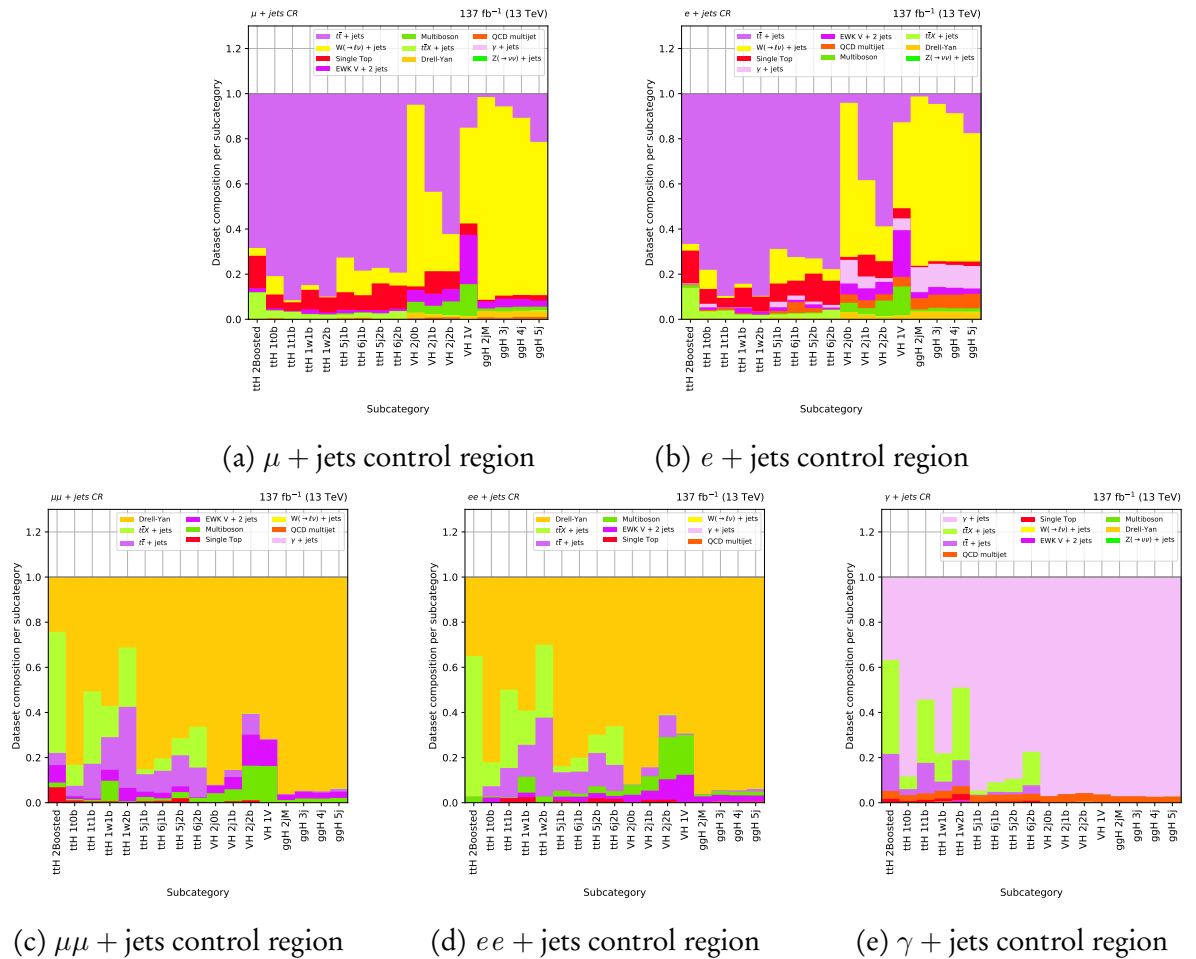


Figure 6.3: Composition of each subcategory in each of the control regions for simulated background processes after the analysis-level selection.

6.5.2.1 Photon purity measurement for the $\gamma + \text{jets}$ control region

Photons are reconstructed from clusters in the ECAL. They can usually be discriminated from other sources leaving ECAL deposits due to the properties of the deposits themselves, as well as the lack of other signatures that typically belong to other particles. However, this method is imperfect, and occasionally other particles will incorrectly be identified as photons (known as *fakes*). The leading sources of fake photons is from QCD multijet events where a jet is misidentified as such. Due to the high cross section of the process, even a small rate of fake photons becomes important to consider.

In order to separate real photons from fakes in the $\gamma + \text{jets}$ control region, a purity measurement is performed. We define the purity as the fraction of reconstructed photons that are from an isolated photon emerging from the hard scatter of the event, rather than a fake. The variable $\sigma_{i\eta i\eta}$ is able to distinguish between real and fake photons with sufficient power. A peak with a hard cut off at $\sigma_{i\eta i\eta} \approx 0.01$ is observed for real photons, while fakes possess a less pronounced peak and much slower decline above that threshold. As such, we perform a template fit to the distribution in data to extract the purity.

As inputs to the fit, we select photons in data by applying the medium identification requirements in Tab. 4.6 with the exception of $\sigma_{i\eta i\eta}$ to observe the full range. Photons from $\gamma + \text{jets}$ simulation are selected with the same criteria and are used to define the real photon template. A fake photon template is obtained from data by requiring at least one of the isolation criteria from the medium ID in Tab. 4.6 to be unfulfilled. This ensures the photons from this set do not overlap with the real photons from data.

The templates are derived in separate bins of photon p_T , and the purity measurement is performed separately for each data taking year. The following event selection is applied:

- Photon trigger requirement for the respective dataset from Tab. 6.4
- p_T^{miss} filters from Chpt. 6.6.2
- $p_T^{\text{miss}} < 60 \text{ GeV}$
- At least one jet with $p_T > 80 \text{ GeV}$ and $|\eta| < 2.4$ that is separated from any photon with $\Delta R > 0.4$
- If a second jet is present, it is required to have $p_T > 40 \text{ GeV}$ and $|\eta| < 2.4$, also separated from any photon with $\Delta R > 0.4$
- $H_T > 200 \text{ GeV}$

A combination of cuts are used to select photons appropriately and ensure the phase space resembles that of the $\gamma + \text{jets}$ control region. The shapes of the real and fake templates are

fit to the data using a likelihood function in the range $0.004 \leq \sigma_{inj\eta} \leq 0.02$. By calculating the purity within acceptance (i.e., $\sigma_{inj\eta} \leq 0.01$ as given by the medium ID requirement), the *impurity* can be derived as a function of photon p_T . An exponential function is fitted to interpolate within the range that also serves to extrapolate above it. Fig. 6.4 illustrates the impurity vs photon p_T for each data taking year. A 25 % uncertainty around the fit is assumed to account for effects related to the binning of the $\sigma_{inj\eta}$ distribution.

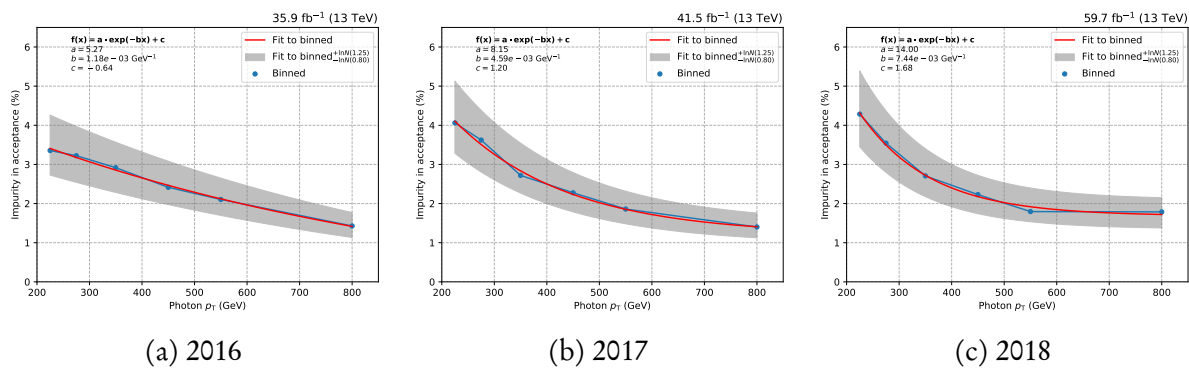


Figure 6.4: The fraction of impure photons in data as a function of p_T for each data taking year in Run-2. An exponential is fit to the binned data with a 25 % uncertainty assigned to account for binning effects.

In the analysis, the purity measurement is used to estimate the QCD multijet background in the $\gamma + \text{jets}$ control region, replacing the contribution from MC. For each event in data that enters the region, a QCD multijet pseudo-event is created with the same properties—notably p_T^{miss} and photon p_T . The value of the impurity calculated from the photon's p_T weights the event. The new QCD background is therefore generated with the same shape as the data and weighted to represent the rate of non-prompt photons. A 25 % uncertainty is attributed to the normalisation of the yield.

6.5.3 Sidebands to the signal region

As explained in Chpt. 6.3.3, it is difficult to accurately estimate the QCD multijet content in the signal region. Several kinematic cuts in the analysis are designed to reject QCD in the signal region, so by inverting one or two of them, we can construct multijet-enriched regions: *sidebands*.

We invert the requirements on the two angular variables designed to reject multijet events and optimise the categorisation of the production modes (see Chpt. 6.4.4). Several sidebands are constructed where each cut is inverted separately, and also when both are inverted. When

the angular cut is inverted, the remaining phase space may be split into two sidebands, dubbed *loose* and *tight*. These are summarised in Tab. 6.5.

	$\tilde{\omega}_{\min} < 0.2$	$0.2 \leq \tilde{\omega}_{\min} \leq 0.3$	$\tilde{\omega}_{\min} > 0.3$
$\Delta\phi_{\min}(j_{1,2,3,4}, \vec{p}_T^{\text{miss}}) > 0.5$	Tight $\tilde{\omega}_{\min}$ SB	Loose $\tilde{\omega}_{\min}$ SB	Signal region
$\Delta\phi_{\min}(j_{1,2,3,4}, \vec{p}_T^{\text{miss}}) \leq 0.5$	Tight double SB	Loose double SB	$\Delta\phi_{\min}$ SB

Table 6.5: Definitions of the sidebands (SBs) used to determine the QCD multijet background in the signal region for all categories in the analysis.

The sidebands follow the same categorisation as for the other regions, i.e., Tab. 6.1, and are binned in p_T^{miss} with the same scheme as the other regions. A sideband composed of the inversion of only one variable maintains similar kinematic properties to the signal region. When performing analysis while still blind to data in the signal region, inspecting one of these sidebands is a good indicator of how new cuts or corrections will affect the signal region composition, and compatibility between data and MC. Like the control regions, sidebands serve a secondary purpose.

Figs. 6.5, 6.6, 6.7, 6.8, and 6.9 illustrate the p_T^{miss} distributions in each sideband after the analysis-level selections with the full Run-2 dataset. The combined $t\bar{t}H$ and VH subcategories for boosted and resolved topologies are used to demonstrate the shapes and data–simulation resemblance. Background estimation is performed separately for each year due to the differing running conditions, detector configuration, and the different effects or problems seen in the data.^{10,11}

6.6 Event selection

The event selection aims to strike a balance between rejecting as many background events while retaining as much signal as possible. The preselection, in Chpt. 6.6.1, is applied to data and simulation in all regions and categories to do just that. Filters to reject potentially-mismeasured events and those that lead to incorrect p_T^{miss} calculations are documented in Chpt. 6.6.2. A strategy to combat the HEM issue faced in 2018 (detailed in Chpt. 6.3.1) is given in Chpt. 6.6.3.

¹⁰Might not need to show all of these plots. They’re just here for now, and can be tidied up later. For the SR and CRs, we have mountain range plots to showcase the yields, but nothing similar for the sidebands. May be worth showing ggH in the same capacity as the other categories, however.

¹¹Some of the sidebands are unpopulated for VH because of the $\Delta\phi_{\min}$ cut in scenario 5. Make sure to fix.

CHAPTER 6. SEARCH FOR INVISIBLY DECAYING HIGGS BOSONS

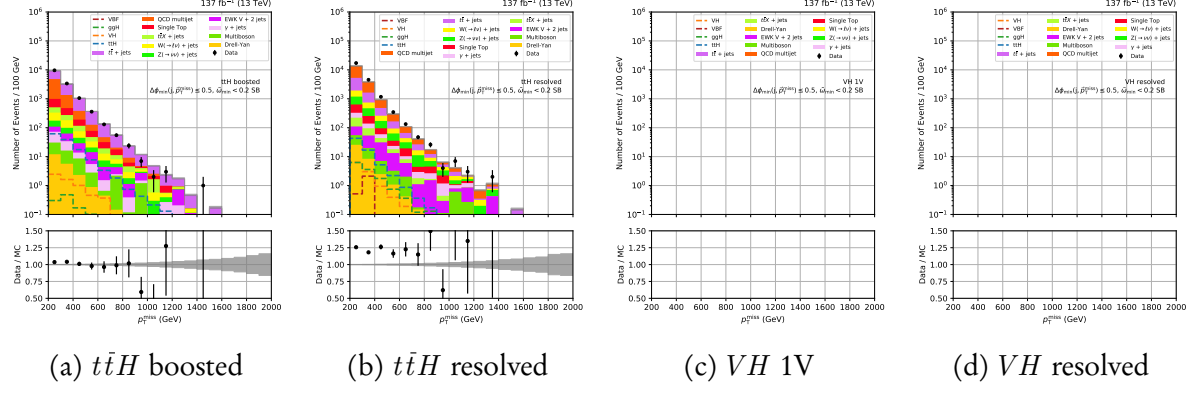


Figure 6.5: Data-simulation comparisons of the p_T^{miss} distribution in the tight double sideband for the combined boosted and resolved categories for the $t\bar{t}H$ and VH processes, using the full Run-2 dataset.

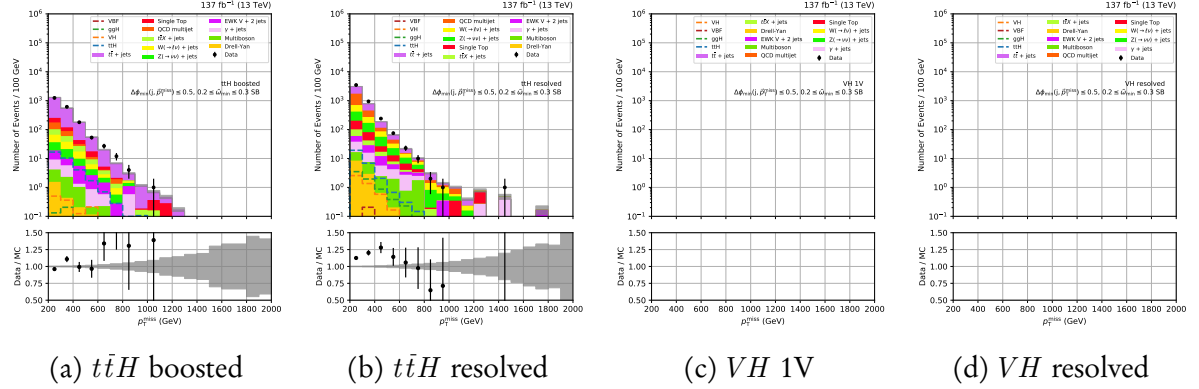


Figure 6.6: Data-simulation comparisons of the p_T^{miss} distribution in the loose double sideband for the combined boosted and resolved categories for the $t\bar{t}H$ and VH processes, using the full Run-2 dataset.

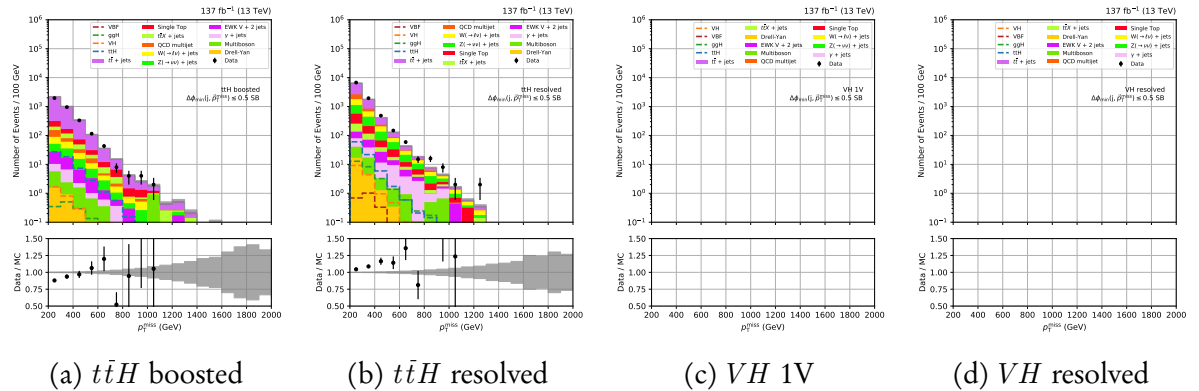


Figure 6.7: Data-simulation comparisons of the p_T^{miss} distribution in the $H_T^{\text{miss}} / p_T^{\text{miss}}$ sideband for the combined boosted and resolved categories for the $t\bar{t}H$ and VH processes, using the full Run-2 dataset.

6.6. EVENT SELECTION

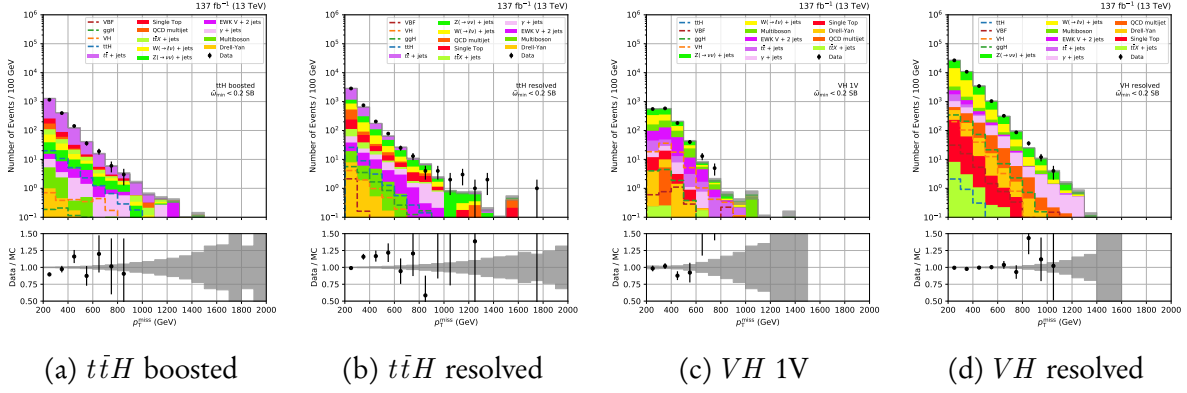


Figure 6.8: Data-simulation comparisons of the p_T^{miss} distribution in the tight $\tilde{\omega}_{\min}$ sideband for the combined boosted and resolved categories for the $t\bar{t}H$ and VH processes, using the full Run-2 dataset.

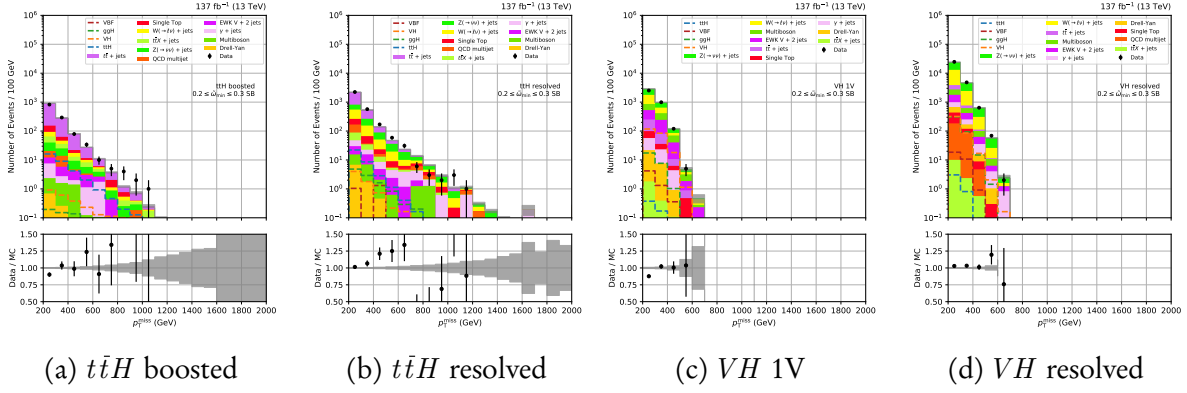


Figure 6.9: Data-simulation comparisons of the p_T^{miss} distribution in the loose $\tilde{\omega}_{\min}$ sideband for the combined boosted and resolved categories for the $t\bar{t}H$ and VH processes, using the full Run-2 dataset.

6.6.1 Preselection

The preselection is designed to discriminate between signal and background events, and is characterised by applying the following cuts:

- $p_T^{j_1} > 80 \text{ GeV}$
- $p_T^{j_2} > 40 \text{ GeV}$ (if $n_{\text{jet}} > 1$)
- $H_T > 200 \text{ GeV}$
- $H_T^{\text{miss}} > 200 \text{ GeV}$
- $p_T^{\text{miss}} > 200 \text{ GeV}$
- $H_T^{\text{miss}} / p_T^{\text{miss}} > 0.8$

- $H_T^{\text{miss}}/p_T^{\text{miss}} < 1.2$
- $\Delta\phi(\vec{H}_T^{\text{miss}}, \vec{p}_T^{\text{miss}}) < 0.5$

To ensure orthogonality with the phase space occupied by their analysis, the two leading jets must be within the acceptance of the tracker, and events must fail the following VBF kinematic selection:

- $p_T^{j_1} > 80 \text{ GeV}$
- $p_T^{j_2} > 40 \text{ GeV}$
- $|\eta_{j_1}| < 5.0$
- $|\eta_{j_2}| < 5.0$
- $\eta_{j_1} \cdot \eta_{j_2} < 0$
- $p_T^{\text{miss}} \geq 250 \text{ GeV}$
- $|\Delta\eta(j_1, j_2)| > 1.0$
- $m_{jj} > 200 \text{ GeV}$
- $\Delta\phi(j_1, j_2) < 1.5$
- $\Delta\phi_{\text{min}}(j, \vec{p}_T^{\text{miss}}) > 0.5$

6.6.2 Additional filters

Further selections are applied to filter poorly measured or mis-reconstructed events in both data and MC. These are applied to all years, regions, and categories unless stated otherwise. A “muon jet filter” rejects events with mis-reconstructed muons by requiring all jets with $p_T > 200 \text{ GeV}$ to have a muon energy fraction $f_E^\mu < 0.5$, and $\Delta\phi(j, \vec{p}_T^{\text{miss}}) < \pi - 0.4$.

Charged ($f_E^{h\pm}$) and neutral hadron energy fraction (f_E^{h0}) requirements are applied to all jets via fulfillment of the tight jet ID criteria (see Chpt. 4.2.1). Furthermore, stricter selections are placed on the leading two jets as follows:

- $f_E^{h\pm}(j_1) > 0.1$
- $f_E^{h0}(j_1) < 0.8$
- $f_E^{h\pm}(j_2) > 0.1$
- $f_E^{h0}(j_2) < 0.8$

In the QCD sidebands, despite the requirement of $p_T^{\text{miss}} > 200 \text{ GeV}$, an excess in data was observed for events with low missing transverse momentum calculated from tracker hits

($p_{T,\text{trk.}}^{\text{miss}}$). This indicated a significant presence of neutral particles in such events, warranting a cut of $p_{T,\text{trk.}}^{\text{miss}} > 80 \text{ GeV}$ in the signal region and sidebands.

The filters described below were recommended by the p_T^{miss} POG to remove events with potentially miscalculated p_T^{miss} :

- Primary vertex filter to remove events failing vertex quality criteria
- Beam halo filter
- HCAL barrel and end cap noise filters
- Filter for dead cells in the ECAL when constructing trigger primitives
- Filter for low-quality PARTICLE FLOW muons

There are supplementary filters applied only to data. These are to generally mitigate ECAL end cap supercrystal noise, as well as crystals where losses of transparency would otherwise require large laser corrections.

A fraction of events in data that entered the $t\bar{t}H$ category in the sidebands were found to disagree in the direction of missing transverse momentum calculated in different regimes. Large differences between the azimuthal angle of the missing transverse momentum calculated with PARTICLE FLOW (\vec{p}_T^{miss}), and either from tracker hits ($\vec{p}_{T,\text{trk.}}^{\text{miss}}$) or jets (\vec{H}_T^{miss}) are indicative of poorly measured objects. An elliptical cut is therefore placed in the plane of $\Delta\phi(\vec{p}_T^{\text{miss}}, \vec{p}_{T,\text{trk.}}^{\text{miss}})$ and $\Delta\phi(\vec{H}_T^{\text{miss}}, \vec{p}_T^{\text{miss}})$ for events in the signal region and sidebands that were categorised by $t\bar{t}H$:

$$\circ \sqrt{\Delta\phi(\vec{p}_T^{\text{miss}}, \vec{p}_{T,\text{trk.}}^{\text{miss}})^2 + 4 \cdot \Delta\phi(\vec{H}_T^{\text{miss}}, \vec{p}_T^{\text{miss}})^2} < 1.0$$

6.6.3 Mitigating the HEM issue

During the 2018 data taking period, the HEM issue (see Chpt. 6.3.1) forced additional measures to be taken that suppressed its effect on the events. For the data recorded within affected period, region-dependent selections were updated to remove events that met the following criteria:

- $\circ -1.8 < \phi(\vec{p}_T^{\text{miss}}) < -0.6$ in the signal region and sidebands
- \circ Any veto electron e_{veto} with $p_T > 10 \text{ GeV}$, $-3.0 < \eta < -1.4$, and $-1.57 < \phi < -0.87$ in the $e + \text{jets}$ and $ee + \text{jets}$ control regions

Events in simulation that met the same criteria were instead weighted by the integrated luminosity from 2018 that was not affected by the issue (i.e., 21.1 fb^{-1}) rather than the entire

year. It is applicable under the assumption that both data and simulation are distributed comparably in the $\eta - \phi$ portions of the detector when the issue was not present. Given geometric variables agree very well between data and simulation, and corrections are implemented to further synchronise them, the assumption is valid.

The effect of the above treatment can be seen in Figs. 6.10 and 6.11.

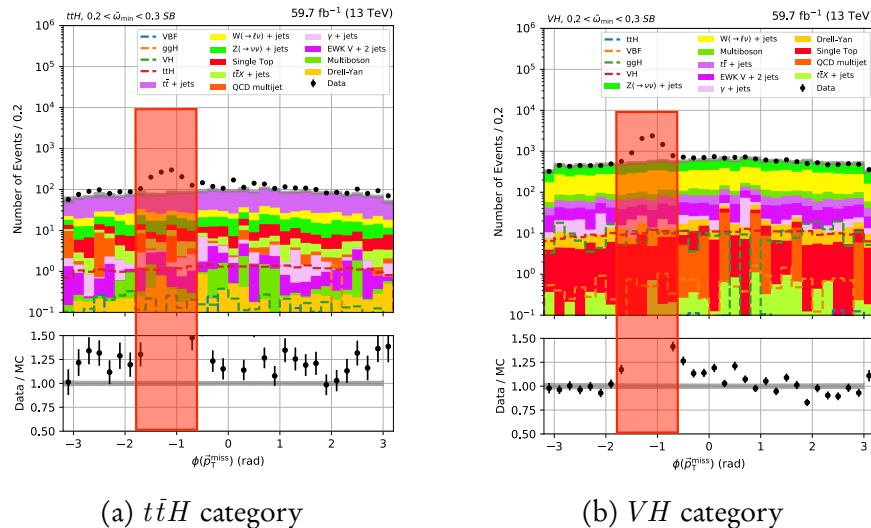


Figure 6.10: The azimuthal angle of the \vec{p}_T^{miss} in the $t\bar{t}H$ and VH categories before and after applying the selections designed to mitigate the HEM issue in 2018. The loose $\tilde{\omega}_{\min}$ sideband is used to demonstrate the effect since it kinematically resembles the signal region, and the data–simulation discrepancy can be removed while still blind in said region. A red box encloses the sector that is removed by the selection applied in the signal region and sidebands.

6.7 Weights, corrections, and systematic uncertainties for simulation

In order for simulated events, particularly for background processes, to resemble LHC data as closely as possible, many corrections and weights are applied. These are discussed in more detail in the subsequent sections. All weights and associated systematic uncertainties are applied to all samples for all data taking years, unless stated otherwise. They are summarised in Tab. 6.7. A final event weight w_{event} is the product of the weights from all of the individual sources i that provide one:

$$(6.8) \quad w_{\text{event}} = \prod_i w_i$$

6.7. WEIGHTS, CORRECTIONS, AND SYSTEMATIC UNCERTAINTIES FOR SIMULATION

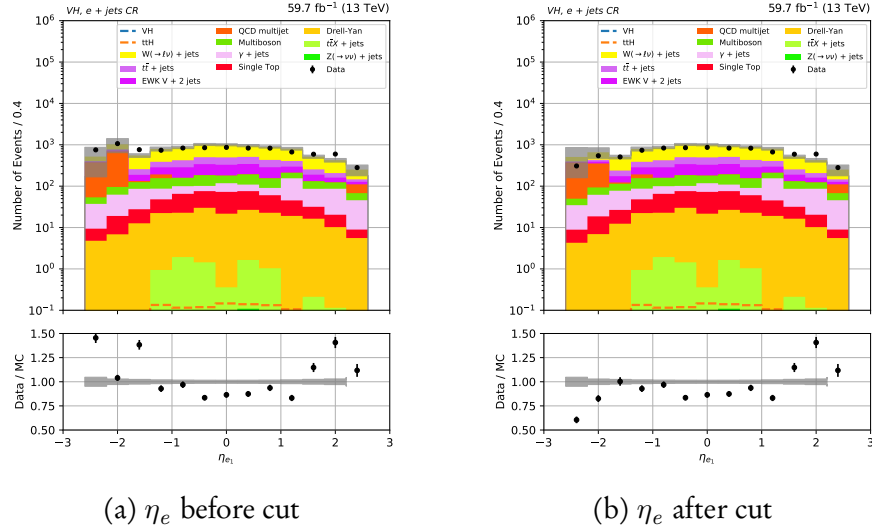


Figure 6.11: The pseudorapidity of the electron in the VH category of the $e + \text{jets}$ control region before applying the selection designed to mitigate the HEM issue in 2018.

When representing these events in histograms, the yield in a given bin $N_{\text{corr.}}$ is the sum of these event weights:

$$(6.9) \quad N_{\text{corr.}} = \sum_j^{N_{\text{MC}}} w_{\text{event } j}$$

where N_{MC} is the number of unweighted, simulated events in the bin. In the data-MC distributions, the statistical uncertainty ascribed to the MC yield in a bin is estimated from the unweighted number of events (k in a Poisson statistical treatment):

$$(6.10) \quad \Delta N_{\text{corr.}} = \pm \frac{N_{\text{corr.}}}{\sqrt{N_{\text{MC}}}}$$

While the statistical uncertainty for the number of events in data is simply the Poissonian error,

$$(6.11) \quad \Delta N_{\text{data}} = \pm \frac{N_{\text{data}}}{\sqrt{N_{\text{data}}}}$$

6.7.1 Pileup reweighting

Pileup interactions at the LHC are frequent (see Chpt. 3.1.3) and must be modelled appropriately in simulation. Simulated samples are generated with a certain distribution of the number of pileup interactions which usually does not match the data recorded by CMS. This is due to changing conditions in the beam over a period of data taking. In order to

make them comparable, the simulated events are reweighted; in this context it is known as *pileup reweighting*. ROOT files containing histograms of the number of pileup interactions from short runs in the LHC are available centrally and are used as the reference for which to reweight the simulated events.

Simulated events are nominally reweighted according to data, where the inelastic pp cross section is measured to be 69.2 mb. An uncertainty of $\pm 4.6\%$ in the measurement is used to calculate the systematic uncertainty on this weight. The pileup distributions, and therefore the weights, are different for each data taking year. However, the inelastic cross section and associated uncertainty are consistent for the entirety of Run-2.

6.7.2 Higher order corrections to $V + \text{jets}$ samples

Vector boson +jets processes present a sizeable background in some of the categories and regions of the analysis. At the dataset sizes required to provide sufficient statistical coverage of the phase space, NLO MC samples are not available with the complete detector simulation applied. To circumvent this, LO samples are used in the analysis and reweighted at generator level on an event-by-event basis to NLO accuracy. This method is usually referred to as a “ k -factor” correction, where k is the ratio of the NLO to LO cross section.

Separate QCD and electroweak corrections are applied to QCD processes. NLO $W + \text{jets}$ samples are used to derive the k -factors for the respective LO process. Drell-Yan $Z(\rightarrow \ell\bar{\ell}) + \text{jets}$ samples are utilised for both the LO Drell-Yan and $Z(\rightarrow \nu\bar{\nu}) + \text{jets}$ processes. The k -factors are calculated independently for the two processes as the LO samples and cross sections are different. One or two additional jets in the matrix element calculations are permitted in the NLO samples. Events from the above datasets are processed through the following generator-level event selection to ensure they are in a similar phase space to the analysis:

- $p_T^{j_1} > 80 \text{ GeV}$
- $p_T^V > 200 \text{ GeV}$
- $H_T^{\text{Gen}} > 200 \text{ GeV}$
- $H_T^{\text{Gen}}/p_T^V < 1.2^{12}$

where p_T^V is the generator-level boson p_T , and H_T^{Gen} is the scalar sum of generator-level jet p_T . The final selection in the list mimics the $H_T^{\text{miss}}/p_T^{\text{miss}}$ cut in Chpt. 6.6.1. The k -factors are binned in two dimensions, p_T^V and $p_T^{j_1}$. Uncertainties for the QCD renormalisation

¹²Not sure if we'll need updated k-factors if we switch to another scenario where we don't use the MHT/MET cut.

scale, factorisation scale, and in the parton distribution function are treated as individual, uncorrelated sources. The same values for the nominal k -factors and uncertainties are used for each data taking year in Run-2. Distributions of the NLO QCD k -factors are presented in Fig. 6.12.

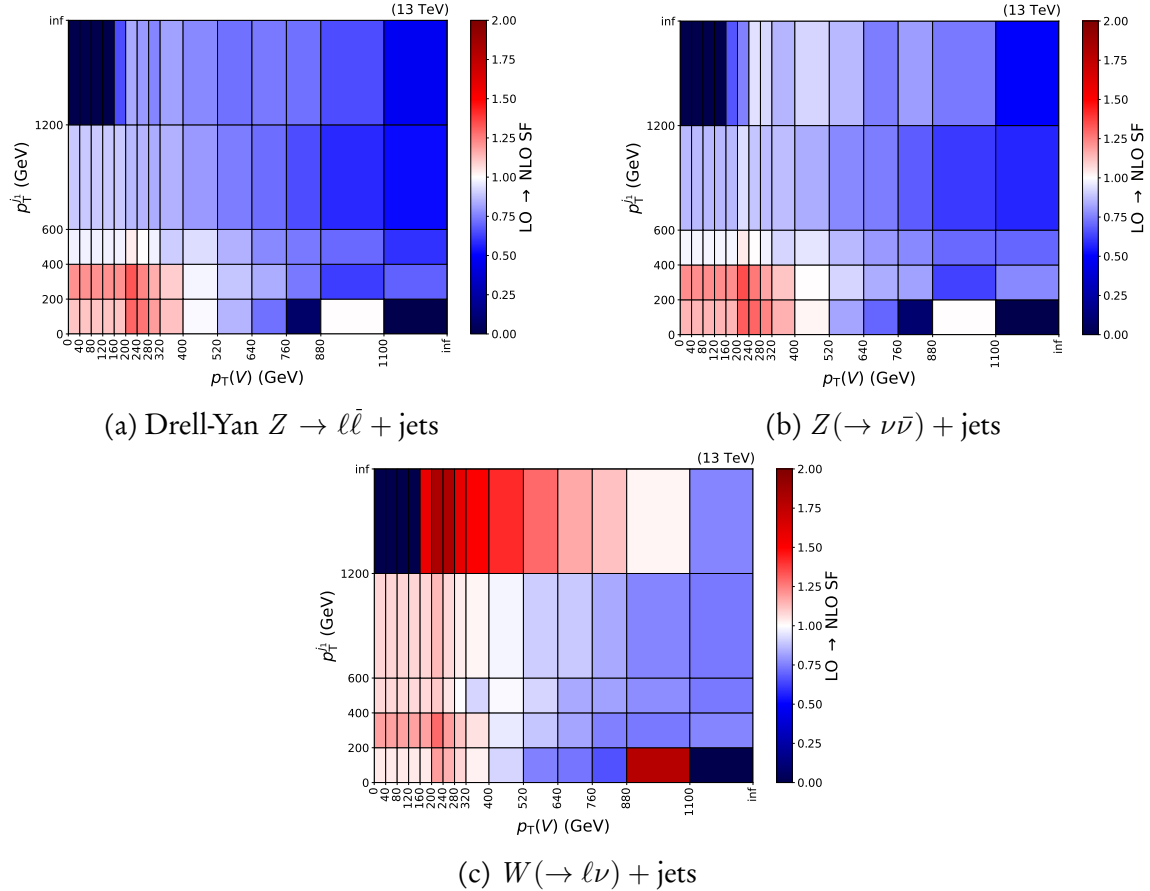


Figure 6.12: NLO k -factors—as a function of the generator-level boson p_{T} and leading jet p_{T} —used to reweight events in LO QCD W and $Z + \text{jets}$ simulation to NLO accuracy in QCD.

Since all of the $V + \text{jets}$ samples were generated at LO electroweak accuracy, an additional k -factor is needed to reweight events to NLO. Ref. 111 provides NLO electroweak corrections for W , Z , and $\gamma + \text{jets}$ processes as a function of p_{T}^V , depicted in Fig. 6.13. The Z k -factor is adopted by both the Drell-Yan and $Z \rightarrow \nu\bar{\nu}$ processes.

6.7.3 Efficiency of the triggers

Given the modelling of the Level-1 and High-Level Trigger systems in simulation is only an approximation of their behaviour with data, corrections must be made to unite them.

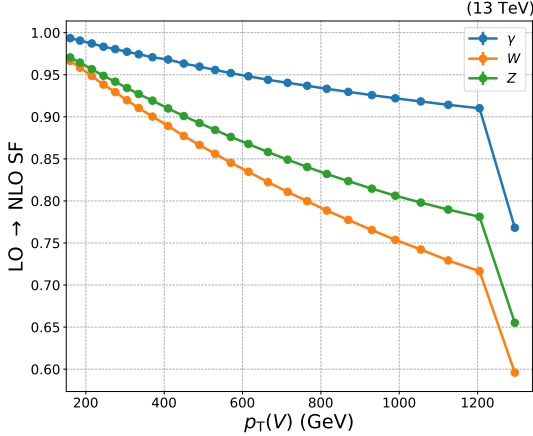


Figure 6.13: NLO k -factors as a function of generator-level boson p_T used to reweight QCD $V + \text{jets}$ events generated at NLO electroweak accuracy. Separate k -factors correct the W , Z , and $\gamma + \text{jets}$ processes.

A dedicated control region is formed to assure orthogonality with the signal region and avoid unblinding of data, but with a similar kinematic selection to the analysis for accuracy in our phase space. Events are selected in data from the primary dataset consisting of muon-based triggers, and in simulation from the $W(\rightarrow \ell\nu) + \text{jets}$ process at LO. Analysed events consist of these containing a single, tightly-isolated muon with $p_T > 30 \text{ GeV}$ that triggers the HLT path for an isolated muon with $p_T > 27 \text{ GeV}$.¹³ An offline selection is then applied to keep those with similar kinematic properties to those in our signal region:

- $p_T^{j_1} > 80 \text{ GeV}$
- $p_T^{j_2} > 40 \text{ GeV}$
- $H_T > 200 \text{ GeV}$
- $H_T^{\text{miss}}/p_{T,\mu}^{\text{miss}} < 1.2$

where $p_{T,\mu}^{\text{miss}} = p_T^{\text{miss}} + p_T^\mu$ to approximate the PF calculation at HLT level. Of these, events that additionally pass the online selection of the trigger requirements in the signal region (Tab. 6.2) are also recorded. The efficiency of a trigger—or collection of triggers— ϵ_{trg} is defined as

$$(6.12) \quad \epsilon_{\text{trg}} = \frac{s_{\text{offline}} \cap s_{\text{online}}}{s_{\text{offline}}}$$

where s denotes the set of events that have passed the selection given by its subscript. For simulation, events are weighted by cross section as per Eq. 6.1. The efficiencies are binned in

¹³Why exactly do we use single muon events. Is it the high efficiency from the muon subsystem? Or that they won't bias the METMHT trigger efficiencies, or something?

two dimensions as a function of $p_{T,\mu}^{\text{miss}}$ and H_T^{miss} . The weight applied to events in simulation w_{trg} is then simply the efficiency in data divided by the efficiency in simulation for the values of p_T^{miss} and H_T^{miss} in the event:

$$(6.13) \quad w_{\text{trg}}(p_T^{\text{miss}}, H_T^{\text{miss}}) = \frac{\epsilon_{\text{trg, data}}(p_T^{\text{miss}}, H_T^{\text{miss}})}{\epsilon_{\text{trg, MC}}(p_T^{\text{miss}}, H_T^{\text{miss}})}$$

Uncertainties are estimated using the Clopper-Pearson method [48]. In the signal region, sidebands, and muon control regions, weights from the efficiencies of the $p_T^{\text{miss}} - H_T^{\text{miss}}$ cross triggers are used. The weights are provided for each data taking year in Fig. 6.14. In the electron and photon control regions, the efficiencies are calculated in the same manner, instead from the triggers in Tabs. 6.3 and 6.4.

6.7.4 Top quark processes

$t\bar{t} + \text{jets}$ is the dominant background for the $t\bar{t}H$ category. The $t\bar{t}X$ backgrounds also have a non-negligible presence. As such, much effort ensures they are modelled correctly. Variations of the QCD renormalisation and factorisation scales provide an uncertainty only to the shape of the p_T^{miss} spectrum of $t\bar{t}$ and $t\bar{t}X$ backgrounds, and $t\bar{t}H$ signal. Reweighting of the top quark p_T distribution to NNLO accuracy is also performed for $t\bar{t}$, yielding a shape correction and associated uncertainty.

6.7.4.1 QCD scale systematic uncertainty

The renormalisation μ_R and factorisation scale μ_F chosen for MC samples at generation may be somewhat arbitrary, and therefore not representative of nature. Relative to the nominal, weights were derived centrally for each combination of these scales being varied independently (and together) up or down by a factor of two. Eight variations then exist for each event:

- $\mu_{R\downarrow} \& \mu_{F\downarrow}$
- $\mu_{R\downarrow} \& \mu_{F\text{ nom.}}$
- $\mu_{R\downarrow} \& \mu_{F\uparrow}$
- $\mu_{R\text{ nom.}} \& \mu_{F\downarrow}$
- $\mu_{R\text{ nom.}} \& \mu_{F\uparrow}$
- $\mu_{R\uparrow} \& \mu_{F\downarrow}$
- $\mu_{R\uparrow} \& \mu_{F\text{ nom.}}$
- $\mu_{R\uparrow} \& \mu_{F\uparrow}$

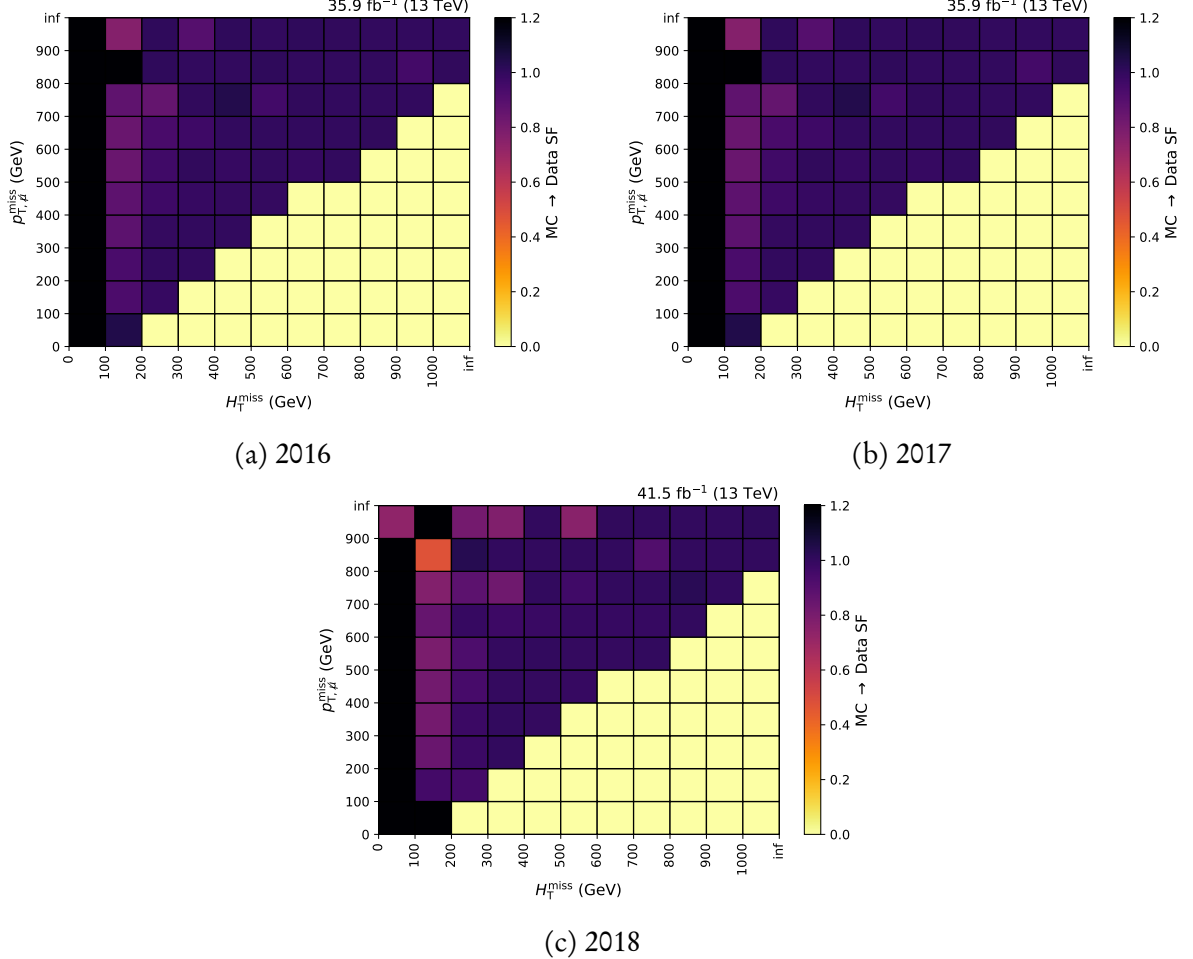


Figure 6.14: Scale factors accounting for the efficiencies of the HLT $p_T^{\text{miss}} - H_T^{\text{miss}}$ cross triggers in each data taking year of Run-2. The momentum of the muon used to select events that compute the efficiency is added to the \vec{p}_T^{miss} (with a magnitude $p_{T,\mu}^{\text{miss}}$) in order to approximate the calculation in the High-Level Trigger.

To remove the dependence on normalisation (since the skim and event selection may bias it) and ensure the systematic is only shape-based, each variation was also multiplied by an additional factor f_{var} :

$$(6.14) \quad f_{\text{var}} = \frac{\sum_{\text{unskimmed events}} w_{\mu_R \text{ nom.} \& \mu_F \text{ nom.}}}{\sum_{\text{unskimmed events}} w_{\text{var}}}$$

These are computed individually for each decay and data taking year. The envelope is characterised by the correlated variations $\mu_{R\uparrow} \& \mu_{F\uparrow}$, and $\mu_{R\downarrow} \& \mu_{F\downarrow}$. Confirmed by Fig. 6.15, an example is given for the $t\bar{t}$ background in the signal region. While the sizes of the variations appear large, they are very similar between the signal and control regions, cancelling to a large degree to minimally impact the results.

6.7. WEIGHTS, CORRECTIONS, AND SYSTEMATIC UNCERTAINTIES FOR SIMULATION

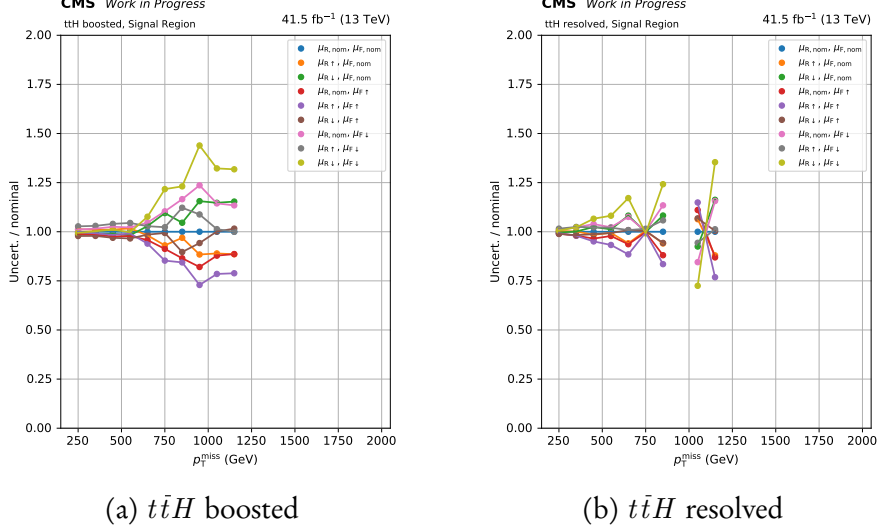


Figure 6.15: The deviations relative to the nominal weight of the combinations of QCD renormalisation and factorisation scale variations. They are presented as a function of p_T^{miss} in the $t\bar{t}H$ categories for the $t\bar{t}$ samples. Events are from the signal region in the 2017 dataset after the analysis-level selection.

For each process (i.e., $t\bar{t}$, and the accompanying boson X in $t\bar{t}X$), a separate systematic uncertainty is derived.¹⁴ Since different generators and settings may be used for each dataset, it is appropriate to ensure they are uncorrelated.

6.7.4.2 Top quark p_T reweighting

The top quark p_T distribution has been shown to be harder in simulation at NLO than in data [133]. NLO $t\bar{t} + \text{jets}$ MC generated in POWHEG is reweighted to NNLO QCD + NLO electroweak accuracy as function of top quark p_T . An analytic function is used to fit the distribution that determines the weight. The same nominal function is used for all $t\bar{t} + \text{jets}$ samples for all data taking years:

$$(6.15) \quad f(p_T) = \exp(a + b \cdot p_T + c \cdot p_T^2)$$

where the coefficients are $a = 1.614 \times 10^{-2}$, $b = -1.966 \times 10^{-4}$, and $c = 1.454 \times 10^{-8}$. For a top or antitop quark, the scale factor is given by the value of f for the particle's generator-level p_T . The event weight is then the square root of the product of the top and antitop scale factors.

¹⁴ $t\bar{t}H(H \rightarrow \text{invisible})$ signal and $t\bar{t}H(H \rightarrow \text{visible})$ background are grouped as one process since the kinematics and generation procedure are consistent.

The uncertainties are acquired from the fit itself over theoretical uncertainties inherent in MC calculations. This was to avoid double counting with respect to the renormalisation and factorisation scale uncertainty in Chpt. 6.7.4.1, as overlap would be present and otherwise difficult to disentangle. For each parameter in the fit, the upward and downward variations were estimated. The fit function was then recalculated, fixing the parameter of interest to the variation. Providing upward and downward functions, the systematic uncertainty attributed to the parameter is simply the event weight calculated with these functions over the nominal. Separate, uncorrelated uncertainties were estimated for each parameter in the fit. The nominal function and associated variations are shown in Fig. 6.16.

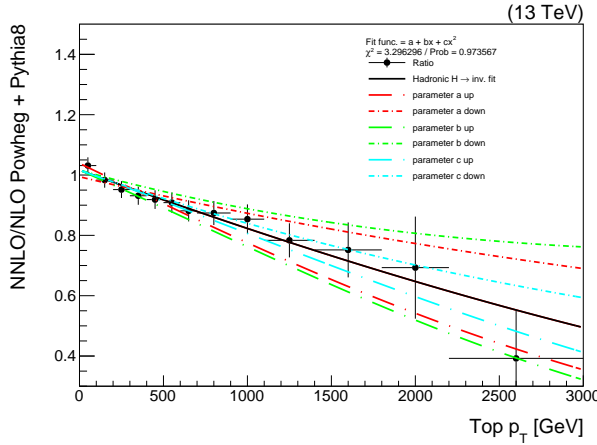


Figure 6.16: The ratio of the NNLO to NLO $t\bar{t}$ cross section as a function of top quark p_T . The fit to the distribution—along with the uncertainties in the parameters—are shown.

We aimed to remove the dependence on normalisation in the same fashion as for the QCD scale to consider the correction only to the shape of the distributions and not also the normalisation. However, the normalisation factors were found to be unity for all datasets. Hence, no additional factor was required.

6.7.5 Object-level scale factors and uncertainties

There are multiple corrections applied to simulation based on the physics objects with an event as opposed to the event topology as a whole. One example of which is Chpt. 6.7.4.2. A weight or efficiency ϵ attributed to an object itself is typically referred to as a *scale factor*, while the event-level selection weight $w_{\text{sel.}}$ is the efficiency for successfully tagging or selecting an event with those object contents, and is the product of the scale factors:

$$(6.16) \quad w_{\text{sel.}} = \prod_i^{N_{\text{objects}}} \epsilon_i$$

These weights are calculated individually for each class of object in an event. For electrons, muons, and photons, these scale factors are usually from the reconstruction efficiency, identification efficiency, and p_T - or η -dependent energy corrections. In the case of b -tagged jets, it is the data-simulation scale factor at the given working point from the algorithm used to identify them. Systematic uncertainties associated with the scale factors are aggregated in the same manner. Unless stated otherwise, the following scale factors and systematics are derived separately for each year in Run-2.

6.7.5.1 Lepton and photon identification, isolation, and reconstruction

Electrons and photons are identified using the cut-based identification described in Chpts. 4.2.4 and 4.2.5, respectively. Scale factors are applied separately to each of these objects in simulation that account for the efficiency of identification, isolation, and reconstruction in data. They are derived as a function of η and ECAL supercluster p_T and binned as such. Uncertainties are given as the error in the (η, p_T) bin of the histogram that describes the efficiencies. The ID and isolation are grouped as a single uncertainty, while reconstruction is another. Event weights simply are the products of the individual object scale factors. The uncertainty on the event weight is the product of the scale factor plus/minus its uncertainty. For each source, they are on the order of 1–5 %.

Muons follow a similar prescription, where the ID and isolation efficiencies are calculated in bins of η and p_T . The systematic uncertainties for each of the two sources are separated—contrary to electrons and photons—and are usually 1 % or smaller in size. An equivalent reconstruction efficiency is not given as the dedicated muon chambers and reconstruction algorithms are more than sufficient.¹⁵

Tau leptons are identified with a multivariate discriminator, as noted in Chpt. 4.2.6. Data to simulation scale factors are applied and their uncertainties propagated through the analysis.¹⁶

6.7.5.2 b -jets tagged by the DEEPCSV algorithm

Data-simulation scale factors are calculated for each b -jet as tagged by the DEEPCSV algorithm. They are defined as the tagging efficiency in data divided by the efficiency for simulation for a given working point, and as a function of jet p_T . Various methods are employed to derive separate scale factors for separate topologies, such as QCD multijet or $t\bar{t}$ events, and

¹⁵For electrons, muons, and photons, not really sure of the actual procedures for getting the scale factors for each source. Twikis do a pretty poor job of explaining them.

¹⁶If we hard veto on taus, obviously won't have sys.

are described in Sec. 8.4 of Ref. 129. A weighted average of the scale factors computed by each method are then taken to yield the final scale factor for a b -tagged jet. The resultant systematic uncertainty is typically less than 5 %.¹⁷

6.7.5.3 Boosted jets tagged by the DEEPAK8 algorithm

In a similar fashion to the section above, objects classified by the DEEPAK8 algorithm are given scale factors according to the data/MC efficiencies as a function of AK8 jet p_{T} . Scale factors are derived separately for jets tagged as originating from a top quark and V boson. Systematic uncertainties associated with the scale factors on the order of 1–10 % are also derived separately, according to Sec. 8.1 of Ref. 60.

6.7.6 Minor contributions

6.7.6.1 Pre-firing in the ECAL

Derived by members of the Collaboration, the nominal weight applied to events in simulation that emulates the effect of pre-firing in 2016 and 2017 data, is given in Ref. 62:

$$(6.17) \quad w_{\text{pre-firing}} = \prod_{i=\gamma, \text{jet}} 1 - \epsilon_i^{\text{pre-firing}}(\eta, p_{\mathrm{T}}^{\text{EM}})$$

where ϵ is the probability for an object to pre-fire as a function of its η and electromagnetic p_{T} (simply p_{T} for photons, and p_{T} multiplied by the sum of the charged and neutral electromagnetic energy fractions for jets). The systematic uncertainty in the event weight is found by taking the uncertainty on ϵ : the maximum of 0.2ϵ and the statistical uncertainty in the $(\eta, p_{\mathrm{T}}^{\text{EM}})$ bin of the pre-firing map from which ϵ is extracted. Pre-firing probabilities are assumed to be uncorrelated between photons and jets.¹⁸

6.7.6.2 Jet energy scale and resolution

6.7.6.3 Luminosity

Uncertainties are associated with the various methods designed to measure the luminosity received by CMS. For 2016, 2017, and 2018, the total systematic uncertainties on certified data are 2.5 %, 2.3 %, and 2.5 %, respectively. They may be decomposed into several individual

¹⁷We don't seem to take any explicit systematics at the skimming stage where our b -jets are defined and SFs taken. So I don't really know where the up and down variations come from.

¹⁸Do we correlate the systematic between years?

sources, some of which are correlated between years. These are documented in Tab. 6.6 with further information available in Refs. 50, 51, and 52.¹⁹

Uncertainty source	Impact in 2016	Impact in 2017	Impact in 2018
Uncorrelated sources	2.2	2.0	1.5
$x\text{-}y$ factorisation	0.9	0.8	2.0
Length scale	—	0.3	0.2
Beam-beam deflection	0.4	0.4	—
Dynamic β	0.5	0.5	—
Beam current calibration	—	0.3	0.2
Ghosts and satellites	0.4	0.1	—

Table 6.6: Sources of uncertainty in the luminosity measurements for each year of Run-2, and their impacts in percent. For each row except the first, the source of uncertainty is assumed to be correlated between years for which it was present.

6.7.6.4 Cross section for signal processes

There are several sources of uncertainty in the computation of high order cross sections, from both theoretical and experimental sides. As with the nominal cross sections for signal processes, the uncertainties are retrieved from Ref. 42. Every source for every signal process is treated as a separate uncertainty on the normalisation. They are correlated across years as the cross section is constant across them.

6.8 Statistical model and fit

A likelihood model is used in the fit to data, simultaneously over the signal and control regions to obtain the standard model expectation values as well as testing for signals of the $H \rightarrow$ invisible decay. Events are categorised in two dimensions: the subcategories that target specific Higgs boson production modes and final state topologies as per Tab. 6.1, and in bins of p_T^{miss} as per Chpt. 6.8.1. The observed event counts from data in each subcategory and p_T^{miss} bin are modelled as Poisson-distributed variables around the SM expectation with a potential contribution from signal (assumed to be zero in the null hypothesis). Expected event counts in the signal region are obtained from simulation, aided by predictions from the control regions and sidebands for non-multijet and QCD multijet processes, respectively. These are elaborated upon in Chpt. 6.8.2. Systematic uncertainties associated with the non-multijet

¹⁹Not sure if I even need the table, to be honest. It may ask more questions regarding each source rather than answering anything. Or, could fold into summary syst table.

Source	Type	Years	Samples
Pileup	Normalisation, shape	All, correlated	All
NLO renorm. scale	Normalisation, shape	All, correlated	LO $V + \text{jets}$
NLO fact. scale	Normalisation, shape	All, correlated	LO $V + \text{jets}$
NLO PDF	Normalisation, shape	All, correlated	LO $V + \text{jets}$
Trigger efficiency	Normalisation, shape	All, uncorrelated(?)	All
QCD renorm. & fact. scale	Shape	All, correlated	$t\bar{t}H, t\bar{t}, t\bar{t}X$
Top p_T reweighting	Shape	All, correlated	$t\bar{t}$
μ ID efficiency	Normalisation	All, correlated	All
μ isolation efficiency	Normalisation	All, correlated	All
e ID & isolation efficiency	Normalisation	All, correlated	All
e reconstruction efficiency	Normalisation	All, correlated	All
γ ID & isolation efficiency	Normalisation	All, correlated	All
τ ID efficiency	Normalisation	All, correlated	All
b -tagging	?	All, correlated	All
Boosted object tagging	Normalisation	All, correlated	All
ECAL pre-firing	Normalisation	2016–17, uncorrelated	All
JER and JES	Normalisation, shape(?)	All, correlated(?)	All
Luminosity	Normalisation	All	All
Photon purity	Normalisation	All, uncorrelated	QCD est. from data
Signal cross section	Normalisation	All, correlated	Signal

Table 6.7: The experimental uncertainties present in the analysis, the type of uncertainty, and impact on (the p_T^{miss} distribution/signal strength parameter), along with the years and simulated samples affected.

processes, discussed in Chpt. 6.7, are incorporated as nuisance parameters within the model. The likelihood function $\mathcal{L}_{H \rightarrow \text{invisible}}$ can be summarised as

$$(6.18) \quad \mathcal{L}_{H \rightarrow \text{invisible}} = \mathcal{L}_{\text{SR}} \cdot \mathcal{L}_\mu \cdot \mathcal{L}_{\mu + \text{jets CR}} \cdot \mathcal{L}_{\mu\mu + \text{jets CR}} \cdot \mathcal{L}_e \cdot \mathcal{L}_{e + \text{jets CR}} \cdot \mathcal{L}_{\mu\mu + \text{jets CR}} \cdot \mathcal{L}_\gamma \cdot \mathcal{L}_{\gamma + \text{jets CR}}$$

where the aim of the fit is to minimise $-\ln \mathcal{L}_{H \rightarrow \text{invisible}}$. The likelihood in a given region of the analysis may be written as multiple Poisson likelihoods, denoting $\mathcal{P}(n|\lambda) \equiv \frac{e^{-\lambda} \lambda^n}{n!}$. In the signal region,

$$(6.19) \quad \begin{aligned} \mathcal{L}_{\text{SR}}(r, a_{\ell_{\text{lost}}}, a_{Z \rightarrow \nu\bar{\nu}}, \rho) &= \prod_i \prod_{j(i)} \mathcal{P}(N_{\text{obs.}}^{i,j} | N_{\text{pred.}}^{i,j}), \text{ where} \\ N_{\text{pred.}}^{i,j} &= r \cdot s^{i,j} \cdot \rho_s^{i,j} \\ &\quad + b_{\ell_{\text{lost}}}^{i,j} \cdot a_{\ell_{\text{lost}}}^{i,j} \cdot \rho_{\ell_{\text{lost}}}^{i,j} \\ &\quad + b_{Z \rightarrow \nu\bar{\nu}}^{i,j} \cdot a_{Z \rightarrow \nu\bar{\nu}}^{i,j} \cdot \rho_{Z \rightarrow \nu\bar{\nu}}^{i,j} \\ &\quad + c_{\text{QCD}}^{i,j} \cdot \omega_{\text{QCD}}^{i,j} \end{aligned}$$

where the indices i and j refer to each subcategory and p_T^{miss} bin, respectively, r is the unconstrained signal strength parameter, i.e., $\sigma \times \mathcal{B}(H \rightarrow \text{invisible})/\sigma_{\text{SM}}$, s is the signal expectation determined from simulation, ρ encodes the systematic uncertainties associated with simulation, b is the number of events from simulation, a is an unconstrained rate parameter connecting the signal and corresponding control regions, c is the predicted number of events, and ω contains the uncertainties on the QCD multijet background estimate. Similarly for the control regions, the likelihood functions are

$$(6.20) \quad \begin{aligned} \mathcal{L}_{\mu + \text{jets CR}} &= \prod_i \prod_{j(i)} \mathcal{P}(N_{\text{obs.}, \mu}^{i,j} | r \cdot s_{\mu}^{i,j} \cdot \rho_{s, \mu}^{i,j} + b_{\mu}^{i,j} \cdot a_{\ell_{\text{lost}}}^{i,j} \cdot \rho_{\mu}^{i,j}) \\ \mathcal{L}_{\mu\mu + \text{jets CR}} &= \prod_i \prod_{j(i)} \mathcal{P}(N_{\text{obs.}, \mu\mu}^{i,j} | r \cdot s_{\mu\mu}^{i,j} \cdot \rho_{s, \mu\mu}^{i,j} + b_{\mu\mu}^{i,j} \cdot a_{Z \rightarrow \nu\bar{\nu}}^{i,j} \cdot \rho_{\mu\mu}^{i,j}) \\ \mathcal{L}_{e + \text{jets CR}} &= \prod_i \prod_{j(i)} \mathcal{P}(N_{\text{obs.}, e}^{i,j} | r \cdot s_e^{i,j} \cdot \rho_{s, e}^{i,j} + b_e^{i,j} \cdot a_{\ell_{\text{lost}}}^{i,j} \cdot \rho_e^{i,j}) \\ \mathcal{L}_{ee + \text{jets CR}} &= \prod_i \prod_{j(i)} \mathcal{P}(N_{\text{obs.}, ee}^{i,j} | r \cdot s_{ee}^{i,j} \cdot \rho_{s, ee}^{i,j} + b_{ee}^{i,j} \cdot a_{Z \rightarrow \nu\bar{\nu}}^{i,j} \cdot \rho_{ee}^{i,j}) \\ \mathcal{L}_{\gamma + \text{jets CR}} &= \prod_i \prod_{j(i)} \mathcal{P}(N_{\text{obs.}, \gamma}^{i,j} | r \cdot s_{\gamma}^{i,j} \cdot \rho_{s, \gamma}^{i,j} + b_{\gamma}^{i,j} \cdot a_{Z \rightarrow \nu\bar{\nu}}^{i,j} \cdot \rho_{\gamma}^{i,j} + c_{\text{QCD}}^{i,j} \cdot \omega_{\text{QCD}}^{i,j}) \end{aligned}$$

where the products over the indices i and j are the same as in Eq. 6.19. Signal contamination s is accounted for in all control regions. The rate parameters a are shared across the complementary control regions for the same subcategories and p_T^{miss} bins, i.e., $a_{\ell_{\text{lost}}}$ in the single lepton regions, and $a_{Z \rightarrow \nu\bar{\nu}}$ in the dilepton and single photon regions. QCD multijet MC is not included in any of the lepton control regions, but is estimated in the $\gamma + \text{jets}$ control region from the photon purity measurement recounted in Chpt. 6.5.2.1.

The asymptotic formula [70] for setting a limit on r is used in the case no new physics is observed. Statistical uncertainties from simulation are accommodated as a single nuisance parameter per bin as documented in based on Ref. 27. Above 10 weighted events, the uncertainty is profiled according to a Gaussian distribution centred on its value. Below that threshold, a Poisson distribution is instead invoked to provide stability in the fit for bins with small event counts. These methods are implemented, along with the likelihood function, in the HiggsAnalysis-CombinedLimit package.

6.8.1 Binning

In addition to the categories in Chpt. 6.4, events are further separated into bins of p_T^{miss} as that distribution is expected to maximally differentiate signal and background in the fit. Since the number of events can significantly differ between categories in the different regions of

the analysis, a global binning configuration is inadequate. For each subcategory, the number and widths of the bins are tuned to ensure sufficient statistical precision. These schemes are tied to the subcategory, so are reflected in all regions such that the background estimation methods can operate on a bin-by-bin basis. The binning configuration is outlined in Tab. 6.8.

Category	Subcategory	p_T^{miss} bins (GeV)
$t\bar{t}H$	2Boosted	[200, 300), [300, 400), [400, ∞)
	1t1b	[200, 300), [300, 400), [400, ∞)
	1t2b	[200, 300), [300, 400), [400, 600), [600, ∞)
	1W1b	[200, 300), [300, 400), [400, ∞)
	1W2b	[200, 300), [300, 400), [400, ∞)
	5j1b	[200, 300), [300, 400), [400, ∞)
	6j1b	[200, 300), [300, 400), [400, ∞)
	5j2b	[200, 300), [300, 400), [400, ∞)
	6j2b	[200, 300), [300, 400), [400, ∞)
VH	2j0b	[200, 300), [300, 400), [400, ∞)
	2j1b	[200, 300), [300, 400), [400, ∞)
	2j2b	[200, ∞)
	1V	[200, 300), [300, 400), [400, ∞)
ggH	2jM	[200, 300), [300, 400), [400, 600), [600, ∞)
	3j	[200, 300), [300, 400), [400, 600), [600, ∞)
	4j	[200, 300), [300, 400), [400, 600), [600, ∞)
	5j	[200, 300), [300, 400), [400, 600), [600, ∞)

Table 6.8: The binning scheme used to categorise events in terms of p_T^{miss} .

6.8.2 Background estimation

Accurate estimation of the standard model background processes in the signal region is paramount to a search for new physics. Mismeasured backgrounds and uncertainties can wash out traces of signal and affect the fit to data. In the signal region and QCD sidebands, simulated samples in Chpt. 6.3.3 are grouped into three processes for the purposes of background estimation in the fit:

- Lost lepton: Comprised of electroweak $W+2$ jets, $\gamma+\text{jets}$, single top, $t\bar{t}+\text{jets}$, $t\bar{t}\gamma+\text{jets}$, $t\bar{t}W+\text{jets}$, $t\bar{t}H+\text{jets}$, and $W(\rightarrow \ell\nu)+\text{jets}$
- $Z \rightarrow \nu\bar{\nu}$: Comprised of Drell-Yan ($Z \rightarrow \ell\ell$) + jets, multiboson, electroweak $Z+2$ jets, $t\bar{t}Z+\text{jets}$, and $Z(\rightarrow \nu\bar{\nu})+\text{jets}$
- QCD: QCD multijet

In the lepton control regions, all samples are grouped into a single “electroweak” process with the exception of QCD multijet that is absent entirely. In the $\gamma + \text{jets}$ control region, the non-multijet datasets are also under the electroweak label, and the presence of QCD is estimated from the photon purity measurement.

The single lepton control regions are used to constrain the lost lepton background in the signal region, arising primarily from $t\bar{t} + \text{jets}$ and $W(\rightarrow \ell\nu) + \text{jets}$. The dilepton and photon control regions predict the $Z(\rightarrow \nu\bar{\nu}) + \text{jets}$ background. These estimations rely on the data and Monte Carlo yields in those regions, controlled via a rate parameter to connect them to the signal region. Sidebands to the signal region estimate QCD multijet contributions from data. The prediction in this case takes the form of a *transfer factor* method—a constrained application of a rate parameter. Prediction of the background yields from each of these methods is done so within the fit and expressed in the likelihoods. Further explanation is given below. Fig. 6.17 illustrates the correspondence between the analysis regions and background predictions.

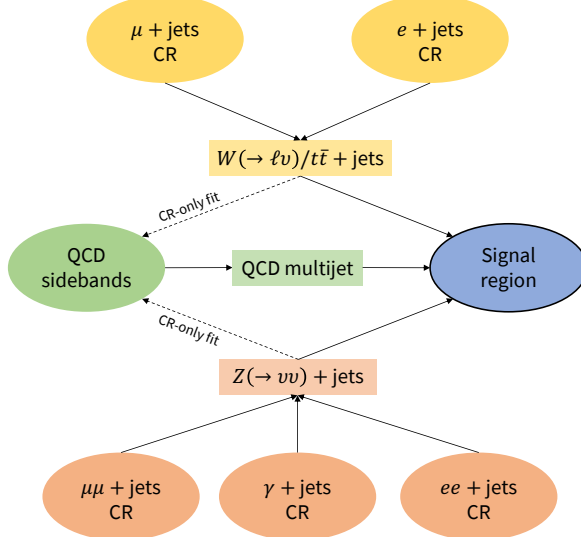


Figure 6.17: An infographic showcasing the role of each analysis region in the final fit. The control regions predict the lost lepton and $Z \rightarrow \nu\bar{\nu}$ backgrounds, and a control region-only fit informs the QCD multijet prediction that contributes to the eventual background determination in the signal region.

6.8.2.1 Lost lepton (W and $t\bar{t} + \text{jets}$)

In order to predict the lost lepton background in the signal region, a freely floating rate parameter $a_{\ell_{\text{lost}}}$ is introduced in the fit. It is shared across the single lepton control regions

and signal region, where it scales the event count from simulation in these regions to obtain the expected values. Events are categorised and binned in the same manner in the single lepton control regions as in the signal region, such that the rate parameters—and therefore the prediction—is derived bin-by-bin. The predicted number of lost lepton events in Eqs. 6.19 and 6.20 is then simply $b_{\ell_{\text{lost}}} \cdot a_{\ell_{\text{lost}}}$.

6.8.2.2 $Z(\rightarrow \nu\bar{\nu}) + \text{jets}$

The irreducible background from invisibly decaying Z bosons is estimated in the same manner as the lost lepton background. A rate parameter $a_{Z \rightarrow \nu\bar{\nu}}$ ties together the dilepton control regions, the photon control region, and the signal region. The yields from simulation are scaled by the best fit value of the parameter, obtained during the simultaneous fit to the analysis regions. As with the lost lepton background, event categorisation is the same in these regions, allowing the predictions to be derived independently for each subcategory and p_T^{miss} bin.

6.8.2.3 QCD multijet

The effects of jet mismeasurements are difficult to quantify. With a final state of several jets in the QCD multijet process, low, or even no, \vec{p}_T^{miss} is expected. Therefore, a single mismeasured jet will introduce artificial \vec{p}_T^{miss} in the direction of that jet. A low $\Delta\phi_{\min}(j, \vec{p}_T^{\text{miss}})$ is therefore expected. Though it is not just this process that suffers—jets from “cleaner” processes may also be affected—those with real p_T^{miss} in an event (e.g., $Z(\rightarrow \nu\bar{\nu}) + \text{jets}$) are unlikely to be significantly affected by one stray object. The enormous cross section of QCD multijet also amplifies the problem, making the process as a whole more sensitive to, e.g., fluctuations in the calorimeter response that would affect the energy measurement.

Contributions to the signal region from QCD multijet events should be adequately suppressed by the analysis-level selection requirements. However, it is still a process that must be accurately accounted for considering its rate of production at CMS. A metric by which to estimate the number of events a dataset should require is by calculating the equivalent luminosity:

$$(6.21) \quad L_{\text{eq.}} = \frac{N_{\text{events}}}{\sigma}$$

A general rule is that the equivalent luminosity of a given dataset should be comparable to, or even exceed, that of the data collected by the experiment. Since the QCD multijet process has a very large cross section, simulating the required number of events to match

the luminosity of the data recorded during Run-2 is not feasible. This can be mitigated by using a data-driven method to estimate it from the multijet-enriched sidebands described in Chpt. 6.5.3.

To estimate the presence of QCD in the signal region, a data driven approach is taken utilising the sidebands defined in Chpt. 6.5.3. These are derived separately for each category and data taking year. Firstly, a fit using the control regions is performed to extract the rate parameters (a from Eq. 6.20) that scale the non-multijet background in each subcategory and p_T^{miss} bin. Applying these to the corresponding backgrounds in the sidebands changes the event distribution and hence the data/MC agreement. The excess in data in a sideband is assumed to arise solely from multijet events, and as such the difference between data and the non-multijet background is attributed to QCD (denoted as $N_{\text{SB}}^{\text{QCD}}$).

QCD in the signal region $N_{\text{pred.}}^{\text{QCD}}$ (corresponding to c_{QCD} in Eq. 6.19) is predicted in each subcategory and p_T^{miss} bin as follows:

$$(6.22) \quad N_{\text{pred.}}^{\text{QCD}}(\text{subcategory}, p_T^{\text{miss}}) = N_{\text{SB}}^{\text{QCD}} \cdot \mathcal{T}_{\text{QCD}} \cdot f_s(\text{subcategory}) \cdot f_p(p_T^{\text{miss}})$$

where \mathcal{T}_{QCD} is the transfer factor relating the QCD in the sideband to the multijet simulation in the signal region. As the signal region is depleted in simulated multijet events, the transfer factor is inclusive over the region rather than per p_T^{miss} bin and subcategory, i.e.,

$$(6.23) \quad \mathcal{T}_{\text{QCD}} = \frac{N_{\text{MC, SR}}^{\text{QCD}}}{N_{\text{MC, SB}}^{\text{QCD}}}$$

The distribution of the QCD background for each subcategory and p_T^{miss} bin is extrapolated from the sidebands with the factors f_s and f_p . f_s is the fraction of QCD in a given subcategory of a given sideband, inclusive of p_T^{miss} . f_p is the fraction of QCD in a given p_T^{miss} bin of a given sideband, inclusive of subcategory.²⁰

6.9 Analysis of the $t\bar{t}H$ mode

The fit of signal and background to the observed data is performed for each subcategory of $t\bar{t}H$, in addition to the category as a whole.²¹ Due to limited statistical precision, the dilepton control regions in the boosted subcategories are combined into a single bin, i.e., inclusive of both subcategory and p_T^{miss} . The rate parameter for the prediction of the $Z \rightarrow \nu\bar{\nu}$ background

²⁰Need to mention how uncertainty is handled for the predicted QCD. Probably some log normal uncertainty estimated from the other sidebands.

²¹Might make more sense to have a section called “Results”, and then these “Analysis of the X mode” and combined results as subsections.

in the signal region is therefore a single value shared across the boosted subcategories and their p_T^{miss} bins. The $\gamma + \text{jets}$ control region is not used in constraining the $Z \rightarrow \nu\bar{\nu}$ prediction for any of the subcategories.

To predict the QCD event counts in the signal region, Eq. 6.22 incorporates the MC counts in said region and from one or more sidebands. The tight double sideband from Tab. 6.5—the most enriched in multijet MC—is employed to derive the category fraction f_s . Yields from the loose double sideband compute the remaining terms: the p_T^{miss} fraction f_p , $N_{\text{SB}}^{\text{QCD}}$, and \mathcal{T}_{QCD} .

Results are presented in terms of the upper limit on the signal strength parameter $\sigma \times \mathcal{B}(H \rightarrow \text{invisible})/\sigma_{\text{SM}}$. The observed limit in the signal plus background hypothesis at 95 % confidence level is overlaid on the expectation from the background-only hypothesis. In the latter, the median expected limit is illustrated with accompanying boundaries for its 1σ and 2σ deviations. Fig. 6.18 showcases the limits for each $t\bar{t}H$ subcategory and the combination of them all, for each data taking year individually and over the full Run-2 dataset.

Distributions of the pre-fit and post-fit yields in the signal region for 2016, 2017, and 2018 are displayed in Figs. 6.19, 6.20, and 6.21, respectively.^{22,23} Corresponding figures for the control regions are given in App. A.1.

²²Not sure if it's worth including pre-fit and post-fit on the same plot to halve the number of them. Risks clutter.

²³Not sure if it's worth combining all signal into one $H \rightarrow \text{invisible}$ line or keeping them separate.

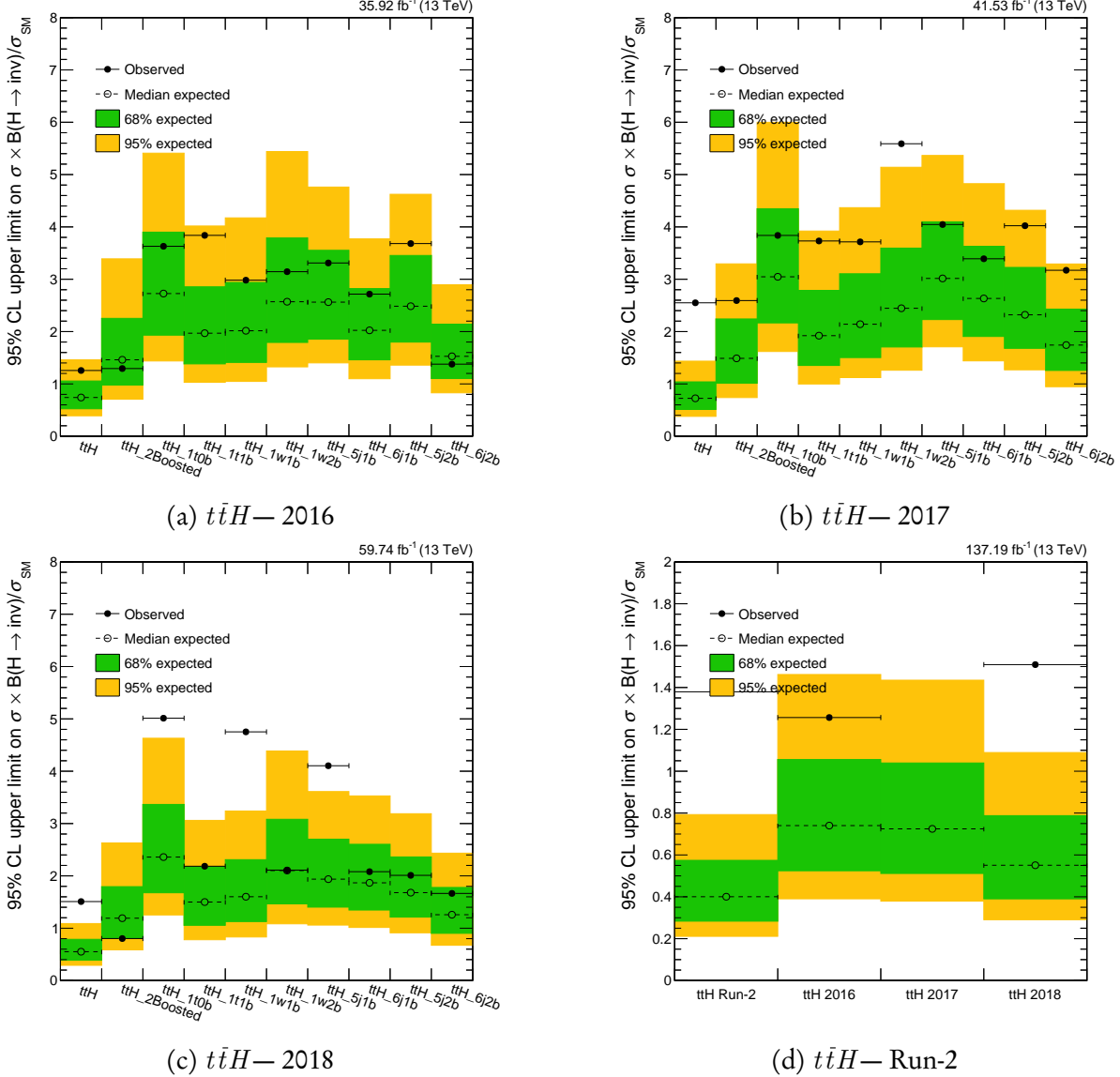


Figure 6.18: Observed and expected 95 % CL upper limits on the Higgs boson to invisible state branching fraction in the $t\bar{t}H$ category, for both the individual subcategories, and the combination of them, for each data-taking year in Run-2.

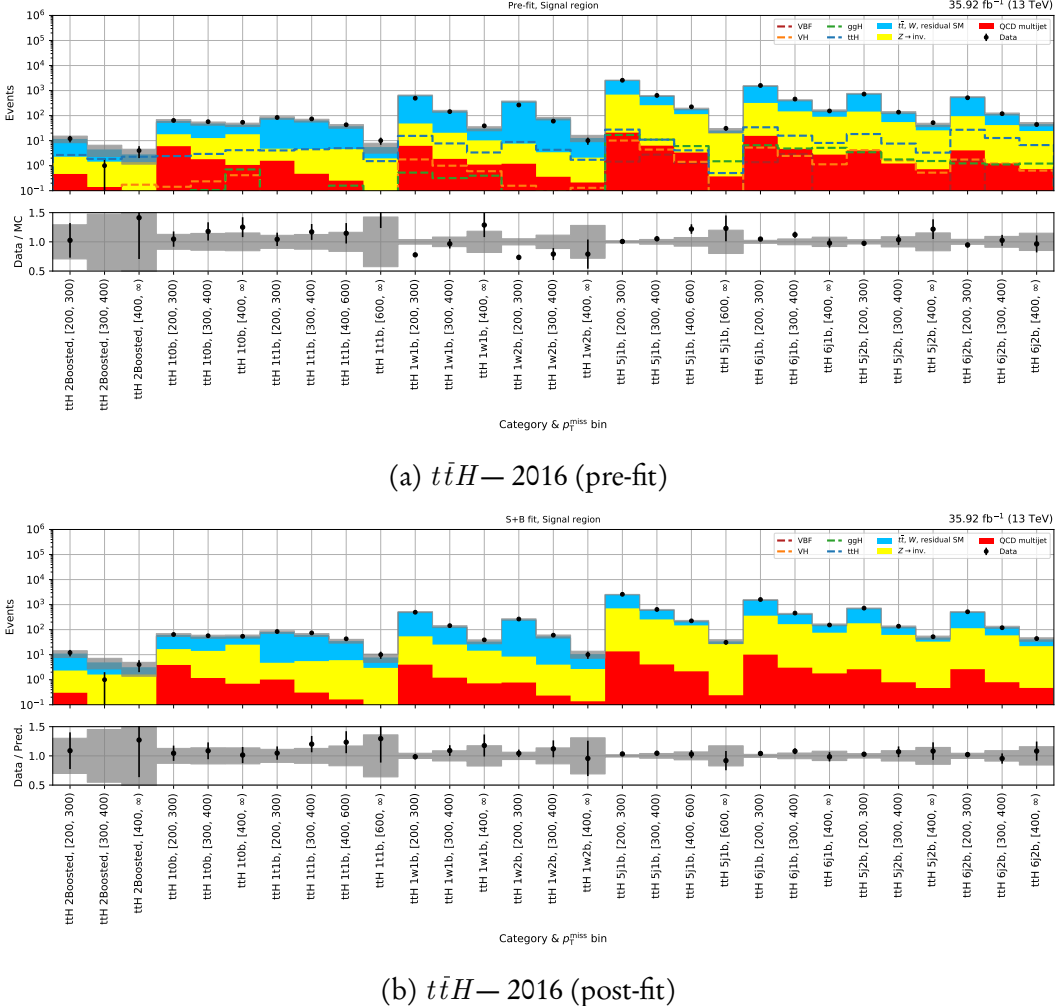


Figure 6.19: Pre-fit and post-fit yields in the signal region for each $t\bar{t}H$ subcategory and p_T^{miss} bin for the 2016 dataset. In bottom panel of post-fit plot, the ratio of data to signal plus background is calculated.

6.9. ANALYSIS OF THE $t\bar{t}H$ MODE

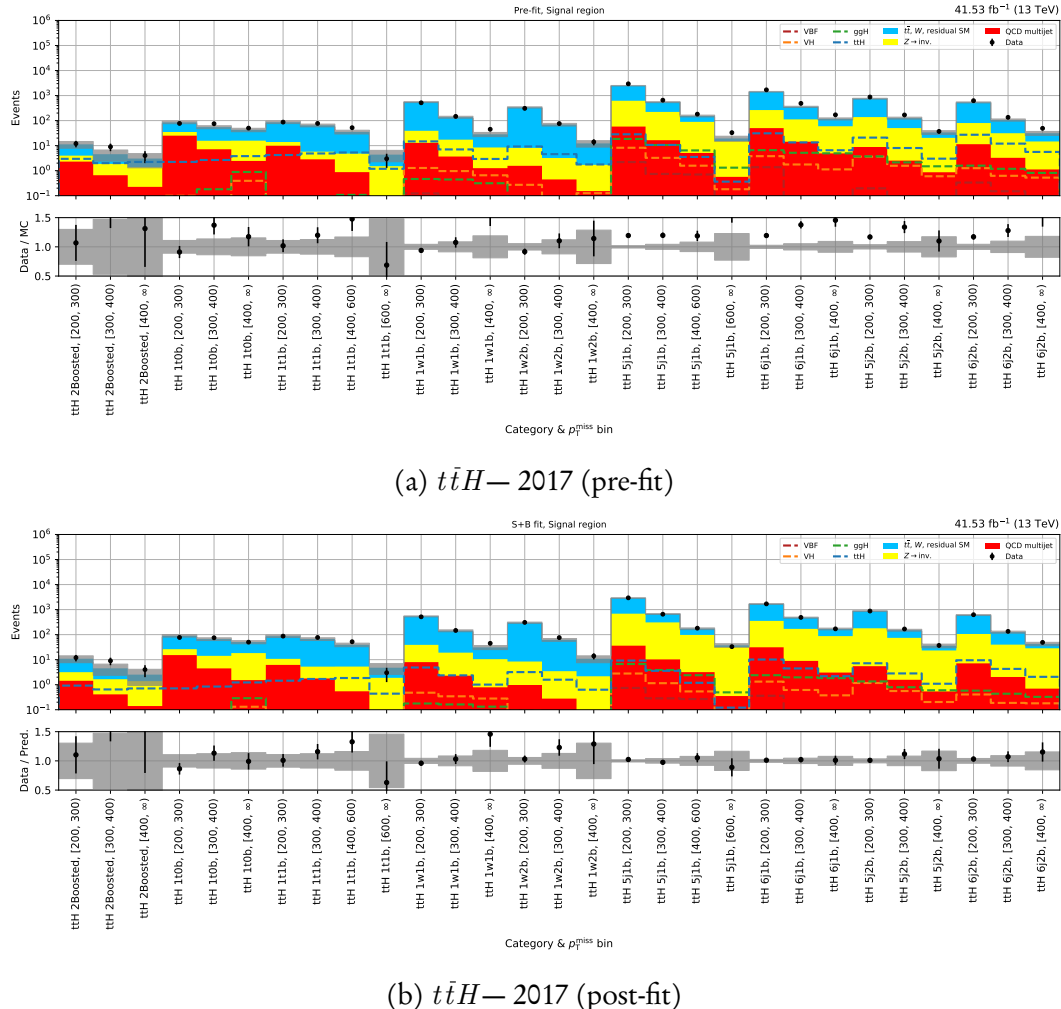


Figure 6.20: Pre-fit and post-fit yields in the signal region for each $t\bar{t}H$ subcategory and p_T^{miss} bin for the 2017 dataset. In bottom panel of post-fit plot, the ratio of data to signal plus background is calculated.

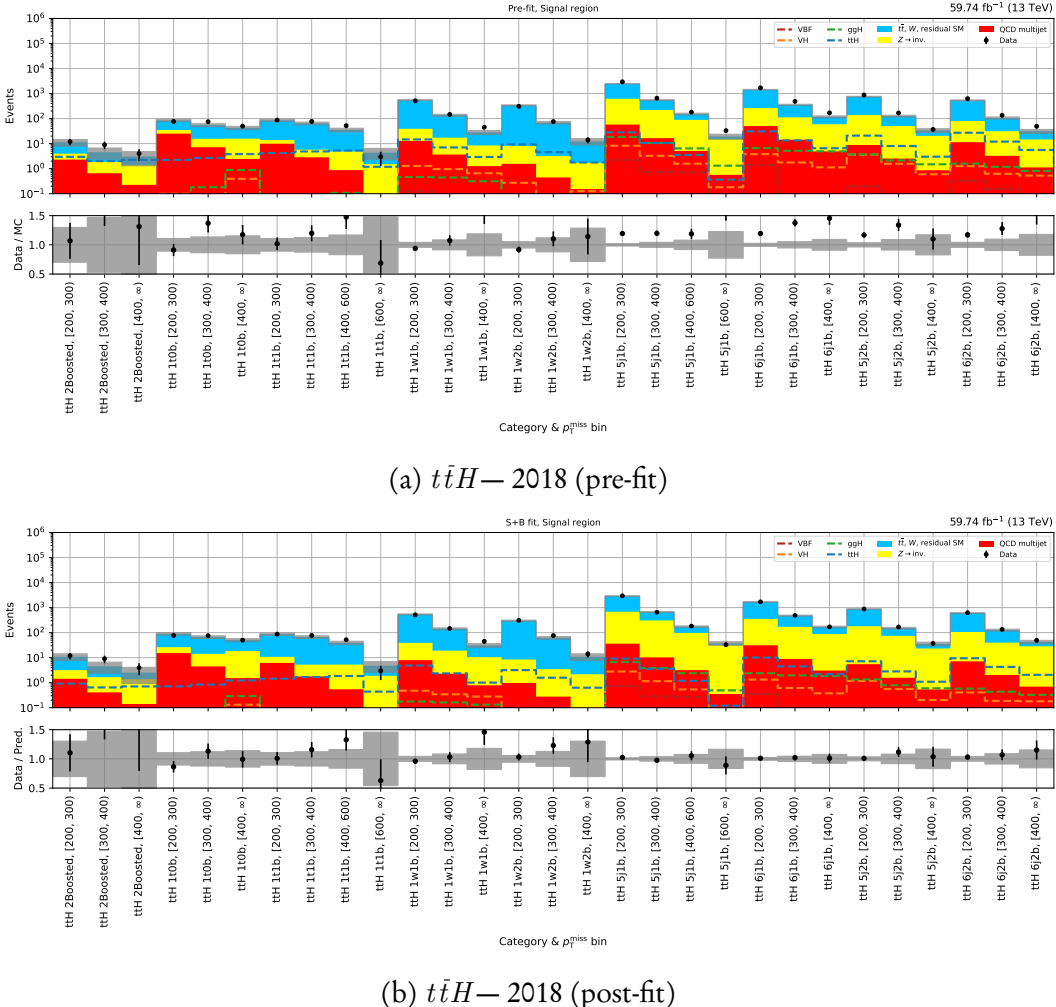


Figure 6.21: Pre-fit and post-fit yields in the signal region for each $t\bar{t}H$ subcategory and p_T^{miss} bin for the 2018 dataset. In bottom panel of post-fit plot, the ratio of data to signal plus background is calculated.

6.10 Analysis of the VH mode

Contrary to $t\bar{t}H$, all of the control regions are utilised in the non-multijet background predictions with a fully granular correspondence to the signal region.²⁴

Fig. 6.22 showcases the expected and observed limits for the VH subcategories and their combination for each data taking year as well the result for the full Run-2 dataset.

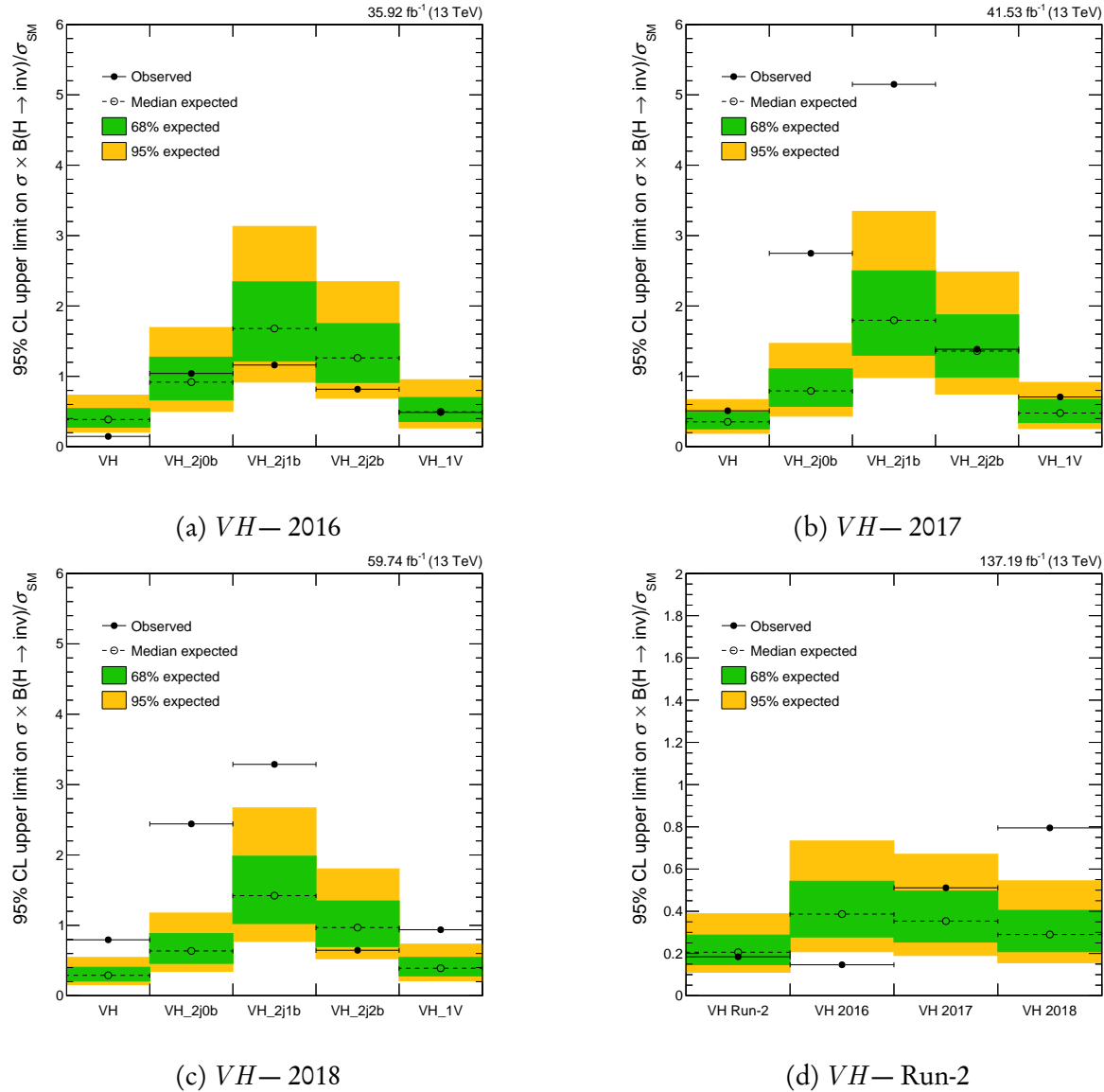


Figure 6.22: Observed and expected 95 % CL upper limits on the Higgs boson to invisible state branching fraction in the VH category, for both the individual subcategories, and the combination of them, for each data-taking year in Run-2.

²⁴ Add a sentence or two about how QCD prediction is done. Might be different from ttH .

Distributions of the pre-fit and post-fit yields for 2016, 2017, and 2018 are displayed in Figs. 6.23, 6.24, and 6.25, respectively. Corresponding figures for the control regions are given in App. A.2.

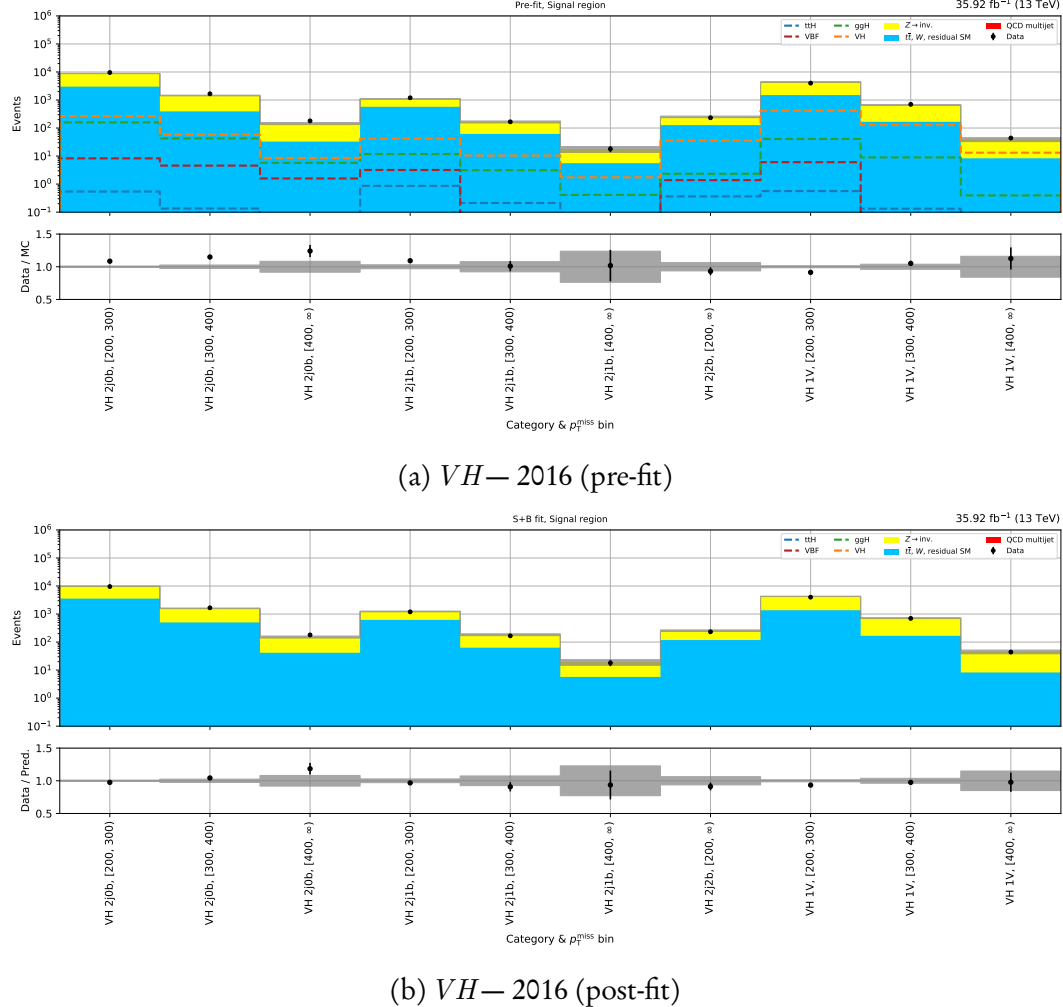


Figure 6.23: Pre-fit and post-fit yields in the signal region for each VH subcategory and p_T^{miss} bin for the 2016 dataset. In bottom panel of post-fit plot, the ratio of data to signal plus background is calculated.

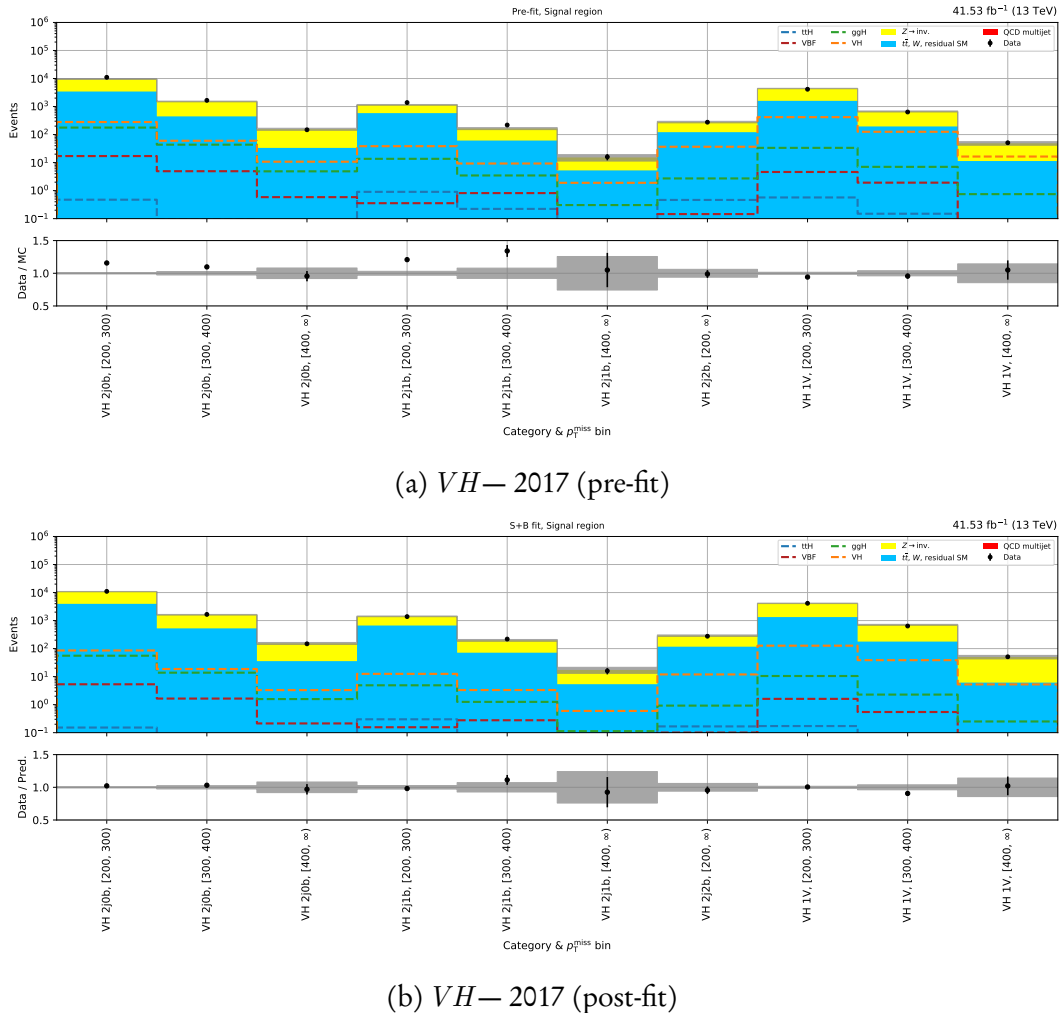


Figure 6.24: Pre-fit and post-fit yields in the signal region for each VH subcategory and p_T^{miss} bin for the 2017 dataset. In bottom panel of post-fit plot, the ratio of data to signal plus background is calculated.

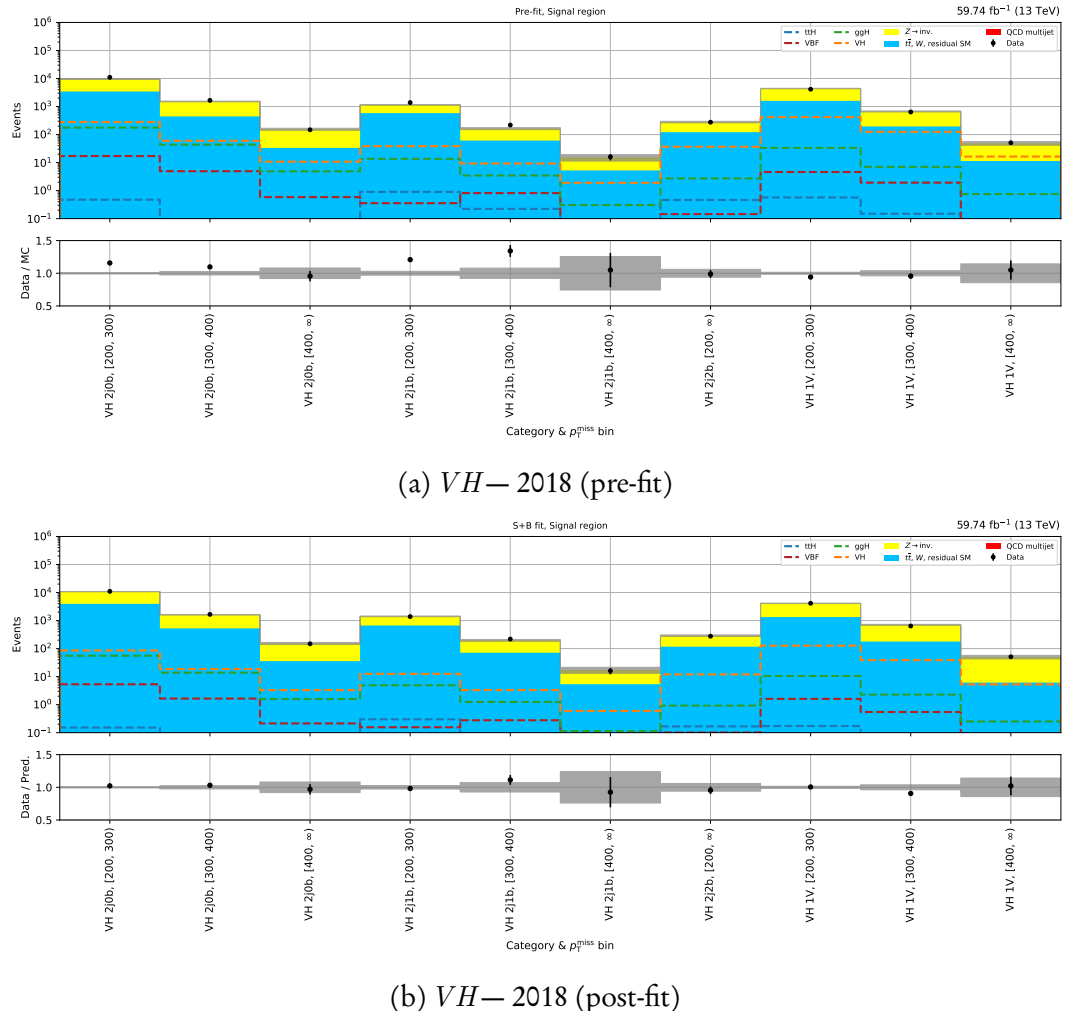


Figure 6.25: Pre-fit and post-fit yields in the signal region for each VH subcategory and p_T^{miss} bin for the 2018 dataset. In bottom panel of post-fit plot, the ratio of data to signal plus background is calculated.

6.11 Analysis of the ggH mode

As with the VH category, all of the control regions are involved in estimating the non-multijet backgrounds in the signal region of the ggH category. Equivalently to $t\bar{t}H$, the QCD presence is derived using the tight and loose double sidebands. The category fractions f_s are calculated by the former, while the remaining terms in Eq. 6.22 are computed from the latter.

Expected and observed limits on the signal strength parameter are presented in Fig. 6.26 for each ggH subcategory and their combination in each data taking year as well as over the full Run-2 dataset.

Distributions of the pre-fit and post-fit yields for 2016, 2017, and 2018 are displayed in Figs. 6.27, 6.28, and 6.29, respectively. Corresponding figures for the control regions are given in App. A.3.

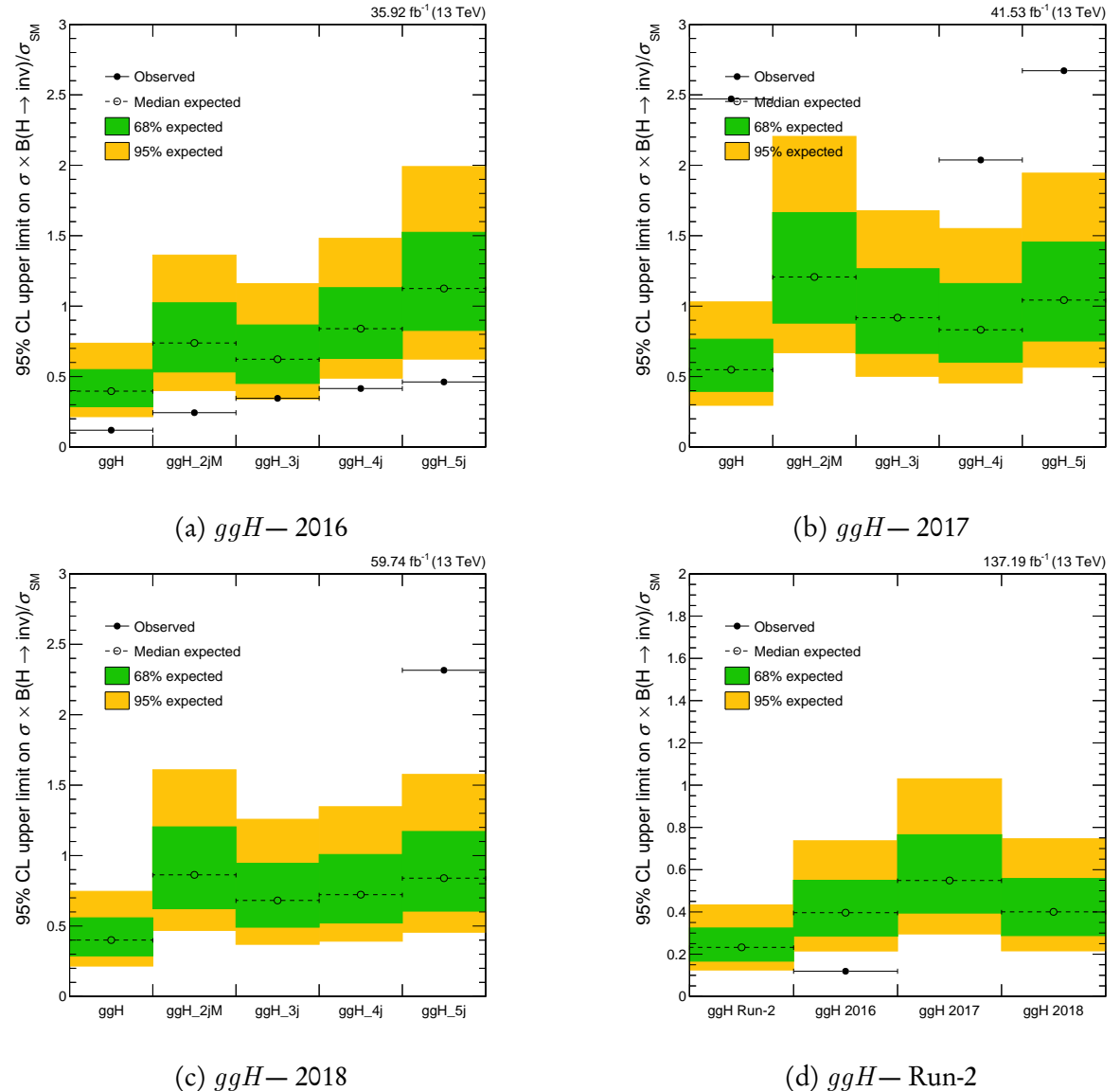


Figure 6.26: Observed and expected 95 % CL upper limits on the Higgs boson to invisible state branching fraction in the ggH category, for both the individual subcategories, and the combination of them, for each data-taking year in Run-2.

6.11. ANALYSIS OF THE ggH MODE

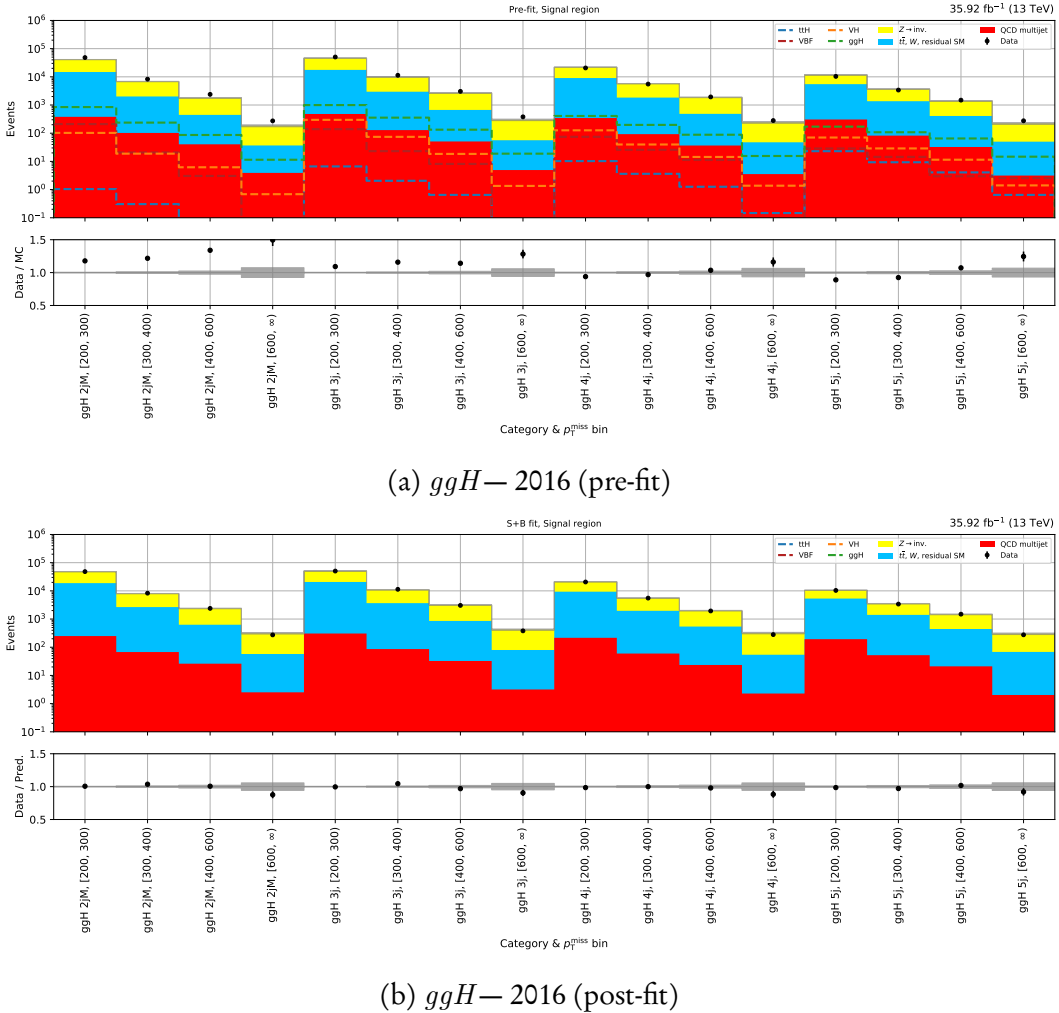


Figure 6.27: Pre-fit and post-fit yields in the signal region for each ggH subcategory and p_T^{miss} bin for the 2016 dataset. In bottom panel of post-fit plot, the ratio of data to signal plus background is calculated.

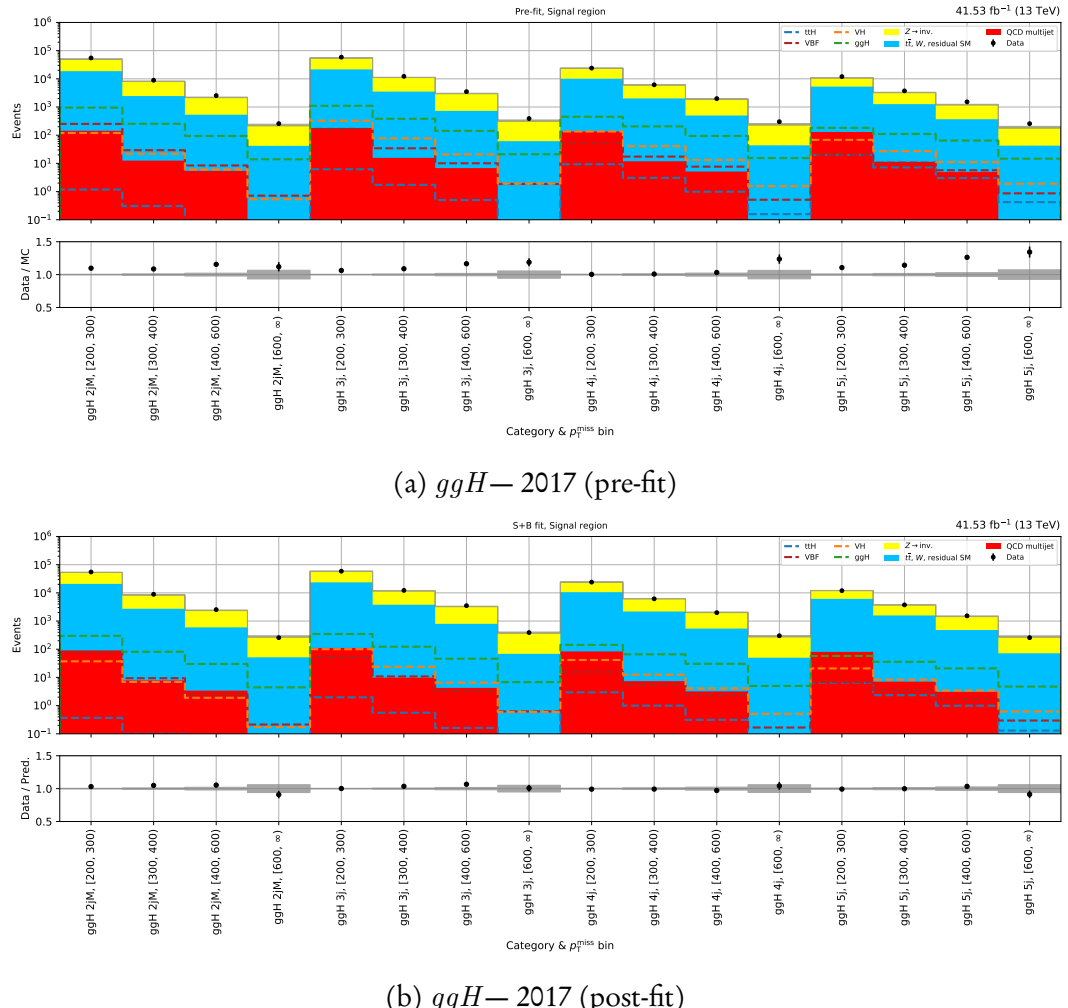


Figure 6.28: Pre-fit and post-fit yields in the signal region for each ggH subcategory and p_T^{miss} bin for the 2017 dataset. In bottom panel of post-fit plot, the ratio of data to signal plus background is calculated.

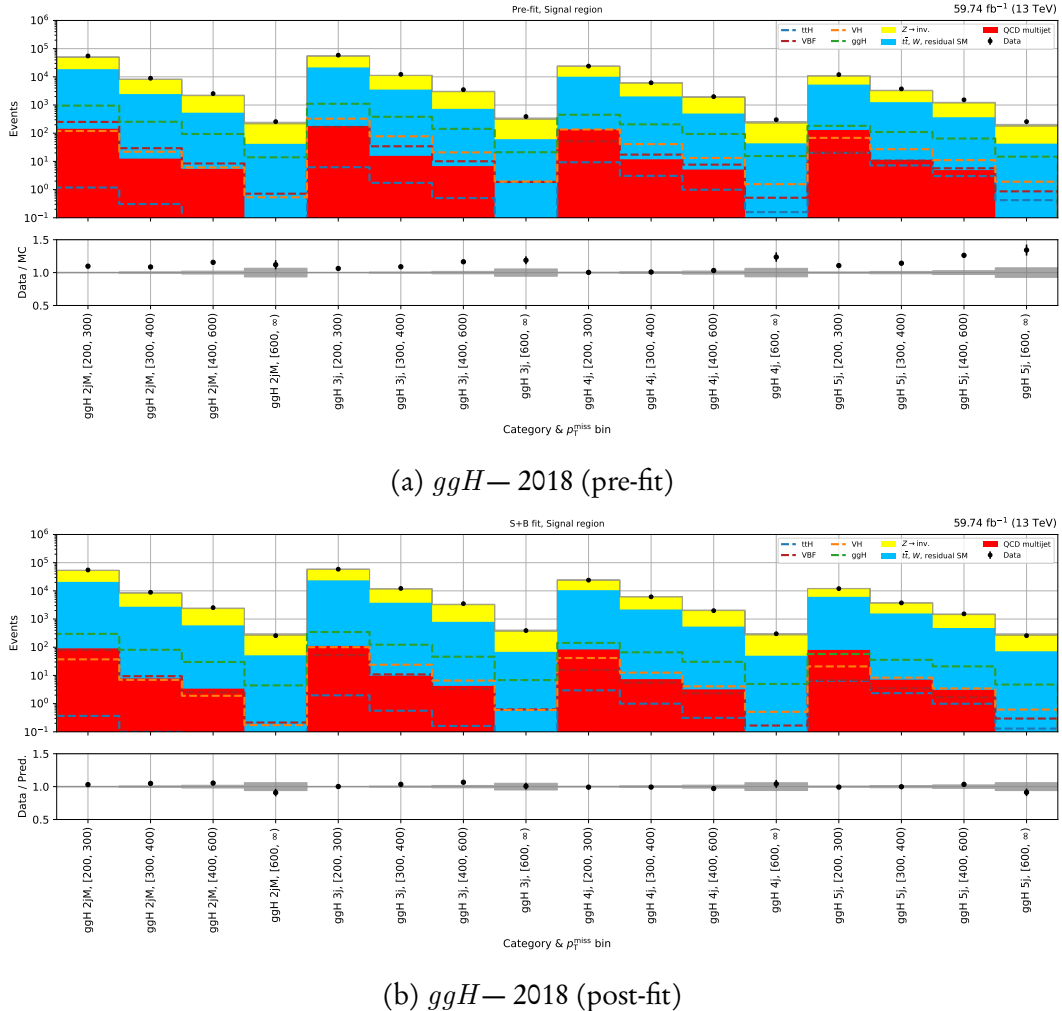


Figure 6.29: Pre-fit and post-fit yields in the signal region for each ggH subcategory and p_T^{miss} bin for the 2018 dataset. In bottom panel of post-fit plot, the ratio of data to signal plus background is calculated.

6.12 Combined results

Upper limits for $\mathcal{B}(H \rightarrow \text{invisible})$ by combining all categories for a given year are given for 2016, 2017, and 2018 in Figs. 6.30, 6.31, 6.32, respectively. For the full Run-2 dataset, they are broken down by data taking year in Fig. 6.33 and by category in Fig. 6.34. Profile likelihood ratios as a function of $\mathcal{B}(H \rightarrow \text{invisible})$ are also presented opposite the limits.

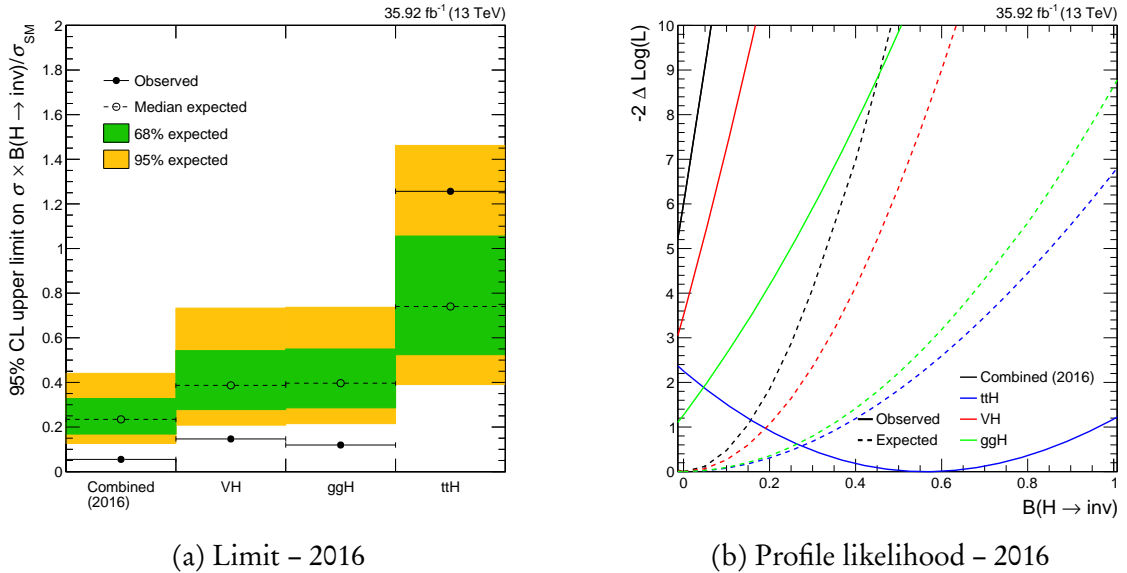
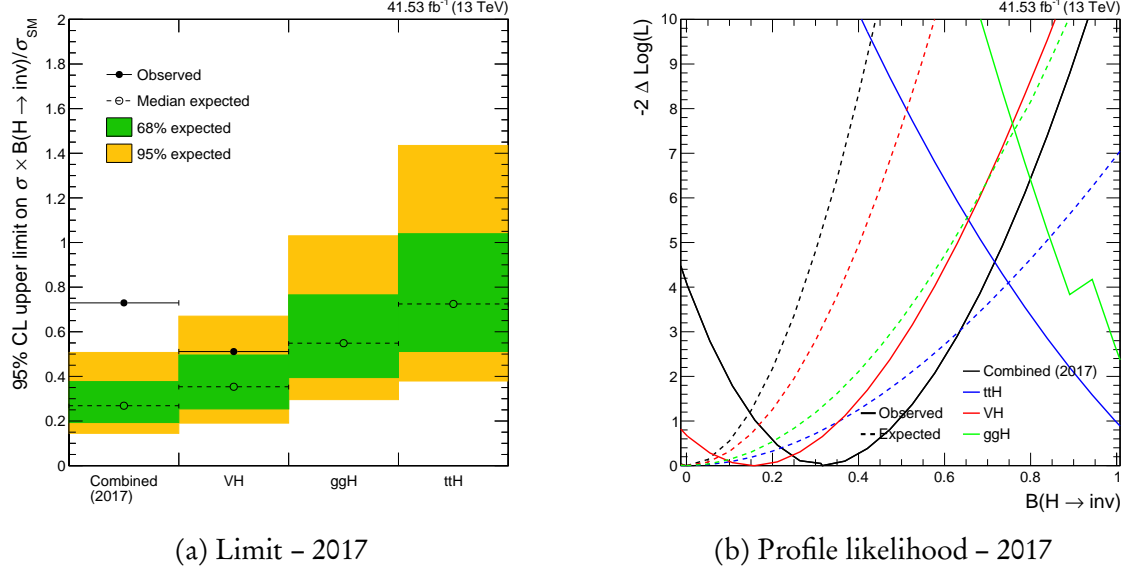


Figure 6.30: Observed and expected 95 % CL upper limit on the Higgs boson to invisible state branching fraction $\mathcal{B}(H \rightarrow \text{invisible})$ (left) and the corresponding profile likelihood ratio as a function of it (right), for both the individual categories that target a specific production mode, as well as the combination of them, for the 2016 dataset. The standard model Higgs boson with its associated mass and production cross section are assumed.

Dataset	$t\bar{t}H$	VH	ggH	Combined
2016	X (obs.)	X (obs.)	X (obs.)	X (obs.)
	69 % (exp.)	43 % (exp.)	48 % (exp.)	29 % (exp.)
2017	X (obs.)	X (obs.)	X (obs.)	X (obs.)
	65 % (exp.)	40 % (exp.)	53 % (exp.)	29 % (exp.)
2018	X (obs.)	X (obs.)	X (obs.)	X (obs.)
	62 % (exp.)	36 % (exp.)	34 % (exp.)	23 % (exp.)
Run-2	X (obs.)	X (obs.)	X (obs.)	X (obs.)
	40 % (exp.)	24 % (exp.)	27 % (exp.)	16 % (exp.)

Table 6.9: Observed and expected upper limits on $\mathcal{B}(H \rightarrow \text{invisible})$ for each category and dataset in the analysis.

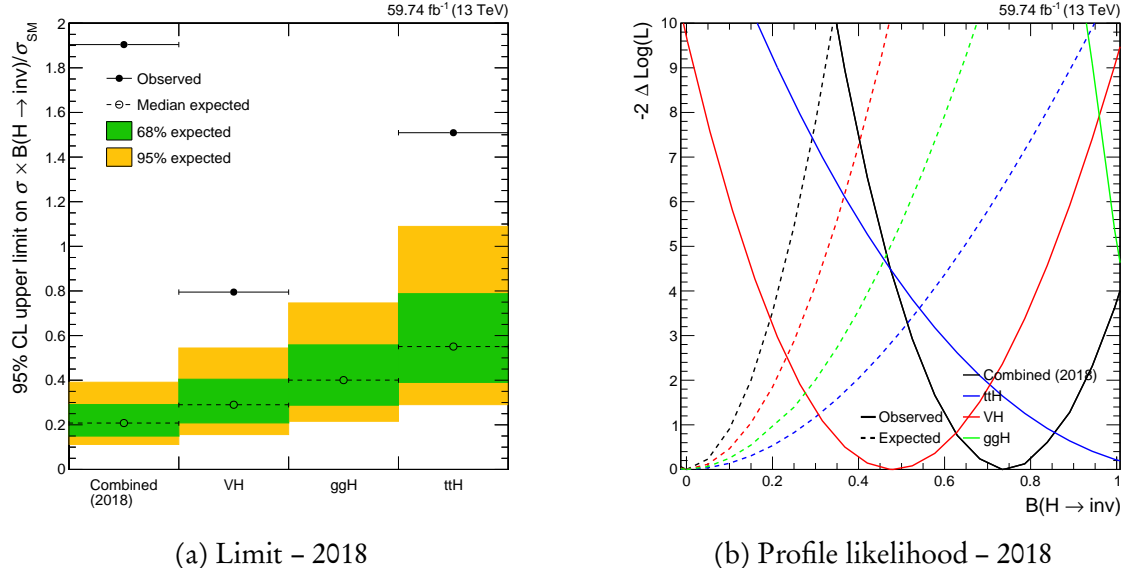
6.12. COMBINED RESULTS



(a) Limit – 2017

(b) Profile likelihood – 2017

Figure 6.31: Observed and expected 95 % CL upper limit on the Higgs boson to invisible state branching fraction $\mathcal{B}(H \rightarrow \text{invisible})$ (left) and the corresponding profile likelihood ratio as a function of it (right), for both the individual categories that target a specific production mode, as well as the combination of them, for the 2017 dataset. The standard model Higgs boson with its associated mass and production cross section are assumed.



(a) Limit – 2018

(b) Profile likelihood – 2018

Figure 6.32: Observed and expected 95 % CL upper limit on the Higgs boson to invisible state branching fraction $\mathcal{B}(H \rightarrow \text{invisible})$ (left) and the corresponding profile likelihood ratio as a function of it (right), for both the individual categories that target a specific production mode, as well as the combination of them, for the 2018 dataset. The standard model Higgs boson with its associated mass and production cross section are assumed.

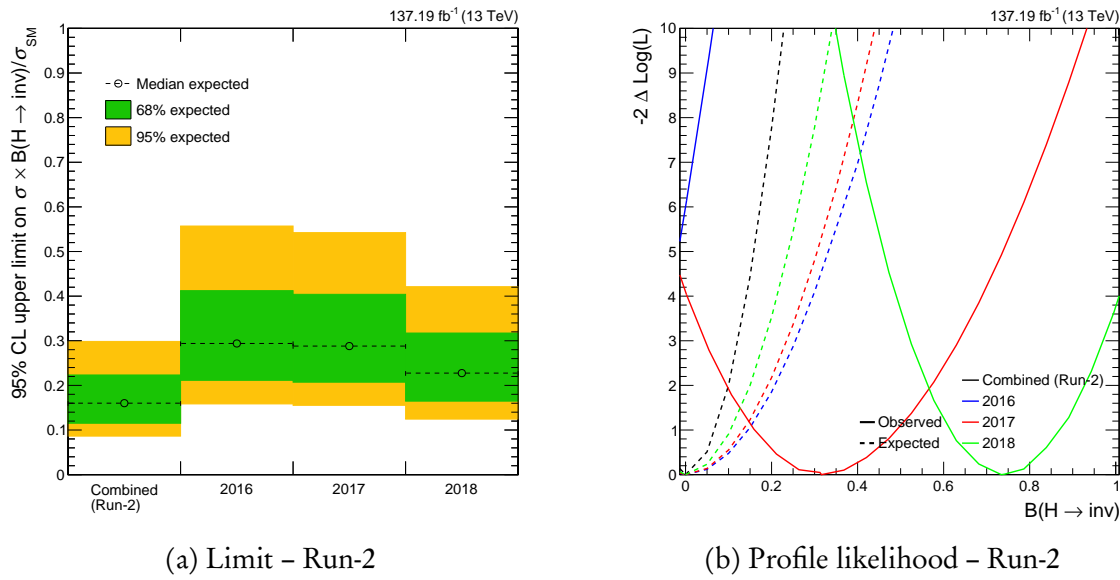


Figure 6.33: Observed and expected 95 % CL upper limit on the Higgs boson to invisible state branching fraction $\mathcal{B}(H \rightarrow \text{invisible})$ (left) and the corresponding profile likelihood ratio as a function of it (right), for both the individual data taking years, as well as the combination of them, for the full Run-2 dataset. The standard model Higgs boson with its associated mass and production cross section are assumed.

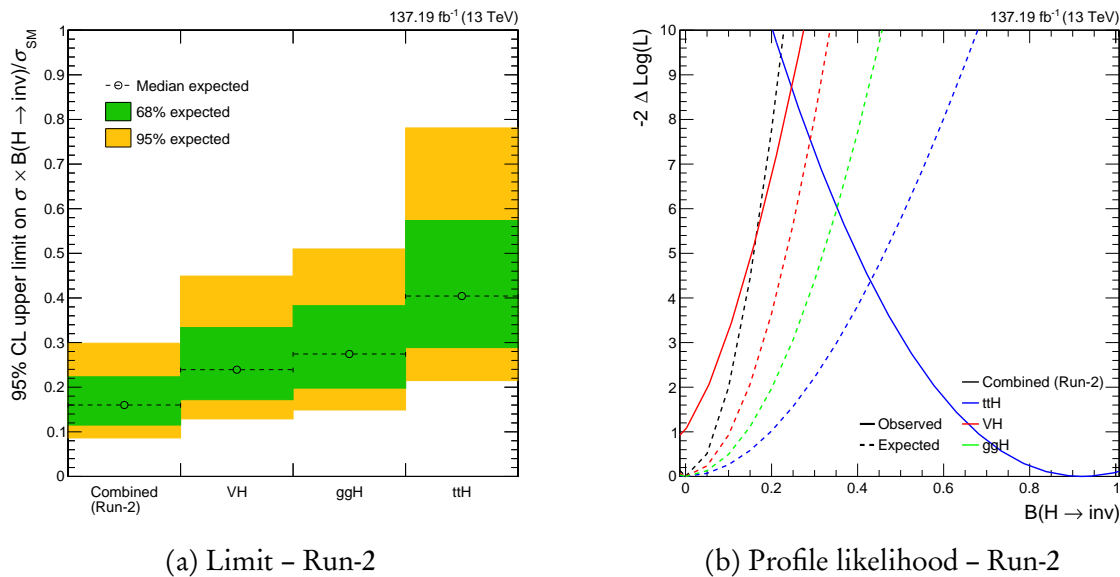


Figure 6.34: Observed and expected 95 % CL upper limit on the Higgs boson to invisible state branching fraction $\mathcal{B}(H \rightarrow \text{invisible})$ (left) and the corresponding profile likelihood ratio as a function of it (right), for both the individual categories, as well as the combination of them, for the full Run-2 dataset. The standard model Higgs boson with its associated mass and production cross section are assumed.

6.13 Interpretations in simplified dark matter scenarios

The results of the analysis fail to accurately constrain the branching ratio on the Higgs boson to invisible state decays, with a value XXX times that of the standard model and no observation of the process. However, limits on certain properties of dark matter may be set. Two BSM interpretations are presented: a Higgs portal model where the SM acts as the mediator, and the existence of an additional, invisibly decaying, SM-like Higgs boson.

6.13.1 Higgs portal model with the standard model Higgs boson

One interpretation of our results may be in terms of a simplified Higgs portal model—coupling the dark sector to the visible where the SM Higgs boson acts as the mediator bridging them. An effective field theory approach assumes that the invisible decays of the Higgs boson results in the pair production of dark matter particles χ , with a frequency constrained by the upper limit on $\mathcal{B}(H \rightarrow \text{invisible})$. If $m_\chi < m_H/2$, on-shell production allows the translation of the $H \rightarrow \text{invisible}$ width $\Gamma_{\text{inv.}}$ into the spin-independent χ -nucleon scattering cross section σ_{SI} , as in Ref. 76. The interaction between dark and baryonic matter may be mediated by a Higgs boson, making direct detection experiments particularly sensitive to the recoil. The sensitivity of these experiments is typically parametrised by σ_{SI} as a function of dark matter mass m_χ . Comparisons can therefore be made between direct detection and collider experiments.

In this Higgs portal model, two cases are considered: the dark matter candidate is a scalar, or a Majorana fermion. The branching ratio is $\mathcal{B}(H \rightarrow \text{invisible}) = \Gamma_{\text{inv.}}/(\Gamma_{\text{SM}} + \Gamma_{\text{inv.}})$, where we assume $\Gamma_{\text{SM}} = 4.07 \text{ MeV}$ [91]. From Ref. 76, $\Gamma_{\text{inv.}}$ can be calculated for scalar χ_S and fermion dark matter χ_f as

$$(6.24) \quad \begin{aligned} \Gamma_{H \rightarrow \chi_S \chi_S}^{\text{inv.}} &= \frac{\lambda_{HSS}^2 v^2 \beta_S}{64\pi m_H}, \\ \Gamma_{H \rightarrow \chi_f \chi_f}^{\text{inv.}} &= \frac{\lambda_{Hff}^2 v^2 m_H \beta_f^3}{32\pi \Lambda^2} \end{aligned}$$

where λ is the coupling (scaled by Λ in the case of fermions)²⁵, v is the vacuum expectation value of the SM Higgs field, and $\beta_i = \sqrt{1 - 4m_{\chi_i}^2/m_H^2}$. The masses of the dark matter particles m_{dark} are the physical masses after electroweak symmetry breaking with this new Higgs

²⁵Is Λ some sort of scale, similar to Λ_{QCD} ?

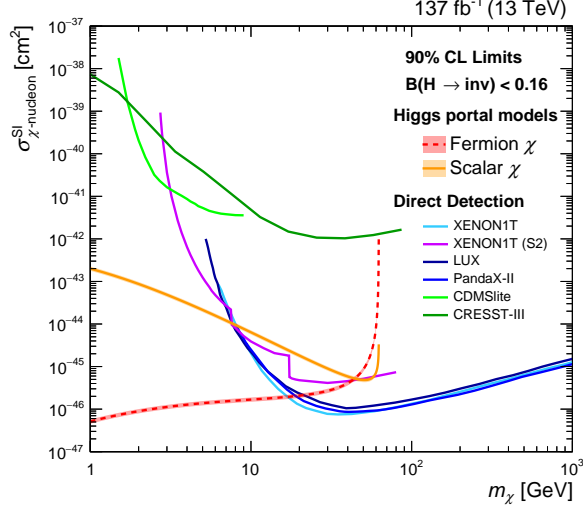


Figure 6.35: 90 % confidence level upper limits on the spin-independent dark matter-nucleon scattering cross section in Higgs portal models, where the standard model Higgs boson decays into a pair of scalar (solid orange) or fermion (dashed red) dark matter particles. Comparisons to direct detection experiments are also provided: XENON1T [18] (additionally with the S2-only analysis [19]), LUX [12], PandaX-II [72], CDMSlite [9], and CRESST-III [6].

field. The spin-independent χ -nucleon scattering cross sections are

$$(6.25) \quad \begin{aligned} \sigma_{\chi_S-N}^{\text{SI}} &= \frac{\lambda_{HSS}^2}{16\pi m_H^4} \frac{m_N^4 f_N^2}{(m_{\chi_S} + m_N)^2}, \\ \sigma_{\chi_f-N}^{\text{SI}} &= \frac{\lambda_{Hff}^2}{4\pi \Lambda^2 m_H^4} \frac{m_N^4 m_{\chi_f}^2 f_N^2}{(m_{\chi_f} + m_N)^2} \end{aligned}$$

where f_N parametrises the Higgs-nucleon coupling. The value $f_N = 0.308 \pm 0.018$ is taken from Ref. 95, recommended over that proposed in Ref. 76. Limits on these cross sections as a function of dark matter mass are displayed in Fig. 6.35,²⁶ computed at 90 % confidence level to compare with direct detection experiments, whose latest results are also presented.

For $\mathcal{B}(H \rightarrow \text{invisible}) < XX$, the Higgs portal models assuming scalar and fermion dark matter candidates set the lowest limits on σ_{SI} for m_χ below Y and Z GeV, respectively.

6.13.2 Constraints on a standard model-like Higgs boson

If the SM Higgs boson does not decay into invisible particles beside the neutrino, one may still hypothesize a scenario in which the Higgs field is associated with dark matter. The

²⁶The plot is a placeholder for now, since we don't have final non-VBF/combined limits.

next-to-minimal branch of supersymmetry and models with two Higgs doublets are examples that accommodate an additional Higgs boson with a different mass that does not couple to the SM variant. It is denoted as “standard model-like,” since it may be produced via the same mechanisms as the SM Higgs boson ($t\bar{t}H$, VH , ggH , and VBF) with the same relative contributions from each one. This extra Higgs is assumed to decay exclusively to invisible states.

We perform our analysis where we assume an additional Higgs boson, and show the limit on the branching ratio as a function of mass.

CONCLUSIONS

Satisfaction lies in the effort, not in the attainment.

— Mahatma Gandhi

Scientific research can often be imagined as searching for bright city lights at the end of a dimly-lit, winding road. One hopes to reach it quickly with minimal setbacks. Despite somewhat stumbling in the dark and following the faintest strands, and unexpected twists and turns, progress is made through effort and determination even if the destination seems still out of sight. Reflecting on the work carried out over the course of this PhD and documented in this thesis, the seemingly unscalable wall that is the nature of dark matter has been modestly chipped away.¹

7.1 $H \rightarrow \text{invisible}$

Constraining the Higgs boson to invisible state branching ratio is important in understanding whether it couples to dark matter at all, and if so how strongly. The measurement can also refute or restrict the viability of several dark matter models. From the analysis in Chpt. 6 utilising the full Run-2 dataset from CMS, a combined upper limit on $\sigma \times \mathcal{B}(H \rightarrow \text{invisible})/\sigma_{\text{SM}}$ of XX was observed at 95 % confidence level, and YY expected in the background-only hypo-

¹Not sure if it's worth making a combined "Results and conclusions" chapter, rather than having results at the end of the Hinv chapter and a relatively short conclusions one.

thesis. While still far above the standard model prediction of 0.1 %, significant improvements have been made with respect to those obtained from Run-1 or 2016-only data.²

Further improvements from a full combination over all Higgs production modes are inevitable. Given VBF is the most sensitive channel—and leptonic final states such as Ref. 83 have been discussed little—a grand combination with the other full Run-2 analyses will provide a much stronger limit. If there is a significant enhancement to the SM value of $\mathcal{B}(H \rightarrow \text{invisible})$ due to a coupling to dark matter, it may be observable at the HL-LHC. The volume of available data is expected to increase by more than ten times. Coupled with improvements to the CMS detector for improved particle identification, noise mitigation, higher bandwidth links to read out more detector information, and more precise measurements of particle properties, a promising result is within the realm of possibility.³ New and improved machine learning algorithms, for example to tag resolved decays of the top quark, and more generally to discriminate signal from background, will also contribute. In summary, advancements in several areas can each incrementally boost the sensitivity to this process.

Failing any enhancement from a dark matter coupling, observing the SM rate of $H \rightarrow 4\nu$ may require a precision-focused experiment. FCC-*ee* and the ILC are strong candidates. Such “Higgs factories” would produce large quantities of Higgs bosons in e^+e^- collisions predominantly through the VH and VBF mechanisms.

7.2 Semi-visible jets

The search for semi-visible jets pushes into unexplored territory. This novel array of theoretical models—with final states overlooked by most dark matter searches—provides a rich and diverse playground with many avenues to consider. Only a small fraction of signal models for the s - and t -channel production mechanisms were analysed in Chpt. 5. However, their characteristics suggest unique signatures compared to the expected standard model background and can be exploited with variables as simple as m_T .

The analysis focused on the s -channel mode, performed by collaborators in CMS, is nearing completion at the time of writing. A dedicated search for the t -channel mechanism has recently begun, as well as for semi-visible jets originating from the decays of boosted Z' bosons. Any of these could yield important results with the full Run-2 dataset. With the aid of Run-3 and HL-LHC data, and the other experimental improvements noted above, the

²Make quantitative comparisons between previous results and mine. Add info about dark matter interpretations as well.

³Maybe say something about work in JECs? Weaving it into the talk about detector upgrades improving sensitivity.

boundaries will be further pushed. More advanced and versatile tagging algorithms could categorise a wide range of signal-like topologies while rejecting background to a larger degree. Higher energy future colliders, such as FCC–hh would widen the search window. Mediator masses up to several tens of TeV could be probed, with a commensurate increase to the dark quark mass range. Additional topologies arising from variations of the s - and t -channel modes, such as searches for displaced vertices/long-lived particles, open an even greater assortment of avenues to explore.



POST-FIT DISTRIBUTIONS FROM THE HIGGS TO INVISIBLE ANALYSIS

To avoid detracting too much from the predominant results in Chpt. 6, some figures were omitted from the main text. The following sections illustrate the post-fit distributions in the control regions for each subcategory and p_T^{miss} bin, and for each data taking period. While the yields for each process are post-fit, the total background pre-fit is also displayed for comparisons to data as well as the post-fit prediction. App. A.1, A.2, and A.3 contain the distributions for the $t\bar{t}H$, VH , and ggH categories, respectively.

A.1 Post-fit distributions of the control regions in the $t\bar{t}H$ category

APPENDIX A. POST-FIT DISTRIBUTIONS FROM THE HIGGS TO INVISIBLE ANALYSIS

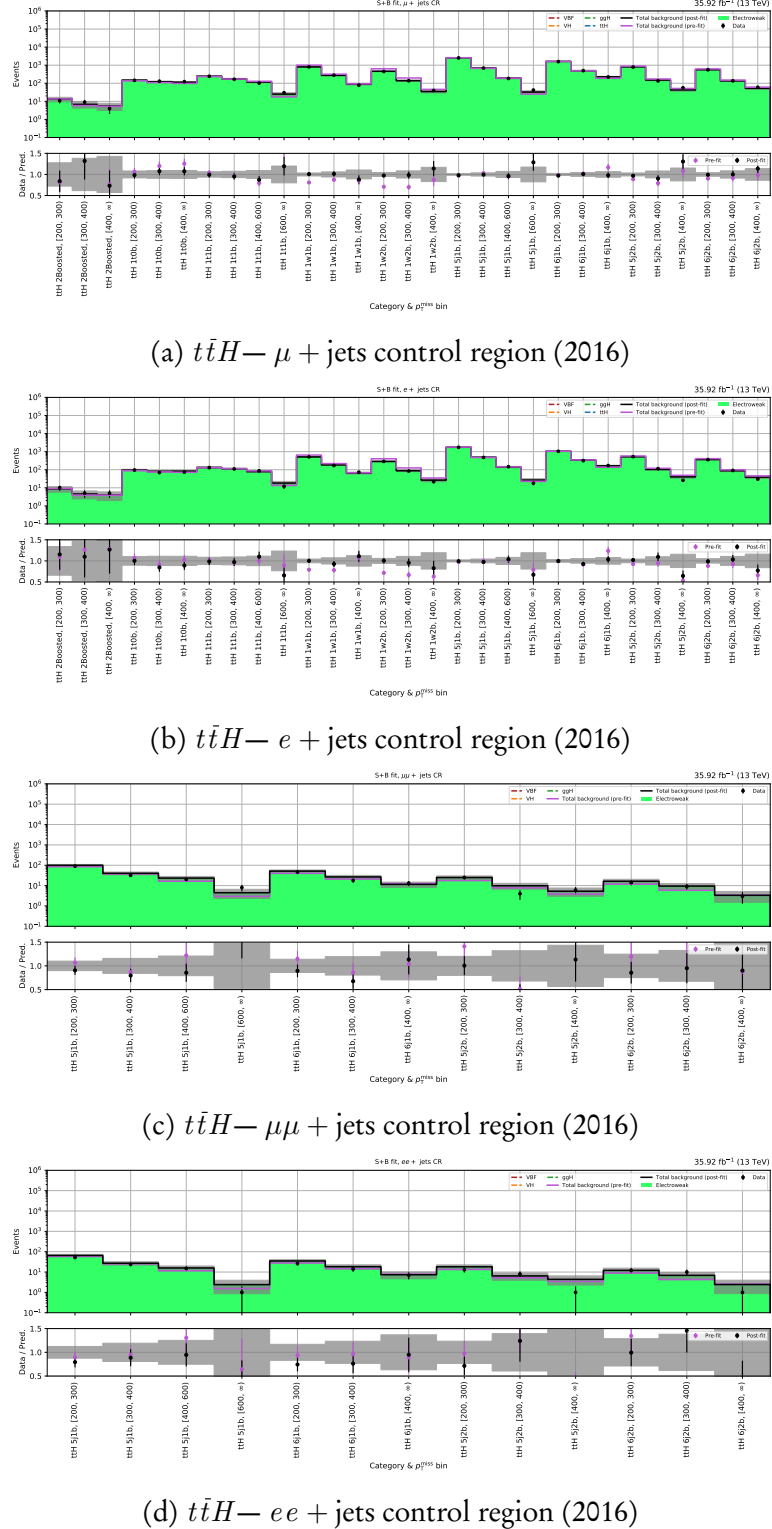


Figure A.1: Post-fit yields for each $t\bar{t}H$ subcategory and p_T^{miss} bin in the lepton control regions for the 2016 dataset. The total background pre-fit and post-fit is compared to data in the lower panel of each subfigure.

A.1. POST-FIT DISTRIBUTIONS OF THE CONTROL REGIONS IN THE $t\bar{t}H$ CATEGORY

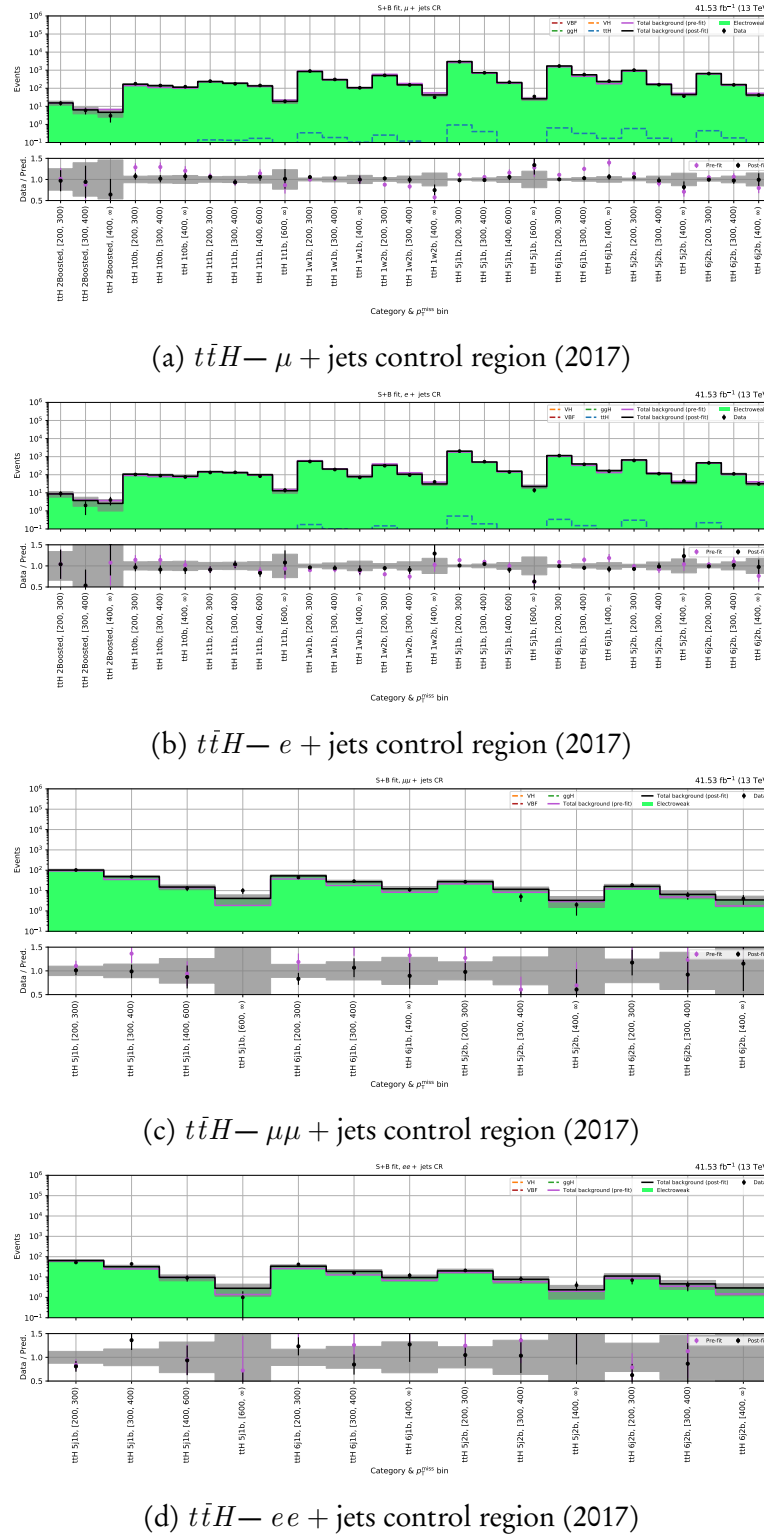


Figure A.2: Post-fit yields for each $t\bar{t}H$ subcategory and p_T^{miss} bin in the lepton control regions for the 2017 dataset. The total background pre-fit and post-fit is compared to data in the lower panel of each subfigure.

APPENDIX A. POST-FIT DISTRIBUTIONS FROM THE HIGGS TO INVISIBLE ANALYSIS

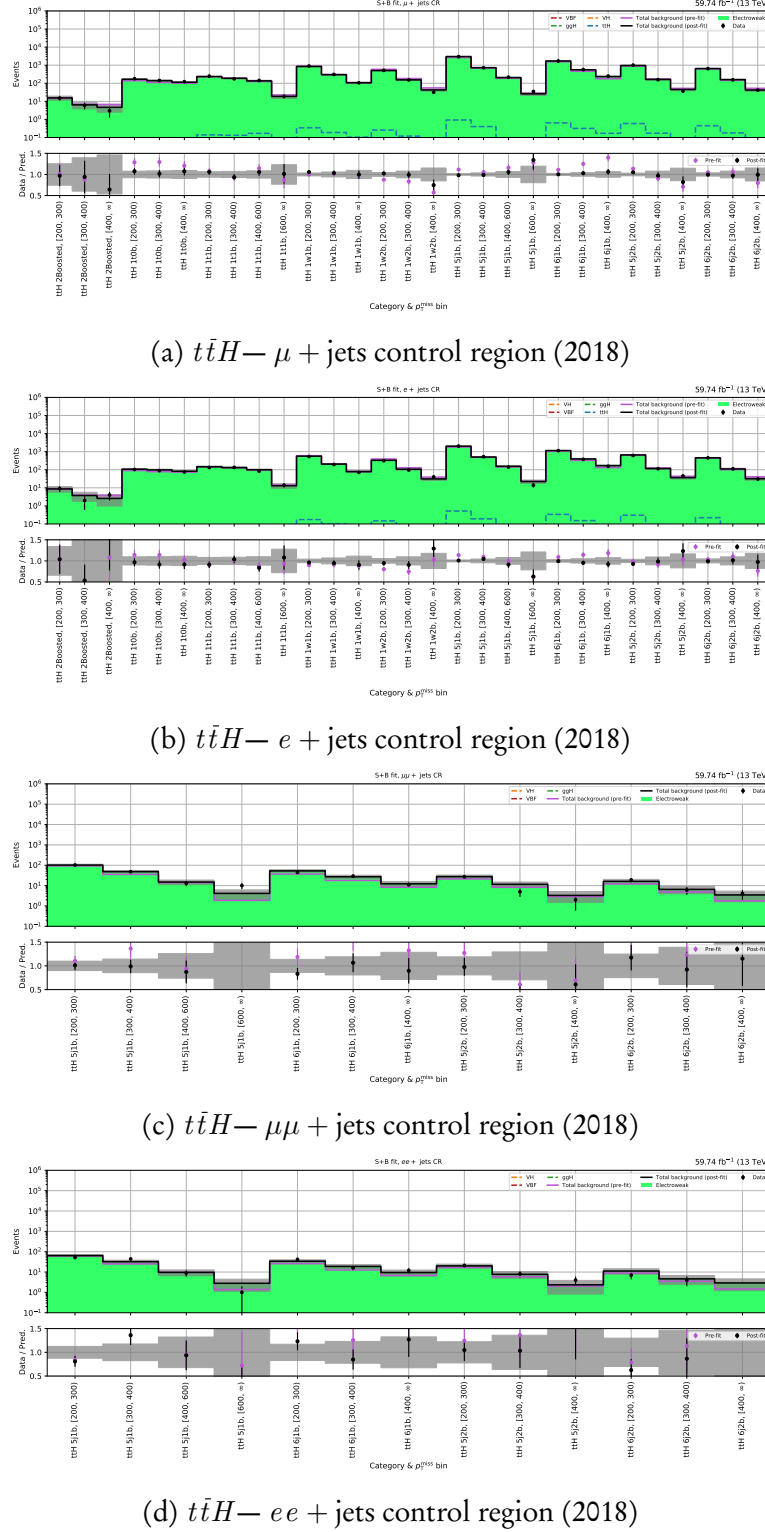


Figure A.3: Post-fit yields for each $t\bar{t}H$ subcategory and p_T^{miss} bin in the lepton control regions for the 2018 dataset. The total background pre-fit and post-fit is compared to data in the lower panel of each subfigure.

A.2. POST-FIT DISTRIBUTIONS OF THE CONTROL REGIONS IN THE VH CATEGORY

A.2 Post-fit distributions of the control regions in the VH category

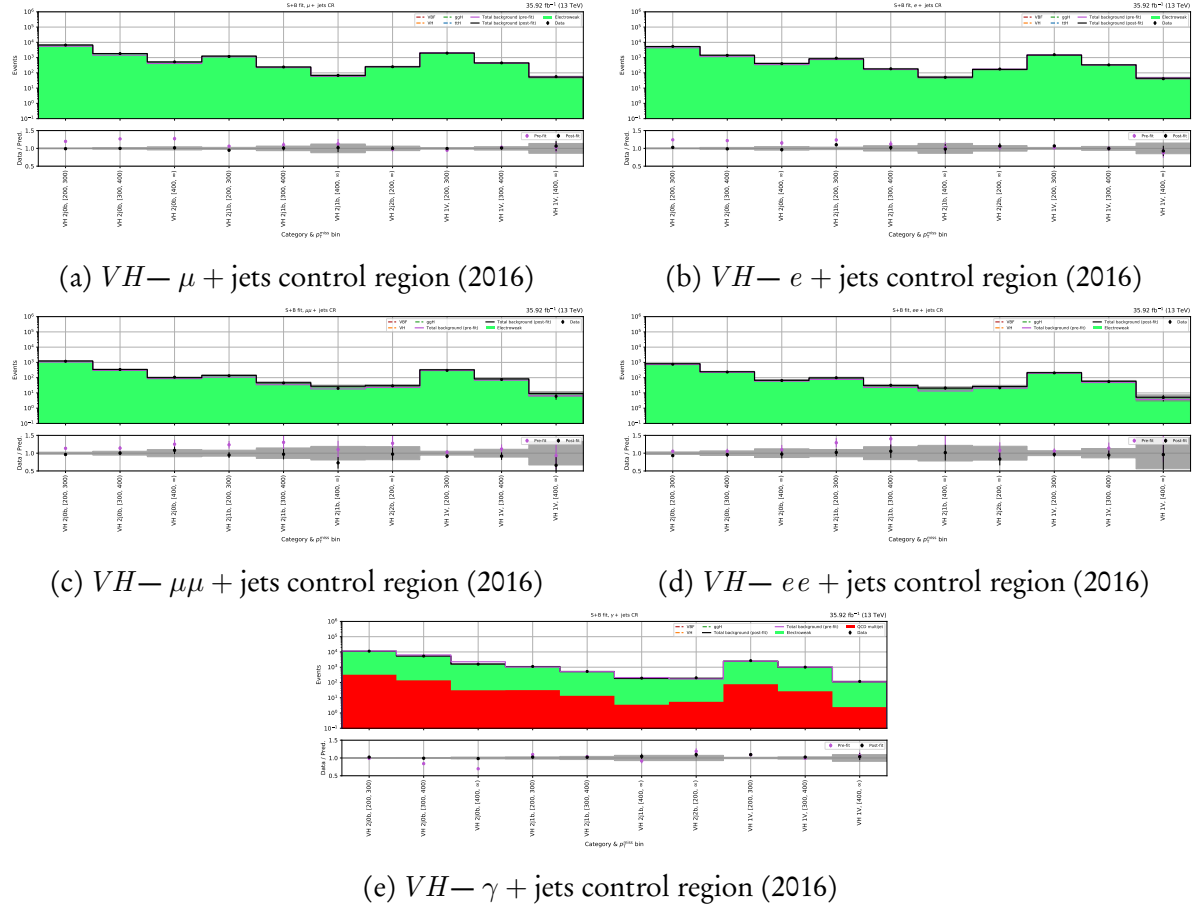


Figure A.4: Post-fit yields for each VH subcategory and p_T^{miss} bin in the lepton and photon control regions for the 2016 dataset. The total background pre-fit and post-fit is compared to data in the lower panel of each subfigure.

APPENDIX A. POST-FIT DISTRIBUTIONS FROM THE HIGGS TO INVISIBLE ANALYSIS

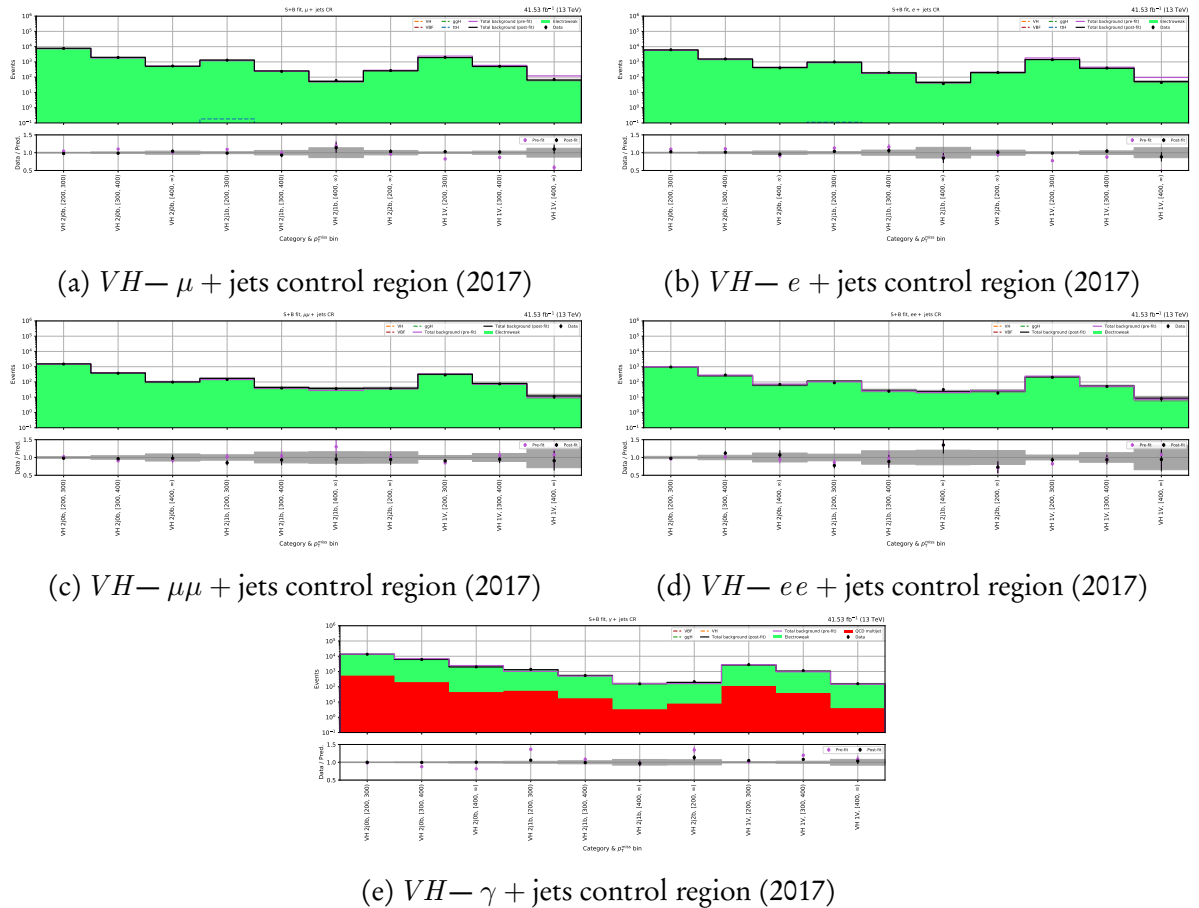


Figure A.5: Post-fit yields for each VH subcategory and p_T^{miss} bin in the lepton and photon control regions for the 2017 dataset. The total background pre-fit and post-fit is compared to data in the lower panel of each subplot.

A.2. POST-FIT DISTRIBUTIONS OF THE CONTROL REGIONS IN THE VH CATEGORY

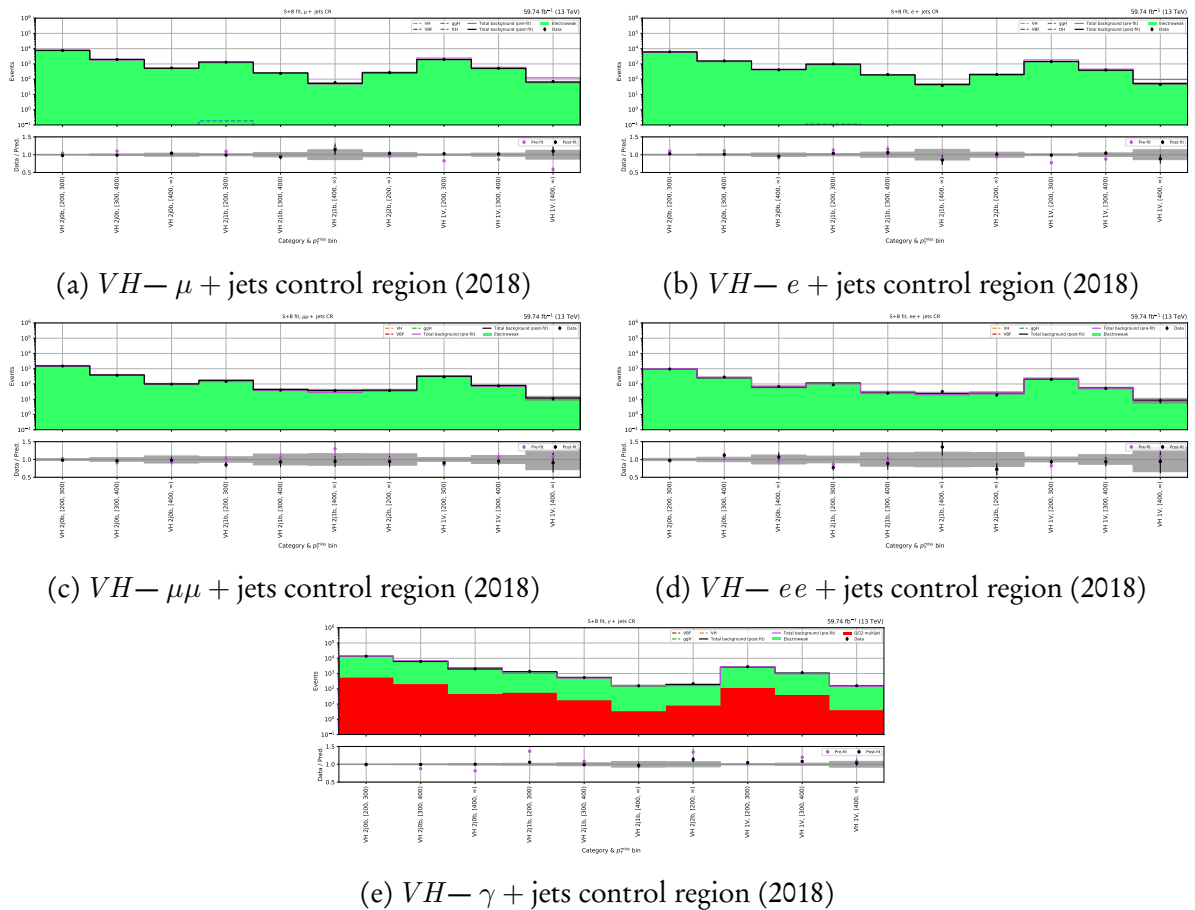


Figure A.6: Post-fit yields for each VH subcategory and p_T^{miss} bin in the lepton and photon control regions for the 2018 dataset. The total background pre-fit and post-fit is compared to data in the lower panel of each subfigure.

A.3 Post-fit distributions of the control regions in the ggH category

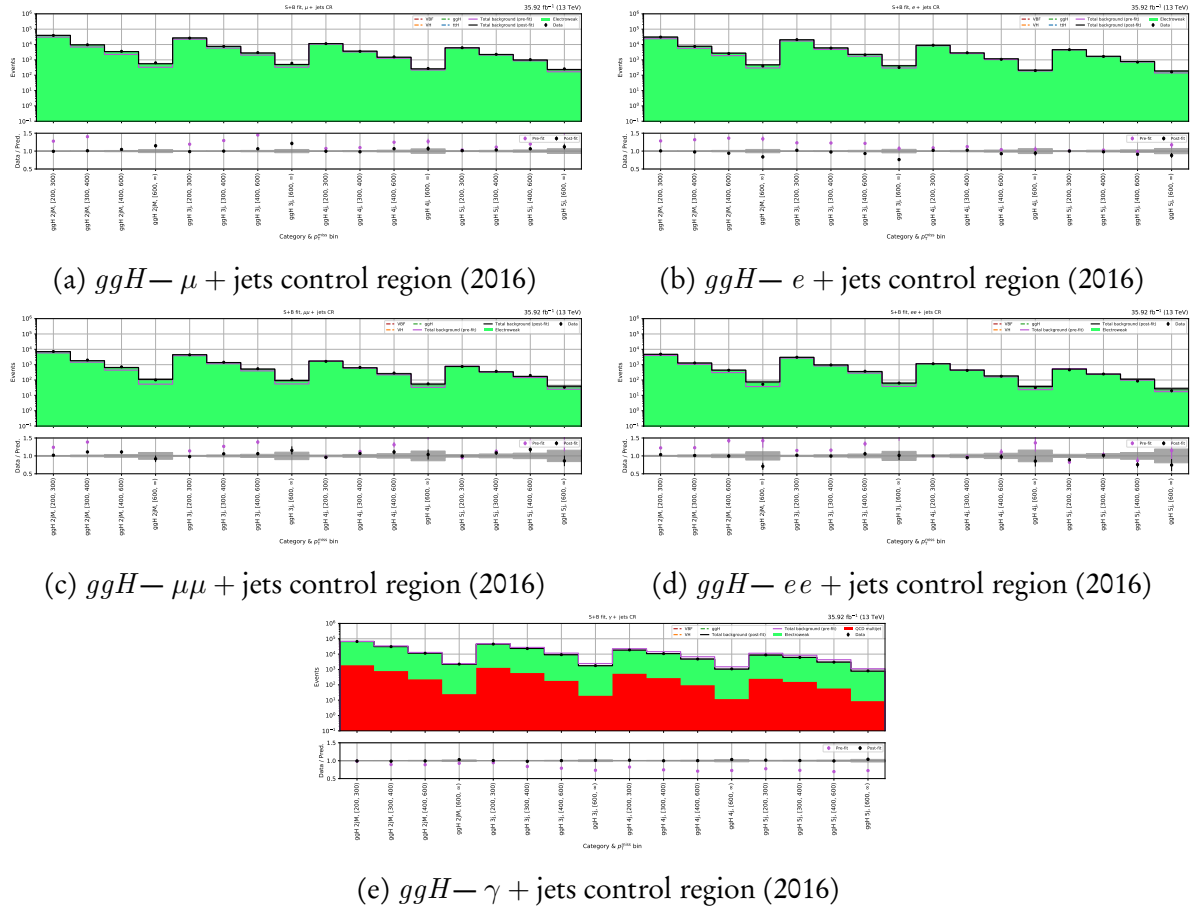


Figure A.7: Post-fit yields for each ggH subcategory and p_T^{miss} bin in the lepton and photon control regions for the 2016 dataset. The total background pre-fit and post-fit is compared to data in the lower panel of each subfigure.

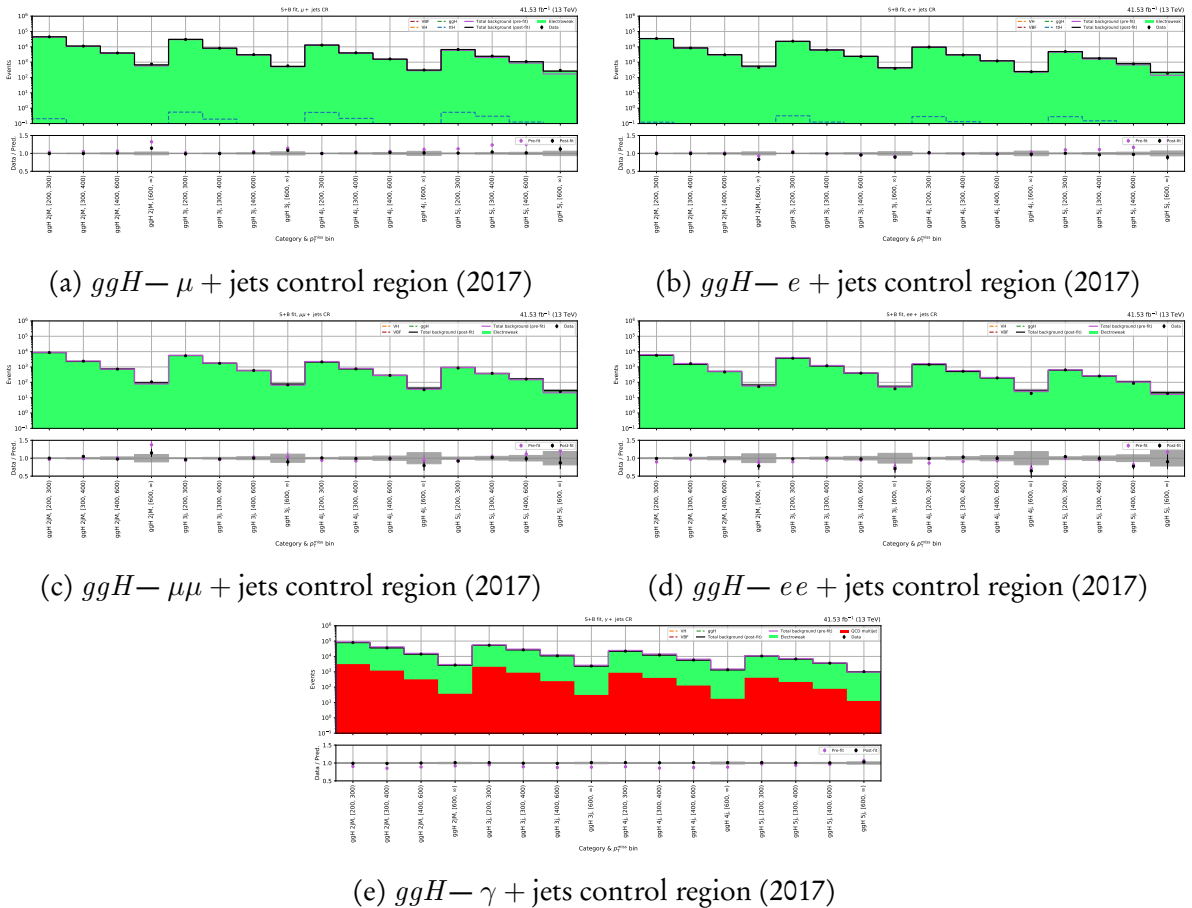


Figure A.8: Post-fit yields for each ggH subcategory and p_T^{miss} bin in the lepton and photon control regions for the 2017 dataset. The total background pre-fit and post-fit is compared to data in the lower panel of each subfigure.

APPENDIX A. POST-FIT DISTRIBUTIONS FROM THE HIGGS TO INVISIBLE ANALYSIS

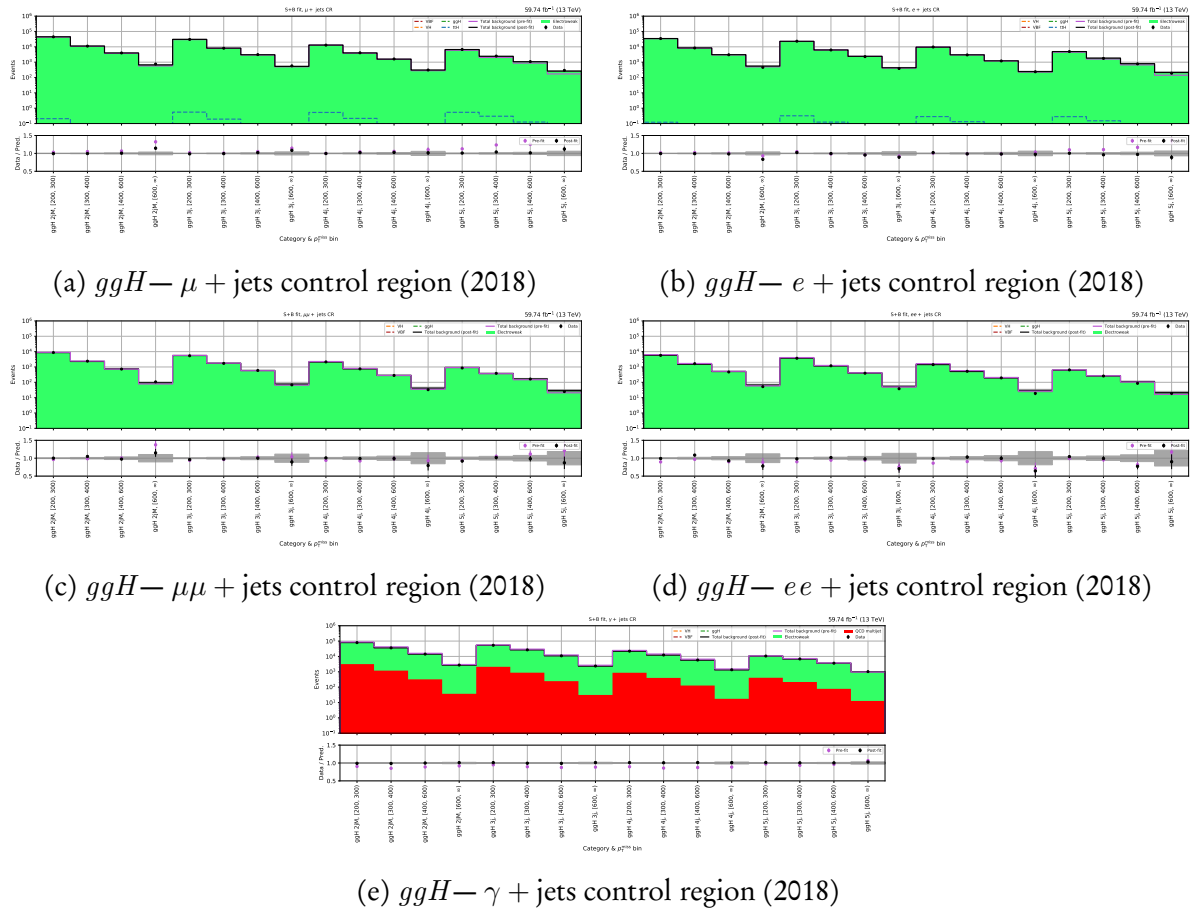


Figure A.9: Post-fit yields for each ggH subcategory and p_T^{miss} bin in the lepton and photon control regions for the 2018 dataset. The total background pre-fit and post-fit is compared to data in the lower panel of each subplot.

BIBLIOGRAPHY

- [1] M. AABOUD et al., *Performance of the ATLAS Track Reconstruction Algorithms in Dense Environments in LHC Run 2*, Eur. Phys. J. C 77.10 (2017), p. 673, doi: [10.1140/epjc/s10052-017-5225-7](https://doi.org/10.1140/epjc/s10052-017-5225-7), arXiv: [1704.07983 \[hep-ex\]](https://arxiv.org/abs/1704.07983).
- [2] M. AABOUD et al., *Combination of searches for invisible Higgs boson decays with the ATLAS experiment*, Phys. Rev. Lett. 122.23 (2019), p. 231801, doi: [10.1103/PhysRevLett.122.231801](https://doi.org/10.1103/PhysRevLett.122.231801), arXiv: [1904.05105 \[hep-ex\]](https://arxiv.org/abs/1904.05105).
- [3] M. AABOUD et al., *Observation of $H \rightarrow b\bar{b}$ decays and VH production with the ATLAS detector*, Phys. Lett. B 786 (2018), pp. 59–86, doi: [10.1016/j.physletb.2018.09.013](https://doi.org/10.1016/j.physletb.2018.09.013), arXiv: [1808.08238 \[hep-ex\]](https://arxiv.org/abs/1808.08238).
- [4] G. AAD et al., *Observation of a new particle in the search for the Standard Model Higgs boson with the ATLAS detector at the LHC*, Phys. Lett. B 716 (2012), pp. 1–29, doi: [10.1016/j.physletb.2012.08.020](https://doi.org/10.1016/j.physletb.2012.08.020), arXiv: [1207.7214 \[hep-ex\]](https://arxiv.org/abs/1207.7214).
- [5] R. AAIJ et al., *Measurement of the inelastic pp cross-section at a centre-of-mass energy of 13 TeV*, J. High Energy Phys. 06 (2018), p. 100, doi: [10.1007/JHEP06\(2018\)100](https://doi.org/10.1007/JHEP06(2018)100), arXiv: [1803.10974 \[hep-ex\]](https://arxiv.org/abs/1803.10974).
- [6] A. ABDELHAMEED et al., *First results from the CRESST-III low-mass dark matter program*, Phys. Rev. D 100.10 (2019), p. 102002, doi: [10.1103/PhysRevD.100.102002](https://doi.org/10.1103/PhysRevD.100.102002), arXiv: [1904.00498 \[astro-ph.CO\]](https://arxiv.org/abs/1904.00498).
- [7] D. ABERCROMBIE et al., *Dark Matter Benchmark Models for Early LHC Run-2 Searches: Report of the ATLAS/CMS Dark Matter Forum*, Phys. Dark Univ. 27 (2020), ed. by A. BOVEIA et al., p. 100371, doi: [10.1016/j.dark.2019.100371](https://doi.org/10.1016/j.dark.2019.100371), arXiv: [1507.00966 \[hep-ex\]](https://arxiv.org/abs/1507.00966).
- [8] N. AGHANIM et al., *Planck 2018 results. VI. Cosmological parameters* (2018), arXiv: [1807.06209 \[astro-ph.CO\]](https://arxiv.org/abs/1807.06209).

BIBLIOGRAPHY

- [9] R. AGNESE et al., *Search for Low-Mass Dark Matter with CDMSlite Using a Profile Likelihood Fit*, Phys. Rev. D 99.6 (2019), p. 062001, doi: [10.1103/PhysRevD.99.062001](https://doi.org/10.1103/PhysRevD.99.062001), arXiv: [1808.09098 \[astro-ph.CO\]](https://arxiv.org/abs/1808.09098).
- [10] S. AGOSTINELLI et al., *Geant4—a simulation toolkit*, Nucl. Instrum. Methods Phys. Res. A 506.3 (2003), pp. 250–303, doi: [10.1016/S0168-9002\(03\)01368-8](https://doi.org/10.1016/S0168-9002(03)01368-8).
- [11] D. S. AKERIB et al., *The LUX-ZEPLIN (LZ) Experiment*, Nucl. Instrum. Methods Phys. Res. A 953 (2020), p. 163047, doi: [10.1016/j.nima.2019.163047](https://doi.org/10.1016/j.nima.2019.163047), arXiv: [1910.09124 \[physics.ins-det\]](https://arxiv.org/abs/1910.09124).
- [12] D. AKERIB et al., *Results from a search for dark matter in the complete LUX exposure*, Phys. Rev. Lett. 118.2 (2017), p. 021303, doi: [10.1103/PhysRevLett.118.021303](https://doi.org/10.1103/PhysRevLett.118.021303), arXiv: [1608.07648 \[astro-ph.CO\]](https://arxiv.org/abs/1608.07648).
- [13] A. ALLOUL et al., *FeynRules 2.0 - A complete toolbox for tree-level phenomenology*, Comput. Phys. Commun. 185 (2014), p. 2250, doi: [10.1016/j.cpc.2014.04.012](https://doi.org/10.1016/j.cpc.2014.04.012), arXiv: [1310.1921 \[hep-ph\]](https://arxiv.org/abs/1310.1921).
- [14] J. ALWALL et al., *The automated computation of tree-level and next-to-leading order differential cross sections, and their matching to parton shower simulations*, J. High Energy Phys. 07 (2014), p. 079, doi: [10.1007/JHEP07\(2014\)079](https://doi.org/10.1007/JHEP07(2014)079), arXiv: [1405.0301 \[hep-ph\]](https://arxiv.org/abs/1405.0301).
- [15] J. ALWALL et al., *MadGraph 5 : Going Beyond*, J. High Energy Phys. 06 (2011), p. 128, doi: [10.1007/JHEP06\(2011\)128](https://doi.org/10.1007/JHEP06(2011)128), arXiv: [1106.0522 \[hep-ph\]](https://arxiv.org/abs/1106.0522).
- [16] A. A. ANUAR, *Electrons and photons at High Level Trigger in CMS for Run II*, Journal of Physics: Conference Series 664.8 (Dec. 2015), p. 082001, doi: [10.1088/1742-6596/664/8/082001](https://doi.org/10.1088/1742-6596/664/8/082001).
- [17] G. APOLLINARI et al., *High Luminosity Large Hadron Collider HL-LHC*, CERN Yellow Rep. 5 (2015), pp. 1–19, doi: [10.5170/CERN-2015-005.1](https://doi.org/10.5170/CERN-2015-005.1), arXiv: [1705.08830 \[physics.acc-ph\]](https://arxiv.org/abs/1705.08830).
- [18] E. APRILE et al., *Dark Matter Search Results from a One Ton-Year Exposure of XENON1T*, Phys. Rev. Lett. 121.11 (2018), p. 111302, doi: [10.1103/PhysRevLett.121.111302](https://doi.org/10.1103/PhysRevLett.121.111302), arXiv: [1805.12562 \[astro-ph.CO\]](https://arxiv.org/abs/1805.12562).
- [19] E. APRILE et al., *Light Dark Matter Search with Ionization Signals in XENON1T*, Phys. Rev. Lett. 123.25 (2019), p. 251801, doi: [10.1103/PhysRevLett.123.251801](https://doi.org/10.1103/PhysRevLett.123.251801), arXiv: [1907.11485 \[hep-ex\]](https://arxiv.org/abs/1907.11485).

- [20] G. ARCADI, A. DJOUADI and M. RAIDAL, *Dark Matter through the Higgs portal*, Phys. Rept. 842 (2020), pp. 1–180, doi: [10.1016/j.physrep.2019.11.003](https://doi.org/10.1016/j.physrep.2019.11.003), arXiv: [1903.03616 \[hep-ph\]](https://arxiv.org/abs/1903.03616).
- [21] G. ARNISON et al., *Experimental Observation of Lepton Pairs of Invariant Mass Around $95\text{GeV}/c^2$ at the CERN SPS Collider*, Phys. Lett. B 126.5 (1983), pp. 398–410, doi: [10.1016/0370-2693\(83\)90188-0](https://doi.org/10.1016/0370-2693(83)90188-0).
- [22] P. ARTOISENET et al., *Automatic spin-entangled decays of heavy resonances in Monte Carlo simulations*, JHEP 03 (2013), p. 015, doi: [10.1007/JHEP03\(2013\)015](https://doi.org/10.1007/JHEP03(2013)015), arXiv: [1212.3460 \[hep-ph\]](https://arxiv.org/abs/1212.3460).
- [23] P. ATHRON et al., *Global analyses of Higgs portal singlet dark matter models using GAMBIT*, Eur. Phys. J. C 79.1 (2019), p. 38, doi: [10.1140/epjc/s10052-018-6513-6](https://doi.org/10.1140/epjc/s10052-018-6513-6).
- [24] M. BACKOVIĆ et al., *Higher-order QCD predictions for dark matter production at the LHC in simplified models with s-channel mediators*, Eur. Phys. J. C 75.10 (2015), p. 482, doi: [10.1140/epjc/s10052-015-3700-6](https://doi.org/10.1140/epjc/s10052-015-3700-6), arXiv: [1508.05327 \[hep-ph\]](https://arxiv.org/abs/1508.05327).
- [25] P. BAGNAIA et al., *Evidence for $Z^0 \rightarrow e^+e^-$ at the CERN $\bar{p}p$ Collider*, Phys. Lett. B 129 (1983), pp. 130–140, doi: [10.1016/0370-2693\(83\)90744-X](https://doi.org/10.1016/0370-2693(83)90744-X).
- [26] I. BALDES and K. PETRAKI, *Asymmetric thermal-relic dark matter: Sommerfeld-enhanced freeze-out, annihilation signals and unitarity bounds* (2017), arXiv: [1703.00478 \[hep-ph\]](https://arxiv.org/abs/1703.00478).
- [27] R. BARLOW and C. BEESTON, *Fitting using finite Monte Carlo samples*, Computer Physics Communications 77.2 (1993), pp. 219–228, issn: 0010-4655, doi: [https://doi.org/10.1016/0010-4655\(93\)90005-W](https://doi.org/10.1016/0010-4655(93)90005-W).
- [28] G. BATTAGLIA et al., *Erratum: The radial velocity dispersion profile of the Galactic halo: constraining the density profile of the dark halo of the Milky Way*, Mon. Not. R. Astron. Soc. 370.2 (Aug. 2006), pp. 1055–1056, doi: [10.1111/j.1365-2966.2006.10688.x](https://doi.org/10.1111/j.1365-2966.2006.10688.x).
- [29] G. BATTAGLIA et al., *The radial velocity dispersion profile of the Galactic halo: constraining the density profile of the dark halo of the Milky Way*, Mon. Not. R. Astron. Soc. 364.2 (Dec. 2005), pp. 433–442, doi: [10.1111/j.1365-2966.2005.09367.x](https://doi.org/10.1111/j.1365-2966.2005.09367.x), arXiv: [astro-ph/0506102 \[astro-ph\]](https://arxiv.org/abs/astro-ph/0506102).
- [30] G. L. BAYATYAN et al., *CMS TriDAS project: Technical Design Report, Volume 1: The Trigger Systems*, Technical Design Report CMS.

BIBLIOGRAPHY

- [31] C. M. BENDER and S. SARKAR, *Asymptotic Analysis of the Boltzmann Equation for Dark Matter Relics*, J. Math. Phys. 53 (2012), p. 103509, doi: [10.1063/1.4753990](https://doi.org/10.1063/1.4753990), arXiv: [1203.1822 \[hep-th\]](https://arxiv.org/abs/1203.1822).
- [32] M. BENEDIKT, D. SCHULTE and F. ZIMMERMANN, *Optimizing integrated luminosity of future hadron colliders*, Phys. Rev. Spec. Top. Accel. Beams 18.CERN-ACC-2015-0166. 10 (Oct. 2015), 101002. 19 p, doi: [10.1103/PhysRevSTAB.18.101002](https://doi.org/10.1103/PhysRevSTAB.18.101002).
- [33] D. BERTOLINI et al., *Pileup Per Particle Identification*, JHEP 10 (2014), p. 059, doi: [10.1007/JHEP10\(2014\)059](https://doi.org/10.1007/JHEP10(2014)059), arXiv: [1407.6013 \[hep-ph\]](https://arxiv.org/abs/1407.6013).
- [34] P. BHATTACHARJEE et al., *Sizing-up the WIMPs of Milky Way : Deriving the velocity distribution of Galactic Dark Matter particles from the rotation curve data*, Phys. Rev. D87 (2013), p. 083525, doi: [10.1103/PhysRevD.87.083525](https://doi.org/10.1103/PhysRevD.87.083525), arXiv: [1210.2328 \[astro-ph.GA\]](https://arxiv.org/abs/1210.2328).
- [35] P. BLOCH et al., *Changes to CMS ECAL electronics: addendum to the Technical Design Report*, Technical Design Report CMS, CERN, Geneva, 2002.
- [36] A. BOVEIA and C. DOGLIONI, *Dark Matter Searches at Colliders*, Ann. Rev. Nucl. Part. Sci. 68 (2018), pp. 429–459, doi: [10.1146/annurev-nucl-101917-021008](https://doi.org/10.1146/annurev-nucl-101917-021008), arXiv: [1810.12238 \[hep-ex\]](https://arxiv.org/abs/1810.12238).
- [37] A. H. BROEILS, *The mass distribution of the dwarf spiral NGC 1560*, Astron. Astrophys. 256 (Mar. 1992), pp. 19–32.
- [38] O. S. BRÜNING et al., *LHC Design Report*, CERN Yellow Reports: Monographs, CERN, Geneva, 2004, doi: [10.5170/CERN-2004-003-V-1](https://doi.org/10.5170/CERN-2004-003-V-1).
- [39] M. CACCIARI, G. P. SALAM and G. SOYEZ, *FastJet User Manual*, Eur. Phys. J. C 72 (2012), p. 1896, doi: [10.1140/epjc/s10052-012-1896-2](https://doi.org/10.1140/epjc/s10052-012-1896-2), arXiv: [1111.6097 \[hep-ph\]](https://arxiv.org/abs/1111.6097).
- [40] M. CACCIARI, G. P. SALAM and G. SOYEZ, *The Anti- $k(t)$ jet clustering algorithm*, J. High Energy Phys. 04 (2008), p. 063, doi: [10.1088/1126-6708/2008/04/063](https://doi.org/10.1088/1126-6708/2008/04/063), arXiv: [0802.1189 \[hep-ph\]](https://arxiv.org/abs/0802.1189).
- [41] A. CANEPA, *Searches for supersymmetry at the Large Hadron Collider*, Reviews in Physics 4 (2019), p. 100033, doi: [10.1016/j.revip.2019.100033](https://doi.org/10.1016/j.revip.2019.100033).
- [42] M. CEPEDA et al., *Report from Working Group 2: Higgs Physics at the HL-LHC and HE-LHC*, in: *Report on the Physics at the HL-LHC, and Perspectives for the HE-LHC*, ed. by A. DAINESE et al., vol. 7, Dec. 2019, pp. 221–584, doi: [10.23731/CYRM-2019-007.221](https://doi.org/10.23731/CYRM-2019-007.221), arXiv: [1902.00134 \[hep-ph\]](https://arxiv.org/abs/1902.00134).

- [43] D. G. CERDEÑO et al., *B anomalies and dark matter: a complex connection*, Eur. Phys. J. C 79.6 (2019), p. 517, doi: [10.1140/epjc/s10052-019-6979-x](https://doi.org/10.1140/epjc/s10052-019-6979-x).
- [44] S. CHATRCHYAN et al., *Description and performance of track and primary-vertex reconstruction with the CMS tracker*, JINST 9.10 (2014), P10009, doi: [10.1088/1748-0221/9/10/P10009](https://doi.org/10.1088/1748-0221/9/10/P10009), arXiv: [1405.6569 \[physics.ins-det\]](https://arxiv.org/abs/1405.6569).
- [45] S. CHATRCHYAN et al., *Observation of a New Boson at a Mass of 125 GeV with the CMS Experiment at the LHC*, Phys. Lett. B 716 (2012), pp. 30–61, doi: [10.1016/j.physletb.2012.08.021](https://doi.org/10.1016/j.physletb.2012.08.021), arXiv: [1207.7235 \[hep-ex\]](https://arxiv.org/abs/1207.7235).
- [46] S. CHATRCHYAN et al., *Search for invisible decays of Higgs bosons in the vector boson fusion and associated ZH production modes*, Eur. Phys. J. C 74 (2014), p. 2980, doi: [10.1140/epjc/s10052-014-2980-6](https://doi.org/10.1140/epjc/s10052-014-2980-6), arXiv: [1404.1344 \[hep-ex\]](https://arxiv.org/abs/1404.1344).
- [47] S. CITTOLIN, A. RÁCZ and P. SPHICAS, *CMS The TriDAS Project: Technical Design Report, Volume 2: Data Acquisition and High-Level Trigger. CMS trigger and data-acquisition project*, Technical Design Report CMS, CERN, Geneva, 2002.
- [48] C. J. CLOPPER and E. S. PEARSON, *The use of confidence or fiducial limits illustrated in the case of the binomial*, Biometrika 26.4 (Dec. 1934), pp. 404–413, ISSN: 0006-3444, doi: [10.1093/biomet/26.4.404](https://doi.org/10.1093/biomet/26.4.404).
- [49] D. CLOWE, A. GONZALEZ and M. MARKEVITCH, *Weak-Lensing Mass Reconstruction of the Interacting Cluster 1E 0657-558: Direct Evidence for the Existence of Dark Matter*, Astrophys. J. 604.2 (2004), p. 596.
- [50] CMS COLLABORATION, *CMS luminosity measurement for the 2016 data taking period*, tech. rep. CMS-PAS-LUM-17-001, CERN, Geneva, 2017.
- [51] CMS COLLABORATION, *CMS luminosity measurement for the 2017 data-taking period at $\sqrt{s} = 13$ TeV*, tech. rep. CMS-PAS-LUM-17-004, CERN, Geneva, 2018.
- [52] CMS COLLABORATION, *CMS luminosity measurement for the 2018 data-taking period at $\sqrt{s} = 13$ TeV*, tech. rep. CMS-PAS-LUM-18-002, CERN, Geneva, 2019.
- [53] CMS COLLABORATION, *CMS Luminosity Public Results*, URL: <https://twiki.cern.ch/twiki/bin/view/CMSPublic/LumiPublicResults> (visited on 22/02/2020).
- [54] CMS COLLABORATION, *Cut Based Electron ID for Run 2*, access may be restricted, URL: <https://twiki.cern.ch/twiki/bin/view/CMS/CutBasedElectronIdentificationRun2> (visited on 18/05/2020).

BIBLIOGRAPHY

- [55] CMS COLLABORATION, *Cut Based Photon ID for Run 2*, access may be restricted, URL: <https://twiki.cern.ch/twiki/bin/viewauth/CMS/CutBasedPhotonIdentificationRun2> (visited on 19/05/2020).
- [56] CMS COLLABORATION, *Jet Identification for the 13 TeV data Run2016*, access may be restricted, URL: <https://twiki.cern.ch/twiki/bin/view/CMS/JetID13TeVRun2016> (visited on 18/05/2020).
- [57] CMS COLLABORATION, *Jet Identification for the 13 TeV data Run2017*, access may be restricted, URL: <https://twiki.cern.ch/twiki/bin/view/CMS/JetID13TeVRun2017> (visited on 18/05/2020).
- [58] CMS COLLABORATION, *Jet Identification for the 13 TeV data Run2018*, access may be restricted, URL: <https://twiki.cern.ch/twiki/bin/view/CMS/JetID13TeVRun2018> (visited on 18/05/2020).
- [59] CMS COLLABORATION, *Luminosity Physics Object Group (Lumi POG)*, access may be restricted, URL: <https://twiki.cern.ch/twiki/bin/viewauth/CMS/TWikiLUM> (visited on 16/03/2020).
- [60] CMS COLLABORATION, *Machine learning-based identification of highly Lorentz-boosted hadronically decaying particles at the CMS experiment*, tech. rep. CMS-PAS-JME-18-002, CERN, Geneva, 2019.
- [61] CMS COLLABORATION, *Particle-Flow Event Reconstruction in CMS and Performance for Jets, Taus, and MET*, tech. rep. CMS-PAS-PFT-09-001, CERN, Geneva, Apr. 2009.
- [62] CMS COLLABORATION, *Reweighting recipe to emulate Level 1 ECAL prefireing*, access may be restricted, URL: <https://twiki.cern.ch/twiki/bin/viewauth/CMS/L1ECALPrefiringWeightRecipe> (visited on 09/07/2020).
- [63] CMS COLLABORATION, *The CMS electromagnetic calorimeter project: Technical Design Report*, Technical Design Report CMS, CERN, Geneva, 1997.
- [64] CMS COLLABORATION, *The CMS hadron calorimeter project: Technical Design Report*, Technical Design Report CMS, CERN, Geneva, 1997.
- [65] CMS COLLABORATION, *The CMS magnet project: Technical Design Report*, Technical Design Report CMS, CERN, Geneva, 1997.
- [66] CMS COLLABORATION, *The CMS tracker: addendum to the Technical Design Report*, Technical Design Report CMS, CERN, Geneva, 2000.

- [67] T. COHEN, M. LISANTI and H. K. LOU, *Semi-visible Jets: Dark Matter Undercover at the LHC*, Phys. Rev. Lett. 115.17 (2015), p. 171804, doi: [10.1103/PhysRevLett.115.171804](https://doi.org/10.1103/PhysRevLett.115.171804), arXiv: [1503.00009 \[hep-ph\]](https://arxiv.org/abs/1503.00009).
- [68] T. COHEN et al., *LHC Searches for Dark Sector Showers*, J. High Energy Phys. 11 (2017), p. 196, doi: [10.1007/JHEP11\(2017\)196](https://doi.org/10.1007/JHEP11(2017)196), arXiv: [1707.05326 \[hep-ph\]](https://arxiv.org/abs/1707.05326).
- [69] J. CONRAD and O. REIMER, *Indirect dark matter searches in gamma and cosmic rays*, Nature Phys. 13.3 (2017), pp. 224–231, doi: [10.1038/nphys4049](https://doi.org/10.1038/nphys4049), arXiv: [1705.11165 \[astro-ph.HE\]](https://arxiv.org/abs/1705.11165).
- [70] G. COWAN et al., *Asymptotic formulae for likelihood-based tests of new physics*, Eur. Phys. J. C 71 (2011), [Erratum: Eur.Phys.J.C 73, 2501 (2013)], p. 1554, doi: [10.1140/epjc/s10052-011-1554-0](https://doi.org/10.1140/epjc/s10052-011-1554-0), arXiv: [1007.1727 \[physics.data-an\]](https://arxiv.org/abs/1007.1727).
- [71] B. COX and J. FORSHAW, *Universal: A Journey Through the Cosmos*, Penguin Books Limited, 2016, ISBN: 9780141968346.
- [72] X. CUI et al., *Dark Matter Results From 54-Ton-Day Exposure of PandaX-II Experiment*, Phys. Rev. Lett. 119.18 (2017), p. 181302, doi: [10.1103/PhysRevLett.119.181302](https://doi.org/10.1103/PhysRevLett.119.181302), arXiv: [1708.06917 \[astro-ph.CO\]](https://arxiv.org/abs/1708.06917).
- [73] M. DELLA NEGRA et al., *CMS: letter of intent by the CMS Collaboration for a general purpose detector at LHC*, tech. rep. CERN-LHCC-92-003. LHCC-I-1, Open presentation to the LHCC 5 November 1992, M. Della Negra/CERN, CMS Spokesman, CERN, Geneva, 1992.
- [74] N. DEV et al., *The CMS Level-1 electron and photon trigger: for Run II of LHC*, J. Instrum. 12.02 (Feb. 2017), C02014. 10 p, doi: [10.1088/1748-0221/12/02/c02014](https://doi.org/10.1088/1748-0221/12/02/c02014).
- [75] A. DJOUADI et al., *Direct Detection of Higgs-Portal Dark Matter at the LHC*, Eur. Phys. J. C 73.6 (2013), p. 2455, doi: [10.1140/epjc/s10052-013-2455-1](https://doi.org/10.1140/epjc/s10052-013-2455-1), arXiv: [1205.3169 \[hep-ph\]](https://arxiv.org/abs/1205.3169).
- [76] A. DJOUADI et al., *Implications of LHC searches for Higgs-portal dark matter*, Phys. Lett. B 709 (2012), pp. 65–69, doi: [10.1016/j.physletb.2012.01.062](https://doi.org/10.1016/j.physletb.2012.01.062), arXiv: [1112.3299 \[hep-ph\]](https://arxiv.org/abs/1112.3299).
- [77] M. DREWES, *The Phenomenology of Right Handed Neutrinos*, Int. J. Mod. Phys. E 22.08 (2013), p. 1330019, doi: [10.1142/S0218301313300191](https://doi.org/10.1142/S0218301313300191).
- [78] J. EINASTO, *Dark Matter*, ArXiv e-prints (Jan. 2009), arXiv: [0901.0632 \[astro-ph.CO\]](https://arxiv.org/abs/0901.0632).
- [79] R. K. ELLIS, W. J. STIRLING and B. R. WEBBER, *QCD and collider physics*, Camb. Monogr. Part. Phys. Nucl. Phys. Cosmol. 8 (1996), pp. 1–435.

BIBLIOGRAPHY

- [80] F. ENGLERT and R. BROUT, *Broken Symmetry and the Mass of Gauge Vector Mesons*, Phys. Rev. Lett. 13 (9 Aug. 1964), pp. 321–323, doi: [10.1103/PhysRevLett.13.321](https://doi.org/10.1103/PhysRevLett.13.321).
- [81] M. FARINA, M. PERELSTEIN and N. REY-LE LORIER, *Higgs Couplings and Naturalness*, Phys. Rev. D90.1 (2014), p. 015014, doi: [10.1103/PhysRevD.90.015014](https://doi.org/10.1103/PhysRevD.90.015014), arXiv: [1305.6068 \[hep-ph\]](https://arxiv.org/abs/1305.6068).
- [82] B. D. FIELDS et al., *Big-Bang Nucleosynthesis After Planck*, J. Cosmol. Astropart. Phys. 2003.03 (2020), p. 010, doi: [10.1088/1475-7516/2020/03/010](https://doi.org/10.1088/1475-7516/2020/03/010), arXiv: [1912.01132 \[astro-ph.CO\]](https://arxiv.org/abs/1912.01132).
- [83] *First constraints on invisible Higgs boson decays using $t\bar{t}H$ production at $\sqrt{s} = 13 \text{ TeV}$* , tech. rep. CMS-PAS-HIG-18-008, CERN, Geneva, 2019.
- [84] K. C. FREEMAN, *On the Disks of Spiral and S0 Galaxies*, Astrophys. J. 160 (June 1970), p. 811, doi: [10.1086/150474](https://doi.org/10.1086/150474).
- [85] S. FRIXIONE, P. NASON and C. OLEARI, *Matching NLO QCD computations with Parton Shower simulations: the POWHEG method*, J. High Energy Phys. 11 (2007), p. 070, doi: [10.1088/1126-6708/2007/11/070](https://doi.org/10.1088/1126-6708/2007/11/070), arXiv: [0709.2092 \[hep-ph\]](https://arxiv.org/abs/0709.2092).
- [86] P. GONDOLO and G. GELMINI, *Cosmic Abundances of Stable Particles: improved analysis*, Nucl. Phys. B 360 (Aug. 1991), pp. 145–179, doi: [10.1016/0550-3213\(91\)90438-4](https://doi.org/10.1016/0550-3213(91)90438-4).
- [87] G. S. GURALNIK, C. R. HAGEN and T. W. B. KIBBLE, *Global Conservation Laws and Massless Particles*, Phys. Rev. Lett. 13 (20 Nov. 1964), pp. 585–587, doi: [10.1103/PhysRevLett.13.585](https://doi.org/10.1103/PhysRevLett.13.585).
- [88] L. J. HALL et al., *Freeze-In Production of FIMP Dark Matter*, J. High Energy Phys. 03 (2010), p. 080, doi: [10.1007/JHEP03\(2010\)080](https://doi.org/10.1007/JHEP03(2010)080), arXiv: [0911.1120 \[hep-ph\]](https://arxiv.org/abs/0911.1120).
- [89] T. HAN, Z. LIU and A. NATARAJAN, *Dark matter and Higgs bosons in the MSSM*, J. High Energy Phys. 11 (2013), p. 008, doi: [10.1007/JHEP11\(2013\)008](https://doi.org/10.1007/JHEP11(2013)008), arXiv: [1303.3040 \[hep-ph\]](https://arxiv.org/abs/1303.3040).
- [90] T. HAN, J. D. LYKKEN and R.-J. ZHANG, *On Kaluza-Klein states from large extra dimensions*, Phys. Rev. D59 (1999), p. 105006, doi: [10.1103/PhysRevD.59.105006](https://doi.org/10.1103/PhysRevD.59.105006), arXiv: [hep-ph/9811350 \[hep-ph\]](https://arxiv.org/abs/hep-ph/9811350).
- [91] S. HEINEMEYER et al., *Handbook of LHC Higgs Cross Sections: 3. Higgs Properties: Report of the LHC Higgs Cross Section Working Group*, ed. by S. HEINEMEYER, CERN Yellow Reports: Monographs, July 2013.
- [92] W. HERR and B. MURATORI, *Concept of luminosity* (2006), doi: [10.5170/CERN-2006-002.361](https://doi.org/10.5170/CERN-2006-002.361).

- [93] J. HERZOG-ARBEITMAN et al., *Empirical Determination of Dark Matter Velocities using Metal-Poor Stars*, Phys. Rev. Lett. 120.4 (2018), p. 041102, doi: [10.1103/PhysRevLett.120.041102](https://doi.org/10.1103/PhysRevLett.120.041102), arXiv: [1704.04499 \[astro-ph.GA\]](https://arxiv.org/abs/1704.04499).
- [94] P. W. HIGGS, *Broken Symmetries and the Masses of Gauge Bosons*, Phys. Rev. Lett. 13 (16 Oct. 1964), pp. 508–509, doi: [10.1103/PhysRevLett.13.508](https://doi.org/10.1103/PhysRevLett.13.508).
- [95] M. HOFERICHTER et al., *Improved limits for Higgs-portal dark matter from LHC searches*, Phys. Rev. Lett. 119.18 (2017), p. 181803, doi: [10.1103/PhysRevLett.119.181803](https://doi.org/10.1103/PhysRevLett.119.181803), arXiv: [1708.02245 \[hep-ph\]](https://arxiv.org/abs/1708.02245).
- [96] D. HUTERER, *Weak lensing, dark matter and dark energy*, Gen. Relativ. Gravit. 42 (Sept. 2010), pp. 2177–2195, doi: [10.1007/s10714-010-1051-z](https://doi.org/10.1007/s10714-010-1051-z), arXiv: [1001.1758 \[astro-ph.CO\]](https://arxiv.org/abs/1001.1758).
- [97] Q. INGRAM, *Energy resolution of the barrel of the CMS Electromagnetic Calorimeter*, Journal of Instrumentation 2.04 (Apr. 2007), P04004–P04004, doi: [10.1088/1748-0221/2/04/p04004](https://doi.org/10.1088/1748-0221/2/04/p04004).
- [98] P. R. KAFLE et al., *On the Shoulders of Giants: Properties of the Stellar Halo and the Milky Way Mass Distribution*, Astrophys. J. 794.1 (2014), p. 59, doi: [10.1088/0004-637X/794/1/59](https://doi.org/10.1088/0004-637X/794/1/59), arXiv: [1408.1787 \[astro-ph.GA\]](https://arxiv.org/abs/1408.1787).
- [99] M. KAKIZAKI et al., *Phenomenological constraints on light mixed sneutrino dark matter scenarios*, Phys. Lett. B 749 (2015), pp. 44–49, doi: [10.1016/j.physletb.2015.07.030](https://doi.org/10.1016/j.physletb.2015.07.030).
- [100] J. C. KAPTEYN, *First Attempt at a Theory of the Arrangement and Motion of the Sidereal System*, Astrophys. J. 55 (May 1922), p. 302, doi: [10.1086/142670](https://doi.org/10.1086/142670).
- [101] V. KARIMÄKI et al., *The CMS tracker system project: Technical Design Report*, Technical Design Report CMS, CERN, Geneva, 1997.
- [102] V. KHACHATRYAN et al., *A search for new phenomena in pp collisions at $\sqrt{s} = 13$ TeV in final states with missing transverse momentum and at least one jet using the α_T variable*, Eur. Phys. J. C 77.5 (2017), p. 294, doi: [10.1140/epjc/s10052-017-4787-8](https://doi.org/10.1140/epjc/s10052-017-4787-8), arXiv: [1611.00338 \[hep-ex\]](https://arxiv.org/abs/1611.00338).
- [103] V. KHACHATRYAN et al., *Event generator tunes obtained from underlying event and multiparton scattering measurements*, Eur. Phys. J. C 76.3 (2016), p. 155, doi: [10.1140/epjc/s10052-016-3988-x](https://doi.org/10.1140/epjc/s10052-016-3988-x), arXiv: [1512.00815 \[hep-ex\]](https://arxiv.org/abs/1512.00815).

BIBLIOGRAPHY

- [104] V. KHACHATRYAN et al., *Search for dark matter, extra dimensions, and unparticles in monojet events in proton–proton collisions at $\sqrt{s} = 8\text{ TeV}$* , Eur. Phys. J. C 75.5 (2015), p. 235, doi: [10.1140/epjc/s10052-015-3451-4](https://doi.org/10.1140/epjc/s10052-015-3451-4), arXiv: [1408.3583 \[hep-ex\]](https://arxiv.org/abs/1408.3583).
- [105] V. KHACHATRYAN et al., *Search for Microscopic Black Hole Signatures at the Large Hadron Collider*, Phys. Lett. B 697 (2011), pp. 434–453, doi: [10.1016/j.physletb.2011.02.032](https://doi.org/10.1016/j.physletb.2011.02.032), arXiv: [1012.3375 \[hep-ex\]](https://arxiv.org/abs/1012.3375).
- [106] V. KHACHATRYAN et al., *Searches for invisible decays of the Higgs boson in pp collisions at $\sqrt{s} = 7, 8,$ and 13 TeV* , J. High Energy Phys. 02 (2017), p. 135, doi: [10.1007/JHEP02\(2017\)135](https://doi.org/10.1007/JHEP02(2017)135), arXiv: [1610.09218 \[hep-ex\]](https://arxiv.org/abs/1610.09218).
- [107] F. KRAUSS and D. NAPOLETANO, *Towards a fully massive five-flavor scheme*, Phys. Rev. D 98.9 (2018), p. 096002, doi: [10.1103/PhysRevD.98.096002](https://doi.org/10.1103/PhysRevD.98.096002), arXiv: [1712.06832 \[hep-ph\]](https://arxiv.org/abs/1712.06832).
- [108] G. KRŇAJIC, *Freezing In, Heating Up, and Freezing Out: Predictive Nonthermal Dark Matter and Low-Mass Direct Detection*, J. High Energy Phys. 10 (2018), p. 136, doi: [10.1007/JHEP10\(2018\)136](https://doi.org/10.1007/JHEP10(2018)136), arXiv: [1711.11038 \[hep-ph\]](https://arxiv.org/abs/1711.11038).
- [109] A. J. LARKOSKI et al., *Soft Drop*, JHEP 05 (2014), p. 146, doi: [10.1007/JHEP05\(2014\)146](https://doi.org/10.1007/JHEP05(2014)146), arXiv: [1402.2657 \[hep-ph\]](https://arxiv.org/abs/1402.2657).
- [110] J. G. LAYTER, *The CMS muon project: Technical Design Report*, Technical Design Report CMS, CERN, Geneva, 1997.
- [111] J. M. LINDERT et al., *Precise predictions for $V + \text{jets}$ dark matter backgrounds*, The European Physical Journal C 77.12 (Dec. 2017), issn: 1434-6052, doi: [10.1140/epjc/s10052-017-5389-1](https://doi.org/10.1140/epjc/s10052-017-5389-1).
- [112] M. LISANTI, *Lectures on Dark Matter Physics*, in: *Proceedings, Theoretical Advanced Study Institute in Elementary Particle Physics: New Frontiers in Fields and Strings (TASI 2015): Boulder, CO, USA, June 1-26, 2015*, 2017, pp. 399–446, doi: [10.1142/9789813149441_0007](https://doi.org/10.1142/9789813149441_0007), arXiv: [1603.03797 \[hep-ph\]](https://arxiv.org/abs/1603.03797).
- [113] S. P. MARTIN, *A Supersymmetry primer*, Adv. Ser. Direct. High Energy Phys 18 (1998), pp. 1–98, doi: [10.1142/9789812839657_0001](https://doi.org/10.1142/9789812839657_0001), [10.1142/9789814307505_0001](https://doi.org/10.1142/9789814307505_0001), arXiv: [hep-ph/9709356 \[hep-ph\]](https://arxiv.org/abs/hep-ph/9709356).
- [114] S. MERTENS, *Direct Neutrino Mass Experiments*, J. Phys. Conf. Ser. 718.2 (2016), p. 022013, doi: [10.1088/1742-6596/718/2/022013](https://doi.org/10.1088/1742-6596/718/2/022013), arXiv: [1605.01579 \[nucl-ex\]](https://arxiv.org/abs/1605.01579).

- [115] J. MOUSA et al., *Overview of the CMS Detector Performance at LHC Run 2*, Universe 5 (Jan. 2019), p. 18, doi: [10.3390/universe5010018](https://doi.org/10.3390/universe5010018).
- [116] P. NASON, *A New method for combining NLO QCD with shower Monte Carlo algorithms*, J. High Energy Phys. 11 (2004), p. 040, doi: [10.1088/1126-6708/2004/11/040](https://doi.org/10.1088/1126-6708/2004/11/040), arXiv: [hep-ph/0409146 \[hep-ph\]](https://arxiv.org/abs/hep-ph/0409146).
- [117] E. NOETHER, *Invariant variation problems*, Transport Theory and Statistical Physics 1.3 (Jan. 1971), pp. 186–207, ISSN: 1532-2424, doi: [10.1080/00411457108231446](https://doi.org/10.1080/00411457108231446).
- [118] M. PERSIC, P. SALUCCI and F. STEL, *The universal rotation curve of spiral galaxies - I. The dark matter connection*, Mon. Not. R. Astron. Soc. 281 (July 1996), pp. 27–47, doi: [10.1093/mnras/281.1.27](https://doi.org/10.1093/mnras/281.1.27), eprint: [astro-ph/9506004](https://arxiv.org/abs/astro-ph/9506004).
- [119] G. RAUCO, *Search for New Physics in All-Hadronic Final States with the CMS Experiment*, PhD thesis, Universität Zürich, 2019.
- [120] T. SAKUMA, *Cutaway diagrams of CMS detector* (May 2019).
- [121] T. SAKUMA, H. FLAECHER and D. SMITH, *Alternative angular variables for suppression of QCD multijet events in new physics searches with missing transverse momentum at the LHC* (Mar. 2018), arXiv: [1803.07942 \[hep-ph\]](https://arxiv.org/abs/1803.07942).
- [122] S. SCHRAMM, *Searching for Dark Matter with the ATLAS Detector*, Springer Theses, Springer International Publishing, 2016, ISBN: 9783319444536.
- [123] M. SCHUMANN, *Direct Detection of WIMP Dark Matter: Concepts and Status*, J. Phys. G46.10 (2019), p. 103003, doi: [10.1088/1361-6471/ab2ea5](https://doi.org/10.1088/1361-6471/ab2ea5), arXiv: [1903.03026 \[astro-ph.CO\]](https://arxiv.org/abs/1903.03026).
- [124] SCIENCE AND TECHNOLOGY FACILITIES COUNCIL, *CERN Accelerator Complex*, URL: <https://stfc.ukri.org/research/particle-physics-and-particle-astronomy/large-hadron-collider/cern-accelerator-complex/> (visited on 22/03/2020).
- [125] A. M. SIRUNYAN et al., *Observation of Higgs boson decay to bottom quarks*, Phys. Rev. Lett. 121.12 (2018), p. 121801, doi: [10.1103/PhysRevLett.121.121801](https://doi.org/10.1103/PhysRevLett.121.121801), arXiv: [1808.08242 \[hep-ex\]](https://arxiv.org/abs/1808.08242).
- [126] A. M. SIRUNYAN et al., *Particle-flow reconstruction and global event description with the CMS detector*, JINST 12 (2017), P10003, doi: [10.1088/1748-0221/12/10/P10003](https://doi.org/10.1088/1748-0221/12/10/P10003), arXiv: [1706.04965 \[physics.ins-det\]](https://arxiv.org/abs/1706.04965).

BIBLIOGRAPHY

- [127] A. M. SIRUNYAN et al., *Search for natural and split supersymmetry in proton-proton collisions at $\sqrt{s} = 13$ TeV in final states with jets and missing transverse momentum*, J. High Energy Phys. 2018.5 (May 2018), p. 25, doi: [10.1007/JHEP05\(2018\)025](https://doi.org/10.1007/JHEP05(2018)025).
- [128] A. M. SIRUNYAN et al., *Search for new physics in final states with an energetic jet or a hadronically decaying W or Z boson and transverse momentum imbalance at $\sqrt{s} = 13$ TeV*, Phys. Rev. D 97.9 (2018), p. 092005, doi: [10.1103/PhysRevD.97.092005](https://doi.org/10.1103/PhysRevD.97.092005), arXiv: [1712.02345 \[hep-ex\]](https://arxiv.org/abs/1712.02345).
- [129] A. SIRUNYAN et al., *Identification of heavy-flavour jets with the CMS detector in pp collisions at 13 TeV*, JINST 13.05 (2018), P05011, doi: [10.1088/1748-0221/13/05/P05011](https://doi.org/10.1088/1748-0221/13/05/P05011), arXiv: [1712.07158 \[physics.ins-det\]](https://arxiv.org/abs/1712.07158).
- [130] A. SIRUNYAN et al., *Performance of the CMS muon detector and muon reconstruction with proton-proton collisions at $\sqrt{s} = 13$ TeV*, JINST 13.06 (2018), P06015, doi: [10.1088/1748-0221/13/06/P06015](https://doi.org/10.1088/1748-0221/13/06/P06015), arXiv: [1804.04528 \[physics.ins-det\]](https://arxiv.org/abs/1804.04528).
- [131] A. SIRUNYAN et al., *Search for new physics in events with a leptonically decaying Z boson and a large transverse momentum imbalance in proton-proton collisions at $\sqrt{s} = 13$ TeV*, Eur. Phys. J. C 78.4 (2018), p. 291, doi: [10.1140/epjc/s10052-018-5740-1](https://doi.org/10.1140/epjc/s10052-018-5740-1), arXiv: [1711.00431 \[hep-ex\]](https://arxiv.org/abs/1711.00431).
- [132] A. M. SIRUNYAN et al., *Extraction and validation of a new set of CMS PYTHIA8 tunes from underlying-event measurements*, Eur. Phys. J. C 80.1 (2020), p. 4, doi: [10.1140/epjc/s10052-019-7499-4](https://doi.org/10.1140/epjc/s10052-019-7499-4), arXiv: [1903.12179 \[hep-ex\]](https://arxiv.org/abs/1903.12179).
- [133] A. M. SIRUNYAN et al., *Measurements of $t\bar{t}$ differential cross sections in proton-proton collisions at $\sqrt{s} = 13$ TeV using events containing two leptons*, JHEP 02 (2019), p. 149, doi: [10.1007/JHEP02\(2019\)149](https://doi.org/10.1007/JHEP02(2019)149), arXiv: [1811.06625 \[hep-ex\]](https://arxiv.org/abs/1811.06625).
- [134] A. M. SIRUNYAN et al., *Search for dijet resonances in proton-proton collisions at $\sqrt{s} = 13$ TeV and constraints on dark matter and other models*, Phys. Lett. B 769 (2017), [Erratum: Phys. Lett.B772,882(2017)], pp. 520–542, doi: [10.1016/j.physletb.2017.09.029](https://doi.org/10.1016/j.physletb.2017.09.029), [10.1016/j.physletb.2017.02.012](https://doi.org/10.1016/j.physletb.2017.02.012), arXiv: [1611.03568 \[hep-ex\]](https://arxiv.org/abs/1611.03568).
- [135] A. M. SIRUNYAN et al., *Search for invisible decays of a Higgs boson produced through vector boson fusion in proton-proton collisions at $\sqrt{s} = 13$ TeV*, Phys. Lett. B 793 (2019), pp. 520–551, doi: [10.1016/j.physletb.2019.04.025](https://doi.org/10.1016/j.physletb.2019.04.025), arXiv: [1809.05937 \[hep-ex\]](https://arxiv.org/abs/1809.05937).

- [136] A. M. SIRUNYAN et al., *Search for new particles decaying to a jet and an emerging jet*, J. High Energy Phys. 02 (2019), p. 179, doi: [10.1007/JHEP02\(2019\)179](https://doi.org/10.1007/JHEP02(2019)179), arXiv: [1810.10069 \[hep-ex\]](https://arxiv.org/abs/1810.10069).
- [137] T. SJÖSTRAND et al., *An Introduction to PYTHIA 8.2*, Comput. Phys. Commun. 191 (2015), pp. 159–177, doi: [10.1016/j.cpc.2015.01.024](https://doi.org/10.1016/j.cpc.2015.01.024), arXiv: [1410.3012 \[hep-ph\]](https://arxiv.org/abs/1410.3012).
- [138] A. SOPCZAK, *Precision Measurements in the Higgs Sector at ATLAS and CMS*, PoS Proc. Sci. FFK2019 (Jan. 2020), p. 006, doi: [10.22323/1.353.0006](https://doi.org/10.22323/1.353.0006), arXiv: [2001.05927 \[hep-ex\]](https://arxiv.org/abs/2001.05927).
- [139] M. J. STRASSLER and K. M. ZUREK, *Echoes of a hidden valley at hadron colliders*, Phys. Lett. B 651 (2007), pp. 374–379, doi: [10.1016/j.physletb.2007.06.055](https://doi.org/10.1016/j.physletb.2007.06.055), arXiv: [hep-ph/0604261 \[hep-ph\]](https://arxiv.org/abs/hep-ph/0604261).
- [140] M. TANABASHI et al., *Review of Particle Physics*, Phys. Rev. D 98 (3 Aug. 2018), p. 030001, doi: [10.1103/PhysRevD.98.030001](https://doi.org/10.1103/PhysRevD.98.030001).
- [141] A. VICENTE, *Anomalies in $b \rightarrow s$ transitions and dark matter*, Adv. High Energy Phys. 2018 (2018), p. 3905848, doi: [10.1155/2018/3905848](https://doi.org/10.1155/2018/3905848), arXiv: [1803.04703 \[hep-ph\]](https://arxiv.org/abs/1803.04703).
- [142] S. WEINBERG, *Cosmology*, Cosmology, OUP Oxford, 2008, ISBN: 9780191523601.
- [143] S. D. M. WHITE and M. J. REES, *Core condensation in heavy halos: a two-stage theory for galaxy formation and clustering*, Mon. Not. R. Astron. Soc. 183.3 (1978), p. 341, doi: [10.1093/mnras/183.3.341](https://doi.org/10.1093/mnras/183.3.341).
- [144] C. YOZIN and K. BEKKI, *The quenching and survival of ultra-diffuse galaxies in the Coma cluster*, Mon. Not. R. Astron. Soc. 452.1 (2015), pp. 937–943, doi: [10.1093/mnras/stv1073](https://doi.org/10.1093/mnras/stv1073), arXiv: [1507.05161 \[astro-ph.GA\]](https://arxiv.org/abs/1507.05161).
- [145] A. ZABI et al., *The CMS Level-1 Calorimeter Trigger for the LHC Run II*, J. Instrum. 12.01 (Jan. 2017), p. C01065, doi: [10.1088/1748-0221/12/01/c01065](https://doi.org/10.1088/1748-0221/12/01/c01065).

GLOSSARY

***b*-jet** A jet identified by a given algorithm or classifier as originating from a b quark.

PARTICLE FLOW algorithm An event reconstruction algorithm used in CMS. Information from all subdetectors is combined so that all stable particles can be identified. Jets are clustered, and complex objects such as b -jets are classified.

anti- k_{T} algorithm A sequential clustering algorithm designed to group hadronic particles into jets with a radius parameter R . The transverse momentum is symbolised as k_{T} instead of p_{T} . In CMS, standard radius parameters are $R = 0.4$ and $R = 0.8$, referred to as AK4 and AK8 jets, respectively.

control region A region of phase space orthogonal to the signal region, typically by requiring an object that would otherwise be vetoed in the signal region. A control region enriched in a background process present in the signal region (such as $W(\rightarrow \ell\nu) + \text{jets}$) can be used to model its influence more accurately.

jet A collimated shower of hadronic particles. High momentum quarks and gluons fragment and radiate; the resulting particles combine into hadrons due to colour confinement and deposit energy in the detector very close to each other and is reconstructed as a single physics object called a jet.

luminosity Instantaneous luminosity is a measure of the collision rate in a particle accelerator (given in units of area per unit time). The integrated luminosity is the instantaneous luminosity integrated over time and is a metric for measuring the total amount of data delivered by an accelerator or collected by a detector.

missing transverse energy The negative vector sum of the transverse momentum of all particles in a collider event. It is sometimes abbreviated to “MET” with the symbol $\vec{E}_{\mathrm{T}}^{\mathrm{miss}}$, and also referred to in literature as “missing transverse momentum” ($\vec{p}_{\mathrm{T}}^{\mathrm{miss}}$).

GLOSSARY

pileup The term ascribed to additional proton-proton collisions during a bunch crossing. Pileup interactions typically produce a large number of low-momentum particles.

semi-visible jet A shower of standard model and dark hadrons from the decay of a leptophobic Z' or Φ mediator that couples the hidden sector to the standard model.

sideband A region of phase space orthogonal to the signal region, typically by inverting kinematic requirements. Similar to a control region, a sideband enriched in a background present in the signal region (such as QCD) can be used to model it more accurately.

ACRONYMS

CMSSW CMS SoftWare.

ALICE A Large Ion Collider Experiment.

AOD Analysis Object Data.

ATLAS A Toroidal LHC ApparatuS.

BSM beyond the standard model.

CERN *Organisation Européenne pour la Recherche Nucléaire* (European Organisation for Nuclear Research).

CMS Compact Muon Solenoid.

DAQ data acquisition.

ECAL electromagnetic calorimeter.

FASER ForwArd Search ExpeRiment.

FCC Future Circular Collider.

FNAL Fermi National Accelerator Laboratory.

GSF gaussian sum filter.

HCAL hadron calorimeter.

HF hadron forward calorimeter.

HL-LHC High Luminosity Large Hadron Collider.

ACRONYMS

HLT High-Level Trigger.

ILC International Linear Collider.

JEC jet energy corrections.

JER jet energy resolution.

JES jet energy scale.

L1 Level-1.

L1T Level-1 Trigger.

LHC Large Hadron Collider.

LO leading order.

LSP lightest supersymmetric particle.

LZ LUX-ZEPLIN.

MC Monte Carlo.

MoEDAL Monopole and Exotics Detector at the LHC.

MOND modified Newtonian dynamics.

NLO next-to-leading order.

NNLO next-to-next-to-leading order.

PF PARTICLE FLOW.

POG Physics Object Group.

PS Proton Synchrotron.

PSB Proton Synchrotron Booster.

QCD Quantum Chromodynamics.

SM standard model.

SPS Super Proton Synchrotron.

SUSY supersymmetry.

TOTEM TOTal Elastic and diffractive cross section Measurement.

VBF vector boson fusion.

WIMP Weakly Interacting Massive Particle.

